

**Stability, Accuracy, and Robustness of the  
Time Domain Integral Equation Method for  
Radar Scattering Analysis**

Elwin van 't Wout



Stability, Accuracy, and Robustness of the  
Time Domain Integral Equation Method for  
Radar Scattering Analysis

PROEFSCHRIFT

ter verkrijging van de graad van doctor  
aan de Technische Universiteit Delft,  
op gezag van de Rector Magnificus prof.ir. K.C.A.M. Luyben,  
voorzitter van het College voor Promoties, in het openbaar te verdedigen op  
maandag 11 november 2013 om 15:00 uur

door

Elwin VAN 'T WOUT

wiskundig ingenieur

geboren te Rotterdam

Dit proefschrift is goedgekeurd door de promotor:  
Prof.dr.ir. C. Vuik

Copromotor: Dr.ir. D.R. van der Heul

Samenstelling promotiecommissie:

Rector Magnificus,	voorzitter
Prof.dr.ir. C. Vuik,	Technische Universiteit Delft, promotor
Dr.ir. D.R. van der Heul,	Technische Universiteit Delft, copromotor
Prof.dr. E. Michielssen,	University of Michigan
Prof.dr. D. De Zutter,	Universiteit Gent
Prof.dr.ir. J. J. W. van der Vegt,	Universiteit Twente
Prof.ir. P. van Genderen,	Technische Universiteit Delft
Dr. H. van der Ven,	Nationaal Lucht- en Ruimtevaartlaboratorium
Prof.dr.ir. C. W. Oosterlee,	Technische Universiteit Delft, reservelid

Dr. H. van der Ven heeft als begeleider in belangrijke mate aan de totstandkoming van het proefschrift bijgedragen.

Stability, accuracy, and robustness of the Time Domain Integral Equation method for radar scattering analysis.

Dissertation at Delft University of Technology.

Copyright © 2013 by Elwin van 't Wout.

ISBN 978-94-6203-463-1





The work described in this thesis is conducted entirely in the framework of the NLR programme “Kennis als Vermogen”.

Supervision has been conducted on a daily basis by Dr. Harmen van der Ven of the Flight Physics and Loads department of NLR in cooperation with the Numerical Analysis group of the Delft Institute of Applied Mathematics.

The NLR is granted publication right for this dissertation as NLR-TP-2013-449, see also [www.nlr.nl](http://www.nlr.nl).



# Preface

*Labour not to be rich:  
cease from thine own wisdom.*

PROVERBS 23:4

This dissertation completes four years of research conducted at the National Aerospace Laboratory NLR, in collaboration with Delft University of Technology. The aim of this research is to design a computational method that can be used by NLR for radar scattering analysis of aircraft. The use of computer predictions can be very powerful, but is only feasible when the simulations are realistic. In this thesis, mathematical techniques are used to design a computational method in which I have confidence it is *stable* and *robust*. This is pictured in the photograph on the cover, where the birds are confident that the rock formation is *stable* and *robust*.

It has been a very enjoyable and valuable experience for me to perform my PhD study in a combination of the company-like environment at NLR and the academic setting at TU Delft. Here, I would like to acknowledge that this thesis cannot be attributed to only one person, as suggested by the single author. This thesis could not have been completed without the support of many people and I want to thank a number of them in this preface.

The research for this dissertation could not have been conducted without the financial support of the National Aerospace Laboratory NLR. I am very grateful to NLR for funding the research and providing me with plenty of resources to perform research and visit international conferences.

I would like to express my sincere appreciation to my promotor Kees Vuik. Kees, we have had many interesting discussions about this research and I have learned a lot from your broad knowledge of applied mathematics. You have taught me how to conduct and disseminate research and I am grateful for your guidance during my academic education triple of BSc-MSc-PhD studies.

During this research project, I have had the privilege of having two daily supervisors, Duncan van der Heul and Harmen van der Ven. Duncan, your careful reading has improved the readability of our papers and this thesis and your modern ideas about presentations have been valuable for the conferences I have visited. Harmen, your knowledge of mathematics has been helpful to



analyze the computational method and you have kick-started the implementation of the computer code. Duncan and Harmen, your help has been more important to the success of this thesis than my solitary hours at the office.

I have been working at NLR for the past four years and I want to thank my colleagues for this memorable time. Koen, as the department manager you have kept an eye on the practical application and have given me freedom to perform my research. Jaap, it has been a pleasure to share an office with you for four years. Wybe, I am glad to have had your company as a fellow PhD student. Okko, Michel, Bimo, and Bambang, we have been walking miles together from our offices to the coffee machine. Michel, Johan, Jan, and Frank, we have had many entertaining discussions during the lunch break. Furthermore, I would like to thank Stephan, Martin, Hans, Bart, and André of the AVFP department, Rosita for administrative support, Rob for computer support and Monique and Ronald for their help with the cover design.

I have visited TU Delft once a week and I am grateful to my colleagues at the numerical analysis group who were always very welcome to me, both the permanent staff and the continuously changing group of PhD students. I would like to thank Martin van Gijzen in particular, who encouraged me to pursue a PhD study and taught me essential mathematical techniques as my MSc supervisor and teacher of the BSc course on numerical analysis.

I have had the opportunity to attend several conferences across the USA and Europe and I am looking back to these visits with great enjoyment. This can be attributed to many people with whom I have had interesting scientific discussions and delightful visits to restaurants and bars.

I want to express my gratitude to the doctoral committee who have read my thesis and have given valuable feedback. I am especially honored by the presence of Eric Michielssen, we have already met in the United States and hopefully we will work together after my graduation.

No matter how much I enjoyed my work as a PhD researcher, it has always been a pleasure to cycle away from office and meet family and friends. Although they might not have had direct influence on this thesis, their companionship has been very important to me.

Ik heb vele huisgenoten meegemaakt in Aalsmeer, waarvan ik Jan, Marco, Deborah en Doreen speciaal wil bedanken voor de gezellige avonden in onze gemeenschappelijke keuken. De weekenden en vakanties waren een plezierige verandering van omgeving, waarvoor ik Bart, Arjan, Arjan, Wilco, Menno, Johan en de andere voetbalvrienden wil bedanken. Daarnaast wil ik Deborah, Matthijs, Marianne en Debby bedanken voor de fijne zondagavonden.

Mijn laatste en belangrijkste dankwoord wil ik richten aan mijn ouders, Joël, Judith en Esther. Dankzij jullie is Ridderkerk voor mij nog steeds *thuis*.

Elwin van 't Wout  
Ridderkerk, October 2013

# Summary

## Stability, accuracy, and robustness of the time domain integral equation method for radar scattering analysis

Elwin van 't Wout

The aim of this thesis is to design a computational method that can be used in modern stealth technology. In particular, the computational method should be capable to simulate scattering of ultra-wideband radar signals for military aircraft constructed with ferromagnetic radar absorbent materials. A full-wave boundary element method has been chosen because of its efficiency for electromagnetic scattering of electrically large structures. A time-domain method has been chosen because wideband signals can be simulated with a single run. Moreover, the future use of nonlinear constitutive equations for ferromagnetic materials requires simulation in time domain. To this end, the Time Domain Integral Equation (TDIE) method is used as computational method. More specifically, the numerical discretization of the Electric Field Integral Equation (EFIE) is given by the Marching-on-in-Time (MoT) scheme, which has been chosen because of its efficiency and accuracy. Instabilities prevent its industrial application to stealth technology, even for smallband and linear constitutive equations. In this thesis, a thorough numerical analysis on stability, accuracy, and robustness has been derived, resulting in clear guidelines for the choice of numerical parameters. Consequently, stable computer simulations have been achieved.

**Stability** The occurrence of instabilities is the principal limitation of the TDIE method and is the most important hurdle to industrial application. They can be categorized as spectral and numerical instabilities, where the numerical ones are the most persistent. An overview of the remedies introduced in literature has been given, but none of them have solved instability altogether. The use of smooth basis functions and very accurate evaluation



of the discretization matrix are the most promising avenues to proceed. The stability of the EFIE can be analyzed with the aid of an available functional framework. For a specific variational problem, uniqueness and boundedness of the solution of the EFIE has been proven. In this thesis, this stability theorem has been extended to the differentiated version of the EFIE, for which an extra order of regularity is required for the test space. However, it can not be applied directly to the MoT scheme. A discrete equivalence with space-time Galerkin methods is derived for this purpose. Then, quadratic spline basis functions can be shown to fit within the stable framework, whereas this is not the case for shifted Lagrange polynomials. Even for the choice of spline basis functions, the expected stability can only be achieved when the computation method uses accurate evaluation procedures for the elements of the discretization matrix.

**Accuracy** The accuracy of the discretization in time of the TDIE method has been analyzed with a derivation of the interpolation accuracy for piecewise polynomial basis functions in MoT schemes. Families of temporal basis functions have been derived for a given order of interpolation accuracy. The degrees of freedom have been chosen with predefined requirements on 1) the inclusion of customary temporal basis functions, 2) smoothness, and 3) conditioning of the system of linear equations that has to be solved. With this framework for the design of temporal basis functions both classical temporal basis functions such as the shifted Lagrange interpolators and novel spline basis functions have been generated. Computational experiments confirm the improved performance of numerical quadrature for smooth basis functions and a dependency of the conditioning of the system of linear equations on the shape of temporal basis functions. Numerical experiments show a higher order of global accuracy for the spline basis functions than for the shifted Lagrange basis functions with equal support.

**Robustness** The quasi-exact integration method is a key to the successful application of MoT schemes in TDIE methods for electromagnetics. Available analytical expressions for the exact evaluation of the radiation fields have to be reformulated for evaluation in finite precision arithmetic. The straightforward formulation does not necessarily lead to the accuracy required for late-time stability of the MoT scheme, because it is ill behaved for a number of limit cases. This is confirmed with a computational experiment. Hence, a novel formulation with well-behaved expressions has been derived in this thesis, along with specifically designed tolerance regions. This robust formulation does not impinge on the overall accuracy of the quasi-exact integration method and results in a stable MoT scheme.

**Application** The applicability of the TDIE method has been verified with a comparison of the radar cross-section of an aircraft with a frequency-domain simulation. As postprocessing of the TDIE method, the scattered electric field has been computed and visualized for a corner reflector and aircraft. High resolution range profiles are promising tools for non-cooperative target recognition. The computation of these profiles can be performed in a single run with TDIE methods. They give valuable information on the characteristics of the scatterer object.

With the aid of the mathematics in this thesis, well-founded choices can be made for the use of the TDIE method as simulation tool. The recommendations result in computer simulations that are stable, accurate, and robust and the scattering of radar signals on aircraft can be predicted realistically.





# Samenvatting

## Stabiliteit, nauwkeurigheid en robuustheid van de tijdsdomein-integraalvergelijkingsmethode voor radarverstrooiingsanalyse

Elwin van 't Wout

In dit proefschrift wordt een rekenmethode ontwikkeld waarmee de verstrooiing van radarsignalen op een vliegtuig uitgerekend kunnen worden. Deze methode is ontwikkeld met als doel om te gebruiken voor stealth-technologie. De zichtbaarheid van militaire vliegtuigen kan verminderd worden door ferromagnetische radarabsorberende materialen te gebruiken. Daarnaast is het van belang dat *ultra-wideband* radargolven gesimuleerd kunnen worden. Voor deze toepassing is de randelementmethode een goede keuze aangezien deze methode efficiënt is voor elektrisch grote voorwerpen. Met een formulering in het tijdsdomein kunnen *ultra-wideband* radargolven in een enkele simulatie doorgerekend worden. Bovendien is dit geschikt voor de toekomstige toepassing van niet-lineaire constitutieve vergelijkingen voor ferromagnetische materialen. Om deze redenen is de tijdsdomein-integraalvergelijkingsmethode (TDIE) gekozen. Als modelvergelijking wordt de *Electric Field Integral Equation* (EFIE) gebruikt en als numerieke discretisatie is gebruik gemaakt van het *Marching-on-in-Time* (MoT) schema, omdat dit een efficiënt en nauwkeurig schema is. Aangezien simulaties met dit schema regelmatig instabiel zijn, kan de huidige versie nog niet gebruikt worden voor industriële toepassing in stealth-technologie, zelfs niet voor smalle bandbreedtes en lineaire constitutieve vergelijkingen. In dit proefschrift wordt een analyse uitgevoerd voor de stabiliteit, nauwkeurigheid en robuustheid. Dit resulteert in duidelijke richtlijnen voor de keuze van numerieke parameters. Met dit verbeterde numerieke schema zijn de computersimulaties stabiel.

**Stabiliteit** De voornaamste tekortkoming van de TDIE-methode is de instabiliteit, waardoor de methode nog niet gebruikt kan worden voor indus-



triële toepassingen. Instabiliteiten kunnen onderverdeeld worden in spectrale en numerieke oorzaken, waarbij de numerieke de meest hardnekkige zijn. Er is een overzicht van oplossingsmethodes uit de literatuur gegeven, maar geen enkele techniek kan de instabiliteit in zijn geheel oplossen. Het gebruik van gladde basisfuncties en het zeer nauwkeurig uitrekenen van de elementen van de discretisatiematrix zijn de meest belovende routes naar stabiliteit. Om de stabiliteit van de EFIE te analyseren wordt gebruik gemaakt van een beschikbaar raamwerk uit de functionaalanalyse. Voor een specifiek variationeel probleem is de uniciteit en begrensdsheid van de EFIE bewezen. Deze stabiliteitsstelling wordt in dit proefschrift uitgebreid naar de gedifferentieerde versie van de EFIE, waarvoor een extra orde van differentieerbaarheid vereist is voor de testruimte. Vervolgens is aangetoond dat de kwadratische spline-basisfuncties binnen het stabiele raamwerk passen, terwijl dit niet het geval is voor de verschoven Lagrange-basisfuncties. Echter, de verwachte stabiliteit voor de keuze van spline-basisfuncties kan alleen verkregen worden als de discretisatiematrix nauwkeurig genoeg wordt uitgerekend.

**Nauwkeurigheid** De nauwkeurigheid van de discretisatie in de tijd van de TDIE-methode is onderzocht met een afleiding van de interpolatienauwkeurigheid van stuksgewijs polynomiale basisfuncties in MoT-schema's. Deze analyse resulteert in families van tijdsbasisfuncties die een gegeven orde van interpolatienauwkeurigheid hebben. De beschikbare vrijheidsgraden zijn aan de hand van de volgende voorschriften gekozen: 1) het inbegrip van de gebruikelijke tijdsbasisfuncties, 2) de differentieerbaarheid en 3) de conditionering van het systeem van lineaire vergelijkingen dat opgelost moet worden. Met dit raamwerk kunnen verschillende tijdsbasisfuncties ontworpen worden, waaronder de klassieke keuze van verschoven Lagrange-interpolatoren en de nieuwe spline-basisfuncties. Met computerexperimenten is de verbeterde prestatie van de numerieke kwadratuur voor gladde basisfuncties bevestigd. Daarnaast is aangetoond dat de conditionering van het systeem van lineaire vergelijkingen afhankelijk is van de vorm van de tijdsbasisfunctie. Ten slotte laten numerieke resultaten een hogere orde van globale nauwkeurigheid zien voor de spline-basisfuncties, vergeleken met verschoven Lagrange-basisfuncties met dezelfde drager.

**Robuustheid** Om er zeker van te zijn dat de rekenmethode robuust is, zijn quasi-exact integratiemethodes noodzakelijk. Met deze technieken kunnen de oppervlakte-integralen zeer nauwkeurig uitgerekend worden. Als dit niet wordt gedaan, kunnen numerieke fouten zorgen voor instabiliteit, wat ook in experimenten wordt waargenomen. De beschikbare analytische uitdrukkingen voor de exacte evaluatie van stralingsvelden bevatten singulariteiten. Hierdoor zijn de berekeningen niet noodzakelijk nauwkeurig genoeg om langdurige stabiliteit van het MoT-schema te verkrijgen, wat wordt bevestigd

door een computereperiment. Daarom zijn er nieuwe uitdrukkingen afgeleid die nauwkeurig uitgerekend kunnen worden, ook als er afrondfouten zijn. Dit vereist wel het gebruik van speciale tolerantiegebieden. Het gebruik van deze robuuste uitdrukkingen behoudt de nauwkeurigheid van de quasi-exacte integratiemethode en zorgt voor een stabiel MoT-schema.

**Toepassing** De toepasbaarheid van de TDIE-methode is geverifieerd door de radardoorsnede (RCS) van een vliegtuig te vergelijken met een simulatie in het frequentiedomein. Als nabewerking van de TDIE-methode is het verstrooide elektrische veld uitgerekend en gevisualiseerd voor een hoekreflector en een vliegtuig. Een veelbelovende techniek voor *non-cooperative target recognition* is het gebruik van *high resolution range profiles*. Om deze profielen uit te rekenen met frequentiedomeinpakketten zijn er meerdere simulaties nodig, terwijl dit met de TDIE-methode in slechts een enkele simulatie uitgerekend is. Met deze techniek kan waardevolle informatie over de eigenschappen van het voorwerp verkregen worden.

Met de wiskunde in dit proefschrift kunnen er gefundeerde keuzes gemaakt worden voor het gebruik van de TDIE-methode als simulatiepakket. Met deze aanbevelingen zijn er computersimulaties uitgevoerd die stabiel, nauwkeurig en robuust zijn en waarmee de verstrooiing van radarsignalen op een vliegtuig realistisch voorspeld kan worden.





# Contents

<b>Preface</b>	<b>v</b>
<b>Summary</b>	<b>vii</b>
<b>Samenvatting</b>	<b>xi</b>
<b>1 Introduction</b>	<b>1</b>
1.1 Significance of this thesis . . . . .	1
1.2 Stealth technology . . . . .	2
1.2.1 Radar signature of airborne platforms . . . . .	2
1.2.2 Radar signature management . . . . .	4
1.2.3 Radar signature analysis . . . . .	5
1.3 Computational electromagnetics . . . . .	6
1.3.1 Electromagnetic scattering models . . . . .	7
1.3.2 Overview of model formulations . . . . .	7
1.3.3 Choice of computational method . . . . .	12
1.4 Outline . . . . .	13
<b>2 Methodology</b>	<b>15</b>
2.1 TDIE method . . . . .	15
2.1.1 Governing equations in electromagnetics . . . . .	15
2.1.2 Boundary integral formulation . . . . .	18
2.1.3 Numerical discretization in space-time . . . . .	21
2.1.4 Discretization method in space . . . . .	23
2.1.5 Discretization method in time . . . . .	25
2.2 MoT scheme . . . . .	31
2.2.1 Numerical discretization . . . . .	31
2.2.2 Temporal basis functions . . . . .	33
2.2.3 Matrix assembly . . . . .	35



2.2.4	Marching procedure . . . . .	36
2.2.5	Acceleration methods . . . . .	37
2.2.6	Incident wave field . . . . .	38
<b>3</b>	<b>Stability</b>	<b>43</b>
3.1	Stability of TDIE methods . . . . .	43
3.2	Analysis of instabilities . . . . .	44
3.2.1	A posteriori stability analyses . . . . .	44
3.2.2	A priori stability analyses . . . . .	49
3.3	Types of instabilities . . . . .	50
3.3.1	Spectral instability . . . . .	51
3.3.2	Numerical instability . . . . .	53
3.4	Remedies for numerical instability . . . . .	53
3.4.1	Numerical discretization . . . . .	54
3.4.2	Model equations . . . . .	54
3.4.3	High-frequency components . . . . .	55
3.4.4	Numerical accuracy . . . . .	55
3.4.5	Functional framework . . . . .	57
3.5	Experimental suggestion . . . . .	57
3.6	Functional analysis of the original EFIE . . . . .	59
3.6.1	Functional framework . . . . .	60
3.6.2	Stability theorem . . . . .	61
3.7	Functional analysis of the differentiated EFIE . . . . .	63
3.7.1	Stability theorem of the differentiated EFIE . . . . .	63
3.7.2	Proof of the stability theorem . . . . .	64
3.8	Space-time Petrov-Galerkin schemes . . . . .	67
3.8.1	Example functions of the Sobolev spaces . . . . .	67
3.8.2	Discretely equivalent Petrov-Galerkin schemes . . . . .	68
3.8.3	Equivalence for the lowest order stable P-G scheme . . . . .	70
3.8.4	Equivalence for the quadratic Lagrange MoT scheme . . . . .	74
3.9	Provably stable MoT schemes . . . . .	76
3.9.1	Computational experiments . . . . .	76
3.9.2	Caveats in the stability theorem . . . . .	77
3.9.3	Extension to other model equations . . . . .	78
<b>4</b>	<b>Accuracy</b>	<b>81</b>
4.1	Accuracy in time of the MoT scheme . . . . .	81
4.2	Framework to design temporal basis functions . . . . .	82
4.3	Derivation of the interpolation accuracy . . . . .	83
4.3.1	Interpolation in finite element methods . . . . .	83
4.3.2	Interpolation accuracy of quadratic basis functions . . . . .	84
4.3.3	Interpolation accuracy of cubic basis functions . . . . .	87
4.4	Design of temporal basis functions . . . . .	88
4.4.1	Customary temporal basis functions . . . . .	88

4.4.2	Smooth temporal basis functions . . . . .	89
4.4.3	Conditioning of the leading interaction matrix . . . . .	90
4.5	Experimental confirmation . . . . .	92
4.5.1	Interpolation accuracy . . . . .	93
4.5.2	Smoothness . . . . .	93
4.5.3	Quadrature accuracy . . . . .	94
4.5.4	Global accuracy . . . . .	96
4.5.5	Condition number . . . . .	98
<b>5</b>	<b>Robustness</b>	<b>103</b>
5.1	The influence of numerical errors on stability . . . . .	103
5.2	Quasi-exact integration methods . . . . .	104
5.3	Analytical formulation of radiation fields . . . . .	106
5.3.1	Derivation of standard intersection integrals . . . . .	107
5.3.2	Derivation of standard contour integrals . . . . .	107
5.3.3	Analytical expression for standard line integrals . . . . .	108
5.3.4	Analytical expression for standard arc integrals . . . . .	111
5.3.5	Analytical expression for standard pole integrals . . . . .	111
5.3.6	Zero projection height . . . . .	111
5.4	Finite precision arithmetic . . . . .	112
5.4.1	Straightforward formulation . . . . .	112
5.4.2	Requirements on robust formulations . . . . .	114
5.5	Robust formulation of analytical expressions . . . . .	115
5.5.1	Robust formulation near an edge . . . . .	115
5.5.2	Robust formulation near the extension of an edge . . . . .	117
5.5.3	Robust formulation near a vertex . . . . .	118
5.5.4	Summary of robust formulation . . . . .	121
5.5.5	Zero projection height . . . . .	121
5.6	Tolerance regions . . . . .	123
5.6.1	Requirements on tolerance regions . . . . .	123
5.6.2	Definition of tolerance regions . . . . .	124
5.7	Experimental confirmation . . . . .	125
<b>6</b>	<b>Application</b>	<b>129</b>
6.1	Verification . . . . .	129
6.1.1	The test case of a generic aircraft . . . . .	129
6.1.2	Comparison with the method of moments . . . . .	130
6.2	Radar scattering analysis . . . . .	132
6.2.1	Scattered electric field . . . . .	132
6.2.2	High resolution range profile . . . . .	138
<b>7</b>	<b>Conclusions</b>	<b>143</b>



<b>8 Recommendations</b>	<b>145</b>
8.1 Best practices . . . . .	145
8.2 Future research . . . . .	146
<b>Curriculum vitae</b>	<b>149</b>
<b>Publications</b>	<b>151</b>
<b>Bibliography</b>	<b>155</b>

# Chapter 1

## Introduction

### 1.1 Significance of this thesis

**Problem area** Stealth technology is key to the survivability of fighter aircraft. Extensive full-scale experiments are used for the design of low-observable structures. Computer simulations complement physical experiments when the platform is unavailable for a measurement campaign, with the added advantage of having low costs. Advanced computational methods can provide high-confidence radar data for most aircraft. The latest developments in stealth technology call for the use of computer simulations in time domain on the scatterer surface, the so-called Time Domain Integral Equation (TDIE) method. However, the radar signature is not always simulated realistically due to instabilities in current implementations. Improvement of the computational robustness is required to be applicable in the industrial design process.

**Description of work** This thesis complements the existing literature by analyzing the stability, accuracy, and robustness of the TDIE method. The stability has been analyzed with an extension of an available mathematical framework. In order to use the resulting stability theorem for the broadly used Marching-on-in-Time (MoT) scheme, an equivalence has been derived with the space-time Galerkin scheme. The accuracy in time of the TDIE method has been analyzed with a derivation of the interpolation error. Finally, a robust implementation of the analytical evaluation of radar fields for discrete interactions between mesh patches has been explained.

**Results and conclusions** The work that is presented in this thesis improves both the theoretical foundation and the practical implementation of



the TDIE method. In particular, the numerical analysis of stability and accuracy has been used to provide clear guidelines on how to choose numerical parameters such as the temporal basis function and the quadrature procedure. Implementation of this improved MoT scheme provides robust computer simulations that are stable and accurate.

## 1.2 Stealth technology

The development of aircraft is one of the major technological advancements made in the military in the latest century. With very few natural obstructions, air forces can achieve quick movement into hostile territory. Evidently, military defense systems try to intercept these missions. For the survivability of the aircraft and the safety of the pilot it is very important to be low observable. Stealth technology aims to design aircraft that are hardly noticeably to adversaries. This includes the reduction of the radar, heat, noise, and infrared observability. This thesis focuses on the management of the radar visibility. The primary reason to use stealth technology in military aircraft is improving the survivability. Furthermore, when applied successfully and a technological advantage over the opponent is obtained, stealth technology has a deep impact on military tactics.

Where aircraft designers reduce the radar visibility with stealth technology, radar developers simultaneously try to improve radar systems that can identify aircraft. Counterstealth measures are used in defensive configurations to detect hostile aircraft. This results in an everlasting process of measures and countermeasures in stealth technology. The following material serves as a short introduction only. For more information, the interested reader is referred to the extensive literature on stealth technology, for example [95, 13, 53, 52, 59].

### 1.2.1 Radar signature of airborne platforms

Aircraft can be distinguished by the scattered radar field, called the *radar signature*. Radar systems are used by military forces for the recognition of both friendly and hostile aircraft. As a consequence, stealth aircraft are designed such that its radar signature can not be identified by the opponent.

#### Low observability

An example of the successful application of stealth technology in the military is the famous F-117 designed by Lockheed for the US Air Force. The ‘Nighthawk’ was able to penetrate deep into hostile territory without being noticed. Striking feature of this stealth fighter is its shape, as can be seen in Fig. 1.1. Faceting has been adopted to reflect incident radar fields away from

the source. The radar visibility has been further reduced with the use of *radar absorbent materials* (RAM) that dissipate part of the radar energy. Nowadays, low observability is always achieved with combined techniques from airframe shape optimization and construction with RAM.



(a) The faceted shape of the airframe reduces the monostatic radar visibility.

(b) Least visible among fighter aircraft. From left to right: an F-22, F-117, F-4, and F-15 of the US Air Force.

Figure 1.1: The F-117 Nighthawk. Source: [www.defense.gov/multimedia](http://www.defense.gov/multimedia).

### Defensive target identification

The main purpose of defensive radar systems is the detection of hostile aircraft. Conventional configurations use pulse-Doppler radar that transmits modulated pulses of a single, fixed carrier frequency. The pulse width is sufficiently long to embed the scattering object in a continuous electromagnetic wave. Since stealth technology has reduced the visibility for these particular radar fields, new radar concepts have been developed. There is a strong interest in ultra-wideband (UWB) radar, which uses very short, nearly square pulses. These high power fields have a wide spectral content and are therefore difficult to dissipate with RAM. Moreover, UWB radar is able to detect slow moving or stationary targets.

### Non-cooperative target recognition

Several combat cases are known in which a friendly platform has been identified as hostile and was fatally attacked. Reducing the fratricide is especially challenging in military missions with joint multinational forces. Usually, friendly aircraft are recognized by interchanging encrypted signals. This is not feasible in certain situations, for instance when the transmitter is deceived or jamming is used by a hostile party. This calls for non-cooperative target recognition (NCTR), for which the active participation of the target is not necessary. The radar is an attractive instrument for this purpose. The



idea is to derive the geometry of the platform from its radar signature with the aid of high resolution range profiles. A comparison with a database results in the decision of friend or foe. The main limitations of this type of target recognition are the need to quickly process the radar data and the comparison with a database in which the radar signatures of both friendly and hostile aircraft have to be present.

### 1.2.2 Radar signature management

The goal of stealth technology is to conceal aircraft by reducing the radar visibility. The main approaches in the radar signature management are the deflection of radar fields and the absorption of radar energy. RAM can dissipate part of the incident radar energy and thus reduces the magnitude of the scattered radar field. In most cases, it is more effective to deflect the radar field away from the source. Then, the deflected radar waves remain unnoticed, because defensive radar systems often have the transmitter and receiver at the same location.

#### Shape optimization

The most critical factor in the radar detectability of aircraft is the shape. This has to be incorporated in the early beginning of the design process and is usually at the expense of other considerations such as cruising speed and agility. Other challenges are in the design of aircraft components that are necessary for the flight performance but have a large radar signature, such as the weapon bays, engines, air intakes and the cockpit canopy.

The airframe shape adopted in early stealth fighters such as the F-117 is largely based on faceting. The idea is that the facets are tilted with a specific angle such that the radar fields from common angles of incidence are deflected in a direction where no receiver is likely to be present. Wings and tails are canted to avoid direct reflection back towards the ground or aircraft at the same altitude. Then, the monostatic radar signature is very small. In later designs of stealth fighters, this deflection has been achieved by smooth surfaces instead of flat facets.

Deflecting the radar field has become less effective with the deployment of bistatic geometries, that is, radar transmitters and receivers at different locations. Moreover, shape alignment poses severe challenges in the design of multirole aircraft. Nevertheless, the shape of an aircraft is still the deciding factor in its radar visibility.

#### Radar absorbent materials

As a complement to shape optimization, radar absorbent materials can be used in the construction of stealth aircraft. Part of the radar energy is dis-

sipated by the RAM, thus reducing the detectability. Although the RAM is effective in reducing the radar signature, the manufacturing and maintenance costs are high and its absorption rate highly depends on the frequency of the radar signal. RAM is being used with two different approaches, namely as a coating or as part of load-bearing structures.

**Radar absorbent coatings** Radar absorbent coatings serve the sole purpose of reducing the radar visibility and are often applied as a paint. To reduce costs of operation, RAM is only used on aircraft parts that have a large radar signature, such as sharp edges and the cockpit canopy. The effective radar reduction of the coatings can be based on interference or absorption.

When a dielectric layer, such as the Salisbury screen, is used with a thickness of a quarter wavelength, the scattered radar field is canceled because of interference. More elaborate multilayer variants such as the Jaumann and Dallenbach layers use resonance patterns to cancel radar fields at different frequencies. These dielectric coatings work for small frequency bands only and become prohibitively thick for low frequencies.

Materials can have the property that radar fields are converted into heat. Application of these materials in stealth technology has the advantage of absorbing the radar energy for a large frequency band with a small coating thickness. Ferromagnetic material is a main candidate for this type of RAM. The magnetization of ferromagnetic materials show a nonlinear response to electromagnetic excitation. The response behavior is dispersive and shows profound hysteresis, which makes the absorption rate history dependent. Although ferromagnetism is usually understood with physical phenomena on a microscopic level, macroscopic models are often used in practice.

**Radar absorbent components** The materials used in the construction of aircraft are mainly chosen according to their influence on the structural characteristics such as stiffness. Nowadays, extensive use is made of composite structures in which many different materials are combined. Radar absorbent materials, such as ferromagnetic nanoparticles, can also be incorporated into these composite matrices. Main advantage of using radar absorbent materials in composite load-bearing structures is that no additional layer is necessary on the surface of the aircraft.

### 1.2.3 Radar signature analysis

The management of the radar signature can only be achieved when the radar signature of aircraft can be analyzed with high confidence. Full-scale experiments with different setups can provide the required radar data. As a complement, computer simulations are being used to predict the radar signature of aircraft.



## Experimental measurements

Full-scale experiments are very effective in measuring the radar signature of available aircraft. Setups with a stationary aircraft measure the radar signature very accurate and for many different angles of incidence. The use of radar systems during training missions achieve data on the radar visibility of aircraft during flight. With these measurement campaigns, indispensable information of one own aircraft is obtained, which can be used in military tactics. For the design of new aircraft types, the radar data of similarly built aircraft can be used. However, for groundbreaking and unconventional concepts such as the F-117, the radar signature is completely different than for other aircraft. Then, physical experiments are applied to separate components or aircraft models.

## Computer simulations

The design of a stealth aircraft is a delicate task that takes a long time and consumes huge costs. Full-scale experiments are an integral part of the design process. However, measuring the radar signature with physical experiments is not feasible in many situations, for instance when

- the platform is in the development phase,
- the platform belongs to a hostile party, or
- there are financial or logistic constraints.

Computer simulations are used to predict the radar signature in these situations. In order to assure realism of the computer simulations, only advanced computational techniques that have been verified with experimental data are used.

There is a continuous development in both stealth capabilities of aircraft and new radar concepts. Most notably the use of ferromagnetic materials for low observability and UWB radar for detection. Naturally, this requires a constant improvement and extension of current computational methods to keep up with the simultaneous developments in stealth technology.

## 1.3 Computational electromagnetics

The use of computer simulations is nowadays an indispensable part in the industrial design of aircraft. The field of computational electromagnetics (CEM) has grown by leaps in past decades and bounds and delivers many different computational methods. In this section, an overview will be given of CEM methods and an explanation will be given for the choice of computational method that will be used in this thesis. All information in this

introductory section can be found in the many textbooks on CEM, for example [63, 17, 74].

### 1.3.1 Electromagnetic scattering models

First step in the development of computer simulations is the modeling of the physical phenomena. Many different models exist that describe physical observations in terms of mathematical equations. The solution of these model equations are then approximated with numerical techniques to provide predictions of specific physical quantities. The ultimate goal of this thesis is the simulation of the radar signature of aircraft designed with advanced types of RAM and excitation with modern radar concepts. This yields the following requirements on the choice of the radar scattering model to simulate

- full electromagnetic wave fields;
- ultra-wideband radar fields;
- radar absorbent materials;
- general geometries.

Maxwell's equations are the classical model for electromagnetic wave fields. Additionally, constitutive equations that model material properties are required to find a unique solutions.

The electromagnetic response of most materials, even advanced dielectric RAM, can be modeled with enough realism by linear equations or can be linearized with sufficient accuracy. This is not the case for RAM that are based on magnetic losses. For these materials, hysteresis has to be incorporated into the model. Although hysteresis and magnetic losses are physical processes that should be described on a microscopic scale, different computational models exists for the radar responses on a macroscopic level. The most promising model is given by the Landau-Lifshitz-Gilbert (LLG) equation. This is not an algebraic equation, but a nonlinear differential equation that models the time-varying and history-dependent material properties encountered in ferromagnetic materials.

### 1.3.2 Overview of model formulations

Many formulations of Maxwell's equations exist and a wide range of different computational methods are used to discretize them. When a particular radar signal is present, such as high-frequent radar fields, specific approximations can be made. Otherwise, full-wave CEM methods are used, which are written in either the frequency or time domain. Furthermore, CEM methods discretize either volume or surface formulations. This yields four different categories,



all with their merits and limitations. Remember that hybrid methods can be used as well.

### High-frequency versus full-wave methods

Most computational methods become impracticable for scattering of a high-frequency signal on an electrically large object, because the computational costs scale with the highest frequency mode. To allow for computer simulations in these cases, several methods are available that adopt high-frequency approximations to reduce the computational complexity. They include the general theory of diffraction (GTD) and physical optics (PO). So-called *full-wave methods* do not use high-frequency approximations and solve Maxwell's equations directly.

High-frequency methods usually assume a combination of: 1) the surface current on the shadowed regions is zero, 2) the observation point is far away, 3) the surface is smooth, and 4) the object is electrically large. These assumptions evidently impinge on the accuracy of the computational method. For instance, edge diffraction, multiple reflection, resonance in cavities, and surface waves that creep into the shadow region are not simulated. In general, the low computational costs of high-frequency methods only outweighs the accuracy limitations when scattering from electrically large objects for radar signals with high-frequency content only is considered. For the application to modern stealth technology, computational methods have to be able to simulate wideband radar scattering from aircraft constructed with cavities and RAM. Then, high-frequency methods are not feasible and full-wave methods are required.

### Differential versus integral methods

In CEM, methods are often categorized as either a differential or integral formulation. Differential formulations solve the electromagnetic field intensity in Maxwell's equations for a certain region of interest. Reflecting and absorbing boundary conditions are necessary to truncate the computational domain. Integral formulations, on the other hand, solve Maxwell's equations for the electric charge and current density. To this end, Maxwell's equations are rewritten into an integral form with the aid of a Green's function. For interfaces between homogeneous materials, it suffices to discretize the interface only. When the materials are heterogeneous, volume discretizations are more effective.

Main drawback of differential formulations is that for unbounded domains an artificial boundary is required to truncate the computation domain, whereas integral formulations automatically satisfy the radiation condition. On the other hand, integral methods result in dense discretization matrices

whereas differential methods result in sparse discretization matrices, which can be solved considerably more efficiently.

Differential formulations are usually discretized with volume methods and integral formulations with surface methods. The only exception is the volume integral equation method, which main merit is its efficiency for thin heterogeneous layers and its natural coupling with surface integral equation methods. In general, the computational cost is very high and the method has been used relatively little compared to other CEM methods.

### Volume versus surface methods

Volume methods discretize a three-dimensional region of interest with a volumetric mesh. Because different material parameters can be used for each mesh element, these methods are especially suited for heterogeneous materials. Major drawback is that a finite region is required. Hence, for scattering problems, the computational mesh has to be truncated with an artificial boundary on which absorbing boundary conditions have to be posed. Although very accurate models for open boundaries have been derived, they are purely artificial and can therefore only reduce the physical realism of the computer simulation. Another drawback of volume methods is the tendency to disperse and dissipate electromagnetic waves.

For scattering problems with two homogeneous materials, the equivalence principle states that the electromagnetic fields are completely determined by the electromagnetic current and charge on the interface. Surface methods make grateful use of this principle by discretizing the scatterer surface instead of a volume around the object. Radiation conditions are automatically satisfied and no artificial boundary is necessary, which is the main merit of surface methods. Modeling heterogeneous materials is challenging and approximate models have to be used. Notice that aircraft are not constructed homogeneously, but when the outside of the aircraft is metallic, scattering is only determined by the surface of the aircraft and volume discretization is not necessary.

It should be noted that a combination of volume and surface methods is possible. This coupling can be advantageous when surface methods are used for heterogeneous objects or as absorbing boundary in volume methods. Furthermore, it will be assumed that volume methods use a differential formulation and surface methods an integral formulation. This excludes only the volume integral equation method, which will be omitted for brevity.

Following is a comparative list of volume and surface methods for modeling electromagnetic scattering.

### Computational mesh

**V:** The volume mesh usually consists of polyhedral elements and has to be fitted around the scatterer, which can be difficult for geometric details. For



curved surfaces, staircasing is often performed, thus introducing spurious reflections.

**S:** Grid generation is easily performed because only the surface of the scatterer has to be meshed. Triangular patches are most commonly used and can capture geometric details and curved surfaces with sufficient accuracy.

### Radiation condition

**V:** The computational domain has to be truncated with an artificial boundary for exterior problems. This open boundary should be modeled such that the full electromagnetic field is absorbed. Usually, an absorbing boundary condition is applied which has the strict requirement of being convex. Alternatively, perfectly matched layers have been derived that can have an arbitrary shape, but are computationally more expensive. As effective as modern versions might be, open boundaries remain computational artifacts.

**S:** Because the equivalence principle is used, the radiation condition is automatically satisfied. The scattered field can be described as function of the surface current and charge. Computing the scattered electromagnetic field is performed as postprocessing and calls for the integration over the whole surface and can be expensive to perform.

### Heterogeneous structures

**V:** Heterogeneous materials can be simulated effectively by using different material parameters for different mesh elements. For accuracy, it is required that the mesh elements should be smaller than the different components in the structure. In particular, coatings have to be meshed with a very high resolution, making it computationally expensive.

**S:** Surface methods are less effective for heterogeneous, penetrable objects, since the equivalence principle is difficult to use. A layered medium Green's function can be used for penetrable objects. For coatings, approximate models such as generalized impedance boundary conditions can be used.

### Efficiency

**V:** The number of spatial degrees of freedom is  $\mathcal{O}(f^3)$  for frequency  $f$ . Because discretization matrices are sparse, fast solution methods scale linear with the number of mesh elements.

**S:** The number of spatial degrees of freedom is  $\mathcal{O}(f^2)$  for frequency  $f$ . Solving the dense system of linear equations usually requires  $\mathcal{O}(n^2)$  computational work, where  $n$  denotes the number of mesh elements. For fast algorithms, most notably the fast multipole method, the computational work scales  $\mathcal{O}(n \log(n))$ , or  $\mathcal{O}(f^2 \log(f))$ . Accelerated surface methods outperform volume methods for large scale objects and high-frequent signals.

### Higher-order accuracy

**V:** Higher-order accurate techniques have been developed. In particular, the

discontinuous Galerkin (DG) method permits the use of hp-refinement. However, with these methods it is difficult to obtain higher-order accuracy for the boundary conditions.

**S:** Although higher-order accurate methods are available, they require curved patches as surface mesh, for which grid generation and postprocessing is difficult.

### **Dispersion and dissipation**

**V:** Most numerical techniques are highly dispersive and dissipative. This can only be avoided with very accurate methods and high resolution grids.

**S:** Dissipation and dispersion is hardly present in surface methods.

### **Stability of time discretization**

**V:** Stability is usually restricted by CFL conditions. When the CFL number is small enough, the stability is achieved with high confidence.

**S:** Numerical instabilities have been persistent and pose major restrictions on the computational method. This is an active field of research and a large portion of this thesis deals with stability.

### **Technology readiness level**

**V:** The robustness is confirmed by the development of commercial codes, both in frequency and time domain.

**S:** Commercial software is available in frequency domain. The time domain variants lack the robustness for application in industry.

### **Frequency versus time methods**

Many computational methods solve the model equations in the frequency domain. That is, the electromagnetic field is decomposed into a range of sinusoidal waves with different frequencies and the Fourier transform is performed. This avoids the use of discretization methods in time and computational techniques in frequency domain are usually more efficient and robust. The main merits of using time methods are that wideband signals can be simulated in a single run and nonlinear or history-dependent models for material properties can be used.

Following is a comparative list of frequency and time methods for modeling electromagnetic scattering.

### **Radar fields**

**F:** A Fourier decomposition of the radar field has to be performed. This is inaccurate in the case of sharp changes, for instance when almost-square pulses are used.

**T:** Hardly any conditions on the radar fields are imposed. Some methods require the field to be differentiable in time.



**Material properties**

**F:** Linear models for material properties can be used effectively. Moreover, frequency-dependent models are especially suited for frequency methods. However, nonlinear or history-dependent models are not feasible.

**T:** Many models for electromagnetic responses in materials can be used. In particular, nonlinear or history-dependent models can be incorporated. Time methods are less suited for frequency-dependent models.

**Causality**

**F:** The electromagnetic field is a finite series expansion with respect to sinusoidal wave fields and has thus an infinite support in time. Causality is therefore not meaningful in frequency domain.

**T:** Causality is taken into account in most discretization schemes.

**Efficiency**

**F:** In general, frequency methods are more efficient than time methods. The efficiency depends on the bandwidth of the radar signal. In particular, efficiency deteriorates significantly for wideband signals.

**T:** Time methods simulate the full electromagnetic wave in a single run. Efficiency does not depend on the bandwidth but on the highest frequency component, which is advantageous for wideband signals and low frequencies. For a small bandwidth, the computation time and storage requirements are larger than frequency methods.

**Technology readiness level**

**F:** Robust implementations are available and stability is no issue. Frequency methods have been used in industry for both the volume and surface variants.

**T:** Stability is difficult to achieve and robust implementations are burdensome, especially for surface methods. Volume methods in time domain have been used in commercial computer codes.

### 1.3.3 Choice of computational method

Many computational methods are available to model electromagnetic scattering phenomena. All of them have their specific merits and limitations. The choice of computational method depends on the type of application, which is in this case the stealth technology for aircraft. This results in the following requirements on the computational method:

1. full-wave scattering of electrically large structures have to be computed efficiently;
2. wideband signals have to be modeled;

3. nonlinear and time-varying models for material properties have to be incorporated.

The choice of computational method for this thesis is the *Time Domain Integral Equation* (TDIE) method, also known as the *Marching-on-in-Time* (MoT) scheme, which is a surface method in time domain. At first, this might sound surprising because industrial application is aimed for, whereas the surface method in time domain is the only part of the CEM spectrum that has not found its way into commercial software packages. In short, the reason to choose the TDIE method is that it has striking features for application in modern stealth technology that are not encountered in other CEM methods.

Simulating electromagnetic scattering of electrically large objects in an unbounded domain is a typical merit of boundary element methods. No artificial boundary is required and efficient computations for electrically large objects can be performed. A time-domain formulation is necessary for efficiently modeling wideband signals and incorporating sophisticated models for RAM. Modern configurations of RAM include ferromagnetic materials, which have time-varying characteristics and can only be modeled accurately with nonlinear constitutive equations. Frequency-domain methods are not feasible for these models. Concluding, the TDIE method is necessary to use for the specific application this thesis aims for.

## 1.4 Outline

The TDIE method is a promising method for application to stealth technology and has been developed and improved in the latest two decades. Still, it has not yet reached the maturity for application in an industrial environment and the incorporation of nonlinear constitutive equations remains an open question. Therefore, this thesis restricts to radar scattering of metallic structures, for which a robust implementation is a prerequisite for further development towards sophisticated RAM models.

The goal of this thesis is to improve the technology readiness level of the TDIE method. Instability of the TDIE method is the single most important problem that precludes industrial application. To this end, a large portion of this thesis concerns the numerical analysis of stability and remedies for instability will be derived. Furthermore, the accuracy in time of the MoT scheme will be analyzed and a robust implementation will be explained. Computer simulations confirm the stability, accuracy, and robustness of the improved TDIE method.

This thesis will proceed as follows. First, an overview of the TDIE method in electromagnetics will be given in Chapter 2. Then, the numerical properties stability, accuracy, and robustness will be analyzed. Finally, several results from computer simulations will be shown in Chapter 6.



Part of this thesis has already been published:

- small parts of Chapter 3 on stability has been published in proceedings [106, 111]; a journal paper is in preparation;
- Chapter 4 on accuracy is largely based on a publication in the *IEEE Transactions on Antennas and Propagation* [108] and the proceeding papers [105, 107];
- Chapter 5 on robustness is largely based on a paper accepted for publication in the *IEEE Transactions on Antennas and Propagation* [109] and a proceedings paper [110].

# Chapter 2

## Methodology

### 2.1 TDIE method

The computational method of choice in this thesis is the Time Domain Integral Equation method, which uses a boundary element formulation in time domain of Maxwell's equations. The focus will be on modeling electromagnetic scattering phenomena, because this thesis aims for applications in stealth technology. Remember that the TDIE method is not restricted to electromagnetics, it has also been applied to acoustics [29, 38, 93, 55] and elastodynamics [10, 72, 79, 51].

In this chapter, an introductory overview will be given of the TDIE method. First, the model equations for electromagnetic scattering will be given. Then, the numerical discretization in space and time will be explained. The emphasis will be on the MoT scheme, which will be used as temporal discretization procedure. The nomenclature will be introduced and literature reference are given along the exposition of the TDIE method.

#### 2.1.1 Governing equations in electromagnetics

Throughout this thesis, it will be assumed that a piecewise smooth surface  $\Gamma$  separates two three-dimensional regions  $\Omega_0$  and  $\Omega_1$ . The unit normal  $\hat{\mathbf{n}}$  on  $\Gamma$  points towards  $\Omega_0$ . Let us assume that  $\Omega_0$  is free space and  $\Omega_1$  a perfect electric conductor (PEC). Notice that scattering of multiple objects can be modeled with a disconnected region  $\Omega_1$ . Besides,  $\Gamma$  does not have to be closed, which allows the modeling of sheets and other objects of zero thickness. Although it is possible to include wires and junctions into the TDIE method, they will not be considered in this thesis.



## Field equations

The classical equations that are used to describe electromagnetic phenomena are *Maxwell's equations*, which read

$$\nabla \times \mathbf{E} = -\frac{\partial \mathbf{B}}{\partial t}, \quad (2.1a)$$

$$\nabla \times \mathbf{H} = -\frac{\partial \mathbf{D}}{\partial t} + \mathbf{J}, \quad (2.1b)$$

$$\nabla \cdot \mathbf{D} = \rho, \quad (2.1c)$$

$$\nabla \cdot \mathbf{B} = 0 \quad (2.1d)$$

for the electric field intensity  $\mathbf{E}(\mathbf{r}, t)$  in  $V/m$ , magnetic field intensity  $\mathbf{H}(\mathbf{r}, t)$  in  $A/m$ , electric flux density  $\mathbf{D}(\mathbf{r}, t)$  in  $C/m^2$  or  $As/m^2$ , magnetic flux density  $\mathbf{B}(\mathbf{r}, t)$  in  $Wb/m^2$  or  $Vs/m^2$ , electric current density  $\mathbf{J}(\mathbf{r}, t)$  in  $A/m^2$ , and electric charge density  $\rho(\mathbf{r}, t)$  in  $C/m^3$  or  $As/m^3$ . The space and time variables are denoted by  $\mathbf{r}$  and  $t$  with dimensions  $m$  and  $s$ , resp. The *continuity equation*

$$\frac{\partial \rho}{\partial t} + \nabla \cdot \mathbf{J} = 0 \quad (2.2)$$

can be derived from Maxwell's equations and relates the electric current and charge density. The electromagnetic field ( $\mathbf{E}, \mathbf{H}$ ) will be the quantity of interest. To solve Maxwell's equations, *constitutive equations* are necessary that relates the electromagnetic flux ( $\mathbf{D}, \mathbf{B}$ ) to the electromagnetic field. These equations depend on the model for the electromagnetic behavior of materials on a macroscopic scale. In this thesis, one of the easiest models will be used, that is,

$$\mathbf{D} = \epsilon \mathbf{E}, \quad (2.3a)$$

$$\mathbf{B} = \mu \mathbf{H} \quad (2.3b)$$

with the constants  $\epsilon$  and  $\mu$  denoting the permittivity and permeability of free space. The impedance and wave speed are given by  $\eta = \sqrt{\mu/\epsilon}$  and  $c = 1/\sqrt{\mu\epsilon}$ , resp. Sophisticated constitutive equations that model media more realistically can include finite conductivity, space-dependent parameters, tensors instead of scalars, or nonlinear partial differential equations such as the Landau-Lifschitz-Gilbert equation for ferromagnetic materials.

## Interface conditions

At interfaces between two media with different electromagnetic properties, additional conditions hold. These *interface conditions* or *jump conditions* relate the electromagnetic fields and fluxes in the two media and are usually derived by a limiting process of Maxwell's equations towards the interface.

For example, in the absence of sources on the interface, the magnetic field intensity is discontinuous across the interface and the electric current density  $\mathbf{J}$  is confined in a thin layer around the interface [7]. To be precise, for arbitrary  $\delta \in \mathbb{R}$ ,

$$\lim_{\delta \downarrow 0} (\hat{\mathbf{n}} \times (\mathbf{E}(\mathbf{r} + \delta \hat{\mathbf{n}}, t) - \mathbf{E}(\mathbf{r} - \delta \hat{\mathbf{n}}, t))) = \mathbf{0}, \quad (2.4a)$$

$$\lim_{\delta \downarrow 0} (\hat{\mathbf{n}} \times (\mathbf{H}(\mathbf{r} + \delta \hat{\mathbf{n}}, t) - \mathbf{H}(\mathbf{r} - \delta \hat{\mathbf{n}}, t))) = \mathbf{J}_S(\mathbf{r}, t) \quad (2.4b)$$

for  $\mathbf{r} \in \Gamma$  and  $\hat{\mathbf{n}} = \hat{\mathbf{n}}(\mathbf{r})$ , where the *electric surface current density*  $\mathbf{J}_S$  is defined as

$$\mathbf{J}_S(\mathbf{r}, t) = \lim_{\delta \rightarrow 0} (\delta \mathbf{J}(\mathbf{r} + \delta \hat{\mathbf{n}}, t)) \quad \text{for } \mathbf{r} \in \Gamma \quad (2.5)$$

with dimension  $A/m$ .

Because the interface  $\Gamma$  encloses the PEC object  $\Omega_1$  in free space  $\Omega_0$ , an equivalence principle can be used. That is, the electromagnetic field inside the object can be taken zero with an equivalent surface current on the interface. Then, the jump conditions reduce to

$$\hat{\mathbf{n}} \times \mathbf{E} = \mathbf{0}, \quad (2.6a)$$

$$\hat{\mathbf{n}} \times \mathbf{H} = \mathbf{J}_S \quad (2.6b)$$

where the equivalent electric surface current density  $\mathbf{J}_S$  is defined on the interface and the electromagnetic field  $(\mathbf{E}, \mathbf{H})$  in the limit towards the interface from free space. In the remainder, the subscript  $S$  will be omitted, so  $\mathbf{J} = \mathbf{J}_S$ .

### Vector wave equation

Using the constitutive equations, Maxwell's equations can be rewritten into the vector wave form given by

$$\nabla \times (\nabla \times \mathbf{E}) + \frac{1}{c^2} \frac{\partial^2 \mathbf{E}}{\partial t^2} = -\mu \frac{\partial \mathbf{J}}{\partial t}. \quad (2.7)$$

A classical technique in the analysis of differential equations is the use of the Green's function. To explain this technique, let us consider a the equation  $Lu = f$  for a linear differential operator  $L$ , unknown function  $u = u(x)$  and data  $f = f(x)$ . The Green's function  $g(x, y)$  is defined as the solution of  $Lg(x, y) = \delta(x - y)$  for the Dirac delta. When such a Green's function can be found,  $\int Lg(x, y)f(y) dy = \int \delta(x - y)f(y) dy$  holds. This can be written as  $L \int g(x, y)f(y) dy = f(x)$ , suggesting the solution  $u(x) = \int g(x, y)f(y) dy$ . A rigorous introduction to Green's functions can be found in many textbooks on function analysis, for example [37].

In the case of the vector wave equation (2.7), the electric field  $\mathbf{E}(\mathbf{r}, t)$ , where  $\mathbf{r}$  and  $t$  are *source coordinates*, can be characterized by the causal



Green's function given by

$$G(\mathbf{r}, t; \mathbf{r}', t') = \frac{\delta(|\mathbf{r} - \mathbf{r}'| + c(t - t'))}{4\pi c|\mathbf{r} - \mathbf{r}'|} \quad (2.8)$$

where  $\mathbf{r}'$  and  $t'$  are *observer coordinates*.

### 2.1.2 Boundary integral formulation

The electromagnetic scattering of an object  $\Omega_1$  has been modeled with Maxwell's equations (2.1) and constitutive equations (2.3) in the exterior volume  $\Omega_0$  and interface conditions (2.6) on the surface  $\Gamma$ . The aim is to reformulate this model into equations that are defined on the surface  $\Gamma$  only.

Reformulating models from a volume to a surface can effectively be performed with the vector Green's theorem. This theorem relates a volume integral with a surface integral as

$$\begin{aligned} & \iiint_V (\mathbf{q} \cdot \nabla \times (\nabla \times \mathbf{p}) - \mathbf{p} \cdot \nabla \times (\nabla \times \mathbf{q})) \, dv \\ &= \iint_{\Sigma} ((\hat{\mathbf{n}} \times \mathbf{p}) \cdot (\nabla \times \mathbf{q}) - (\hat{\mathbf{n}} \times \mathbf{q}) \cdot (\nabla \times \mathbf{p})) \, ds \end{aligned} \quad (2.9)$$

for smooth vectors  $\mathbf{p}$  and  $\mathbf{q}$  and arbitrary volume  $V$  with boundary surface  $\Sigma$ . Now, let us substitute the electric field and the vector wave Green's function (2.8) into the vector Green's theorem, i.e.,  $\mathbf{p} = \mathbf{E}(\mathbf{r}, t)$  and  $\mathbf{q} = G(\mathbf{r}, t; \mathbf{r}', t')\mathbf{a}$  for an arbitrary vector  $\mathbf{a}$ , and the space-time regions  $V = \Omega_0 \times \mathbb{R}$  and  $\Sigma = \Gamma \times \mathbb{R}$ . With the use of Maxwell's equations and the constitutive equations, this equation can be written into the time-domain equivalent of the Stratton-Chu formulation [90]. The derivation assumes that no electromagnetic sources are present outside the object and that the electromagnetic fields at the outer boundary in space can be represented with incident wave fields.

#### Electromagnetic field integral equations

With the use of the interface conditions (2.6), the Stratton-Chu formulation can be rewritten in terms of the surface current density  $\mathbf{J}$  instead of the electric field intensity  $\mathbf{E}$ . Then, one will arrive at

$$-\hat{\mathbf{n}} \times \hat{\mathbf{n}} \times \iint_{\Gamma} \left( \mu \frac{\dot{\mathbf{J}}(\mathbf{r}', \tau)}{4\pi R} - \frac{1}{\epsilon} \nabla' \cdot \frac{\int_{-\infty}^{\tau} \nabla' \cdot \mathbf{J}(\mathbf{r}', \bar{t}) \, d\bar{t}}{4\pi R} \right) \, d\mathbf{r}' = -\hat{\mathbf{n}} \times \hat{\mathbf{n}} \times \mathbf{E}^i(\mathbf{r}, t) \quad (2.10)$$

which is a special case of the Electric Field Integral Equation (EFIE), namely for the surface of a PEC object embedded in free space. In this thesis, this will be called *the EFIE*. The dot notation  $\dot{\mathbf{J}} = \frac{\partial}{\partial t} \mathbf{J}$  has been used for differentiation

in time and  $\nabla$  and  $\nabla'$  denote the nabla operator with respect to  $\mathbf{r}$  and  $\mathbf{r}'$ , resp. The EFIE has to be solved for the electric surface current density  $\mathbf{J}(\mathbf{r}, t)$  for given incident electric field  $\mathbf{E}^i(\mathbf{r}, t)$ . The EFIE makes use of evaluation of the solution in the *retarded time level*

$$\tau = t - \frac{|\mathbf{r} - \mathbf{r}'|}{c} \quad (2.11)$$

where the abbreviation  $R = |\mathbf{R}| = |\mathbf{r} - \mathbf{r}'|$  is used.

When the magnetic field is substituted into Green's theorem instead of the electric field, one will arrive at

$$\hat{\mathbf{n}} \times \hat{\mathbf{n}} \times \iint_{\Gamma} \left( \frac{\mathbf{J}(\mathbf{r}', \tau)}{4\pi R} + \frac{\dot{\mathbf{J}}(\mathbf{r}', \tau)}{4\pi c} \right) \times \frac{\mathbf{R}}{R^2} d\mathbf{r}' - \hat{\mathbf{n}} \times \frac{1}{2} \dot{\mathbf{J}}(\mathbf{r}, t) = -\hat{\mathbf{n}} \times \hat{\mathbf{n}} \times \mathbf{H}^i(\mathbf{r}, t) \quad (2.12)$$

which is a special case of the Magnetic Field Integral Equation (MFIE), namely for the surface of a PEC object embedded in free space. In this thesis, this will be called *the MFIE*. The MFIE is only valid for closed surfaces.

The EFIE and MFIE can be related to the jump conditions (2.6), that is,  $\hat{\mathbf{n}} \times (\mathbf{E}^i + \mathbf{E}^s) = \mathbf{0}$  and  $\hat{\mathbf{n}} \times (\mathbf{H}^i + \mathbf{H}^s) = \mathbf{J}_S$  with

$$\mathbf{E}^s(\mathbf{r}, t) = - \iint_{\Gamma} \left( \mu \frac{\dot{\mathbf{J}}(\mathbf{r}', \tau)}{4\pi R} - \frac{1}{\epsilon} \nabla' \cdot \frac{\int_{-\infty}^{\tau} \nabla' \cdot \mathbf{J}(\mathbf{r}', \bar{t}) d\bar{t}}{4\pi R} \right) d\mathbf{r}' \quad (2.13a)$$

$$\mathbf{H}^s(\mathbf{r}, t) = \iint_{\Gamma} \left( \nabla \times \frac{\mathbf{J}(\mathbf{r}', \tau)}{4\pi R} \right) d\mathbf{r}' \quad (2.13b)$$

denoting the scattered electromagnetic field for  $\mathbf{r} \in \Omega_0$  outside the scatterer surface. Notice that the MFIE uses the Cauchy principle value of the surface integral in the scattered magnetic field for a smooth surface.

**Initial conditions** The incident field will be chosen such that it is present only after a certain point in time. This can be modeled by the initial conditions

$$\mathbf{E}^i(\mathbf{r}, t) = \mathbf{H}^i(\mathbf{r}, t) = \mathbf{0} \text{ for } t \leq 0. \quad (2.14)$$

Causality then states that the scattered field and the electric surface current are zero for  $t \leq 0$  as well.

**Boundary conditions** The surface  $\Gamma$  does not have to be closed and can contain a boundary, for example when a finite sheet is modeled. Then, jump conditions (2.6) hold on the boundary of  $\Gamma$ . In particular, the electric field normal to the boundary is zero on PEC objects, which is equivalent to a zero electric surface current density.



### Differentiated electromagnetic field integral equations

The EFIE contains an integral in time, which results in a dependency of the variables at the current time level on the full time history. Computation and storage of the full history is expensive. To this end, it is more efficient to consider the time derivative of the EFIE, that is,

$$-\hat{\mathbf{n}} \times \hat{\mathbf{n}} \times \iint_{\Gamma} \left( \mu \frac{\ddot{\mathbf{J}}(\mathbf{r}', \tau)}{4\pi R} - \frac{1}{\epsilon} \nabla' \cdot \frac{\mathbf{J}(\mathbf{r}', \tau)}{4\pi R} \right) d\mathbf{r}' = -\hat{\mathbf{n}} \times \hat{\mathbf{n}} \times \dot{\mathbf{E}}^i(\mathbf{r}, t) \quad (2.15)$$

the *differentiated EFIE*. The use of this equation requires an incident electric field that is differentiable in time. Similarly,

$$\hat{\mathbf{n}} \times \hat{\mathbf{n}} \times \iint_{\Gamma} \left( \frac{\dot{\mathbf{J}}(\mathbf{r}', \tau)}{4\pi R} + \frac{\ddot{\mathbf{J}}(\mathbf{r}', \tau)}{4\pi c} \right) \times \frac{\mathbf{R}}{R^2} d\mathbf{r}' - \hat{\mathbf{n}} \times \frac{1}{2} \dot{\mathbf{J}}(\mathbf{r}, t) = -\hat{\mathbf{n}} \times \hat{\mathbf{n}} \times \dot{\mathbf{H}}^i(\mathbf{r}, t) \quad (2.16)$$

is the *differentiated MFIE*. The abbreviations EFIE and MFIE are used in this thesis for both versions. When the difference between the versions is important, this will be emphasized with the names *original EFIE* and *differentiated EFIE*. The differentiated versions are more efficient and more often used in literature and will thus be used in this thesis, unless otherwise stated.

### Combined field integral equations

Two independent model equations have been derived for the same scattering problem. This allows for the use of a linear combination of the EFIE and MFIE into a new model equation. For an arbitrary constant  $\kappa \in [0, 1]$ , this can be written as

$$\text{CFIE} = \frac{\kappa}{\eta} \text{EFIE} + (1 - \kappa) \text{MFIE} \quad (2.17)$$

called the *combined field integral equation* (CFIE). Evidently, for  $\kappa = 0$  and  $\kappa = 1$  the CFIE reduces to the MFIE and EFIE, resp. This is the continuous form of the CFIE. Usually, the CFIE is defined on a discrete level, as a linear combination of the discretized EFIE and MFIE [81].

In this thesis, the EFIE will be used most often. The advantage of the EFIE over the MFIE and CFIE is that its application is not restricted to closed surfaces [81]. Moreover, it suffices to use the RWG function as test and basis function in space to obtain accurate simulations [11]. Furthermore, the mathematical foundation of the EFIE is better developed, see Chapter 3. To this end, the remainder of this chapter focused on the differentiated EFIE (2.15). The numerical discretization of the other model equations can be performed in a similar fashion.

## Dimension analysis

Maxwell's equations contain four basic dimensions, namely time, length, mass, and electric current. The solution of model equations depends on the scatterer surface, characterized by a reference length  $L$  in m; medium parameters wave speed  $c$ , permittivity  $\epsilon$ , and permeability  $\mu$ ; and the excitation. The incident electromagnetic wave field can have arbitrary shape in time-domain simulations and therefore also arbitrary many parameters. In this thesis, it is assumed that the excitation is given by a plane wave that can be characterized by a magnitude  $|\mathbf{E}^i|$  in V/m and a reference frequency  $f$  in Hz. This results in two dimensionless groups, namely the medium property  $\epsilon\mu c^2 = 1$  and the electrical size of the object  $Lf/c$ . For the reference parameters  $|\mathbf{E}^i|$ ,  $L$ ,  $c$ , and  $\sqrt{\mu/\epsilon}$ , the model equations can be rewritten into a dimensionless equation with identical solution.

### 2.1.3 Numerical discretization in space-time

The electric surface current density depends on both space and time. The EFIE has therefore to be discretized with a space-time method. Different discretization schemes have been used in TDIE methods. All of them can be rewritten into the general framework of finite element methods, more specifically the space-time Petrov-Galerkin method. Because the characteristics of the EFIE in space and time are different, separate discretization algorithms in space and time will be used, as explained in subsequent sections.

#### Space-time Petrov-Galerkin method

The space-time Petrov-Galerkin method uses a separation of the space and time variables. To this end, the electric surface current density is expanded in terms of  $N_s$  spatial and  $N_t$  temporal basis functions as

$$\mathbf{J}(\mathbf{r}, t) = \sum_{n=1}^{N_s} \sum_{j=1}^{N_t} J_{n,j} \mathbf{f}_n(\mathbf{r}) T_j(t). \quad (2.18)$$

To obtain a discrete solution, the testing procedure also uses a separation of variables and combines  $N_s$  spatial with  $N_t$  temporal test functions. The numerical discretization results in a space-time system of linear equations



$A\mathbf{x} = \mathbf{b}$ , with

$$A = \begin{bmatrix} A_{1,1} & A_{1,2} & A_{1,3} & \dots & \dots & A_{1,N_t} \\ A_{2,1} & A_{2,2} & A_{2,3} & \dots & \dots & A_{2,N_t} \\ A_{3,1} & A_{3,2} & A_{3,3} & \dots & \dots & A_{3,N_t} \\ \vdots & \vdots & \vdots & \ddots & & \vdots \\ \vdots & \vdots & \vdots & & A_{N_t-1,N_t-1} & A_{N_t-1,N_t} \\ A_{N_t,1} & A_{N_t,2} & A_{N_t,3} & \dots & A_{N_t,N_t-1} & A_{N_t,N_t} \end{bmatrix} \quad (2.19)$$

the *space-time discretization matrix*, and

$$\mathbf{x} = \begin{bmatrix} \mathbf{I}_1 \\ \mathbf{I}_2 \\ \mathbf{I}_3 \\ \vdots \\ \mathbf{I}_{N_t-1} \\ \mathbf{I}_{N_t} \end{bmatrix} \quad \text{and} \quad \mathbf{b} = \begin{bmatrix} \mathbf{V}_1 \\ \mathbf{V}_2 \\ \mathbf{V}_3 \\ \vdots \\ \mathbf{V}_{N_t-1} \\ \mathbf{V}_{N_t} \end{bmatrix} \quad (2.20)$$

representing the discrete electric surface density and discrete incident wave field, resp. The elements  $(\mathbf{I}_j)_n$  of the discrete solution correspond to temporal basis function  $j = 1, 2, \dots, N_t$  and spatial basis function  $n = 1, 2, \dots, N_s$ . The discretization matrix consists of blocks  $A_{i,j}$  corresponding to temporal test and basis functions for  $i = 1, 2, \dots, N_t$  and  $j = 1, 2, \dots, N_t$ , resp. The elements  $(A_{i,j})_{m,n}$  of these blocks correspond to spatial test and basis functions for  $m = 1, 2, \dots, N_s$  and  $n = 1, 2, \dots, N_s$ , resp. The size of the discretization matrix is  $(N_s N_t) \times (N_s N_t)$ .

### Reducing the complexity of the numerical scheme

Computing the discrete electric surface current density requires the solution of the full space-time system. Because of its large size, this will already become prohibitively expensive for electrically small objects and short time scales. Hence, simply solving this system of equations is not feasible for industrial application of TDIE methods. However, with a clever choice of numerical scheme, the efficiency can be increased to an extent that solving the system of linear equations becomes feasible. More specifically, the numerical scheme should be chosen such that the following properties of the discretization matrix hold:

1. **Lower triangular:** if  $A_{i,j} = 0$  for  $j > i$ , then the discretization matrix is lower triangular, which can be solved efficiently with forward substitution;
2. **Banded:** if  $A_{i,j} = 0$  for  $j < i - \ell$ , then the discretization matrix has a diagonal band of size  $\ell$ ;

3. **Toeplitz:** if  $A_{i,j} = Z_{i-j}$  for all  $i, j = 1, 2, \dots, N_t$ , then the discretization matrix is a block Toeplitz matrix for which all diagonals contain a repetition of the same block, thus reducing the storage requirements;
4. **Sparse:** if each block  $A_{i,j}$  contains many zero elements, the matrix becomes sparse.

In next sections, these properties will be related to requirements on the numerical scheme. When all properties hold, the space-time discretization matrix (2.19) can be written as

$$A = \begin{bmatrix} Z_0 & 0 & 0 & \dots & \dots & \dots & \dots & 0 \\ Z_1 & Z_0 & 0 & \dots & \dots & \dots & \dots & 0 \\ Z_2 & Z_1 & Z_0 & & & & & 0 \\ \vdots & \vdots & \ddots & \ddots & & & & \vdots \\ Z_\ell & Z_{\ell-1} & & \ddots & \ddots & & & \vdots \\ 0 & Z_\ell & Z_{\ell-1} & & \ddots & \ddots & & \vdots \\ \vdots & & \ddots & \ddots & & \ddots & Z_0 & 0 \\ 0 & \dots & 0 & Z_\ell & Z_{\ell-1} & \dots & Z_1 & Z_0 \end{bmatrix}. \quad (2.21)$$

The space-time system of linear equations can then be solved very efficiently with forward substitution, that is

$$Z_0 \mathbf{I}_k = \mathbf{V}_k - \sum_{j=1}^{\ell} Z_j \mathbf{I}_{k-j} \text{ for } k = 1, 2, \dots, N_t \quad (2.22)$$

where the matrices  $Z_j$  are called *discrete interaction matrices*. At every time level  $k$  the discrete surface current density  $\mathbf{I}_k$  can be calculated from known solutions only, resulting in a *marching procedure*.

### 2.1.4 Discretization method in space

Early publications on TDIE methods have been using collocation in space [69]. This has been improved with a Galerkin method, which naturally fit within the space-time Petrov-Galerkin framework introduced in Sec. 2.1.3. Then, numerical discretization reduces to the choice of spatial test and basis functions on a specific computational domain.

**Surface mesh** The computational domain in space should approximate curved surfaces accurately. This can effectively be achieved with a surface mesh that consist of flat triangular patches. Usually, each edge has exactly two adjacent faces, except for edges on the boundary of the surface. Furthermore, the resolution of the surface mesh should be high enough to represent

the shortest wavelength of the electromagnetic field. The TDIE method has been applied to quadrilateral elements [115] and curvilinear patches [103] as well. Then, different spatial basis functions are required, which will be outside the scope of this thesis.

**Test and basis functions in space** Because the electric surface current density is a vector function, the test and basis functions are vector functions defined on a surface mesh. This thesis will use the most popular choice in literature, namely the RWG functions, named after Rao, Wilton, and Glisson, who introduced these functions in CEM [70]. In finite element methods, these functions were already in use with the name Raviart-Thomas elements [71]. The RWG functions are linear vector functions, defined as

$$\mathbf{f}_n(\mathbf{r}) = \begin{cases} \frac{\ell_n}{2|\Gamma_n^+|}(\mathbf{r} - \mathbf{r}_n^+), & \mathbf{r} \in \Gamma_n^+, \\ -\frac{\ell_n}{2|\Gamma_n^-|}(\mathbf{r} - \mathbf{r}_n^-), & \mathbf{r} \in \Gamma_n^-, \\ \mathbf{0}, & \text{elsewhere,} \end{cases} \quad (2.23)$$

where the triangular facets  $\Gamma_n^+$  and  $\Gamma_n^-$  share edge  $n$  of length  $\ell_n$ , and  $\mathbf{r}_n^+$  and  $\mathbf{r}_n^-$  the free vertices, see Fig. 2.1. Because the RWG functions are defined edgewise, the number of spatial basis functions equals the number of interior edges. The local support on two triangular facets sparsifies the interaction matrices  $Z_j$ , which makes the marching procedure more efficient.

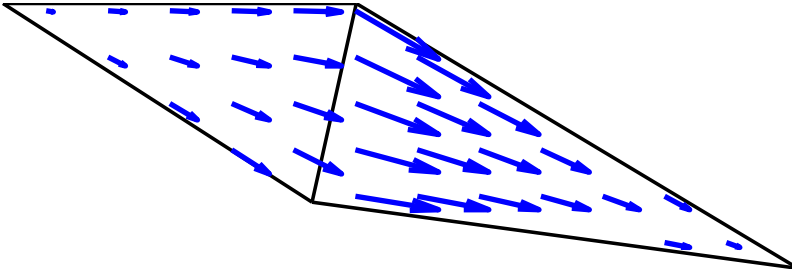


Figure 2.1: The RWG functions (2.23).

Other spatial basis functions have been used in literature as well, for example the higher-order accurate Graglia-Wilton-Peterson functions [103], which require curved patches to obtain accurate solutions on curved surfaces. In the case of MFIE, the use of Buffa-Christiansen basis functions, possibly extended with Calderón preconditioning, can be advantageous [11].

The RWG functions are by far the most often used test and basis functions in literature on TDIE methods. This consensus has been reached because they have been analyzed extensively in the literature on frequency-domain CEM

and general finite element methods, and computational experiments confirm their applicability. Therefore, the RWG functions will be used for all computer simulations in this thesis and the research focus will be on the discretization method in time.

### 2.1.5 Discretization method in time

Before proceeding to the numerical discretization, it should be noted that the model equations are given by boundary integro-differential equations which can not be written into standard formulations that are usually encountered in textbooks on numerical analysis. Two main differences with standard differential equations are present, both can be traced back to the coupling of space and time dependencies with retarded time levels (2.11). That is, the unknown surface current density  $\mathbf{J}(\mathbf{r}, \tau)$  is evaluated in  $\tau = t - |\mathbf{r} - \mathbf{r}'|/c$ .

The first difference with standard formulations is the presence of a surface integral and divergence operator in space and derivatives and antiderivatives in time. Because the unknown function depends on retarded time levels, differential operators in space and time can not be interchanged trivially. This makes it difficult, if not impossible, to rewrite the EFIE into the standard form  $\frac{d}{dt}u(t) = f(t, u(t))$  with unknown  $u$  and differential operator  $f$ . Since virtually all time integration schemes are designed for this standard form, no straightforward use of the extensive theory on numerical integration can be used. Furthermore, with the same reasoning, the EFIE can not be written into a standard form of a more general delay differential equation, given by  $\frac{d}{dt}u(t) = f(t, u(t), u(t - \sigma_1), u(t - \sigma_2), \dots, u(t - \sigma_n))$  for real  $\sigma_i > 0$  [12].

The second difference with standard formulations is that the retarded time levels are not restricted to a discrete set of time levels. For standard numerical schemes, the approximated solution is defined on discrete time levels only. In the case of the EFIE, the retarded time level changes continuously with the spatial coordinates of the surface mesh. This yields that the retarded time levels have to be evaluated within the quadrature procedure for the surface integrals in space. The discretization method in time can therefore not be decoupled from the discretization and quadrature method in space. Concluding, the discretization method in time should allow for an evaluation of the unknown in arbitrary time levels.

Specific discretization methods have to be designed for the model equations because of the strong coupling of space and time dependencies in the EFIE. The discretization method in time should at least be able to handle integration and differentiation in time and evaluation in arbitrary retarded time levels. Many different numerical schemes have been used in the TDIE method, all with their merits and limitations. The choice of discretization scheme has influence on, among others, stability, accuracy, and efficiency of the TDIE method.



In this section, an overview of the following numerical schemes will be given:

- finite differences;
- marching on in time;
- marching on in degree;
- space-time Galerkin; and
- convolution quadrature.

All methods have been developed and presented in literature as different numerical schemes. However, it should be noticed that the last four schemes can all be written as a special case of a space-time Petrov-Galerkin scheme.

### Discrete time axis

First, a discrete time axis has to be defined. Because of the zero initial conditions for  $t \leq 0$ , the discrete time axis has to partition the region  $0 < t \leq t_{\text{end}}$  for  $t_{\text{end}}$  the simulation time. The tessellation of the discrete time axis is given by

$$t_k = k\Delta t \quad \text{for } k = 1, 2, \dots, N_t \quad (2.24)$$

where  $N_t$  denotes the number of time levels, such that  $t_{N_t} = t_{\text{end}}$  upon rounding. The time step size  $\Delta t$  has been chosen uniform, which is by far the most common choice in literature. Variable time step sizes have been used in the TDIE method [77], but the space-time discretization matrix is not lower triangular nor has a Toeplitz structure in these methods, thus preventing a marching procedure. Moreover, adaptive methods require the recalculation of interaction matrices for each change in the time step size.

To capture all waves in the electromagnetic field, the time step size has to satisfy Nyquist's criterium. That is, the maximum frequency  $f_{\text{max}}$  needs to be sampled with at least two points. In practice, an oversampling factor  $\nu$  will be used, that is,

$$\Delta t = \frac{1}{\nu 2f_{\text{max}}} \quad (2.25)$$

where  $\nu$  is usually chosen between 5 and 10 [102]. Notice that  $f_{\text{max}}$  should be the maximum frequency of the total electromagnetic field, which is not known in advance. In the case of PEC objects, the scattered field will have the same frequency band as the incident field. This allows to choose  $f_{\text{max}}$  based on the incident wave field only.

It is not necessary to satisfy a CFL condition, because stability of space-time Petrov-Galerkin schemes for TDIE methods is independent of the CFL number, as will be explained in Chapter 3. Still, computational experiences suggest that a CFL number around one is advantageous for accuracy and efficiency. Notice that this will be obtained when both the surface mesh width

and time step size are chosen as an oversampling factor of the highest frequency mode.

### Finite differences

Initial versions of the TDIE method used finite differences to approximate the time derivatives in combination with interpolation for the evaluation of the discrete surface current density in retarded time levels [69]. The finite difference approximation allows for analysis of the TDIE method with available techniques from ODEs, such as the Von Neumann analysis (see Sec. 3.2.2). However, these techniques have been found to be very unstable and have become obsolete with the inception of the more accurate schemes that will be explained subsequently.

### Marching on in time

The most popular discretization scheme for TDIE methods is the *Marching-on-in-Time* (MoT) scheme. Especially in engineering literature, a large number of papers on the development of the MoT scheme can be found, see [17, 5] and references therein. Collocation is used in the MoT scheme, that is, the EFIE is point matched in discrete time levels. Thus, the model equation is solved on discrete time levels only. However, one still needs to compute the surface current density and its derivatives in retarded time levels. Temporal basis functions are simultaneously being used for differentiation and interpolation.

For correctly chosen temporal basis functions, the MoT scheme satisfies all four properties listed in Sec. 2.1.3 to reduce the computational complexity. Consequently, the MoT scheme is the most efficient TDIE method, certainly when the available accelerators are being used, see Sec. 2.2.5. Besides, implementation is relatively easy and related model equations can readily be discretized. For these reasons, the MoT scheme is the method of choice in this thesis. The details of this method will be explained in Sec. 2.2.

### Marching on in degree

The *Marching-on-in-Degree* (MoD) or *Marching-on-in-Order* (MoO) scheme discretizes the EFIE with a Galerkin method in time, see [48] for a review. As test and basis functions, Laguerre polynomials are used, which are causal and defined on the entire time history. Therefore, the space-time discretization matrix is lower triangular and has a Toeplitz structure, thus allowing for a marching procedure. On the downside, the matrix is not banded and the blocks are densely populated, which makes the method inefficient compared to the MoT scheme. In fact, the computational costs scale with an additional factor  $N_t$  and computational results show long computation times and large

storage requirements [47]. Although many stable results have been shown, there is no stability proof available. For these reasons, the MoD scheme will not be used in this thesis.

### Space-time Galerkin

An elegant and well-founded method for numerical discretization of the EFIE is the use of a *space-time Galerkin* method [91, 39, 20]. Following the customary approach in finite element methods, first a variational formulation is derived. Then, the test and basis functions are chosen as a subspace of certain space-time function spaces. This approach allows for a thorough mathematical analysis of computational properties such as stability. In fact, it has been proven that the variational formulation of the EFIE admits a unique and bounded solution. So, stable results are expected when all requirements for the proof are fulfilled, see Chapter 3.

Notice that both the MoT and space-time Galerkin scheme can be written as a special case of the space-time Petrov-Galerkin scheme. For specific versions of MoT and space-time Galerkin schemes, they are even equivalent, as will be shown in Sec. 3.8. Still, both methods have largely been developed independently in literature and several differences between the methods are given in Table 2.1. The efficiency of space-time Galerkin schemes is competitive with MoT schemes. The main merit of the space-time Galerkin scheme is the availability of a thorough mathematical framework, including a stability proof. However, its application in the engineering community has been restricted because of its scarce documentation in literature. An attempt will be made in Chapter 3 to bridge the gap between the two methods such that the favorable properties of both methods can be joined together.

Table 2.1: Comparison of the MoT scheme and space-time Galerkin scheme.

MoT scheme	space-time Galerkin
collocation in time	variational formulation
applied to differentiated EFIE	applied to original EFIE
only a posteriori stability analyses	a priori stability proof derived
accelerators developed	no accelerators known
straightforward implementation	elaborate implementation
engineering context	mathematical background
well documented	scarce documentation

### Convolution quadrature

The EFIE consists of a convolution in time of the Green's function and the electric surface current density. The presence of this convolution can be used to design specific numerical schemes, as is done for general convolutional integral equations for decades [56, 58, 9]. The so-called *Convolution Quadrature* (CQ) scheme has been applied to the EFIE, but with the name *finite difference delay modeling* [99].

The CQ scheme uses a series of transformations to obtain a discrete solution of the model equation. First, the time-dependent equations are transformed to the Laplace domain. Then, discretization is carried out in the Laplace domain. With an inverse  $z$ -transform, discrete equations in the time domain are obtained. An advantage of this detour in the Laplace domain is that computational properties are more easily derived. In particular, stability of the CQ scheme has been proven, provided an  $A$ -stable discretization scheme is used.

At first sight, the CQ scheme might look very different to space-time Galerkin and MoT schemes, but many similarities can be found. For instance, the stability proofs of both methods make use of the same mathematical foundation in the Fourier-Laplace domain. On a discrete level, the CQ scheme ultimately results in a space-time discretization matrix as well. When backward differences are used in the CQ scheme, a lower triangular Toeplitz structure will be obtained, thus allowing for an efficient marching procedure. However, the matrix is not banded and its blocks are densely populated because of the dependence on the full time history. Since the CQ scheme and MoT scheme are two of the most promising discretization methods for TDIE methods, let us compare the computational characteristics:

**Efficiency** The large support in time of the CQ weights results in a non-banded space-time discretization matrix and dense interaction matrices in the marching procedure. The CQ scheme is therefore less efficient than the MoT scheme, in terms of both computation time and storage requirements. Efficiency of the CQ scheme has been improved with cutoff strategies and FFT techniques [40, 8]. However, MoT schemes have been accelerated as well, with plane-wave and FFT techniques. The weaker efficiency of large support carries over to accelerated versions and the MoT scheme remains more efficient than the CQ scheme.

**Stability** The main computational advantage of the CQ scheme is its superior stability characteristics. Numerical stability is assured for all  $A$ -stable time integration methods, which is a wide class of backward differentiation formulas and Runge-Kutta methods. Moreover, stability is moderately sensitive to quadrature errors in the evaluation of the interaction matrices [57, 25].

**Robustness** Whereas the MoT scheme uses temporal basis functions, the CQ scheme uses so-called CQ weights to interpolate the discrete surface current density. For example, when backward Euler is used, the CQ weights read  $w_k = (\xi^k e^{-\xi})/(k!)$  for  $k = 1, 2, \dots, N_t$  and arbitrary retarded levels  $\xi = R/(c\Delta t)$  [99]. Because of the smoothness of the CQ weights, numerical quadrature procedures are very effective. The use of quasi-exact integration methods is therefore not necessary to obtain sufficient accuracy for the evaluation of interaction matrices in the CQ scheme. This makes the stability of the CQ scheme less sensitive to numerical errors and thus more robust than the MoT scheme [25]. On the other hand, finite precision arithmetic can result in large errors when electrically large structures are modeled. Then,  $N_t$  becomes large and the evaluation of the CQ weights in finite precision arithmetic becomes inaccurate for large values of  $k$ . Furthermore, when Runge-Kutta discretization is used in the CQ scheme, no analytical expression for the CQ weights in time domain can be obtained. Computational algorithms for the inverse  $z$ -transform have to be used, thus introducing additional numerical errors and difficulties [80, 9].

**Convergence** Higher-order spatial basis functions can be used in the CQ scheme and higher-order convergence in time can be obtained with Runge-Kutta schemes [98]. Higher-order convergence in time can be obtained in MoT schemes as well, see Chapter 4, but this has not yet been achieved in combination with the higher-order spatial basis functions due to the need of quasi-exact integration rules.

**Accuracy** A major drawback of the CQ scheme is the dispersion and dissipation of the surface current density [16]. Computational experiments confirm that dispersion and dissipation in the CQ scheme is far worse than in the MoT scheme [25].

**Model equations** Although this thesis focuses on the EFIE for PEC objects, the computational methods should also be applicable to different model equations and other types of materials, for which the Green's function might differ from the standard Green's function for scattering in an unbounded homogeneous space. Because the CQ scheme discretizes the model equations in the Laplace domain, a formulation of the Green's function in the Laplace domain is required. This restriction to Green's functions that are Laplace-transformable might look as a drawback, for instance when nonlinearities are present. On the other hand, the CQ scheme does not need the Green's function in the time domain. This is a strong merit in applications such as viscoelastics where the Green's function is only available in the Laplace domain [80]. On the downside, the formulation in the Laplace domain of the CQ scheme makes it difficult to use physically meaningful variables [9].

With MoT schemes, one can develop algorithms inspired on physical phenomena [62].

**Hybridization** Instead of emphasizing the differences between the methods, one can also join forces and combine the CQ and MoT scheme in one TDIE method. The main insight that resulted in this fusion is that the CQ scheme can be written as an MoT scheme with specific temporal basis functions. That is, a large set of differently shaped temporal basis functions is obtained. With this observation, spline basis functions for the MoT scheme have been analyzed with techniques in the Laplace domain [25]. Another remarkable union of the CQ and MoT scheme is the ‘arrested CQ method’ [101], which uses a hybrid method of CQ weights for near interactions and MoT basis functions for far interactions. This combines the stability of the CQ scheme with the efficiency and lack of dispersion and dissipation of the MoT scheme.

## 2.2 MoT scheme

In this thesis, the electromagnetic scattering from conducting surfaces is modeled with the EFIE and solved with the TDIE method. As explained in Sec. 2.1, the numerical discretization procedures can be analyzed for a general space-time Petrov-Galerkin scheme, resulting in the space-time discretization matrix (2.19). The choice of test and basis functions in space is given by the RWG functions, which is a standard choice. No consensus on the numerical discretization in time has been reached in the CEM community. The MoT scheme, space-time Galerkin, and convolution quadrature are the major schemes being used in literature. Because of its efficiency and ease of implementation, the MoT scheme will be adopted in this thesis. Remember that the MoT scheme shares many properties with space-time Galerkin and for specific versions, the two schemes are equivalent, as will be shown in Chapter 3.

### 2.2.1 Numerical discretization

The MoT scheme uses collocation in time, that is, the model equations are point matched in discrete time levels  $t_i = i\Delta t$  with  $i = 1, 2, \dots, N_t$ . This is equivalent to using a Petrov-Galerkin scheme with the Dirac delta  $\delta(t - t_i)$  as test function. The temporal basis functions  $T_j(t)$  with  $j = 1, 2, \dots, N_t$  are the defining parameters of the MoT scheme. Their definition determines many computational properties of the TDIE method. In particular, all properties of the space-time discretization matrix given in Sec. 2.1.3 that allow for an efficient marching procedure depend on the choice of the temporal basis function.

Remember that the unknown electric surface current density has to be evaluated in retarded time levels  $\tau = t - R/c$  where the distance  $R$  can take

arbitrary values. Because of the series expansion (2.18) in terms of spatial and temporal basis functions, the temporal basis function needs to be evaluated in retarded time levels as well. This remains the case when collocation in time is used, because then one needs to evaluate  $T_j(\tau_i) = T_j(t_i - R/c)$  which can still obtain arbitrary values, in particular outside the discrete time levels  $t_k$ . Notice that each term  $T_j(\tau_i)$  for  $i, j = 1, 2, \dots, N_t$  contributes to the block  $A_{i,j}$  in the space-time discretization matrix (2.19).

Now, let us reformulate the properties of the space-time discretization matrix given in Sec. 2.1.3 into requirements on the temporal basis functions:

1. Lower triangular: if  $T_j(t) = 0$  for  $t \leq t_{j-1}$  then  $T_j(\tau_i) = 0$  for  $\tau_i \leq t_{j-1}$  or  $i < j$  and thus  $A_{i,j} = 0$  for  $j > i$ ; this property is called **discrete causality** or **marching criterion**;
2. Banded: if  $T_j(t) = 0$  for  $t > t_{j+\ell}$  then  $T_j(\tau_i) = 0$  for  $\tau_i > t_{j+\ell}$  or  $i > j + \ell$  and thus  $A_{i,j} = 0$  for  $j < i - \ell$ ; this property is called **locality** as opposed to global or entire-domain basis functions; notice that this property only leads to bandedness when no time integral is present in the model equation;
3. Toeplitz: if  $T_j(t) = T(t - t_j)$  for all  $j = 1, 2, \dots, N_t$  then  $T_j(\tau_i) = T(\tau_i - t_j) = T(\tau_{i-j})$  and thus  $A_{i,j} = Z_{i-j}$  for all  $i, j = 1, 2, \dots, N_t$ ; this property is called **convolution** or **translation invariant**;
4. Sparse: if  $T_j(t) = 0$  for  $|t - t_j| > t_d$  with  $d \in \mathbb{N}$  fixed and independent on  $N_t$  then the number of nonzero elements scales with  $\mathcal{O}(N_t)$  instead of  $\mathcal{O}(N_t^2)$  in time and thus is each block  $A_{i,j}$  sparse; this property is called **compactness** or **short support**.

When the temporal basis functions are chosen such that they fulfill all above mentioned requirements, the solution of the space-time system (2.19) reduces to the marching procedure (2.22). This is a huge reduction of computational costs in both simulation time and memory. Therefore, all of these properties will be required for MoT schemes.

The convolution property requires that all temporal basis functions  $T_j$  are written as translations of a single function  $T$ , i.e.,

$$T_j(t) = T(t - j\Delta t) \text{ for } j = 1, 2, \dots, N_t. \quad (2.26)$$

Because all temporal basis functions  $T_j$  are simple geometrical transformations of the same function, this function  $T$  is also called the *temporal basis function* of the MoT scheme. To obtain the other three properties, it satisfies to require

$$T(t) = 0 \text{ for } t \leq -\Delta t \text{ and } t > d\Delta t. \quad (2.27)$$

The causality and compactness can be derived immediately from this requirement and the locality is obtained for

$$\ell = \left\lfloor \frac{\max_{\mathbf{r}, \mathbf{r}' \in \Gamma} |\mathbf{r} - \mathbf{r}'|}{c\Delta t} \right\rfloor + d. \quad (2.28)$$

The only remaining requirement on the definition of  $T$  is that its derivatives and antiderivative can be evaluated in retarded time levels, because terms like  $T'(\tau)$ ,  $T''(\tau)$  and  $\int^\tau T$  are present in the discrete model equations. In order to make things not unnecessary complicated, piecewise polynomials will be used as temporal basis function in this thesis. Remember that the customary choices of shifted Lagrange and spline basis functions are piecewise polynomials. They can conveniently be written as

$$T(t) = \begin{cases} F_0(t), & -1 < \tilde{t} \leq 0, \\ F_1(t), & 0 < \tilde{t} \leq 1, \\ \vdots & \vdots \\ F_d(t), & d-1 < \tilde{t} \leq d, \\ 0, & \text{else,} \end{cases} \quad (2.29)$$

with  $F_0, F_1, \dots, F_d$  polynomials of degree  $d$ , and  $\tilde{t} = \frac{t}{\Delta t}$  the scaled time. The *degree* of this temporal basis function is  $d$ .

## 2.2.2 Temporal basis functions

The main choice in MoT schemes is the definition of the temporal basis function (2.26). This choice has a profound influence on the computational properties of the MoT scheme, including stability, accuracy, and efficiency. Choosing the correct temporal basis function is not evident and there is no consensus in literature. Three of the most popular temporal basis functions are depicted in Fig. 2.2.

The main characteristics of temporal basis functions are causality, compactness, bandlimitedness, and smoothness. Causality and compactness have been explained in Sec. 2.2.1. Bandlimitedness means that the frequency band of a temporal basis function is limited. Smoothness is given by the continuity or regularity of the temporal basis functions. Following is a cornucopia of temporal basis functions, with the year of introduction in literature:

I. Interpolants (causal, compact, not bandlimited, not smooth):

1. Hat, 1991 [69];
2. Quadratic Lagrange, 1997 [60];
3. Cubic Lagrange, 1999 [30];

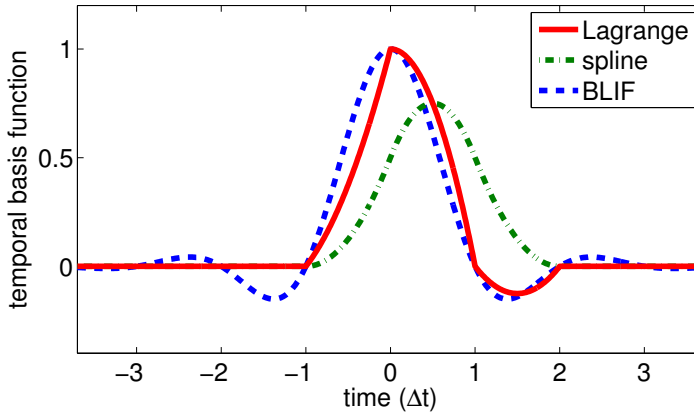


Figure 2.2: Three of the most popular temporal basis functions, namely the quadratic Lagrange (4.22), quadratic spline (4.25), and bandlimited interpolation function (BLIF) [102].

4. Quartic Lagrange, 2005 [6];
  5. Shifted Lagrange, 2009 [84];
- II. Splines (causal, compact, not bandlimited, moderate smoothness):
6. Quadratic spline, 2007 [97];
  7. Cubic  $C^2$  spline, 2009 [33];
  8. Cubic  $C^1$  spline, 2011 [105];
  9. Cubic B-spline, 2002 [73];
  10. Noncausal B-spline, 2011 [32];
  11. Cardinal B-spline, 1994 [72];
  12. Convolution spline, 2013 [26];
- III. Bandlimited functions (not causal, not compact, bandlimited, smooth):
13. Bandlimited APSWF, 2004 [102];
  14. Bandlimited semi-hat, 2010 [41];
  15. Bandlimited spline, 2012 [35];
  16. Bandlimited Lagrange, 2012 [31];
- IV. Smooth (not causal, compact, not bandlimited, smooth):
17. Partition of unity, 2012 [77];

18. Convolution error, 2013 [25];

V. Diverse:

19. Cosine squared, 1999 [45];

20. Exponential, 2001 [44];

21. Rational fractional, 2001 [43];

22. Sinusoidal dome, 2007 [46];

23. Polynomial dome, 2007 [112];

24. Gauss, 2012 [14];

VI. Entire-domain functions used in MoD schemes:

25. Weighted Laguerre, 2004 [49];

26. Associated Laguerre, 2011 [61];

27. Hermite, 2007 [86];

VII. Entire-domain functions used in CQ schemes:

28. Backward differentiation formula, 2013 [26];

29. Runge-Kutta, 2013 [25].

As impressive as this list might look, it is not exhaustive, because a novel family of spline basis functions will be derived in this thesis. In Chapter 4, a framework will be presented which can be used to design temporal basis functions according to user-specified requirements on computational characteristics.

### 2.2.3 Matrix assembly

The MoT scheme has been designed such that solving the space-time discretization system reduces to a marching procedure (2.22). Before this marching procedure can be performed, all interaction matrices  $Z_j$  for  $j = 0, 1, 2, \dots, \ell$  have to be computed. Each element  $(Z_j)_{mn}$  can be related to a discrete model of the electromagnetic interaction between spatial elements  $m$  and  $n$  at retarded time level  $j$ . Because the discretization methods can be written as a space-time Petrov-Galerkin scheme of an integral equation, each matrix element is given by two integrals in time and two surface integrals in space, totaling a six-dimensional integral. In time, the inner integral can be evaluated analytically as a convolution of the Green's function and the surface current density. The outer integral in time can be evaluated analytically as well because this is point matching in time. The remaining four-dimensional integral in space is not easily evaluated. Because of the presence of retarded time

levels and the use of piecewise polynomial temporal basis functions, shadow regions are present in the integrand. That is, the integrand is only smooth on intersections of discrete light cones and triangular patches. In Chapter 5 a quasi-exact integration method will be explained that takes this into account and computes the integrals with a high accuracy.

In general, quadrature procedures are used to compute (parts of) the four-dimensional integrals in space. The effectiveness of the numerical quadrature depends on the choice of temporal basis function and the quadrature accuracy has profound influence on the stability of the MoT scheme, see Sec. 3.4.4. The incorporation of quasi-exact integration methods is necessary for stability, but is computationally demanding. In many cases, the matrix assembly consumes more computation time than the marching procedure.

### 2.2.4 Marching procedure

When all interaction matrices have been computed, the discrete solution can be obtained with a marching procedure. This contains two parts, namely the computation of the history and the current state. Computing the history is given by matrix-vector multiplications of the interaction matrices and the discrete solutions on past time levels. Computing the solution at the new time level requires the solution of a system of linear equations.

#### Matrix-vector multiplication

The computation of the right-hand side of the marching procedure (2.22) requires the computation of  $\sum_{j=1}^{\ell} Z_j \mathbf{I}_{k-j}$ . The interaction matrices  $Z_j$  have already been computed and stored and the discrete solutions  $\mathbf{I}_j$  have been computed in previous iterations of the marching procedure. Standard routines for matrix-vector multiplication can thus be used and parallelization can be performed easily. Also, remember that the interaction matrices are sparse in MoT schemes.

#### Linear solver

To obtain the discrete solution at a new time level, a system of linear equations  $Z_0 \mathbf{I}_k = \mathbf{b}_k$  has to be solved for a known right-hand side  $\mathbf{b}_k$  containing the excitation and history. The leading matrix  $Z_0$  contains near interactions only, which makes it a sparse matrix. This calls for the use of efficient linear solvers. However, this procedure takes only very little computation time compared to matrix assembly and matrix-vector multiplications for current test cases. Therefore, an computationally expensive but very accurate full LU-decomposition is used in this thesis. Still, the linear solver consumes less than 1% of the total computation time for all simulations performed in this thesis.

It is expected that the linear solver will consume relatively more computation power for electrically large objects discretized with high spatial resolution. Then, the use of an iterative linear solver will become advantageous. For example, the TFQMR and GMRES solvers have been used in literature [2, 94]. No information about preconditioners of the linear solver has been found in literature. Because this system of linear equations has to be solved at each iteration in the marching procedure, with every time iteration the same matrix, an accurate preconditioner is expected to improve the efficiency.

### Tail component of marching procedure

When the MoT scheme is applied to the differentiated EFIE, a marching procedure (2.22) will be obtained with a fixed number of interaction matrices for previous time levels. In the case of the original EFIE, an integral in time is present which will result in an infinite tail, even when all requirements on the temporal basis function listed in Sec. 2.2.1 are fulfilled. Because of the initial conditions, the iterations start at zero time and run until the present time level in the marching procedure. However, one can show that the interaction matrices are constant inside the tail. Therefore, the original EFIE results in a marching procedure given by

$$Z_0 \mathbf{I}_k = \mathbf{V}_k - \sum_{j=1}^{\ell} Z_j \mathbf{I}_{k-j} - Z_{\text{tail}} \sum_{j=\ell+1}^k \mathbf{I}_{k-j} \quad (2.30)$$

where  $\ell$  is given by the number of active interaction matrices, see Eq. (2.28). Besides the additional tail, the matrices  $Z_j$  are more dense than in the case of differentiated model equations, because of the large support of the antiderivative of the temporal basis function. This yields that the use of the original EFIE is computationally more expensive than the differentiated EFIE, both in computation time and storage requirements. For this reason, the differentiated EFIE will be used throughout this thesis.

### 2.2.5 Acceleration methods

The advantage of a BEM is that the number of spatial mesh elements scales quadratically with the frequency whereas for volume methods it scales cubically. However, this gain is usually diminished by the fact that dense matrices are present in BEM whereas sparse matrices are present in volume methods. For the TDIE method to be competitive with volumetric time-domain methods, the efficiency has to be improved. Two accelerators have been presented in literature, one based on plane wave expansions and the other on fast Fourier transforms (FFT) [82, 115]. Both are inspired from frequency-domain CEM and reduce the computational complexity of MoT schemes.

Remember that computation time and memory requirements scale  $\mathcal{O}(N_t N_s^2)$  in MoT schemes [17].

The incorporation of an acceleration method will be necessary to perform a scattering analysis for objects of industrial interest, because these tend to have dimensions that make them electrically large, while a high resolution discretization is required to obtain an accurate solution. The acceleration methods have already a long history of improvements and large scale computations have been performed, but implementation is tedious. For these reasons and because robust stability is more critical for industrial application, no acceleration methods will be used in this thesis. For completeness, the acceleration methods will be explained very briefly.

### Fast Fourier transforms

The *Time Domain Adaptive Integral Method* (TD-AIM) [115, 113, 5] uses FFT techniques to reduce the complexity to  $\mathcal{O}(N_t N_s^{\frac{3}{2}} \log_2 N_s)$  for the computation time. The memory requirements remain  $\mathcal{O}(N_t N_s^2)$ . The TD-AIM can be implemented in parallel relatively easy and improves the computation time already for small scale objects. The algorithm does not impose specific requirements on the Green's function. When quasiplanar structures are modeled, an additional reduction in complexity can be achieved, namely  $\mathcal{O}(N_t N_s \log_2 N_s)$  for computation time and  $\mathcal{O}(N_t N_s^{\frac{3}{2}})$  for memory.

### Plane wave expansions

Similar to the fast multipole method in frequency-domain CEM, plane wave expansions can be used to improve the efficiency of the MoT scheme. The *Plane Wave Time Domain* (PWTD) method [82, 83, 17] uses a multilevel framework with groups of near and far interactions. The computational complexity is  $\mathcal{O}(N_t N_s \log_2 N_s)$  for both computation time and memory and thus outperforms the TD-AIM asymptotically. The implementation of the PWTD method depends on the definition of the Green's function, which makes the extension to different model equations nontrivial.

## 2.2.6 Incident wave field

TDIE methods compute the electric surface current density for a given incident electromagnetic wave field. When the differentiated EFIE is used, the incident wave field has to be differentiable. In this thesis, plane wave fields will be used, with the shapes depicted in Fig. 2.3. Following are the definitions of the incident electric wave fields, where  $E_0$  denotes the pulse strength in  $V$  and  $\hat{\mathbf{p}}$  and  $\hat{\mathbf{k}}$  denote the nondimensional polarization and propagation direction, resp. The magnetic field is given by the same shape, but with polarization  $\hat{\mathbf{k}} \times \hat{\mathbf{p}}$  and the amplitude divided by the impedance. Furthermore, instead of

using seconds as unit of time, we will often use *lightmeter* (lm), that is,  $1 \text{ s} = c \text{ lm}$  with  $c$  the speed of light.

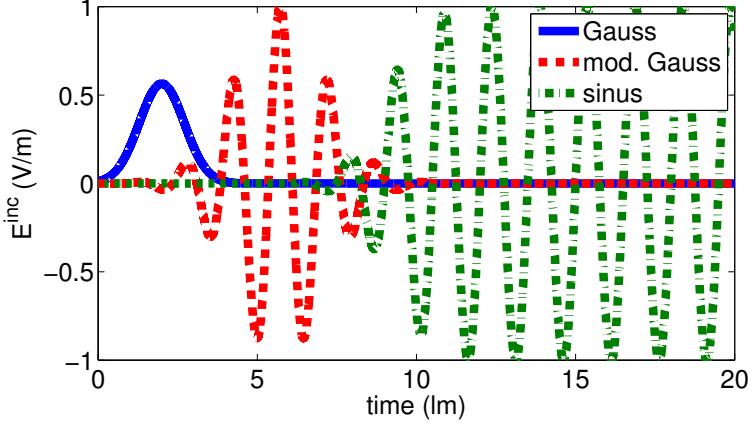


Figure 2.3: Examples of the incident wave fields, given by the Gaussian pulse (2.35), modulated Gaussian pulse (2.37), and causal sinusoidal wave (2.38).

**Modulated Gaussian pulses** The most popular incident wave field in literature is based on the modulated Gaussian pulse, given by

$$g(t) = \frac{1}{\sigma\sqrt{2\pi}} \cos(\gamma(t - \mu)) e^{-\frac{(t-\mu)^2}{2\sigma^2}} \quad (2.31)$$

for  $\mu, \sigma, \gamma \in \mathbb{R}$ . This function is symmetric around its peak value in  $t = \mu$  and its magnitude outside the region  $[\mu - 4\sqrt{\ln(100)}\sigma, \mu + 4\sqrt{\ln(100)}\sigma]$  is at least  $10^{16}$  times smaller than the maximum. The Fourier transform of this pulse is given by

$$\widehat{g}(\omega) = \frac{1}{2} e^{i\omega\mu} \left( e^{-\frac{1}{2}(\omega+\gamma)^2\sigma^2} + e^{-\frac{1}{2}(\omega-\gamma)^2\sigma^2} \right) \quad (2.32)$$

for  $\omega \in \mathbb{R}$ ,  $i^2 = -1$ , and  $\widehat{g}(\omega) = \int_{-\infty}^{\infty} g(t) e^{i\omega t} dt$ . The center frequency  $\omega_c$  of a pulse is defined as the frequency with maximum contribution, whereas the bandwidth frequency  $\omega_{\text{bw}}$  is defined as

$$\frac{|\widehat{g}(\omega_c)|}{|\widehat{g}(\omega_c \pm \omega_{\text{bw}})|} = 10^8. \quad (2.33)$$

For the modulated Gaussian pulse (2.31),

$$\omega_c = \gamma, \quad (2.34a)$$

$$\omega_{\text{bw}} = \frac{4\sqrt{\ln(10)}}{\sigma} \quad (2.34b)$$

This means that the strength of the modulated Gaussian pulse at frequency  $\omega_c \pm \omega_{\text{bw}}$  is down by  $10^8$  or 160 dB from its peak value. The *essential frequency spectrum* is thus given by  $[\omega_c - \omega_{\text{bw}}, \omega_c + \omega_{\text{bw}}]$ . Notice that this is the angular frequency, the ordinary frequency is given by  $f = \omega/(2\pi)$ .

A special case is the *Gaussian plane wave*, given by

$$\mathbf{E}^i(\mathbf{r}, t) = E_0 \frac{4}{\sqrt{\pi w}} e^{-\left(\frac{4}{w}(c(t-t_0) - \mathbf{r} \cdot \hat{\mathbf{k}})\right)^2} \hat{\mathbf{p}} \quad (2.35)$$

for  $w$  the pulse width in m and  $t_0$  the pulse delay in s. This is a modulated Gaussian function (2.31) with  $\gamma = 0$ ,  $\mu = t_0 + (\mathbf{r} \cdot \hat{\mathbf{k}})/c$ , and  $\sigma^2 = \frac{1}{2}\left(\frac{T}{4c}\right)^2$ . The magnitude of the pulse at  $t = t_0 \pm w/c$  is 140 dB below the peak value. Because the center frequency is zero, the frequency bandwidth is also the maximum frequency content, given by

$$f_{\text{max}} = \frac{8\sqrt{\ln(100)}}{\pi} \frac{c}{T}. \quad (2.36)$$

For example, a pulse width of 4 m results in a maximum frequency of 410 MHz, which corresponds to a minimum wavelength of 0.73 m.

A more general incident wave field is the *modulated Gaussian plane wave*, given by

$$\begin{aligned} \mathbf{E}^i(\mathbf{r}, t) &= E_0 \cos(2\pi f_c \rho) e^{-\frac{\rho^2}{2\sigma^2}} \hat{\mathbf{p}}, \quad (2.37) \\ \sigma &= \frac{3}{2\pi f_b}, \\ \rho &= t - t_0 - \frac{\mathbf{r} \cdot \hat{\mathbf{k}}}{c} \end{aligned}$$

for  $f_c$  and  $f_b$  the center and bandwidth frequency in Hz, resp. The magnitude of the field at frequencies  $f_c \pm f_b$  reduces to approximately 40 dB below the peak value. The field is reduced by 160 dB at frequencies  $f_c \pm 2f_b$  because  $4\sqrt{\ln(10)} \approx 6.1$ .

**Stationary waves** Frequency-domain methods use stationary waves, that is, sinusoidal fields with a given frequency. Due to the zero initial conditions, these wave fields are not feasible in the TDIE method. This can be solved by

using a *causal sinusoidal* plane wave, given by

$$\begin{aligned} \mathbf{E}^i(\mathbf{r}, t) &= E_0 \sin(\sigma_{\text{wave}}) \left( \frac{1}{2} + \frac{1}{2} \text{erf}(\sigma_{\text{shape}}) \right) \hat{\mathbf{p}}, & (2.38) \\ \sigma_{\text{wave}} &= 2\pi \frac{ct - \mathbf{r} \cdot \hat{\mathbf{k}}}{\lambda}, \\ \sigma_{\text{shape}} &= 6 \left( \frac{\sigma_{\text{wave}}}{2\pi n} - 1 \right) \end{aligned}$$

for  $\lambda$  the wave length in m and  $n$  the time offset in number of wave lengths. Notice that this wave field has been defined such that  $|\mathbf{E}^i| < 10^{-16}$  for  $t < 0$  and from  $t = 2n\lambda/c$  a sinusoidal plane wave is obtained in machine precision, with amplitude  $E_0$  and wave length  $\lambda$ .



# Stability

## 3.1 Stability of TDIE methods

Computer simulations always produce an approximate solution of the physical model. This approximation should be realistic enough for computational methods to be useful. One of the requirements on physical realism is that the approximation remains bounded. This is guaranteed when the numerical scheme is *stable*. Evidently, lack of stability should always be prevented.

TDIE methods for electromagnetic scattering analysis have a long history of instability. Early schemes were hard to stabilize, even for small problem sizes. Extensive research has improved the MoT scheme such that stable results can be obtained for many different objects. The instabilities that are still present arise only when simulation times are very long with respect to the time scale of the excitation. This *late-time instability* can be very deceptive and computational experiments suggest that the instabilities will be visible in early time for more complicated geometries.

The stability of TDIE methods depends on different numerical parameters, such as the time step size and the number of quadrature points. Repeating computer simulations with carefully adjusted parameters will most often lead to stability. However, this is not feasible in industry due to constraints in time, computer power, and financial resources. Furthermore, nonexpert users should be able to generate robust simulations. For these reasons, stability of the computational method has to be assured without fiddling with numerical parameters. In theory, the TDIE method can be proven to be unconditionally stable, so without conditions on the choice of time step size and mesh width. In practice, the expected stability can only be achieved with specific numerical schemes and very accurate evaluation of the discrete interaction matrices.

Stability is a classical property of numerical schemes and its definition

can be found in almost all textbooks on numerical analysis. Stability of a numerical scheme depends on the model equation and its analysis can be very elaborate. First, the instabilities that have been found in computer simulations will be analyzed. In Sec. 3.2, several techniques for analyzing stability of TDIE methods will be presented. The instabilities observed in the MoT scheme will be categorized in Sec. 3.3. The most persistent instability originates from the numerical discretization and is visible as a diverging solution in time that alternates on discrete time levels. This type of instability has been observed by many practitioners of the TDIE method and in Sec. 3.4 a large number of the remedies available in literature are explained. Computational experiments in Sec. 3.5 suggest that the choice of temporal basis function is of paramount importance to the stability. The most thorough stability analysis is based on a functional analysis of the variational formulation and results in a functional framework for which a stability proof is available, as explained in Sec. 3.6. This stability theorem will be extended in Sec. 3.7 to the model equations of choice, i.e., the differentiated EFIE. The requirements of the stability theorem prohibits a straightforward use of the MoT scheme. This limitation can be circumvented by rewriting the MoT scheme into an equivalent Petrov-Galerkin scheme, as derived in Sec. 3.8. With these extensions, the stability theorem can be used for the MoT schemes with quadratic spline basis functions. Finally, several nuances for this stable scheme will be discussed in Sec. 3.9.

## 3.2 Analysis of instabilities

Instabilities of numerical schemes typically manifest themselves as solutions that grow beyond any bound. This can easily be seen in a picture of the time evolution of the discrete solution. However, other analyses are available that give more information about how the instability behaves and where it originates from. In this section, several algorithms will be explained to analyze the instabilities in TDIE methods. This will be partitioned into *a posteriori* analyses that require the numerical solution to be computed and *a priori* analyses that work without first performing the computational simulation.

### 3.2.1 A posteriori stability analyses

A posteriori analyses can be used to obtain information about the stability of the TDIE method with high confidence. Drawback of a posteriori analyses is that the information is only valid for the particular test case and can therefore hardly be used to draw conclusions about stability for other test cases. Moreover, these procedures can be computationally expensive.

### Discrete surface current density

The electric surface current density on the scatterer can easily be computed from the discrete solution with the series expansion (2.18). An example of this is given in Fig. 3.1(a), where the discrete surface current density has been depicted for one point on the scatterer surface. In TDIE methods, the instability is often present at late time only, that is, long after the incident wave field has passed the object. Long time simulations are therefore necessary to check stability, which can be computationally demanding. Moreover, stability cannot be verified with this method, only instability can be confirmed.

### Polynomial spectrum

Many computational properties of numerical schemes can be deduced from the discretization matrix. In the case of MoT schemes, the stability can be characterized by the interaction matrices  $Z_j$  for  $j = 0, 1, 2, \dots, \ell$ . To this end, let us rewrite the MoT scheme (2.22) as

$$\mathbf{x}_k = Q\mathbf{x}_{k-1} + \mathbf{f}_k \quad (3.1)$$

for  $\mathbf{x}_k = [\mathbf{I}_k \ \mathbf{I}_{k-1} \ \dots \ \mathbf{I}_{k-\ell+1}]^T$  denoting the solution vector over  $\ell$  time levels,  $\mathbf{f}_k$  the excitation and

$$Q = \begin{bmatrix} -Z_0^{-1}Z_1 & -Z_0^{-1}Z_2 & \dots & -Z_0^{-1}Z_{\ell-1} & -Z_0^{-1}Z_\ell \\ I & 0 & & & \\ & I & \ddots & & \\ & & \ddots & 0 & \\ & & & I & 0 \end{bmatrix}. \quad (3.2)$$

This amplification matrix has size  $\ell N_s \times \ell N_s$  and is in block companion form. Solutions of the recurrence relation are bounded if the spectral radius of the amplification matrix  $Q$  is smaller than unity. So, when all eigenvalues of  $Q$  are contained within the unit circle of the complex plane, the numerical stability has been confirmed [27, 3]. This property can also be derived via the  $z$ -transform of the MoT algorithm [60]. An example of this so-called *polynomial spectrum* is given in Fig. 3.1(b).

Computation of the polynomial spectrum can be prohibitively expensive for large problem sizes. Notice that the spectral radius of the amplification matrix already determines numerical stability, which makes it redundant to compute the full polynomial spectrum. Algorithms exist that approximate the spectral radius efficiently. However, for the MoT scheme these methods are not effective due to the special structure of the polynomial spectrum. More precisely, an eigenvalue of 1 with a large multiplicity is always present because DC currents reside in the nullspace of the EFIE, see Sec. 3.3.1. This deteriorates the performance of most approximation techniques for the spectral

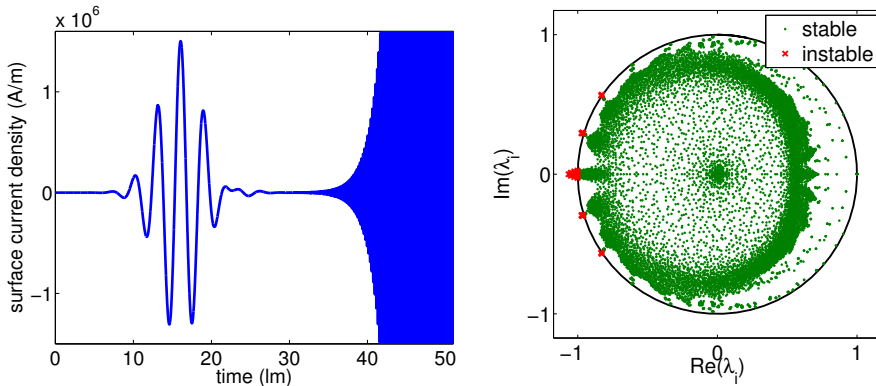
radius. The polynomial spectrum analysis can thus be performed for small test cases only.

Several techniques exist that compute an upper bound of the spectral radius, for instance the Gerschgorin circle theorem [34]. Computational experiences show that the computed upper bound is impracticable.

The MoT scheme (2.30) for the original EFIE contains an additional tail, which necessitates the adjustment of the recurrence relation (3.1). Now, the solution vector reads  $\mathbf{x}_k = [\mathbf{I}_k \ \mathbf{I}_{k-1} \dots \mathbf{I}_{k-\ell+1} \ \sum_{j=\ell}^k \mathbf{I}_{k-j}]^T$  and the amplification matrix is given by

$$Q = \begin{bmatrix} -Z_0^{-1}Z_1 & -Z_0^{-1}Z_2 & \dots & -Z_0^{-1}Z_{\ell-1} & -Z_0^{-1}Z_{\ell} & -Z_0^{-1}Z_{\text{tail}} \\ I & 0 & & & & \\ & I & \ddots & & & \\ & & \ddots & & & \\ & & & 0 & & \\ & & & I & 0 & \\ & & & & I & I \end{bmatrix}. \quad (3.3)$$

A different procedure to compute the polynomial spectrum of the original EFIE is given in [68]. There, the discrete solution for the current and charge are decoupled, yielding a system with size  $2\ell N_s \times 2\ell N_s$  instead of  $(\ell + 1)N_s \times (\ell + 1)N_s$ , which makes it computationally more expensive.



(a) Discrete surface current density. Instability is visible as a diverging solution.

(b) Polynomial spectrum. Instability is visible as eigenvalues outside the unit disk.

Figure 3.1: A posteriori stability analyses of numerical instability for scattering of a modulated Gaussian pulse (2.37) on a cube. The instability has been generated with a very small number of quadrature points.

### Polynomial pseudospectrum

The spectrum provides insight in many characteristics of a matrix. If the matrix is nonnormal, as is the case for companion matrices, the pseudospectrum can reveal more information [92]. The pseudospectrum  $\Lambda_\epsilon$  of a matrix  $A$  is defined as

$$\Lambda_\epsilon(A) = \{z \in \mathbb{C} : \|(zI - A)^{-1}\| \geq \epsilon^{-1}\} \quad (3.4)$$

for  $\epsilon \in \mathbb{R}$ . For an eigenvalue  $\lambda$  of  $A$ , the resolvent  $(\lambda I - A)^{-1}$  is not correctly defined and  $\|(\lambda I - A)^{-1}\| = \infty$  by convention. Hence, the spectrum  $\Lambda$  is a special case of a pseudospectrum, namely  $\Lambda(A) = \Lambda_0(A)$ . The pseudospectrum can be also be expressed as the spectrum of a perturbed matrix, i.e.,

$$\Lambda_\epsilon(A) = \{z \in \mathbb{C} : z \in \Lambda(A + E) \text{ for some } E \text{ with } \|E\| \leq \epsilon\}. \quad (3.5)$$

This states that the  $\epsilon$ -pseudospectrum is equivalent to the spectrum of all  $\epsilon$ -perturbations of a matrix. Consequently, this theorem can be used to analyse the stability of MoT schemes for perturbations in the discretization matrix. When the  $\epsilon$ -pseudospectrum is contained within the unit circle in the complex plane, all MoT schemes with a perturbation of at most  $\epsilon$  in a matrix norm will be stable as well. Perturbations of the discrete interaction matrices for instance be caused by quadrature and rounding errors. The pseudospectrum can thus be used as a measure for the robustness of the MoT scheme.

An example of the pseudospectrum is depicted in Fig. 3.2 for two different temporal basis functions. The small values of  $\epsilon$  in the positive real plane are caused by DC modes, which result in a large number of eigenvalues near  $1 + 0i$ , as will be explained in Sec. 3.3.1. Interesting is the contour level of  $\epsilon = 10^{-1}$  which is close to the unit circle in the complex plane. This contour is slightly tighter for the quadratic Lagrange basis function, suggesting that this choice is less susceptible to perturbations. However, it is actually the quadratic Lagrange basis function that results in instability, as confirmed by the eigenvalue at  $-1.024 + 0i$ .

The computation of the pseudospectrum is very expensive, even a lot more than computing the spectrum. Furthermore it is difficult to draw conclusions from pseudospectra because of the large influence of DC modes and only small differences between temporal basis functions have been noticed. This technique, although insightful, will therefore not be used in this thesis.

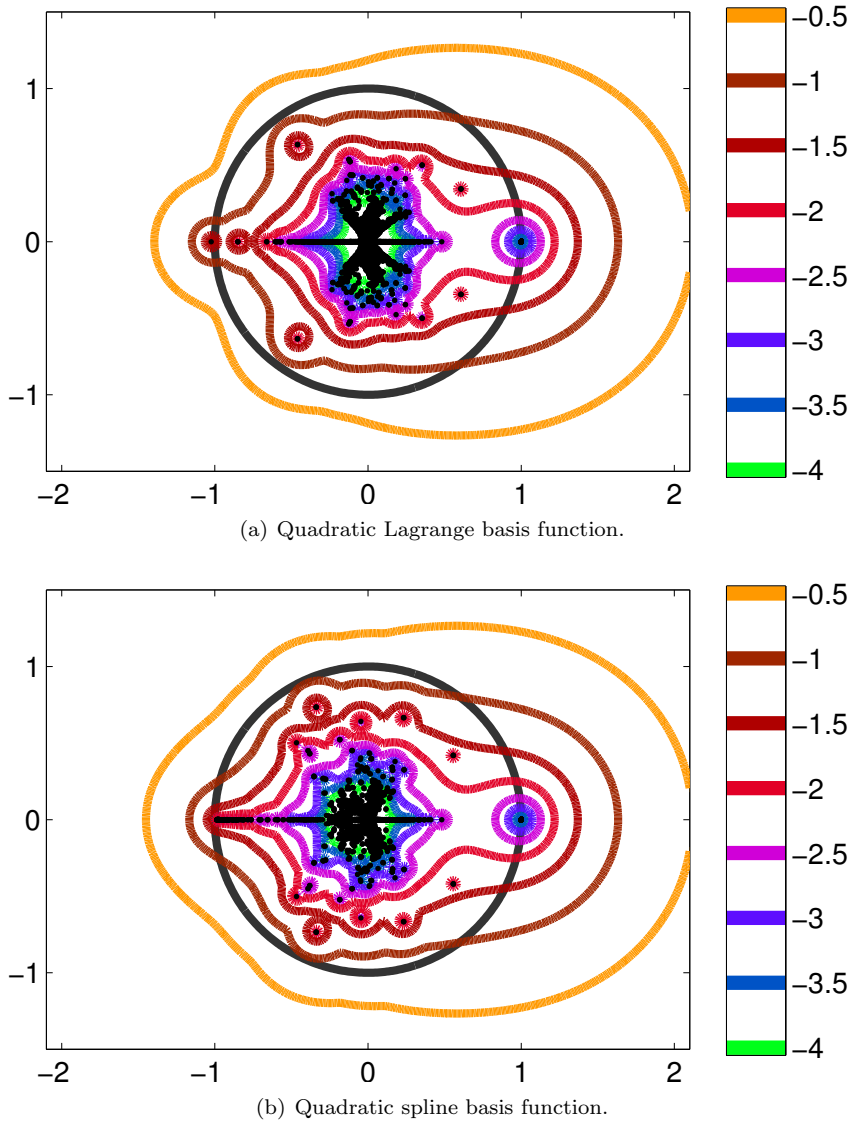


Figure 3.2: The pseudospectrum of the differentiated EFIE, for a unit cube with a mesh of 720 edges,  $\Delta t = 0.5$  lm, and quasi-exact integration. The contours of the pseudospectrum  $\Gamma_\epsilon(Q)$  of the amplification matrix (3.2) are given by  $\log_{10}(\epsilon)$ . The unit circle is depicted in black and the spectrum is depicted by black dots. The pseudospectrum has been computed with `EigTool`, a free Matlab package made by Thomas G. Wright, University of Oxford, [www.comlab.ox.ac.uk/pseudospectra/eigtool/](http://www.comlab.ox.ac.uk/pseudospectra/eigtool/).

### 3.2.2 A priori stability analyses

A priori analyses are necessary to obtain general conditions for stability. Advantage is that insight can be obtained in the stability characteristics of the TDIE method such that stable schemes can be designed for a wide range of numerical parameters. Drawback is that the assumptions used in the analyses make it difficult to draw conclusions on the stability of the actual computer simulations. Loosely speaking, there is a gap between theory and practice.

#### Test equation

A standard approach to analyze numerical schemes for initial value problems is by considering the test equation

$$\frac{d}{dt}y = \lambda y + f \quad (3.6)$$

for the unknown  $y(t)$ , forcing term  $f(t)$ , and parameter  $\lambda \in \mathbb{C}$ . When the MoT scheme with quadratic Lagrange basis functions is applied to the test equation, the discretization error  $e_n$  at time level  $t_n$  satisfies the recurrence relation

$$\left(\frac{3}{2} - \lambda\Delta t\right) e_n - 2e_{n-1} + \frac{1}{2}e_{n-2} = 0. \quad (3.7)$$

Similar to the polynomial spectrum analysis, an amplification matrix can be derived, for which all eigenvalues should be smaller than one. In this case, the two eigenvalues can be computed analytically. This results in a region in the complex plane for which all values of  $\lambda$  result in a stable scheme, see Fig. 3.3. The same analysis can be performed for other temporal basis functions, for which interesting relations with classical schemes are obtained. The family of shifted Lagrange basis functions can be related to the backward differentiation formulas (BDF) and the quadratic spline basis function to the trapezoidal rule. In general, temporal basis functions (2.29) result in linear multistep methods, for which the Dahlquist barrier states that A-stable schemes can be at most second order accurate [21].

These stability results are only valid for the test equation, which is far more simple than the EFIE. In particular, the presence of retarded time levels can change the stability properties of numerical schemes dramatically [12]. This analysis can therefore only be used as circumstantial evidence. Furthermore, the use of a test equation with a delay will have similar restrictions because the EFIE can not be written as a standard delay differential equation, as explained in Sec. 2.1.5. Stability analyses of delay differential equations have therefore not found its way to the TDIE method.



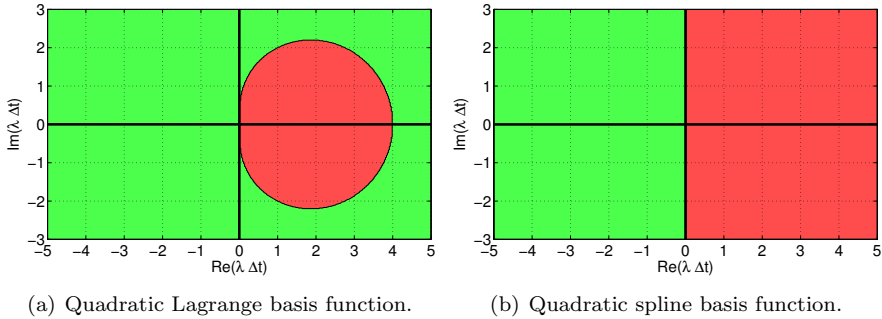


Figure 3.3: Stability regions for the test equation; green area denotes stability and red area instability.

### Von Neumann

A more elaborate way to analyze numerical schemes for ODEs is the ‘Von Neumann analysis’. This technique uses Fourier transforms and has been applied to TDIE methods in which finite differences are used as numerical scheme. For a flat plate with square patches, conditions on the CFL number have been derived [22, 24]. Because a different discretization procedure is used and the method is only valid for flat plates with uniform patches, it is difficult to draw conclusions for stability of general TDIE methods.

### Functional framework

A rigorous approach to analyze TDIE methods is the functional framework of the variational formulation. For the EFIE, the analysis in [91] results in guidelines for the choice of test and basis functions for which the solution of the variational formulation is bounded. This is the most sophisticated and promising analysis of TDIE methods and will be discussed extensively in Sec. 3.6.

## 3.3 Types of instabilities

With the stability analyses, different types of instabilities can be characterized in MoT schemes, all with different causes and implications. In this section, instabilities will be subdivided into three categories, namely *direct current*, *resonance*, and *numerical* instabilities.

### 3.3.1 Spectral instability

The origin of spectral instabilities can be traced back to the spectral properties of the continuous EFIE [3]. For instance, solutions in the null space of the EFIE should remain constant in time. Discretization errors might shift the corresponding eigenvalues slightly such that these solutions increase in size. Two types of this instability will be considered, related to direct currents (DC) and resonances.

#### DC instability

Static solenoidal currents generate no electric field on the surface of a PEC structure. This makes the EFIE blind to these DC modes. Mathematically, DC solutions reside within the null space of the EFIE. For the differentiated EFIE, this extends to solenoidal currents that are linear in time. DC modes are characterized by an eigenvalue 1 in the polynomial spectrum. Discretization errors shift these eigenvalues slightly outside the unit disk. This results in slowly growing solutions, called *DC instability* or *low frequency breakdown*.

Remedies for DC instability of TDIE methods include the use of loop-tree decompositions [102], conditions on the normal magnetic field [64], hierarchical spatial basis functions [2], and Calderón preconditioning [3]. The use of Calderón preconditioning is the most effective one, because a model equation is derived that does not include DC modes in its null space, thus solving the DC instability altogether. Notice that when nontoroidal closed surfaces are analyzed, the CFIE is free of DC modes as well [19].

DC instabilities typically correspond to polynomial eigenvalues very close to 1, resulting in solutions that grow without any bound, but at a very slow pace. In all computer simulations in this thesis, the size of the DC modes is several orders of magnitude smaller than the peak in the incident wave field. Consequently, the DC instability is hardly visible in the discrete solution. For this reason, and because remedies are available, DC instabilities will not be covered in this thesis.

As illustration, two test cases will be presented in which a DC instability can be recognized in the solution. Both have been generated with unrealistically chosen parameters that will never be used in actual computer simulations for radar signature analysis. The DC instability depicted in Fig. 3.4 is visible because a tremendous amount of 1 000 000 time levels has been simulated with a total simulation time of 100 000 fm. Notice that the magnitude of excitation has dropped by a factor of  $10^{-16}$  of its peak value after 21 000 time levels already. The DC instability depicted in Fig. 3.5 has been generated with an insane time step size of 100 000 fm, for a sphere with a radius of 1 m. This means that the time step size has been chosen 50 000 times larger than the electrical size of the object.



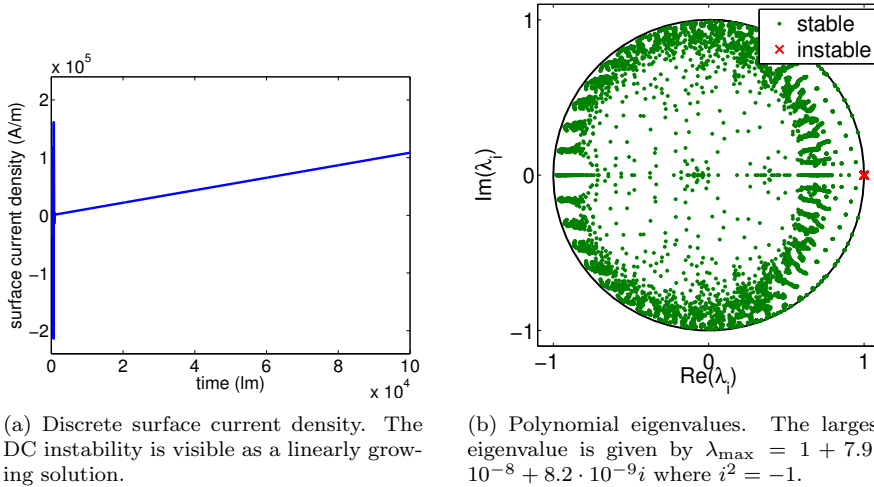


Figure 3.4: Simulation of the differentiated EFIE, for a sphere with radius 1 m,  $\Delta t = 0.1$  lm, and a modulated Gaussian plane wave (2.37) with  $f_c = f_b = 1$  MHz.

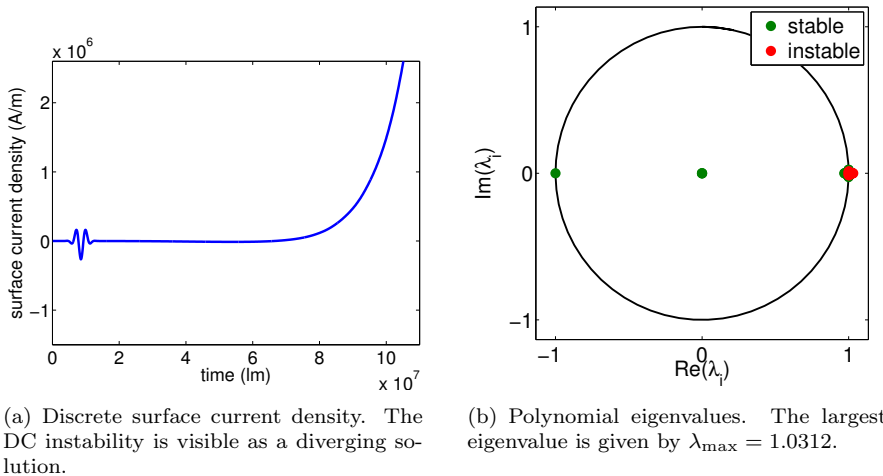


Figure 3.5: DC instability of the differentiated EFIE, for a sphere with radius 1 m,  $\Delta t = 100\,000$  lm, and a modulated Gaussian plane wave (2.37) with  $f_c = f_b = 100$  Hz.

### Resonance instability

Similar to DC modes, resonances reside within the null space of the EFIE. Resonances are oscillating solutions that have constant size in time. They are characterized by polynomial eigenvalues on the unit circle in the complex plane. These eigenvalues might shift outside the unit disk due to discretization errors and cause instabilities [85]. The classical remedy is to use the CFIE, which does not support resonant solutions [81]. Another approach is to use a localized Calderón preconditioner [3]. In our experience, resonances are hardly visible in the surface current density and resonances will be outside the scope of this thesis.

### 3.3.2 Numerical instability

The most problematic type of instability is the numerical instability that results in alternating, exponentially increasing solutions. This corresponds to polynomial eigenvalues on the negative real axis outside the unit disk, see Fig. 3.1. Because the unstable solution alternates on discrete time levels, this instability is also called *high-frequency breakdown*. When the unstable eigenvalue is close to the unit disk, the exponentially increasing solution will start very slow compared to the incident wave field. The unstable solution is thus only visible in the total field after the incident wave field has passed the object, leading to its euphemistic name *late-time instability*. For simulations of industrial interest, the surface mesh will have a higher resolution and the instability will arise in early time. The simulations depicted in Fig. 3.6 and 3.7 corroborates on the idea that the more degrees of freedom, the earlier the instability in time.

This kind of instability is not related to the null space of the EFIE and is caused by the discretization procedure [3]. Computational experiences and a posteriori stability analyses suggest that the choice of temporal basis function and the accuracy of the numerical quadrature for the evaluation of interaction matrices have a profound influence on the numerical stability. A priori stability analyses support these observations.

Solving numerical instability has drawn a lot of attention in literature and is still an ongoing topic of research [87, 68]. Most remedies that have been proposed in literature will be explained in Sec. 3.4. In subsequent sections, a new approach will be presented that improves stability by using a functional framework to derive guidelines for the design of temporal basis functions.

## 3.4 Remedies for numerical instability

Numerical instabilities have been found in MoT schemes since their early inception. Many techniques have been introduced in literature to remedy



stability, namely

1. adjust the numerical discretization;
2. adjust the model equations;
3. eliminate high frequency components by:
  - (a) filtering and averaging,
  - (b) large time step sizes, and
  - (c) bandlimited temporal basis functions;
4. increase the numerical accuracy by:
  - (a) large CFL number,
  - (b) smooth temporal basis functions,
  - (c) quasi-exact quadrature, and
  - (d) separable approximation of convolutions; and
5. derive a functional framework.

Although these approaches improve stability, all have their own drawbacks, as will be explained subsequently.

### 3.4.1 Numerical discretization

The numerical instability originates from the discretization procedure of the MoT scheme. An obvious way to solve numerical instability in TDIE methods is to use another numerical scheme. In Sec. 2.1.5 many numerical schemes for use in TDIE methods have been summarized. In particular, the CQ scheme has been proven to be stable, but is dispersive and dissipative. Also, all common choices of numerical scheme can be written as a space-time Petrov-Galerkin method, including the MoT scheme. This section therefore focuses on MoT schemes only.

### 3.4.2 Model equations

Computational experiences confirm that the same MoT scheme can be unstable for the EFIE and stable for the MFIE, or vice versa. In general, the MoT scheme is reported to be more stable for second order integral equations, such as the MFIE [114]. However, there is no sound theory for this observation and instabilities are still present in both models. Moreover, the MFIE is restricted to closed surfaces.

### 3.4.3 High-frequency components

Numerical instability usually manifests itself as an alternating solution that grows exponentially in time. This corresponds to the highest frequency mode possible on the discrete time axis. Eliminating high-frequency components is the idea behind several stabilization procedures.

#### Filtering and averaging

One of the earliest stabilization methods is the *filtering* or *averaging* of the numerical solution. Different filtering techniques have been used, both in time and space. In certain cases, this method is capable to eliminate instability and Fourier analysis confirms an extended stability region [89]. However, these techniques do not eliminate instability [75]. In fact, simulations have been found where averaging introduces instability [23].

#### Large time step sizes

If the time step size increases, then the highest frequency that can be represented by the discrete solution will decrease. Computational methods indeed show a dependency between time step size, or implicitness, and stability [27]. However, no clear bounds on the time step size are available and stability cannot be guaranteed [96].

#### Bandlimited temporal basis functions

Because the solution is approximated with temporal basis functions, one might exclude high-frequency content by using temporal basis functions with limited frequency content. The approximate prolate spheroidal wave functions have been used as a bandlimited interpolation function (BLIF) to prevent the buildup of high-frequency spurious modes [102]. The performance of these bandlimited temporal basis functions heavily depends on a large support in time. This necessitates extrapolation schemes and increases computation time and memory requirements. Furthermore, this scheme is still unstable in rare cases and only works for a limited range of time step sizes [98].

### 3.4.4 Numerical accuracy

Computational experiences suggest that the accuracy with which the interaction matrices are computed influences the stability of the MoT scheme. This observation is supported by the fact that a priori stability analyses assume that all interaction matrices are evaluated exactly. The idea to remedy instability is thus to increase the accuracy of the evaluation of interaction matrices.



Here, *numerical accuracy* is defined as the accuracy with which the discrete model equations are calculated and implemented on a computer architecture. This excludes the discretization errors originating from the choice of test and basis functions. The main sources of numerical errors are the quadrature procedure and the use of finite precision arithmetic. The quadrature procedure is used to approximate the four-dimensional integrals over the scatterer surface that are present in the interaction matrices of the discrete EFIE. As will be explained in Sec. 5.3, the integrand contains discontinuities, thus reducing the effectiveness of standard quadrature rules. The smoothness of the integrand depends on the time step size, the size of the triangular patches, and the choice of temporal basis function.

The improvement in robustness that will be achieved in Chapter 5 corroborates on the idea that numerical accuracy is required to obtain stability.

### Large CFL number

As will be explained in Chapter 5, the smoothness of the integrand depends on the electrical size of each surface mesh element. To be more precise, the larger the size of triangular patch w.r.t. the time step size, the less smooth the integrand. Therefore, increasing the CFL number, or mesh ratio, increases the smoothness of the integrand and the quadrature procedures become more effective. This remedy can only be used *ad hoc* and impinges on accuracy and efficiency [27].

### Smooth temporal basis functions

The performance of numerical quadrature depends on the smoothness of the integrand. In MoT schemes, the discontinuities in the expressions for the interaction matrices originate from the nonsmooth character of the temporal basis functions. To this end, smooth temporal basis functions will be designed in Chapter 4, similar to the design of BLIFs [102]. However, smoothness can in general only be achieved at the expense of other design criteria such as efficiency.

### Quasi-exact quadrature

Instead of increasing the smoothness of the integrand, one can also use quadrature schemes that are more accurate [22]. To obtain accurate evaluation of the surface integrals, the quadrature rule has to be designed specifically for the TDIE method, because the discontinuities in the integrand are only present at prescribed locations. The location of the discontinuities is known and can be computed for flat patches, resulting in subregions for which the integrand is smooth. Use of analytical expressions of radiation fields can further improve the accuracy of the evaluation of interaction matrices. These quasi-exact

quadrature rules have been shown to improve stability [84, 87]. A quasi-exact quadrature rule will be explained in detail in Chapter 5, where the discontinuities are depicted in Fig. 5.1.

Main advantage of this approach is that it does not affect the choice of temporal basis functions and mesh sizes in space and time. On the other hand, robust implementation of these quasi-exact quadrature rules is burdensome [109], is difficult if not impossible to apply to curved patches [98], difficult to integrate in fast solvers [68], increases the computation time [87], and depends on the Green's function [84]. Nonetheless, computational experiences confirm that the use of quasi-exact quadrature is necessary to obtain stability in MoT schemes [87, 109].

### Separable approximation of convolutions

A delicate approach to improve the regularity of the integrand without adjusting the time step size or temporal basis function is the separable approximation of the convolution [68]. In this method, the convolution in time of the Green's function and the temporal basis function is approximated by a series expansion in Legendre polynomials. Then, the time and space dependencies can be separated and quadrature rules become effective. A stability analysis has been derived [66] and the method has been applied to curvilinear elements [67]. However, to the best of our understanding, the analysis of the accuracy and robustness has not been published in literature.

#### 3.4.5 Functional framework

The most rigorous approach to remedy the numerical instability of MoT schemes is to derive a functional framework for its discretization procedure. For the space-time Galerkin scheme, a thorough mathematical foundation has been derived, resulting in a specific variational formulation of the EFIE with a unique and bounded solution. Application of this functional framework to the MoT scheme has to be done carefully. In the remainder of this chapter, this functional framework will be used to derive guidelines for the choice of temporal basis functions such that stability can be expected.

### 3.5 Experimental suggestion

In previous sections, a review of the stability of TDIE methods has been given. Instability has been categorized in spectral and numerical causes. The many remedies for the numerical instability that are given in literature have been explained. The most thorough approach is the use of a functional framework. In next sections, an available functional framework will be explained and extensions to the MoT scheme for the differentiated EFIE will be derived.



Before proceeding to this analysis, let us look at some computer simulations that will illustrate the importance of the functional analysis. In particular, the computational experiments suggest that a proper choice of temporal basis function is of paramount importance to numerical stability.

Let us consider a sphere of radius 1 m with a triangular surface mesh consisting of 356 edges. The time step size is chosen as  $\Delta t = 10^{-9}$  s. The incident wave field is given by a Gaussian plane wave (2.35) and traverses the sphere in approximately 7 time steps. The outer surface integral is approximated with a Gaussian quadrature with 73 points, whereas the inner integral is computed analytically [84]. The MoT scheme has been performed for the differentiated EFIE. The electric surface current density, depicted in Fig. 3.6, clearly shows an alternating, exponentially increasing solution for the quadratic Lagrange basis function. The use of quadratic spline basis functions results in a stable MoT scheme, as verified by the polynomial spectrum that resides within the unit disk of the complex plane.

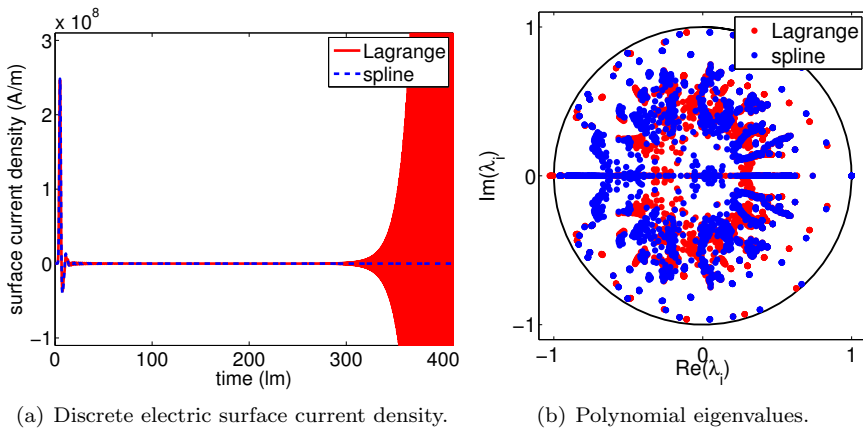


Figure 3.6: Discrete solution on a sphere with quadratic basis functions.

The second computer simulation uses the MoT scheme for the differentiated EFIE as well. A generic aircraft, depicted in Fig. 6.1, is meshed with 6756 edges and scaled to fit within the unit cube. The time step size is chosen as 0.01 lm. Again, the outer surface integral is approximated with a Gaussian quadrature with 73 points, whereas the inner integral is computed analytically. As incident wave field, a modulated Gaussian plane wave (2.37) is used with center frequency 1 GHz and bandwidth 0.5 GHz. Fig. 3.7 depicts the electric surface current density at the tail tip. The quadratic Lagrange basis function clearly results in an unstable computer simulation, whereas the quadratic spline basis functions remains stable for this test case. Notice that computing the polynomial spectrum is computationally too expensive because of the

dimensions, but from Fig. 3.7(b) it is clear that the MoT scheme is stable for late time, in this case 10 000 discrete time levels.

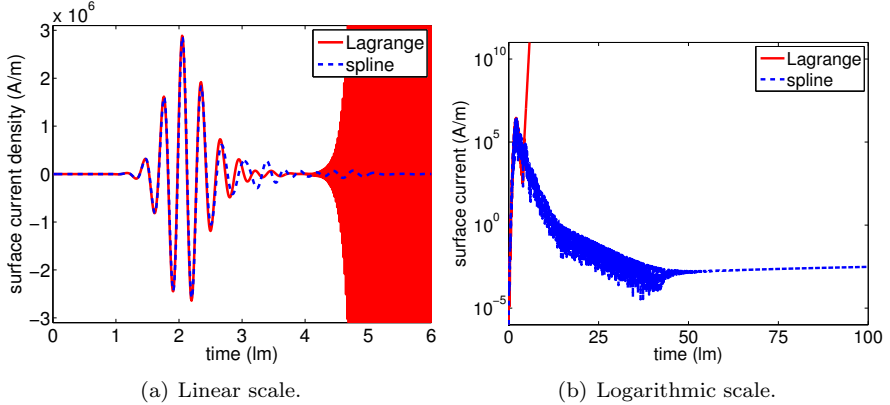


Figure 3.7: Discrete electric surface current density on a generic aircraft with quadratic basis functions.

Main conclusion from these two computational experiments is that the choice of temporal basis function influences the stability of the MoT scheme. In particular, the computer simulations suggest that the quadratic spline basis functions (4.25) yield better stability characteristics than the quadratic Lagrange basis functions (4.22). The functional analysis in subsequent sections supports this observation and will result in guidelines for the choice of temporal basis functions for which stability is expected.

### 3.6 Functional analysis of the original EFIE

The numerical discretization procedure in TDIE methods is given by the boundary element method (BEM). Model equations in a BEM are specified on a two-dimensional manifold in  $\mathbb{R}^3$ . On this surface, a finite element method is used to obtain discrete equations. To this end, the model equations are written into a *variational formulation* or *weak formulation* containing test and basis functions. The choice of these test and basis functions determines the properties of the computational method to a great extent. In particular, numerical stability is affected by this choice, as confirmed by the computational experiments in Sec. 3.5. To obtain guidelines for this choice, a functional framework has to be designed for which a unique and bounded solution is guaranteed [1]. In this section, a summary of an available functional framework for the original EFIE will be given. In next sections, this approach will be extended such that a stable MoT scheme can be designed.



The review articles [39, 20] explain the variational formulation of general retarded potential integral equations. The special case of the EFIE for electromagnetics, a functional framework has been designed by Terrasse in her PhD thesis [91]. This section serves as an introduction to this functional framework and the resulting stability theorem.

### 3.6.1 Functional framework

The functional analysis of the original EFIE will make extensive use of the function spaces  $\mathcal{H}^s$  for  $s \in \mathbb{R}$ , defined as

$$\mathcal{H}^s = H_\sigma^s \left( \mathbb{R}_+, H^{-\frac{1}{2}}(\text{div}, \Gamma) \right) \quad (3.8)$$

for  $\sigma \in \mathbb{R}$  positive:  $\sigma > 0$ . This function space is a special version of a Sobolev space. Its norm is given by

$$\|\mathbf{f}(\mathbf{r}, t)\|_{\sigma, s, -\frac{1}{2}\text{div}}^2 = \int_{-\infty+i\sigma}^{+\infty+i\sigma} |\omega|^{2s} \left\| \widehat{\mathbf{f}}(\mathbf{r}, \omega) \right\|_{H^{-\frac{1}{2}}(\text{div}, \Gamma)}^2 d\omega \quad (3.9)$$

for  $\omega = \eta + i\sigma$ , where  $i$  denotes the imaginary unit:  $i^2 = -1$ . The Fourier-Laplace transform, denoted by  $\widehat{\mathbf{f}}$ , is given by

$$\widehat{\mathbf{f}}(\mathbf{r}, \omega) = \int_{-\infty}^{\infty} e^{i\omega t} \mathbf{f}(\mathbf{r}, t) dt. \quad (3.10)$$

This norm can be used to measure the energy of the electric surface current density. Without specifying all details, let us highlight several requirements for this Sobolev space:

- The spatial part of the Sobolev space requires the functions to be element of  $H^{-\frac{1}{2}}(\text{div}, \Gamma)$ , which is the space of divergence conforming surface functions. RWG functions are element of this space [18].
- The support in time of the functions has to be  $\mathbb{R}_+$ , which is equivalent to causality and the initial conditions stating zero fields for  $t < 0$ .
- The function has to be Fourier-Laplace transformable for  $\sigma > 0$ , which requires the function to decay in time with an exponential rate.
- The function has to have a certain degree of regularity in time, characterized by the parameter  $s$ . More precisely, the function  $(-i\omega)^s \widehat{\mathbf{f}}(\omega)$  has to be inverse Fourier-Laplace transformable. When  $s$  is an integer, this reduces to  $s$ -times differentiable functions.

An important property of the Sobolev space that will be used in subsequent analyses is: if  $\mathbf{f} \in \mathcal{H}^s$  then  $\frac{\partial}{\partial t} \mathbf{f} \in \mathcal{H}^{s-1}$  and  $\mathbf{f} \in \mathcal{H}^{s'}$  for  $s' \leq s$ . A few example functions will be given in Sec. 3.8.1.

The functional framework uses a space-time inner product given by

$$\langle \mathbf{f}(\mathbf{r}, t), \mathbf{g}(\mathbf{r}, t) \rangle_\sigma = \int_{\mathbb{R}} e^{-2\sigma t} \iint_{\Gamma} \mathbf{f}(\mathbf{r}, t) \cdot \mathbf{g}(\mathbf{r}, t) \, d\mathbf{r} \, dt \quad (3.11)$$

which is correctly defined for functions  $\mathbf{f}, \mathbf{g} \in \mathcal{H}^s$ . Special feature of the inner product is the presence of the weight  $e^{-2\sigma t}$  in time. For the functional framework, in particular the proof of the stability theorem, it is required to use  $\sigma > 0$ . The numerical schemes will use  $\sigma = 0$  for convenience and efficiency. This nuance will be explained in Sec. 3.9.2.

Whereas in this thesis the EFIE is solved for the electric surface current density  $\mathbf{J}(\mathbf{r}, t)$ , the functional framework use the electric surface charge density  $\rho(\mathbf{r}, t)$  as an additional unknown. Then, the following function space has to be used:

$$\mathcal{H}_{\rho, \mathbf{J}}^s = \left\{ (\rho, \mathbf{J}) \in H_\sigma^s \left( \mathbb{R}_+, H^{-\frac{1}{2}}(\Gamma) \right) \times H_\sigma^s \left( \mathbb{R}_+, TH^{-\frac{1}{2}}(\Gamma) \right) \right\}. \quad (3.12)$$

This function space will not be used in this thesis, because  $(\rho, \mathbf{J}) \in \mathcal{H}_{\rho, \mathbf{J}}^s$  is equivalent to  $\mathbf{J} \in \mathcal{H}^s$  with the continuity equation (2.2).

### 3.6.2 Stability theorem

The functional framework has been designed for the original EFIE (2.10). For conciseness, the original EFIE can be written as the integral equation

$$\hat{\mathbf{n}} \times (\mathbf{E}^i \times \hat{\mathbf{n}}) = \mathcal{E}(\rho, \mathbf{J}),$$

where  $\mathcal{E}$  denotes the EFIE operator, given by the tangential component of the scattered electric field (2.13a) on the surface, that is  $\mathcal{E}(\rho, \mathbf{J}) = -\hat{\mathbf{n}} \times \hat{\mathbf{n}} \times \mathbf{E}^s$ , where the continuity equation (2.2) has been used.

The stability theorem that has been derived for the original EFIE within the functional framework consists of different parts. First, the integral equations is rewritten into a variational formulation. Then, the uniqueness and boundedness of the solution are derived. The stability theorem of Terrasse reads as follows.

**Variational formulation of Terrasse**  $\forall (\mathbf{E}^i \times \hat{\mathbf{n}}) \in \mathcal{H}^{\frac{3}{2}}$ , the integral equation  $\hat{\mathbf{n}} \times (\mathbf{E}^i \times \hat{\mathbf{n}}) = \mathcal{E}(\rho, \mathbf{J})$  admits the following variational formulation:

$$\begin{aligned} & \text{search for } (\rho, \mathbf{J}) \in \mathcal{H}_{\rho, \mathbf{J}}^{\frac{1}{2}} \text{ such that } \forall (\tilde{\rho}, \tilde{\mathbf{J}}) \in \mathcal{H}_{\rho, \mathbf{J}}^{\frac{1}{2}} \\ b \left( (\rho, \mathbf{J}), (\tilde{\rho}, \tilde{\mathbf{J}}) \right) &= \int_{\mathbb{R}} e^{-2\sigma t} \iint_{\Gamma} (\hat{\mathbf{n}} \times (\mathbf{E}^i \times \hat{\mathbf{n}})) \cdot \frac{\partial^2 \tilde{\mathbf{J}}}{\partial t^2} \, d\mathbf{r} \, dt \end{aligned} \quad (3.13)$$

✓

with

$$\begin{aligned}
b\left((\rho, \mathbf{J}), (\tilde{\rho}, \tilde{\mathbf{J}})\right) &= -\mu \int_{\mathbb{R}} e^{-2\sigma t} \iint_{\Gamma} \iint_{\Gamma} \frac{\partial \mathbf{J}(\mathbf{r}', \tau)}{\partial t} \cdot \frac{\partial^2 \tilde{\mathbf{J}}(\mathbf{r}, t)}{\partial t^2} \, d\mathbf{r} \, d\mathbf{r}' \, dt \\
&\quad - \epsilon \int_{\mathbb{R}} e^{-2\sigma t} \iint_{\Gamma} \iint_{\Gamma} \frac{\rho(\mathbf{r}', \tau)}{4\pi R} \frac{\partial^3 \tilde{\rho}(\mathbf{r}, t)}{\partial t^3} \, d\mathbf{r} \, d\mathbf{r}' \, dt. \quad (3.14)
\end{aligned}$$

**Uniqueness theorem of Terrasse** If  $(\mathbf{E}^i \times \hat{\mathbf{n}}) \in \mathcal{H}^{\frac{3}{2}}$ , the variational formulation admits a unique solution  $(\rho, \mathbf{J})$  in  $\mathcal{H}_{\rho, \mathbf{J}}^{\frac{1}{2}}$ .

**Boundedness theorem of Terrasse** The following bounds hold:

$$\|\rho\|_{\frac{1}{2}, \sigma, H^{-\frac{1}{2}}(\Gamma)} \leq C(\Gamma) \frac{1}{\sigma} \|\mathbf{E}^i \times \hat{\mathbf{n}}\|_{\frac{3}{2}, \sigma, H^{-\frac{1}{2}}(\text{div}, \Gamma)}, \quad (3.15a)$$

$$\|\mathbf{J}\|_{\frac{1}{2}, \sigma, TH^{-\frac{1}{2}}(\Gamma)} \leq C(\Gamma) \frac{1}{\sigma} \|\mathbf{E}^i \times \hat{\mathbf{n}}\|_{\frac{3}{2}, \sigma, H^{-\frac{1}{2}}(\text{div}, \Gamma)}. \quad (3.15b)$$

## Discussion

The stability theorem states that for all incident wave fields in  $\mathcal{H}^{\frac{3}{2}}$ , the original EFIE can be written as a specific variational formulation. For the testing space  $\mathcal{H}_{\rho, \mathbf{J}}^{\frac{1}{2}}$  there is a unique solution of the variational formulation in  $\mathcal{H}_{\rho, \mathbf{J}}^{\frac{1}{2}}$ . Moreover, this solution is bounded by the incident wave field in an energy norm. This concludes that this variational formulation of the original EFIE is stable.

First, let us consider the incident wave field and check whether usual choices of excitation satisfy the requirements of the stability theorem. The stability theorem can only be used when  $(\mathbf{E}^i \times \hat{\mathbf{n}}) \in \mathcal{H}^{\frac{3}{2}}$ . Loosely speaking, the incident wave field has to be smooth and converge to zero at very late time. When the incident wave field is chosen as a realistic representation of a radar field, smoothness will be obtained for physical reasons. Moreover, only simulations of finite time length will be considered, thus satisfying the conditions on the data.

The testing and solution space are given by the Sobolev space  $\mathcal{H}_{\rho, \mathbf{J}}^{\frac{1}{2}}$ , which is equivalent to  $\mathcal{H}^{\frac{1}{2}}$  when the surface charge is eliminated with the continuity equation. In Sec. 3.8, the test and basis functions of the space-time Galerkin scheme will be chosen within these Sobolev spaces. For common choices of test and basis functions, the defining parameter is the regularity of the functions, given by  $s = \frac{1}{2}$ . Furthermore, the unwanted presence of the term  $1/\sigma$  in the bounds will be explained in Sec. 3.9.2.

### 3.7 Functional analysis of the differentiated EFIE

The stability theorem of Terrasse is only applicable to the original EFIE. As argued in Sec. 2.2.4, the differentiated EFIE will result in a more efficient MoT scheme than the original EFIE. Moreover, the vast majority of engineering literature on TDIE methods deals with the differentiated EFIE. To this end, the stability theorem of Terrasse will be extended to the differentiated EFIE. Although the original and differentiated versions of the EFIE are closely related, the extension of the stability theorem of Terrasse is not trivial, as will be apparent in this section. Whereas all information in previous section has been published by Terrasse in [91], the material in this section is new to the literature. First, the resulting stability theorem of the differentiated EFIE will be given, followed by the proof.

#### 3.7.1 Stability theorem of the differentiated EFIE

The differentiated EFIE (2.15) can be written as the integral equation

$$\hat{\mathbf{n}} \times (\dot{\mathbf{E}}^i \times \hat{\mathbf{n}}) = \dot{\mathcal{E}}(\rho, \mathbf{J}),$$

where  $\dot{\mathcal{E}}$  denotes the differentiated EFIE operator, given by the time derivative of the original EFIE operator, that is  $\dot{\mathcal{E}} = \frac{\partial}{\partial t} \mathcal{E}$ . Again, with the continuity equation, the differentiated EFIE operator is given by the tangential component of the time derivative of the scattered electric field on the surface.

**Variational formulation**  $\forall (\dot{\mathbf{E}}^i \times \hat{\mathbf{n}}) \in \mathcal{H}^{\frac{1}{2}}$ , the integral equation  $\hat{\mathbf{n}} \times (\dot{\mathbf{E}}^i \times \hat{\mathbf{n}}) = \dot{\mathcal{E}}(\rho, \mathbf{J})$  admits the following variational formulation:

search for  $\mathbf{J} \in \mathcal{H}^{\frac{1}{2}}$  such that  $\forall \mathbf{w} \in \mathcal{H}^{-\frac{1}{2}}$

$$\left\langle \iint_{\Gamma} \left( \mu \frac{\ddot{\mathbf{J}}(\mathbf{r}', \tau)}{4\pi R} - \frac{1}{\epsilon} \nabla \cdot \frac{\mathbf{J}(\mathbf{r}, \tau)}{4\pi R} \right) d\mathbf{r}', \mathbf{w} \right\rangle_{\sigma} = \left\langle \hat{\mathbf{n}} \times (\dot{\mathbf{E}}^i \times \hat{\mathbf{n}}), \mathbf{w} \right\rangle_{\sigma}. \quad (3.16)$$

**Uniqueness** If  $(\dot{\mathbf{E}}^i \times \hat{\mathbf{n}}) \in \mathcal{H}^{\frac{1}{2}}$ , the variational formulation admits a unique solution  $\mathbf{J}$  in  $\mathcal{H}^{\frac{1}{2}}$ .

**Boundedness** The following bound holds:

$$\|\mathbf{J}\|_{\frac{1}{2}, \sigma, -\frac{1}{2} \text{div}} \leq C(\Gamma) \frac{1}{\sigma} \left\| \dot{\mathbf{E}}^i \times \hat{\mathbf{n}} \right\|_{\frac{1}{2}, \sigma, -\frac{1}{2} \text{div}}. \quad (3.17)$$



### Discussion

Notice that in this variational formulation, the surface charge has been eliminated, as can be performed with the continuity equation. Furthermore, an important difference is in the index of the Sobolev spaces  $\mathcal{H}^s$ , which represents the regularity as defined in Eq. (3.8). Whereas the solution space remains the same, the test space has become  $\mathcal{H}^{-\frac{1}{2}}$ . This means that the test space has one order of regularity more than in the original EFIE. This is reasonable, because using a test function that is more smooth is a natural choice in a differentiated version.

### 3.7.2 Proof of the stability theorem

The backbone of the proof of the stability theorem for the differentiated EFIE is the stability theorem of Terrasse for the original EFIE. When the variational formulations of the two integral equations can be shown to be equivalent, uniqueness and boundedness of the solution will follow. To this end, the following proof will follow the approach of manipulating the variational formulation (3.13) of the original EFIE. This will result in an equivalence with the variational formulation (3.16) of the differentiated EFIE.

#### Eliminating the surface charge

The variational formulation (3.13) of the original EFIE uses both the electric surface charge and current density, denoted by  $\rho(\mathbf{r}, t)$  and  $\mathbf{J}(\mathbf{r}, t)$ , resp. The continuity equation (2.2) can be derived from Maxwell's equation and the constitutive equations. This relation between the charge and current can be used to eliminate one of the two variables. Substitution of the continuity equation into the variational formulation results in:

$$\begin{aligned} & \text{search for } \mathbf{J} \in \mathcal{H}^{\frac{1}{2}} \text{ such that } \forall \tilde{\mathbf{J}} \in \mathcal{H}^{\frac{1}{2}} \\ & \left\langle \iint_{\Gamma} \left( \mu \frac{\mathbf{J}(\mathbf{r}', \tau)}{4\pi R} - \frac{1}{\epsilon} \nabla \cdot \frac{\int_{-\infty}^{\tau} \nabla \cdot \mathbf{J}(\mathbf{r}', t) dt}{4\pi R} \right) d\mathbf{r}', \frac{\partial^2 \tilde{\mathbf{J}}}{\partial t^2} \right\rangle_{\sigma} \\ & = \left\langle \hat{\mathbf{n}} \times (\mathbf{E}^i \times \hat{\mathbf{n}}), \frac{\partial^2 \tilde{\mathbf{J}}}{\partial t^2} \right\rangle_{\sigma} \end{aligned} \quad (3.18)$$

where the equivalence between the Sobolev spaces  $\mathcal{H}_{\rho, \mathbf{J}}^s$  and  $\mathcal{H}^s$  has been used. Notice that for spatial discretization, the gradient of the charge will be moved towards the test function, such that the divergence of both the test and basis function will be used. Since this section focuses on the functional analysis, this will not be performed.

### Petrov-Galerkin variant

Both the test and solution space of the variational formulation are given by the Sobolev space  $\mathcal{H}^{\frac{1}{2}}$ . The variational formulation is therefore written in a so-called Galerkin form. However, the EFIE operator is actually tested with the second derivative, that is  $\langle \mathcal{E}, \frac{\partial^2}{\partial t^2} \tilde{\mathbf{J}} \rangle$ . Because  $\tilde{\mathbf{J}} \in \mathcal{H}^{\frac{1}{2}}$  yields  $\frac{\partial^2 \tilde{\mathbf{J}}}{\partial t^2} \in \mathcal{H}^{-\frac{3}{2}}$ , the variational formulation is equivalent to:

$$\begin{aligned} & \text{search for } \mathbf{J} \in \mathcal{H}^{\frac{1}{2}} \text{ such that } \forall \mathbf{v} \in \mathcal{H}^{-\frac{3}{2}} \\ & \left\langle \iint_{\Gamma} \left( \mu \frac{\dot{\mathbf{J}}(\mathbf{r}', \tau)}{4\pi R} - \frac{1}{\epsilon} \nabla \cdot \frac{\int_{-\infty}^{\tau} \nabla \cdot \mathbf{J}(\mathbf{r}', \bar{t}) d\bar{t}}{4\pi R} \right) d\mathbf{r}', \mathbf{v} \right\rangle_{\sigma} \\ & = \langle \hat{\mathbf{n}} \times (\mathbf{E}^i \times \hat{\mathbf{n}}), \mathbf{v} \rangle_{\sigma}. \end{aligned} \quad (3.19)$$

Because different Sobolev spaces are used for the test and solution space, this is called a Petrov-Galerkin form.

### Integration by parts

So far, the original EFIE operator has been considered, whereas the aim is to use the differentiated EFIE operator. Because the difference between the two versions is only a time derivative, applying integration by parts to the variational formulation is a standard technique to achieve an equivalence. However, integration by parts is complicated by the weighted inner product (3.11) that is being used. More precisely, for arbitrary functions  $\mathbf{p}(\mathbf{r}, t)$  and  $\mathbf{q}(\mathbf{r}, t)$  in  $\mathcal{H}^s$ , integration by parts results in

$$\begin{aligned} \left\langle \frac{\partial \mathbf{p}}{\partial t}, \mathbf{q} \right\rangle_{\sigma} &= \int_{-\infty}^{+\infty} e^{-2\sigma t} \iint_{\Gamma} \iint_{\Gamma} \frac{\partial \mathbf{p}}{\partial t} \cdot \mathbf{q} dx dy dt \\ &= \iint_{\Gamma} \iint_{\Gamma} \int_{-\infty}^{+\infty} e^{-2\sigma t} \frac{\partial \mathbf{p}}{\partial t} \cdot \mathbf{q} dt dx dy \\ &= \iint_{\Gamma} \iint_{\Gamma} \left( [e^{-2\sigma t} \mathbf{q} \cdot \mathbf{p}]_{t=-\infty}^{+\infty} - \int_{-\infty}^{+\infty} \mathbf{p} \cdot \frac{\partial}{\partial t} (e^{-2\sigma t} \mathbf{q}) dt \right) dx dy \\ &= \iint_{\Gamma} \iint_{\Gamma} \left( - \int_{-\infty}^{+\infty} (-2\sigma) e^{-2\sigma t} \mathbf{p} \cdot \mathbf{q} dt - \int_{-\infty}^{+\infty} e^{-2\sigma t} \mathbf{p} \cdot \frac{\partial \mathbf{q}}{\partial t} dt \right) dx dy \\ &= \int_{-\infty}^{+\infty} e^{-2\sigma t} \iint_{\Gamma} \iint_{\Gamma} \left( 2\sigma \mathbf{p} \cdot \mathbf{q} - \mathbf{p} \cdot \frac{\partial \mathbf{q}}{\partial t} \right) dx dy dt \\ &= \left\langle \mathbf{p}, 2\sigma \mathbf{q} - \frac{\partial \mathbf{q}}{\partial t} \right\rangle_{\sigma} \end{aligned} \quad (3.20)$$

where the boundary term is zero for the Sobolev space  $\mathcal{H}^s$ . That is, the functions are zero for  $t < 0$  and decay exponentially in time. For test functions  $\mathbf{w}(\mathbf{r}, t) \in \mathcal{H}^s$ , where the value of  $s$  will be specified later, the variational



formulation of the differentiated EFIE can be abbreviated as

$$\left\langle \dot{\mathcal{E}}(\mathbf{J}), \mathbf{w} \right\rangle_{\sigma} = \left\langle \dot{\mathbf{E}}^i, \mathbf{w} \right\rangle_{\sigma}. \quad (3.21)$$

With integration by parts (3.20), this is equivalent with

$$\left\langle \mathcal{E}(\mathbf{J}), 2\sigma\mathbf{w} - \frac{\partial\mathbf{w}}{\partial t} \right\rangle_{\sigma} = \left\langle \mathbf{E}^i, 2\sigma\mathbf{w} - \frac{\partial\mathbf{w}}{\partial t} \right\rangle_{\sigma}. \quad (3.22)$$

This is the variational formulation of the original EFIE with the test functions given by

$$\mathbf{v} = 2\sigma\mathbf{w} - \frac{\partial\mathbf{w}}{\partial t}. \quad (3.23)$$

### Index of the Sobolev space

In order to use integration by parts to derive a variational formulation (3.21) of the differentiated EFIE that is equivalent to the variational formulation (3.19) of the original EFIE, one has to proof that  $\mathbf{w} \in \mathcal{H}^s$  for  $\mathbf{v} \in \mathcal{H}^{-\frac{3}{2}}$  and the relation (3.23). Remember that most of the properties of the Sobolev spaces (3.8) are defined in the Fourier-Laplace domain, given by  $\widehat{f}(\omega) = \int_{-\infty}^{\infty} e^{i\omega t} f(t) dt$  for  $\omega = \eta + i\sigma$  and  $\sigma > 0$ . In the Fourier-Laplace domain, the relation (3.23) between the test functions reads

$$\widehat{\mathbf{v}} = (2\sigma + i\omega)\widehat{\mathbf{w}} = i\bar{\omega}\widehat{\mathbf{w}} \quad (3.24)$$

where  $\bar{\omega}$  denotes the complex conjugate of  $\omega$ . Because  $\mathbf{f} \in \mathcal{H}^s$  if its norm  $\|\mathbf{f}\|_{\sigma, s, -\frac{1}{2}\text{div}}$  is bounded, let us consider the norm of the test functions, i.e.,

$$\begin{aligned} \|\mathbf{v}(\mathbf{r}, t)\|_{\sigma, s, -\frac{1}{2}\text{div}}^2 &= \int_{-\infty+i\sigma}^{+\infty+i\sigma} |\omega|^{2s} \|\widehat{\mathbf{v}}(\mathbf{r}, \omega)\|_{H^{-\frac{1}{2}}(\text{div}, \Gamma)}^2 d\omega \\ &= \int_{-\infty+i\sigma}^{+\infty+i\sigma} |\omega|^{2s} |i\bar{\omega}|^2 \|\widehat{\mathbf{w}}(\mathbf{r}, \omega)\|_{H^{-\frac{1}{2}}(\text{div}, \Gamma)}^2 d\omega \\ &= \int_{-\infty+i\sigma}^{+\infty+i\sigma} |\omega|^{2(s+1)} \|\widehat{\mathbf{w}}(\mathbf{r}, \omega)\|_{H^{-\frac{1}{2}}(\text{div}, \Gamma)}^2 d\omega \\ &= \|\mathbf{w}(\mathbf{r}, t)\|_{\sigma, s+1, -\frac{1}{2}\text{div}}^2. \end{aligned} \quad (3.25)$$

Hence,  $\mathbf{v} \in \mathcal{H}^{-\frac{3}{2}} \iff \mathbf{w} \in \mathcal{H}^{-\frac{1}{2}}$ . Finally, one can rewrite the variational formulation of the original EFIE into the variational formulation for the differentiated EFIE:

$$\text{search for } \mathbf{J} \in \mathcal{H}^{\frac{1}{2}} \text{ such that } \forall \mathbf{w} \in \mathcal{H}^{-\frac{1}{2}} \\ \left\langle \iint_{\Gamma} \left( \mu \frac{\ddot{\mathbf{J}}(\mathbf{r}', \tau)}{4\pi R} - \frac{1}{\epsilon} \nabla \cdot \mathbf{J}(\mathbf{r}, \tau) \right) d\mathbf{r}', \mathbf{w} \right\rangle_{\sigma} = \left\langle \hat{\mathbf{n}} \times (\dot{\mathbf{E}}^i \times \hat{\mathbf{n}}), \mathbf{w} \right\rangle_{\sigma}.$$

Because of the equivalence between the variational formulations, the solution is also unique and bounded.

## 3.8 Space-time Petrov-Galerkin schemes

With the stability theorem of Terrasse, the variational formulation of the original EFIE has a unique and bounded solution  $\mathbf{J}(\mathbf{r}, t) \in \mathcal{H}^{\frac{1}{2}}$ . This stability theorem has been extended to the differentiated EFIE, for which the testing space reads  $\mathcal{H}^{-\frac{1}{2}}$  instead of  $\mathcal{H}^{-\frac{3}{2}}$  for the original EFIE. In this section, the EFIE will be discretized with the space-time Petrov-Galerkin scheme. Test and basis functions will be chosen as element of these Sobolev spaces. First, a few examples of functions within these Sobolev spaces will be given in Sec. 3.8.1.

The Dirac delta distribution is not an element of the testing space for the differentiated EFIE, which prohibits the use of the MoT scheme. Nonetheless, certain MoT schemes will be shown to be discretely equivalent to Petrov-Galerkin schemes that fit within the functional framework. This results in temporal basis functions for which the stability theorem can be used, as explained in Sec. 3.8.2.

### 3.8.1 Example functions of the Sobolev spaces

The Sobolev space  $\mathcal{H}^s$  is defined in Eq. (3.8) and is given for space-time vector functions. In space, both test and basis functions have to be element of  $H^{-\frac{1}{2}}(\text{div}, \Gamma)$ , the space of divergence conforming functions on a surface. The customary choice RWG functions (2.23) fit within this functional framework [18]. In time, the main requirements are causality, Fourier-Laplace transformability, and regularity, as explained in Sec. 3.6.1. For the discretization in time, only the Dirac delta distribution and the piecewise polynomials (2.29) with compact support will be used. Then, the characterization of the Sobolev spaces reduces to the regularity of the functions. Hence, the parameter  $s$  is the defining parameter of the Sobolev space.

The regularity of the functions is defined in the Fourier-Laplace domain, but for integers  $s$  this reduces to  $s$ -times differentiable functions. For instance, continuous functions are element of  $\mathcal{H}^1$ , which is a subspace of  $\mathcal{H}^{\frac{1}{2}}$ . When the function is not continuously differentiable, it is not an element of  $\mathcal{H}^{\frac{3}{2}}$ . In fact, when restricted to Sobolev spaces  $\mathcal{H}^{\frac{s}{2}}$  with  $s$  an odd integer, the continuity requirement is both necessary and sufficient. See Fig. 3.8 for some example functions of several Sobolev spaces  $\mathcal{H}^s$ .

The MoT scheme uses collocation as discretization in time. A collocation method can be written as a Petrov-Galerkin scheme with the Dirac delta  $\delta$  as test function. Because  $\delta \notin \mathcal{H}^{-\frac{1}{2}}$ , the stability theorem for the differentiated EFIE can not be used for collocation schemes. In other words, the



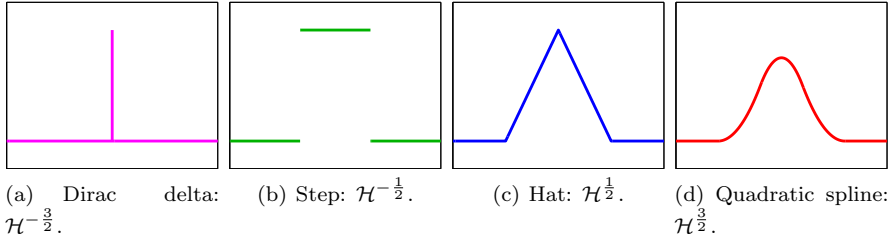


Figure 3.8: Example functions of several Sobolev spaces  $\mathcal{H}^s$ .

MoT scheme can not be proven to be stable with the current functional framework. Nevertheless, in the next section, a derivation will be given that can be used to prove stability for certain classes of MoT schemes.

### 3.8.2 Discretely equivalent Petrov-Galerkin schemes

Although the stability theorem of the differentiated EFIE can not be applied directly to the MoT scheme, the aim of this section is to design MoT schemes that are equivalent to Petrov-Galerkin schemes that fit within the functional framework. To prove an equivalence of two numerical schemes, let us consider their discretization matrix. In the case of a marching procedure (2.22) this is characterized by the discrete interaction matrices  $Z_j$  for  $j = 0, 1, 2, \dots, \ell$ . Now, let us consider a set of interaction matrices  $Z_j^{\text{MoT}}$  for the MoT scheme and  $Z_j^{\text{PG}}$  for a Petrov-Galerkin scheme. If one can derive that both sets of matrices are equal, i.e.,

$$Z_j^{\text{MoT}} = Z_j^{\text{PG}} \text{ for all } j = 0, 1, 2, \dots, \ell, \quad (3.26)$$

then the schemes are *discretely equivalent*. Hence, both schemes have the same computational properties, in particular stability.

In next section, a full derivation of such a discrete equivalence will be given. Let us already state the main conclusions, which are schematically depicted in Fig. 3.9. The lowest order piecewise polynomials that fit within the functional framework of the differentiated EFIE are the step and hat function as test and basis function, resp. This Petrov-Galerkin scheme is discretely equivalent with the MoT scheme employing quadratic spline basis functions. Hence, when using quadratic spline basis functions, the MoT scheme is as stable as the Petrov-Galerkin scheme for which the stability theorem holds. On the other hand, the broadly used quadratic Lagrange basis functions are equivalent with a Petrov-Galerkin scheme that does not fit within the functional framework. Hence, the present functional analysis of the differentiated EFIE can not be used to proof stability of the quadratic Lagrange basis function.

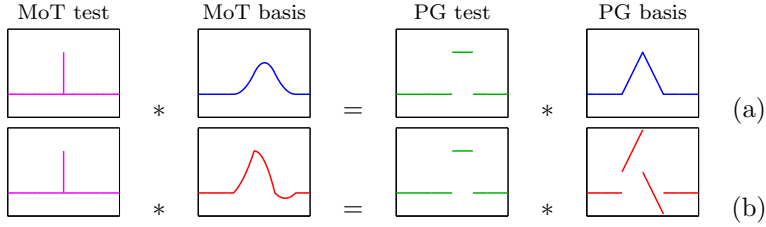


Figure 3.9: Equivalence between the MoT and Petrov-Galerkin scheme for (a) quadratic spline basis functions (4.25) and (b) quadratic Lagrange basis functions (4.22).

The following analyses of discretely equivalent schemes can be used for piecewise polynomial basis functions with an arbitrary degree. Nonetheless, this section will restrict to quadratic basis functions, because these result in efficient MoT schemes. For higher order temporal basis functions, the same analysis can readily be used but will become more elaborate. For example, the MoT scheme with cubic spline basis function (4.27) is discretely equivalent with a Galerkin scheme with the hat function for both test and basis function.

### Derivation of the discrete equivalence

In next sections, the discrete equivalence between the MoT schemes and Petrov-Galerkin schemes that are depicted in Fig. 3.9 will be proven. Let us first specify the discrete equivalence more precisely. The elements of the discrete interaction matrices depend on both space and time, but the time dependency will be isolated for convenience. Remember that RWG functions will always be used in space and that the discrete EFIE operator is linear. Hence, the full space-time discretization matrix of two schemes is identical when all time-dependent terms are equivalent. Because separation of variables is used for the test and basis functions, the only time-dependent terms in the discrete EFIE are the electric surface current density  $\mathbf{J}(\mathbf{r}, t)$  and the test and basis functions in time. Let us consider a MoT scheme with temporal basis functions denoted by  $T_j$  and a Petrov-Galerkin scheme with test and basis functions in time denoted by  $v_k$  and  $u_j$ , resp. Consequently, when

$$\begin{aligned}
 & \sum_{j=1}^{N_t} \left\langle J_{n,j} \frac{d^\alpha}{dt^\alpha} T_j(\tau), \delta(t - t_k) \right\rangle \\
 &= \sum_{j=1}^{N_t} \left\langle J_{n,j} \frac{d^\alpha}{dt^\alpha} u_j(\tau), v_k(t) \right\rangle \quad \forall k = 1, 2, \dots, N_t \quad (3.27)
 \end{aligned}$$



where  $\alpha \in \{-1, 0, 1, 2\}$ , then the two schemes are discretely equivalent. Notice that for the differentiated EFIE, this suffices for  $\alpha$  equal to 0 and 2, and  $-1$  and 1 for the original EFIE. The inner product is given by  $\langle \cdot, \cdot \rangle = \int_{-\infty}^{\infty} \cdot dt$ . Notice that whereas  $\sigma > 0$  in the stability proof,  $\sigma = 0$  will be used for discretization, as justified in Sec. 3.9.2.

### 3.8.3 Equivalence for the lowest order stable P-G scheme

Let us consider the lowest-order functions that fit within the functional framework of the differentiated EFIE, which is given by  $\mathcal{H}^{-\frac{1}{2}}$  and  $\mathcal{H}^{\frac{1}{2}}$  as test and solution space, resp. As test function, let us use the *step function*

$$v_k(t) = \begin{cases} \frac{1}{\Delta t}, & t_{k-1} < t \leq t_k, \\ 0, & \text{else} \end{cases} \quad (3.28)$$

and as basis function the *hat function*

$$u_j(t) = \begin{cases} \frac{t-t_{j-1}}{\Delta t}, & t_{j-1} < t \leq t_j, \\ \frac{t_{j+1}-t}{\Delta t}, & t_j < t \leq t_{j+1}, \\ 0, & \text{else} \end{cases} \quad (3.29)$$

which are depicted in Fig. 3.8. In this section, it will be proven that the corresponding Petrov-Galerkin scheme is discretely equivalent with the MoT scheme employing quadratic spline basis functions.

Because all test and basis functions are translated versions of the step and hat function, it suffices to consider an arbitrary retarded time level  $\tau_k$  that satisfies

$$t_{l-1} < \tau_k \leq t_l$$

for an  $l \in \{1, 2, \dots, N_t\}$ . The aim of the following analysis is to derive temporal basis functions  $T_j(t)$  for which the MoT scheme is equivalent to this Petrov-Galerkin scheme. To this end, all time dependent terms in the discretization matrix will be evaluated separately.

**Petrov-Galerkin terms** First, let us consider the term in Eq. (3.27) with  $\alpha = 0$ , that is,

$$\begin{aligned} \sum_{j=1}^{N_t} \langle J_{n,j} u_j(\tau), v_k(t) \rangle &= \sum_{j=1}^{N_t} J_{n,j} \int_{-\infty}^{\infty} u_j(\tau) v_k(t) dt \\ &= \frac{1}{\Delta t} \sum_{j=1}^{N_t} J_{n,j} \int_{t_{k-1}}^{t_k} u_j(\tau) dt \\ &= \frac{1}{\Delta t} \sum_{j=1}^{N_t} J_{n,j} \int_{\tau_{k-1}}^{\tau_k} u_j(\tau) d\tau \end{aligned}$$

$$\begin{aligned}
&= \frac{1}{\Delta t} \sum_{j=l-2}^l J_{n,j} \int_{\tau_{k-1}}^{\tau_k} u_j(\tau) d\tau \\
&= \frac{1}{\Delta t} J_{n,l} \int_{t_{l-1}}^{\tau_k} \frac{\tau - t_{l-1}}{\Delta t} d\tau + \frac{1}{\Delta t} J_{n,l-1} \left( \int_{\tau_{k-1}}^{t_{l-1}} \frac{\tau - t_{l-2}}{\Delta t} d\tau + \int_{t_{l-1}}^{\tau_k} \frac{t_l - \tau}{\Delta t} d\tau \right) \\
&\quad + \frac{1}{\Delta t} J_{n,l-2} \int_{\tau_{k-1}}^{t_{l-1}} \frac{t_{l-1} - \tau}{\Delta t} d\tau \\
&= J_{n,l} \frac{(\tau_k - t_{l-1})^2}{2\Delta t^2} \\
&\quad + J_{n,l-1} \left( 1 - \frac{(\tau_k - t_{l-1})^2}{2\Delta t^2} - \frac{(t_l - \tau_k)^2}{2\Delta t^2} \right) \\
&\quad + J_{n,l-2} \frac{(t_l - \tau_k)^2}{2\Delta t^2}. \tag{3.30}
\end{aligned}$$

The term in Eq. (3.27) that contains the integral in time reads

$$\begin{aligned}
&\sum_{j=1}^{N_t} \left\langle J_{n,j} \int_{-\infty}^{\tau} u_j(s) ds, v_k(t) \right\rangle \\
&= \sum_{j=1}^{N_t} J_{n,j} \int_{t_{k-1}}^{t_k} \frac{1}{\Delta t} \int_{-\infty}^{\tau} u_j(s) ds dt \\
&= \frac{1}{\Delta t} \sum_{j=1}^{N_t} J_{n,j} \int_{\tau_{k-1}}^{\tau_k} \int_{-\infty}^{\tau} u_j(s) ds d\tau \\
&= \frac{1}{\Delta t} J_{n,l} \int_{t_{l-1}}^{\tau_k} \int_{t_{l-1}}^{\tau} \frac{s - t_{l-1}}{\Delta t} ds d\tau \\
&\quad + \frac{1}{\Delta t} J_{n,l-1} \left( \int_{\tau_{k-1}}^{t_{l-1}} \int_{t_{l-2}}^{\tau} \frac{s - t_{l-2}}{\Delta t} ds d\tau \right. \\
&\quad \quad \left. + \int_{t_{l-1}}^{\tau_k} \left( \int_{t_{l-1}}^{\tau} \frac{t_l - s}{\Delta t} ds + \int_{t_{l-2}}^{t_{l-1}} \frac{s - t_{l-2}}{\Delta t} ds \right) d\tau \right) \\
&\quad + \frac{1}{\Delta t} J_{n,l-2} \left( \int_{\tau_{k-1}}^{t_{l-1}} \left( \int_{t_{l-2}}^{\tau} \frac{t_{l-1} - s}{\Delta t} ds + \int_{t_{l-3}}^{t_{l-2}} \frac{s - t_{l-3}}{\Delta t} ds \right) d\tau \right. \\
&\quad \quad \left. + \int_{t_{l-1}}^{\tau_k} \left( \int_{t_{l-2}}^{t_{l-1}} \frac{t_{l-1} - s}{\Delta t} ds + \int_{t_{l-3}}^{t_{l-2}} \frac{s - t_{l-3}}{\Delta t} ds \right) d\tau \right) \\
&\quad + \frac{1}{\Delta t} \sum_{j=1}^{l-3} H_j \int_{\tau_{k-1}}^{\tau_k} \left( \int_{t_j}^{t_{j+1}} \frac{t_{j+1} - s}{\Delta t} ds + \int_{t_{j-1}}^{t_j} \frac{s - t_{j-1}}{\Delta t} ds \right) d\tau
\end{aligned}$$

~

$$\begin{aligned}
&= \Delta t J_{n,l} \frac{(\tau_k - t_{l-1})^3}{6\Delta t^3} \\
&\quad + \Delta t J_{n,l-1} \left( -\frac{(\tau_k - t_{l-1})^3}{6\Delta t^3} + \frac{\tau_k - t_{l-1}}{\Delta t} + \frac{(t_l - \tau_k)^3}{6\Delta t^3} \right) \\
&\quad + \Delta t J_{n,l-2} \left( 1 - \frac{(t_l - \tau_k)^3}{6\Delta t^3} \right) \\
&\quad + \Delta t \sum_{j=1}^{l-3} H_j.
\end{aligned} \tag{3.31}$$

The term in Eq. (3.27) that contains the derivative in time reads

$$\begin{aligned}
&\sum_{j=1}^{N_t} \left\langle J_{n,j} \frac{d}{dt} u_j(\tau), v_k(t) \right\rangle \\
&= \sum_{j=1}^{N_t} J_{n,j} \int_{t_{k-1}}^{\tau_k} \frac{1}{\Delta t} \frac{d}{dt} u_j(\tau) d\tau \\
&= \frac{1}{\Delta t} \sum_{j=1}^{N_t} J_{n,j} \int_{\tau_{k-1}}^{\tau_k} \frac{d}{dt} u_j(\tau) d\tau \\
&= \frac{1}{\Delta t} J_{n,l} \int_{t_{l-1}}^{\tau_k} \frac{1}{\Delta t} d\tau + \frac{1}{\Delta t} J_{n,l-1} \left( \int_{\tau_{k-1}}^{t_{l-1}} \frac{1}{\Delta t} d\tau + \int_{t_{l-1}}^{\tau_k} \frac{-1}{\Delta t} d\tau \right) \\
&\quad + \frac{1}{\Delta t} H_{l-2} \int_{\tau_{k-1}}^{t_{l-1}} \frac{-1}{\Delta t} d\tau \\
&= \frac{1}{\Delta t} J_{n,l} \frac{\tau_k - t_{l-1}}{\Delta t} + \frac{1}{\Delta t} J_{n,l-1} \left( \frac{t_l - \tau_k}{\Delta t} - \frac{\tau_k - t_{l-1}}{\Delta t} \right) \\
&\quad - \frac{1}{\Delta t} J_{n,l-2} \frac{t_l - \tau_k}{\Delta t}.
\end{aligned} \tag{3.32}$$

For the term in Eq. (3.27) containing the second derivative we need the second derivative of the hat function, which is only continuous differentiable once. With the Dirac delta, the second time derivative can formally be written as

$$\frac{d^2}{dt^2} u_j(t) = \frac{1}{\Delta t} \delta(t - t_{j-1}) - \frac{2}{\Delta t} \delta(t - t_j) + \frac{1}{\Delta t} \delta(t - t_{j+1}).$$

The use of the Dirac delta in the derivation is mathematically not rigorous. Instead, one should use an approximation scheme similar to the one in [38]. With this procedure, the piecewise continuous first derivative of the hat function is approximated with a globally continuous functions. The resulting expression of the interaction matrices will be the same as with the following,

less rigorous but easier, derivation. We have

$$\begin{aligned}
& \sum_{j=1}^{N_t} \left\langle J_{n,j} \frac{d^2}{dt^2} u_j(\tau), v_k(t) \right\rangle \\
&= \frac{1}{\Delta t} \sum_{j=1}^{N_t} J_{n,j} \int_{\tau_{k-1}}^{\tau_k} \frac{d^2}{dt^2} u_j(\tau) d\tau \\
&= \frac{1}{\Delta t} \sum_{j=1}^{N_t} J_{n,j} \int_{\tau_{k-1}}^{\tau_k} \left( \frac{1}{\Delta t} \delta(\tau - t_{j-1}) - \frac{2}{\Delta t} \delta(\tau - t_j) + \frac{1}{\Delta t} \delta(\tau - t_{j+1}) \right) d\tau \\
&= \frac{1}{\Delta t^2} (J_{n,l} - 2J_{n,l-1} + J_{n,l-2}). \tag{3.33}
\end{aligned}$$

**MoT terms** The MoT scheme is given by collocation in time, that is, test functions  $u_k(t) = \delta(t - t_k)$  are used. This is combined with temporal basis functions  $T_j(t) = T(t - j\Delta t)$ . Then, the terms that depend on time read

$$\sum_{j=1}^{N_t} \left\langle J_{n,j} \frac{d^\alpha}{dt^\alpha} T_j(\tau), \delta(t - t_k) \right\rangle = \sum_{j=1}^{N_t} J_{n,j} \frac{d^\alpha}{dt^\alpha} T_j(\tau_k). \tag{3.34}$$

for  $\alpha = -1, 0, 1, 2$ . For temporal basis functions (2.29) defined by piecewise quadratic polynomials, we have

$$\begin{aligned}
& \sum_{j=1}^{N_t} \left\langle J_{n,j} \frac{d^\alpha}{dt^\alpha} T_j(\tau), \delta(t - t_k) \right\rangle \\
&= J_{n,l} \frac{d^\alpha}{dt^\alpha} F_0(\tau_k - t_l) + J_{n,l-1} \frac{d^\alpha}{dt^\alpha} F_1(\tau_k - t_{l-1}) + J_{n,l-2} \frac{d^\alpha}{dt^\alpha} F_2(\tau_k - t_{l-2}) \tag{3.35}
\end{aligned}$$

for  $\alpha = 0, 1, 2$  and with an extra tail variable for the integral term.

**Discretely equivalent temporal basis function** At this moment, we have derived expressions for the time dependent terms in the discretization matrices for both the Petrov-Galerkin scheme and the MoT scheme. Substitution of these terms into Eq. (3.27) will result in an expression for the temporal basis function in the MoT scheme, such that this scheme is discretely equivalent with the Petrov-Galerkin scheme with step test and hat basis functions.



For  $\alpha = 0$ , we have

$$\begin{aligned}
& J_{n,l}F_0(\tau_k - t_l) + J_{n,l-1}F_1(\tau_k - t_{l-1}) + J_{n,l-2}F_2(\tau_k - t_{l-2}) \\
&= J_{n,l} \frac{(\tau_k - t_{l-1})^2}{2\Delta t^2} \\
&+ J_{n,l-1} \left( 1 - \frac{(\tau_k - t_{l-1})^2}{2\Delta t^2} - \frac{(t_l - \tau_k)^2}{2\Delta t^2} \right) \\
&+ J_{n,l-2} \frac{(t_l - \tau_k)^2}{2\Delta t^2} \tag{3.36}
\end{aligned}$$

where Eq. (3.35) and (3.30) have been used. This equation is solved for

$$F_0(\tau_k - t_l) = \frac{1}{2} \left( \frac{\tau_k - t_l}{\Delta t} \right)^2 + \frac{\tau_k - t_l}{\Delta t} + \frac{1}{2}, \tag{3.37a}$$

$$F_1(\tau_k - t_{l-1}) = - \left( \frac{\tau_k - t_{l-1}}{\Delta t} \right)^2 + \frac{\tau_k - t_{l-1}}{\Delta t} + \frac{1}{2}, \tag{3.37b}$$

$$F_2(\tau_k - t_{l-2}) = \frac{1}{2} \left( \frac{\tau_k - t_{l-2}}{\Delta t} \right)^2 - 2 \frac{\tau_k - t_{l-2}}{\Delta t} + 2 \tag{3.37c}$$

where  $t_l = l\Delta t$  has been used. When the terms for the derivatives and the integral are equated, the derivatives and the integral of the functions (3.37a) are obtained. Thus, equating all terms of Petrov-Galerkin scheme and MoT scheme results in the piecewise polynomials (3.37a). Notice that this temporal basis function is the quadratic spline basis function (4.25). Concluding, the MoT scheme with quadratic spline basis functions is discretely equivalent with the Petrov-Galerkin scheme with step test and hat basis functions, for both the original and differentiated EFIE.

### 3.8.4 Equivalence for the quadratic Lagrange MoT scheme

For a given Petrov-Galerkin scheme, a discretely equivalent MoT scheme has been derived in previous section. Now, the reverse will be performed. In particular, a discretely equivalent Petrov-Galerkin scheme for a MoT scheme with the broadly used quadratic Lagrange basis functions (4.22) will be derived. However, two unknowns are present in the Petrov-Galerkin scheme, namely the test and basis function. To obtain a unique Petrov-Galerkin scheme, either the test or basis function has to be chosen in advance. Here, step test functions will be chosen, because these are the lowest-order test functions that fit within the functional framework of the stability theorem. For the term in

Eq. (3.27) with  $\alpha = 0$ , we have

$$\begin{aligned}
& \sum_{j=1}^{N_t} \langle J_{n,j} T_j(\tau), \delta(t - t_k) \rangle \\
&= \sum_{j=l-2}^l J_{n,j} T(\tau_k - t_j) \\
&= J_{n,l} \left( \frac{1}{2} \left( \frac{\tau_k - t_l}{\Delta t} \right)^2 + \frac{3}{2} \frac{\tau_k - t_l}{\Delta t} + 1 \right) \\
&\quad + J_{n,l-1} \left( - \left( \frac{\tau_k - t_{l-1}}{\Delta t} \right)^2 + 1 \right) \\
&\quad + J_{n,l-2} \left( \frac{1}{2} \left( \frac{\tau_k - t_{l-2}}{\Delta t} \right)^2 - \frac{3}{2} \frac{\tau_k - t_{l-2}}{\Delta t} + 1 \right) \\
&= J_{n,l} \left( \frac{1}{2} \left( \frac{\tau_k - t_{l-1}}{\Delta t} \right)^2 + \frac{1}{2} \frac{\tau_k - t_{l-1}}{\Delta t} \right) \\
&\quad + \frac{1}{2} J_{n,l-1} \left( 1 - \left( \frac{\tau_{k-1} - t_{l-2}}{\Delta t} \right)^2 - \frac{\tau_{k-1} - t_{l-1}}{\Delta t} + 1 - \left( \frac{t_l - \tau_k}{\Delta t} \right)^2 - \frac{\tau_k - t_{l-1}}{\Delta t} \right) \\
&\quad + J_{n,l-1} \left( - \frac{1}{2} \left( \frac{\tau_{k-1} - t_{l-2}}{\Delta t} \right)^2 - \frac{1}{2} \left( \frac{t_l - \tau_k}{\Delta t} \right)^2 - \frac{\tau_k - t_{l-1}}{\Delta t} + 1 \right) \\
&\quad + J_{n,l-2} \left( \frac{1}{2} \left( \frac{t_{l-1} - \tau_{k-1}}{\Delta t} \right)^2 - \frac{1}{2} \frac{t_{l-1} - \tau_{k-1}}{\Delta t} \right) \\
&= \frac{1}{\Delta t} J_{n,l} \int_{t_{l-1}}^{\tau_k} \left( \frac{\tau - t_{l-1}}{\Delta t} + \frac{1}{2} \right) d\tau \\
&\quad + \frac{1}{\Delta t} J_{n,l-1} \left( \int_{\tau_{k-1}}^{t_{l-1}} \left( \frac{\tau - t_{l-2}}{\Delta t} + \frac{1}{2} \right) d\tau + \int_{t_{l-1}}^{\tau_k} \left( \frac{t_l - \tau}{\Delta t} - \frac{1}{2} \right) d\tau \right) \\
&\quad + \frac{1}{\Delta t} J_{n,l-2} \int_{\tau_{k-1}}^{t_{l-1}} \left( \frac{t_{l-1} - \tau}{\Delta t} - \frac{1}{2} \right) d\tau \\
&= \frac{1}{\Delta t} \sum_{j=l-2}^l J_{n,j} \int_{\tau_{k-1}}^{\tau_k} u_j(\tau) d\tau \\
&= \frac{1}{\Delta t} \sum_{j=1}^{N_t} J_{n,j} \int_{t_{k-1}}^{t_k} u_j(\tau) dt \\
&= \sum_{j=1}^{N_t} \langle J_{n,j} u_j(\tau), v_k(t) \rangle
\end{aligned} \tag{3.38}$$

~~~~~

where  $v_k$  denotes the step function (3.28) and  $u_j$  is given by

$$u_j(t) = \begin{cases} \frac{t-t_{j-1}}{\Delta t} + \frac{1}{2}, & t_{j-1} < t \leq t_j, \\ \frac{t_{j+1}-t}{\Delta t} - \frac{1}{2}, & t_j < t \leq t_{j+1}, \\ 0, & \text{else} \end{cases} \quad (3.39)$$

called a *shifted hat function*. The terms in Eq. (3.27) with  $\alpha \in \{-1, 1, 2\}$  will result in the same basis function and their derivation will be omitted for brevity. The conclusion of this derivation is that the MoT scheme with the quadratic Lagrange basis function is discretely equivalent to the Petrov-Galerkin scheme with step test function and shifted hat basis function. The shifted hat function is only piecewise continuous and thus an element of  $\mathcal{H}^{-\frac{1}{2}}$ . Hence, the basis function does not fit within the functional framework and the stability theorem can therefore not be used for the MoT scheme with quadratic Lagrange basis functions. Notice that although stability can not be proven with this analysis, this does not mean that the scheme is unstable.

## 3.9 Provably stable MoT schemes

In this chapter, the numerical stability of TDIE methods has been analyzed with the functional framework for the space-time Galerkin discretization of the original EFIE derived by Terrasse. The resulting stability theorem has been extended to the differentiated EFIE with functional analysis. Then, a discrete equivalence between the space-time Galerkin and MoT scheme has been derived. This concludes that the stability theorem of space-time Galerkin can be used for the MoT scheme with quadratic spline basis functions.

### 3.9.1 Computational experiments

Many computer simulations for the differentiated EFIE have been performed with the quadratic spline basis functions, for surface meshes with up to 17 000 degrees of freedom. The objects include spheres and boxes, but also more challenging geometries such as a corner reflector and a generic aircraft, see Chapter 6. All computational experiments with the MoT scheme have been found to be stable, provided the quadrature scheme is accurate enough and the time step size is chosen correctly. More specifically, quasi-exact integration with 7 quadrature points for the outer integral and analytical formulations for the inner integral has been found to be sufficiently accurate. The time step size has been chosen as an oversampling of the highest frequency mode in the incident wave field, as given in Eq. (2.25). See also the recommendations in Chapter 8.

### 3.9.2 Caveats in the stability theorem

The stability analysis of the TDIE method with a functional framework is very valuable for the design of stable MoT schemes. The resulting guideline of choosing the quadratic spline basis function has been confirmed by computer simulations. Nevertheless, this does not conclude that all computer simulations for MoT schemes with quadratic spline basis functions are guaranteed to be stable. There are still some caveats in the stability analysis. The most important subtleties are the presence of a growing stability constant, the numerical discretization in MoT schemes being based on a set of test and basis functions that span a finite-dimensional function space, and the evaluation of interaction matrices using an approximation with finite precision. Each nuance will be explained in subsequent sections.

#### Stability constant

The boundedness theorem of Terrasse contains both a constant  $C(\Gamma)$  and  $\frac{1}{\sigma}$ . Whereas the constant  $C$  is expected, the term  $\frac{1}{\sigma}$  causes some controversy. The parameter  $\sigma$  originates from the usage of the Fourier-Laplace domain in the derivation of the functional analysis. For the stability proof, this parameter can be chosen arbitrarily small but positive. In practice,  $\sigma = 0$  is used during numerical discretization. Strictly speaking, the stability theorem is not valid anymore and can thus not be used to proof stability of the TDIE method.

This is still an open problem in literature [39, 20]. No stability proof has been derived without this parameter, which makes the stability proof of Terrasse still the most attractive option. In [39], it has been argued that for finite simulation times, this parameter will not cause major problems.

#### Finite dimensional subspace

The stability theorem states that the variational formulation  $\langle \mathcal{E}(\mathbf{J}), \mathbf{v} \rangle_\sigma = \langle \mathbf{E}^i, \mathbf{v} \rangle_\sigma \forall \mathbf{v} \in \mathcal{H}^{-\frac{3}{2}}$  of the original EFIE has a unique solution  $\mathbf{J} \in \mathcal{H}^{\frac{1}{2}}$  which is bounded by the incident field in an energy norm. Similar results have been obtained for the differentiated EFIE. Petrov-Galerkin discretization uses test functions  $\mathbf{v}_i$  and basis functions  $\mathbf{u}_j$  for  $i, j = 1, 2, 3, \dots, N$  and solves the discrete variational formulation. The test and basis functions span a finite dimensional function space, denoted by  $\mathcal{H}_{\text{test}}$  and  $\mathcal{H}_{\text{basis}}$ . Naturally, the test and basis functions are chosen such that these functions are  $N$ -dimensional subsets of the Sobolev spaces, i.e.,  $\mathcal{H}_{\text{test}} \subset \mathcal{H}^{-\frac{3}{2}}$  and  $\mathcal{H}_{\text{basis}} \subset \mathcal{H}^{\frac{1}{2}}$ . Since the theorem only proves boundedness of the solution of the continuous variational formulation with infinite dimensional Sobolev spaces, one can not use this theorem to prove stability of the Petrov-Galerkin scheme, which uses only a finite dimensional subset.



The difference between the continuous and discrete variational formulation, or infinite and finite dimensional function space is subtle. Loosely speaking, since the discrete solution is searched for in a finite dimensional subspace of  $\mathcal{H}^{\frac{1}{2}}$ , the continuous solution might be element of its nonempty complement  $\mathcal{H}^{\frac{1}{2}} \setminus \mathcal{H}_{\text{basis}}$ . Moreover, since the equations are tested against a finite dimensional subspace of  $\mathcal{H}^{-\frac{3}{2}}$ , this solution does not have to be found at all. In general, Petrov-Galerkin schemes will approximate the exact solution effectively. However, providing a proof of convergence and boundedness of this discrete solution can be very difficult. The proof usually derives inf-sup conditions on the variational formulation. When the TDIE method is used to discretize the scalar wave equation applied to acoustics, stability of the discrete variational formulation has been proven [38], but details are scarce in literature. For electromagnetics, no proof has been found in literature.

### Computation of surface integrals

The EFIE is a surface integral formulation of Maxwell's equation. Discretization is based on the variational formulation, which introduces a space-time inner product. The time integrals in the variational formulation can be evaluated analytically, see Sec. 3.8. An evaluation of a four-dimensional integral in space remains. Strictly speaking, the stability theorem only holds when this integral is evaluated exactly. This is not feasible in practice and numerical quadrature is used instead. Even when analytical solutions can be applied, rounding errors will be present in computer simulations. The idea is that when these numerical errors are very small, the stability theorem can be used with a high confidence. However, large numerical errors can deviate the scheme to instability. Computational experiments confirm that the stability is very sensitive to numerical errors [84, 87, 109].

To obtain the stability expected from the analysis, one thus has to evaluate the four-dimensional integrals in space with a high accuracy. The presence of retarded time levels in the integrand complicates this evaluation. More precisely, the integrand is nonsmooth on the intersections of light cones and triangular patches. Standard quadrature procedures are not effective anymore and sophisticated algorithms have to be used to approximate the integrals. This phenomenon will be explained in detail in Chapter 5.

### 3.9.3 Extension to other model equations

The stability theorem of Terrasse covers the original EFIE. In this chapter, stability of the differentiated EFIE has been analyzed with the aid of the available functional framework. Since the stability proof explicitly uses the EFIE, the proof can not be used for other model equations such as the MFIE and CFIE. Extensions to these equations will be nontrivial. In the case of scalar wave equations applied to acoustics, stability has been analyzed for

---

second kind integral equation similar to the MFIE [39]. Their recommendation is to use first kind integral equations, such as the EFIE.

Two important extensions to the stability analysis have been derived in literature: for an impedance boundary conditions [54] and a coupling with a volumetric finite element method [78].





# Chapter 4

## Accuracy

### 4.1 Accuracy in time of the MoT scheme

The development of TDIE methods has benefited from the knowledge of its frequency-domain counterpart, the Method-of-Moments (MoM). For example, the discretization in space of the MoT schemes follows the lines of the MoM, that is, a Galerkin method with RWG functions (2.23) is used. The numerical discretization in time of the TDIE method naturally has no counterpart in the MoM. The choice of temporal basis function can therefore not be based on common practices for the MoM. Moreover, most theory on finite element methods is derived for ordinary differential equations, not for retarded potential integro-differential equations such as the EFIE (2.10). An example of this difference is the customary choice of shifted Lagrange basis functions that have been designed such that they interpolate functions in a retarded time level. Many other temporal basis functions have been used in literature on TDIE methods, as listed in Sec. 2.2.2. No clear guidelines are available on how to choose them. This chapter aims to derive a framework for the design of temporal basis functions according to user-defined criteria on interpolation accuracy and smoothness. This framework can be used to verify existing temporal basis functions and to design novel ones.

The accuracy properties of the temporal discretization in the MoT scheme will be the main topic of this chapter. A complete derivation of the global accuracy in time of TDIE methods is not feasible. Instead, a combination of analysis and experiments will be performed. An important part of finite element methods is the projection of the solution of the variational formulation onto a finite element space [15]. Error bounds on this interpolation procedure will be derived for piecewise polynomial basis functions. Evidently, the accuracy of interpolation influences the global accuracy of the MoT scheme. How-



ever, it is not necessary that the orders of interpolation and global accuracy are exactly the same. The global accuracy will be analyzed experimentally for a number of temporal basis functions.

The analysis of the interpolation accuracy will be restricted to temporal basis functions that yield an efficient MoT scheme. We define the efficiency of a numerical scheme by the trade-off between the amount of work and accuracy. Generally speaking, a temporal basis function with small support results in an inexpensive TDIE method whereas a large support results in an accurate method [47, 50]. In order to obtain the fast MoT algorithm (2.22), causal basis functions with small support will be used, as given by Eq. (2.29). This includes shifted Lagrange basis functions [60], but excludes for example the smooth but noncausal BLIFs [102] and PUMs [77] and the entire-domain Laguerre basis functions [49]. Notice that the temporal basis functions that will be used have compact support and have therefore no bandlimited frequency content [102].

First, the objectives for the design of temporal basis functions will be explained in Sec. 4.2. Then, the interpolation accuracy of piecewise polynomials basis functions in time will be derived in Sec. 4.3. For the requirement of maximum order interpolation of interpolation accuracy, the temporal basis functions allow for the incorporation of other design criteria, as performed in Sec. 4.4. Numerical experiments in Sec. 4.5 will confirm the design criteria of the temporal basis functions.

## 4.2 Framework to design temporal basis functions

The interpolation accuracy of TDIE methods depends on the choice of temporal basis function. Therefore, the analysis should be performed for each temporal basis function. However, in this chapter, the analysis will not be performed for a single temporal basis function, but for the class of piecewise polynomial functions. The resulting temporal basis functions that satisfy a prescribed order of interpolation accuracy contain several parameters. Because these parameters can be chosen freely, a framework is obtained for the design of temporal basis functions. The parameters will be chosen according to the following objectives:

- inclusion of popular choices of temporal basis function;
- smoothness of the temporal basis function;
- conditioning of the leading interaction matrix.

The presented framework can be used to design novel temporal basis functions. In order to make a good comparison with the customary basis function, it is necessary that the well-known shifted Lagrange basis functions naturally

fit within this framework, as will be confirmed in Sec. 4.4.1. In Sec. 4.4.2, smooth temporal basis functions will be designed. Smoothness can be obtained without impinging on interpolation accuracy and will improve the accuracy of the quadrature procedure in space, as confirmed experimentally. In Sec. 4.4.3, a family of temporal basis function will be derived that have a direct influence on the conditioning of the leading matrix and therefore also on the effectiveness of the linear solver in the MoT scheme.

One of the most important properties of a numerical scheme is stability. Without stability, TDIE methods are not feasible for industrial application. The functional framework in Chapter 3 suggest a certain smoothness of the test and basis functions in the space-time Galerkin scheme. This results in the preliminary conclusion that stability is expected when the quadratic spline basis function is used in the MoT scheme. This temporal basis function is included in this framework and stability will not be considered further in this chapter.

### 4.3 Derivation of the interpolation accuracy

The interpolation accuracy of piecewise polynomial basis functions will be derived in this section. This will result in families of temporal basis functions that satisfy a specific order of interpolation accuracy.

#### 4.3.1 Interpolation in finite element methods

Intrinsic to the finite element method is the projection of the solution on a function space of finite dimension. This so-called *interpolation* is one of the sources of discretization errors. Temporal basis functions determine the finite element space and thus influence the accuracy of interpolation. A thorough analysis of the interpolation procedure will result in clear conditions on temporal basis functions for interpolation errors of a given order w.r.t. the time step size.

For an arbitrary function  $u(t)$ , the interpolator  $\mathcal{I}$  defines the interpolant  $\hat{u}(t)$  by

$$\hat{u} = \mathcal{I}(u) = \sum_{j=1}^N \tilde{u}_j T_j \quad (4.1)$$

for coefficients  $\tilde{u}_j$  that will be defined in Eq. (4.4) and  $T_j(t)$  temporal basis functions (2.26). The interpolation error is given by  $\|u - \mathcal{I}u\|$  where the type of norm will be specified in Eq. (4.7). Recall that for the CFIE the first and second time derivative have to be evaluated in the retarded time as well. Therefore, the interpolation errors  $\|u' - \mathcal{I}u'\|$  and  $\|u'' - \mathcal{I}u''\|$  are also of interest. The derivative of a function is interpolated with the derivative of



the same basis functions, i.e.,

$$\mathcal{I}(u') = \sum_{j=1}^N \tilde{u}_j T_j', \quad (4.2)$$

$$\mathcal{I}(u'') = \sum_{j=1}^N \tilde{u}_j T_j'' \quad (4.3)$$

where  $\tilde{u}_j$  and  $T_j$  are the same as in Eq. (4.1).

For a correct interpolation procedure, two choices have to be made, namely the definition of the finite element space and the map onto this space. Since piecewise polynomial basis functions (2.29) are used, the finite element space is defined by the space of piecewise polynomials of degree  $d$ . The map onto the finite element space is based on the definition of the coefficients  $\tilde{u}_j$  that depend on  $u$ , i.e.,

$$\tilde{u}_j = \mathcal{N}_j(u) \quad (4.4)$$

for a functional  $\mathcal{N}_j$ , called a *nodal variable* [15]. It is important to choose a nodal variable for which the interpolation can be analyzed easily. Additionally, a natural requirement is that the well-known shifted Lagrange basis functions should fit within this choice for the nodal variables.

It is common practice to use an interpolation that is a projection. A sufficient condition is  $\mathcal{N}_i(T_j) = \delta_{ij}$  for  $i, j = 1, 2, \dots, N$  with  $\delta_{ij}$  denoting the Kronecker delta. Although this will not be required, this condition is checked *a posteriori* for the nodal variables and temporal basis functions that are used in this chapter.

### 4.3.2 Interpolation accuracy of quadratic basis functions

Let us consider temporal basis functions based on quadratic polynomials. For an arbitrary time point  $\tau$  and corresponding level  $\ell$ , satisfying  $t_{\ell-1} < \tau \leq t_\ell$ , the interpolant (4.1) reads

$$\mathcal{I}u(\tau) = \sum_{j=1}^N \tilde{u}_j T_j(\tau) = \sum_{k=0}^2 \tilde{u}_{\ell-k} F_k(k\Delta t - \sigma) \quad (4.5)$$

where  $F_k$  has been defined in Eq. (2.29). With  $\sigma$  defined as  $\sigma = t_\ell - \tau$ , the analysis can be restricted to an arbitrary  $\sigma \in [0, \Delta t)$ . Remember that derivatives have to be interpolated as well. This results in three interpolants

$$\hat{u}(\tau) = F_0(-\sigma)\tilde{u}_\ell + F_1(\Delta t - \sigma)\tilde{u}_{\ell-1} + F_2(2\Delta t - \sigma)\tilde{u}_{\ell-2}, \quad (4.6a)$$

$$\hat{u}'(\tau) = F_0'(-\sigma)\tilde{u}_\ell + F_1'(\Delta t - \sigma)\tilde{u}_{\ell-1} + F_2'(2\Delta t - \sigma)\tilde{u}_{\ell-2}, \quad (4.6b)$$

$$\hat{u}''(\tau) = F_0''(-\sigma)\tilde{u}_\ell + F_1''(\Delta t - \sigma)\tilde{u}_{\ell-1} + F_2''(2\Delta t - \sigma)\tilde{u}_{\ell-2}. \quad (4.6c)$$

The interpolation error will be given by the pointwise norm, that is,

$$\|u - \mathcal{I}u\| = |u(\tau) - \hat{u}(\tau)| \quad (4.7)$$

and similar for the derivatives. To obtain useful expressions for the interpolation accuracy, the interpolants have to be written as function of the solution  $u_\sigma = u(\tau)$  in the retarded time level. To this end, let us use

$$\mathcal{N}_j(u) = u(t_j) + \alpha \Delta t u'(t_j) \quad (4.8)$$

for an arbitrary constant  $\alpha \in \mathbb{R}$  as nodal variable (4.4). This choice allows for a straightforward analysis of the interpolation accuracy by using Taylor series, that is,

$$\begin{aligned} \tilde{u}_\ell &= u_\sigma + \sigma u'_\sigma + \frac{1}{2} \sigma^2 u''_\sigma \\ &\quad + \alpha \Delta t u'_\sigma + \alpha \Delta t \sigma u''_\sigma + \mathcal{O}(\Delta t^3), \end{aligned} \quad (4.9a)$$

$$\begin{aligned} \tilde{u}_{\ell-1} &= u_\sigma + (\sigma - \Delta t) u'_\sigma + \frac{1}{2} (\sigma - \Delta t)^2 u''_\sigma \\ &\quad + \alpha \Delta t u'_\sigma + \alpha \Delta t (\sigma - \Delta t) u''_\sigma + \mathcal{O}(\Delta t^3), \end{aligned} \quad (4.9b)$$

$$\begin{aligned} \tilde{u}_{\ell-1} &= u_\sigma + (\sigma - 2\Delta t) u'_\sigma + \frac{1}{2} (\sigma - 2\Delta t)^2 u''_\sigma \\ &\quad + \alpha \Delta t u'_\sigma + \alpha \Delta t (\sigma - 2\Delta t) u''_\sigma + \mathcal{O}(\Delta t^3) \end{aligned} \quad (4.9c)$$

because  $\mathcal{O}(\sigma) = \mathcal{O}(\Delta t)$ . Substitution of the Taylor series (4.9) into the interpolants (4.6) results in

$$\hat{u}(\tau_k) = \mathcal{A}_{11} u_\sigma + \mathcal{A}_{12} u'_\sigma + \mathcal{A}_{13} u''_\sigma + \mathcal{O}(\Delta t^3), \quad (4.10a)$$

$$\hat{u}'(\tau_k) = \mathcal{A}_{21} u_\sigma + \mathcal{A}_{22} u'_\sigma + \mathcal{A}_{23} u''_\sigma + \mathcal{O}(\Delta t^2), \quad (4.10b)$$

$$\hat{u}''(\tau_k) = \mathcal{A}_{31} u_\sigma + \mathcal{A}_{32} u'_\sigma + \mathcal{A}_{33} u''_\sigma + \mathcal{O}(\Delta t) \quad (4.10c)$$

with  $\mathcal{A}_{ij}$  given by

$$\mathcal{A}_{11} = F_{0,\sigma} + F_{1,\sigma} + F_{2,\sigma}, \quad (4.11a)$$

$$\mathcal{A}_{12} = (\sigma + \alpha \Delta t) F_{0,\sigma} + (\sigma + (\alpha - 1) \Delta t) F_{1,\sigma} + (\sigma + (\alpha - 2) \Delta t) F_{2,\sigma}, \quad (4.11b)$$

$$\begin{aligned} \mathcal{A}_{13} &= \left( \frac{1}{2} \sigma^2 + \alpha \sigma \Delta t \right) F_{0,\sigma} + \left( \frac{1}{2} \sigma^2 + (\alpha - 1) \sigma \Delta t - (\alpha - \frac{1}{2}) \Delta t^2 \right) F_{1,\sigma} \\ &\quad + \left( \frac{1}{2} \sigma^2 + (\alpha - 2) \sigma \Delta t - 2(\alpha - 1) \Delta t^2 \right) F_{2,\sigma}, \end{aligned} \quad (4.11c)$$

$$\mathcal{A}_{21} = F'_{0,\sigma} + F'_{1,\sigma} + F'_{2,\sigma}, \quad (4.11d)$$

$$\mathcal{A}_{22} = (\sigma + \alpha \Delta t) F'_{0,\sigma} + (\sigma + (\alpha - 1) \Delta t) F'_{1,\sigma} + (\sigma + (\alpha - 2) \Delta t) F'_{2,\sigma}, \quad (4.11e)$$

~~~~~

$$\begin{aligned} \mathcal{A}_{23} &= \left(\frac{1}{2}\sigma^2 + \alpha\Delta t\right)F'_{0,\sigma} + \left(\frac{1}{2}\sigma^2 + (\alpha - 1)\sigma\Delta t - \left(\alpha - \frac{1}{2}\right)\Delta t^2\right)F'_{1,\sigma} \\ &\quad + \left(\frac{1}{2}\sigma^2 + (\alpha - 2)\sigma\Delta t - 2(\alpha - 1)\Delta t^2\right)F'_{2,\sigma}, \end{aligned} \quad (4.11f)$$

$$\mathcal{A}_{31} = F''_{0,\sigma} + F''_{1,\sigma} + F''_{2,\sigma}, \quad (4.11g)$$

$$\mathcal{A}_{32} = (\sigma + \alpha\Delta t)F''_{0,\sigma} + (\sigma + (\alpha - 1)\Delta t)F''_{1,\sigma} + (\sigma + (\alpha - 2)\Delta t)F''_{2,\sigma}, \quad (4.11h)$$

$$\begin{aligned} \mathcal{A}_{33} &= \left(\frac{1}{2}\sigma^2 + \alpha\Delta t\right)F''_{0,\sigma} + \left(\frac{1}{2}\sigma^2 + (\alpha - 1)\sigma\Delta t - \left(\alpha - \frac{1}{2}\right)\Delta t^2\right)F''_{1,\sigma} \\ &\quad + \left(\frac{1}{2}\sigma^2 + (\alpha - 2)\sigma\Delta t - 2(\alpha - 1)\Delta t^2\right)F''_{2,\sigma} \end{aligned} \quad (4.11i)$$

with the abbreviations

$$F_{0,\sigma} = F_0(-\sigma), \quad (4.12a)$$

$$F_{1,\sigma} = F_1(\Delta t - \sigma), \quad (4.12b)$$

$$F_{2,\sigma} = F_2(2\Delta t - \sigma). \quad (4.12c)$$

Quadratic polynomials can interpolate arbitrary functions with third order accuracy [15], that is,

$$|u(\tau) - \hat{u}(\tau)| = \mathcal{O}(\Delta t^3). \quad (4.13)$$

This is satisfied if  $\mathcal{A}_{11} = 1$ ,  $\mathcal{A}_{12} = 0$ , and  $\mathcal{A}_{13} = 0$ , which can be rewritten into conditions on the temporal basis functions as

$$F_{0,\sigma} + F_{1,\sigma} + F_{2,\sigma} = 1, \quad (4.14a)$$

$$F_{1,\sigma} + 2F_{2,\sigma} = \frac{\sigma}{\Delta t} + \alpha, \quad (4.14b)$$

$$F_{1,\sigma} + 4F_{2,\sigma} = \frac{\sigma^2}{\Delta t^2} + 2\alpha\frac{\sigma}{\Delta t} + 2\alpha^2. \quad (4.14c)$$

The first equation is the well-known unit sum condition for interpolants. Notice that conditions (4.14) yield  $\mathcal{A}_{21} = 0$ ,  $\mathcal{A}_{22} = 1$ ,  $\mathcal{A}_{23} = 0$ ,  $\mathcal{A}_{31} = 0$ ,  $\mathcal{A}_{32} = 0$ , and  $\mathcal{A}_{33} = 1$  for all  $\sigma \in [0, \Delta t)$ . Hence,

$$|u'(\tau) - \hat{u}'(\tau)| = \mathcal{O}(\Delta t^2), \quad (4.15)$$

$$|u''(\tau) - \hat{u}''(\tau)| = \mathcal{O}(\Delta t), \quad (4.16)$$

which shows that the derivatives are interpolated with a lower order of accuracy. This is expected because the same temporal basis function are used for interpolation of all derivatives. The interpolation is then based on a lower degree of polynomial and thus obtains a lower degree of accuracy.

Since the CFIE contains second order derivatives, the interpolation accuracy will be of first order at most. To obtain this order of interpolation

accuracy, the temporal basis function has to satisfy conditions (4.14). This system of three equations can be solved uniquely for quadratic polynomials as

$$T(t) = \begin{cases} \frac{1}{2}\tilde{t}^2 + (\frac{3}{2} - \alpha)\tilde{t} + \alpha^2 - \frac{3}{2}\alpha + 1, & -1 < \tilde{t} \leq 0, \\ -\tilde{t}^2 + 2\alpha\tilde{t} - 2\alpha^2 + 1, & 0 < \tilde{t} \leq 1, \\ \frac{1}{2}\tilde{t}^2 - (\frac{3}{2} + \alpha)\tilde{t} + \alpha^2 + \frac{3}{2}\alpha + 1, & 1 < \tilde{t} \leq 2, \\ 0, & \text{else.} \end{cases} \quad (4.17)$$

For any constant  $\alpha$  this temporal basis function results in a first order accurate interpolation of the CFIE. The parameter  $\alpha$  is the degree of freedom in the framework to design temporal basis functions.

### 4.3.3 Interpolation accuracy of cubic basis functions

The derivation of the interpolation accuracy for quadratic temporal basis functions can readily be extended to higher order polynomials. The gain of using cubic basis functions is that a higher degree of interpolation accuracy can be achieved. To be precise, an interpolation procedure that satisfies

$$|u(\tau) - \hat{u}(\tau)| = \mathcal{O}(\Delta t^4), \quad (4.18a)$$

$$|u'(\tau) - \hat{u}'(\tau)| = \mathcal{O}(\Delta t^3), \quad (4.18b)$$

$$|u''(\tau) - \hat{u}''(\tau)| = \mathcal{O}(\Delta t^2) \quad (4.18c)$$

is searched for. Moreover, more flexibility in the framework to design temporal basis functions can be obtained. To this end, let us use

$$\mathcal{N}_j(u) = u(t_j) + \alpha \Delta t u'(t_j) + \beta \Delta t^2 u''(t_j) \quad (4.19)$$

as nodal variable. With a straightforward extension of the derivation in Sec. 4.3.2, it can be shown that cubic polynomial basis functions have to satisfy

$$F_{0,\sigma} + F_{1,\sigma} + F_{2,\sigma} + F_{3,\sigma} = 1, \quad (4.20a)$$

$$F_{1,\sigma} + 2F_{2,\sigma} + 3F_{3,\sigma} = \frac{\sigma}{\Delta t} + \alpha, \quad (4.20b)$$

$$F_{1,\sigma} + 4F_{2,\sigma} + 9F_{3,\sigma} = \frac{\sigma^2}{\Delta t^2} + 2\alpha \frac{\sigma}{\Delta t} + 2(\alpha^2 - \beta), \quad (4.20c)$$

$$F_{1,\sigma} + 8F_{2,\sigma} + 27F_{3,\sigma} = \frac{\sigma^3}{\Delta t^3} + \frac{\alpha}{2} \frac{\sigma^2}{\Delta t^2} + (\alpha^2 - \beta) \frac{\sigma}{\Delta t} + \alpha^3 - 2\alpha\beta. \quad (4.20d)$$

~~~~~

This system of equations can be solved uniquely as

$$T(t) = \begin{cases} \frac{1}{6}\tilde{t}^3 + (1 - \frac{1}{2}\alpha)\tilde{t}^2 + (\frac{11}{6} + \alpha^2 - 2\alpha - \beta)\tilde{t} \\ \quad + 1 - \alpha^3 + 2\alpha^2 - \frac{11}{6}\alpha + 2\alpha\beta - 2\beta, & -1 < \tilde{t} \leq 0, \\ -\frac{1}{2}\tilde{t}^3 - (1 - \frac{3}{2}\alpha)\tilde{t}^2 + (\frac{1}{2} - 3\alpha^2 + 2\alpha + 3\beta)\tilde{t} \\ \quad + 1 + 3\alpha^3 - 2\alpha^2 - \frac{1}{2}\alpha - 6\alpha\beta + 2\beta, & 0 < \tilde{t} \leq 1, \\ \frac{1}{2}\tilde{t}^3 - (1 + \frac{3}{2}\alpha)\tilde{t}^2 - (\frac{1}{2} - 3\alpha^2 - 2\alpha + 3\beta)\tilde{t} \\ \quad + 1 - 3\alpha^3 - 2\alpha^2 + \frac{1}{2}\alpha + 6\alpha\beta + 2\beta, & 1 < \tilde{t} \leq 2, \\ -\frac{1}{6}\tilde{t}^3 + (1 + \frac{1}{2}\alpha)\tilde{t}^2 - (\frac{11}{6} + \alpha^2 + 2\alpha - \beta)\tilde{t} \\ \quad + 1 + \alpha^3 + 2\alpha^2 + \frac{11}{6}\alpha - 2\alpha\beta - 2\beta, & 2 < \tilde{t} \leq 3, \\ 0, & \text{else.} \end{cases} \quad (4.21)$$

This a two-parameter family of temporal basis functions that result in a second order accurate interpolation procedure.

## 4.4 Design of temporal basis functions

For MoT schemes with piecewise quadratic polynomials as temporal basis function, the one-parameter family (4.17) results in a first order interpolation procedure. Two degrees of freedom are present in the cubic basis functions (4.21) that result in a second order accurate interpolation. In this section, these parameters will be chosen according to the objectives defined in Sec. 4.2.

### 4.4.1 Customary temporal basis functions

The most popular choice of temporal basis function in the MoT scheme is the shifted Lagrange basis function. For the quadratic basis functions (4.17), the choice  $\alpha = 0$  results in

$$T(t) = \begin{cases} \frac{1}{2}\tilde{t}^2 + \frac{3}{2}\tilde{t} + 1, & -1 < \tilde{t} \leq 0, \\ -\tilde{t}^2 + 1, & 0 < \tilde{t} \leq 1, \\ \frac{1}{2}\tilde{t}^2 - \frac{3}{2}\tilde{t} + 1, & 1 < \tilde{t} \leq 2, \\ 0, & \text{else,} \end{cases} \quad (4.22)$$

which is the quadratic Lagrange basis function [60]. The cubic Lagrange basis function [4], given by

$$T(t) = \begin{cases} \frac{1}{6}\tilde{t}^3 + \tilde{t}^2 + \frac{11}{6}\tilde{t} + 1, & -1 < \tilde{t} \leq 0, \\ -\frac{1}{2}\tilde{t}^3 - \tilde{t}^2 + \frac{1}{2}\tilde{t} + 1, & 0 < \tilde{t} \leq 1, \\ \frac{1}{2}\tilde{t}^3 - \tilde{t}^2 - \frac{1}{2}\tilde{t} + 1, & 1 < \tilde{t} \leq 2, \\ -\frac{1}{6}\tilde{t}^3 + \tilde{t}^2 - \frac{11}{6}\tilde{t} + 1, & 2 < \tilde{t} \leq 3, \\ 0, & \text{else,} \end{cases} \quad (4.23)$$

can be obtained with the choice  $(\alpha, \beta) = (0, 0)$  in Eq. (4.21). Notice that the shifted Lagrange basis functions correspond to the nodal variable  $\mathcal{N}_j(u) = u(t_j)$  in both the quadratic and cubic case.

#### 4.4.2 Smooth temporal basis functions

In this section, the freedom to choose the parameters of the temporal basis functions with maximum order of interpolation accuracy will be used to require smoothness. Since piecewise polynomials are used, this reduces to continuity on discrete time levels. For instance, continuity of quadratic basis function (4.17) on the whole time axis is achieved when

$$\alpha \left( \alpha - \frac{1}{2} \right) = 0. \quad (4.24)$$

The solution  $\alpha = 0$  results in the quadratic Lagrange basis function (4.22), whereas the solution  $\alpha = \frac{1}{2}$  yields

$$T(t) = \begin{cases} \frac{1}{2}\tilde{t}^2 + \tilde{t} + \frac{1}{2} & -1 < \tilde{t} \leq 0, \\ -\tilde{t}^2 + \tilde{t} + \frac{1}{2} & 0 < \tilde{t} \leq 1, \\ \frac{1}{2}\tilde{t}^2 - 2\tilde{t} + 2 & 1 < \tilde{t} \leq 2, \\ 0 & \text{else.} \end{cases} \quad (4.25)$$

This is the temporal basis function based on quadratic B-splines [97, 33]. Although only continuity has been required, the spline basis function has a continuous derivative as well. Thus, the quadratic spline basis function is  $\mathcal{C}^1$  continuous, whereas the quadratic Lagrange basis function is  $\mathcal{C}^0$  continuous.

For the cubic basis functions (4.21), two parameters are present. Now,  $\mathcal{C}^1$  continuity can be imposed, which is achieved when

$$\alpha^3 - \alpha^2 + \frac{1}{3}\alpha - 2\alpha\beta + \beta = 0, \quad (4.26a)$$

$$\frac{1}{3} + \alpha^2 - \alpha - \beta = 0. \quad (4.26b)$$

The unique real-valued solution is  $(\alpha, \beta) = (1, \frac{1}{3})$ , for which the temporal basis function reads

$$T(t) = \begin{cases} \frac{1}{6}\tilde{t}^3 + \frac{1}{2}\tilde{t}^2 + \frac{1}{2}\tilde{t} + \frac{1}{6}, & -1 < \tilde{t} \leq 0, \\ -\frac{1}{2}\tilde{t}^3 + \frac{1}{2}\tilde{t}^2 + \frac{1}{2}\tilde{t} + \frac{1}{6}, & 0 < \tilde{t} \leq 1, \\ \frac{1}{2}\tilde{t}^3 - \frac{5}{2}\tilde{t}^2 + \frac{7}{2}\tilde{t} - \frac{5}{6}, & 1 < \tilde{t} \leq 2, \\ -\frac{1}{6}\tilde{t}^3 + \frac{3}{2}\tilde{t}^2 - \frac{9}{2}\tilde{t} + \frac{9}{2}, & 2 < \tilde{t} \leq 3, \\ 0, & \text{else.} \end{cases} \quad (4.27)$$



Although only  $\mathcal{C}^1$  continuity has been required, the basis function is in fact  $\mathcal{C}^2$  continuous. Therefore, it is called the *cubic spline basis function*. This temporal basis function results in a second order accurate interpolation procedure for the CFIE and has the striking feature of being  $\mathcal{C}^2$  continuous.

The various temporal basis functions introduced in this chapter are depicted in Fig. 4.1 and their properties are summarized in Table 4.1.

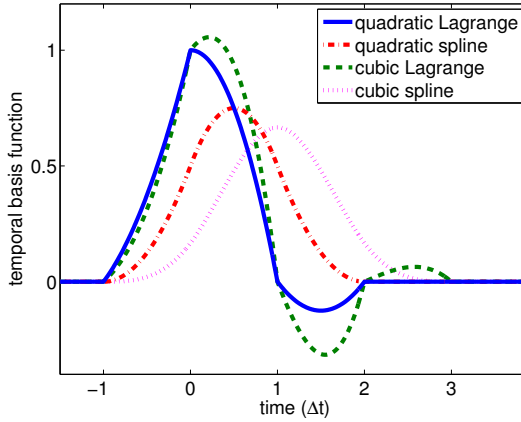


Figure 4.1: The shape of the temporal basis functions.

Table 4.1: Interpolation accuracy for the three temporal terms, the total interpolation accuracy of the CFIE and the smoothness of the various temporal basis functions.

| tbf | acc. $T$                  | acc. $T'$                 | acc. $T''$                | total acc.                | smoothness                  |
|-----|---------------------------|---------------------------|---------------------------|---------------------------|-----------------------------|
| qL  | $\mathcal{O}(\Delta t^3)$ | $\mathcal{O}(\Delta t^2)$ | $\mathcal{O}(\Delta t)$   | $\mathcal{O}(\Delta t)$   | $\mathcal{C}^0(\mathbb{R})$ |
| qs  | $\mathcal{O}(\Delta t^3)$ | $\mathcal{O}(\Delta t^2)$ | $\mathcal{O}(\Delta t)$   | $\mathcal{O}(\Delta t)$   | $\mathcal{C}^1(\mathbb{R})$ |
| cL  | $\mathcal{O}(\Delta t^4)$ | $\mathcal{O}(\Delta t^3)$ | $\mathcal{O}(\Delta t^2)$ | $\mathcal{O}(\Delta t^2)$ | $\mathcal{C}^0(\mathbb{R})$ |
| cs  | $\mathcal{O}(\Delta t^4)$ | $\mathcal{O}(\Delta t^3)$ | $\mathcal{O}(\Delta t^2)$ | $\mathcal{O}(\Delta t^2)$ | $\mathcal{C}^2(\mathbb{R})$ |

### 4.4.3 Conditioning of the leading interaction matrix

At every time level in the MoT scheme (2.22), the solution of a system of linear equations has to be computed. That is,

$$Z_0 \mathbf{I}_k = \mathbf{b}_k \quad (4.28)$$

has to be solved for  $\mathbf{I}_k \in \mathbb{R}^{N_s}$ , where  $Z_0$  is the leading interaction matrix in the MoT scheme. For current test problems, this system of equations can

be solved very efficiently. In fact, less than 1% of the total computation time is consumed by the linear solver, for all computer simulations considered in this thesis. However, this might become relatively more expensive when larger problem sizes are considered. In this section, a family of temporal basis functions will be derived with a parameter that has direct influence on the conditioning of the leading interaction matrix.

The elements  $(Z_j)_{mn}$  of the interaction matrices correspond to the influence of the RWG function of edge  $m$  on edge  $n$  for a retarded time level  $j$ . In particular, the leading matrix  $Z_0$  contains almost-immediate interactions only, that is, all regions of support of RWG functions  $m$  and  $n$  with distance smaller than  $c\Delta t$ . Moreover, the leading matrix depend on the first temporal basis function  $T_1(t)$  only, and only its first piecewise polynomial with support on  $(-\Delta t, 0]$ , see Eq. (2.29). The shape of the temporal basis function will determine the weights on which radiation fields are distributed over different interaction matrices  $Z_j$  and their elements  $(Z_j)_{mn}$ . Therefore, the conditioning of the interaction matrices depend on the shape of temporal basis functions. To this end, a family of temporal basis functions will be designed whose shape can be easily deformed.

Unfortunately, the families of temporal basis functions that have been derived in this chapter are not feasible for the purpose of shape deformation. To this end, the nodal variable (4.19) of cubic basis functions is extended to

$$\mathcal{N}_j(u) = u(t_j) + \alpha\Delta t u'(t_j) + \beta\Delta t^2 u''(t_j) + \gamma\Delta t^3 u'''(t_j) \quad (4.29)$$

for arbitrary constants  $\alpha, \beta, \gamma \in \mathbb{R}$ . With an equivalent derivation as in Section 4.3, a second order interpolation procedure can be required. This will give a family of cubic basis functions with three parameters. The cubic Lagrange and spline basis functions can be derived for  $(\alpha, \beta, \gamma) = (0, 0, 0)$  and  $(1, \frac{1}{3}, 0)$ , resp. This confirms that this family is an extension of Eq. (4.21). Now, let us impose  $\mathcal{C}^1$  continuity, which is achieved when

$$\alpha^3 - \alpha^2 + \frac{1}{3}\alpha - 2\alpha\beta + \beta + \gamma = 0, \quad (4.30a)$$

$$\frac{1}{3} + \alpha^2 - \alpha - \beta = 0. \quad (4.30b)$$

These conditions are satisfied for the temporal basis functions

$$T(t) = \begin{cases} \frac{1}{6}\tilde{t}^3 + (1 - \frac{1}{2}\alpha)\tilde{t}^2 + (\frac{3}{2} - \alpha)\tilde{t} + \frac{2}{3} - \frac{1}{2}\alpha & -1 < \tilde{t} \leq 0, \\ -\frac{1}{2}\tilde{t}^3 + (-1 + \frac{3}{2}\alpha)\tilde{t}^2 + (\frac{3}{2} - \alpha)\tilde{t} + \frac{2}{3} - \frac{1}{2}\alpha & 0 < \tilde{t} \leq 1, \\ \frac{1}{2}\tilde{t}^3 + (-1 - \frac{3}{2}\alpha)\tilde{t}^2 + (-\frac{3}{2} + 5\alpha)\tilde{t} + \frac{8}{3} - \frac{7}{2}\alpha & 1 < \tilde{t} \leq 2, \\ -\frac{1}{6}\tilde{t}^3 + (1 + \frac{1}{2}\alpha)\tilde{t}^2 + (-\frac{3}{2} - 3\alpha)\tilde{t} + \frac{9}{2}\alpha & 2 < \tilde{t} \leq 3, \\ 0 & \text{else.} \end{cases} \quad (4.31)$$

For  $\alpha = 1$ , this *cubic  $\mathcal{C}^1$  spline basis function* reduces to the cubic spline basis function (4.27) that is  $\mathcal{C}^2$  continuous. This one-parameter family of temporal



basis functions satisfies the following properties:

$$\int_{-\infty}^{\infty} T(\tilde{t}) d\tilde{t} = 1, \quad (4.32a)$$

$$\int_{-\infty}^{\infty} \tilde{t} T(\tilde{t}) d\tilde{t} = \alpha \quad (4.32b)$$

for the nondimensional time  $\tilde{t} = t/\Delta t$ . Eq. (4.32a) states that the temporal basis functions have equal contributions for all parameters  $\alpha \in \mathbb{R}$ . The integral in Eq. (4.32b) can be interpreted as the centroid. So the parameter  $\alpha$  specifies the point in time where the temporal basis function has most contribution. This can be seen in Fig. 4.2, where the cubic  $\mathcal{C}^1$  spline basis function (4.31) is depicted for several choices of  $\alpha$ . Changing the parameter  $\alpha$  will deform the shape continuously and is therefore expected to have influence on the conditioning of the leading interaction matrix. This will be experimentally confirmed in Sec. 4.5.5.

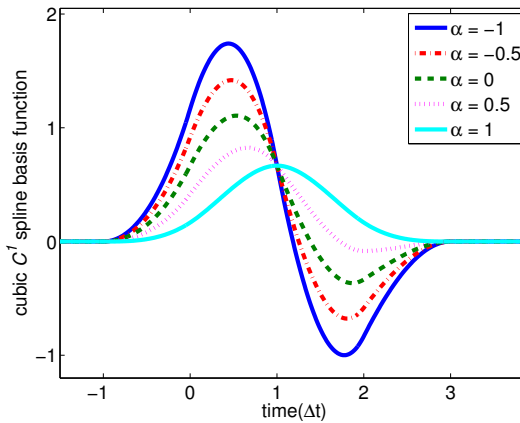


Figure 4.2: The family of cubic  $\mathcal{C}^1$  spline basis functions (4.31).

## 4.5 Experimental confirmation

The interpolation accuracy of temporal basis functions has been derived in Sec. 4.3 for quadratic and cubic polynomials. This has resulted in families of temporal basis functions that satisfy the maximum order of interpolation accuracy. The degrees of freedom have been used to obtain user-defined objectives such as smoothness. In this section, the influence of the choices made in the framework on the numerical properties of the MoT scheme will be confirmed with computational experiments.

Two test cases will be considered, namely a cube with edges of 1 m and a sphere with a diameter of 1 m. As depicted in Fig. 4.3, the cube and sphere are partitioned into 480 and 238 triangular patches, respectively. A Gaussian plane wave (2.35) will be used as incident field, with the parameters given by: pulse strength  $120\pi$  V, pulse width 6 m, pulse delay 4 lm, and polarization and propagation in the  $+\hat{x}$  and  $-\hat{z}$  direction. To get an equal contribution from the EFIE and MFIE, the CFIE-0.5 will be used, i.e.,  $\kappa = 0.5$  in (2.17). The outer spatial integral has been calculated with Gaussian quadrature with 7 points on each triangle patch and the inner integral calculated analytically [84], unless stated otherwise.

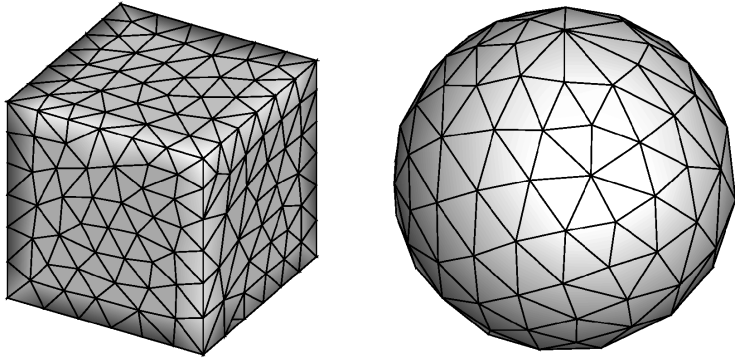


Figure 4.3: The mesh of the cube and sphere used as test problem.

### 4.5.1 Interpolation accuracy

In this chapter, the accuracy in time of the MoT scheme has been analyzed by deriving bounds on the interpolation error, as summarized in Table 4.1. To validate the analysis, a given function will be interpolated, for instance a Gaussian curve  $u(t) = e^{-(12t-6)^2}$  for  $0 \leq t \leq 1$ . The interpolant (4.1) calculated with a time step size  $\Delta t = 1/800$  is denoted by  $\hat{u}_1$  and with  $\Delta t = 1/400$  by  $\hat{u}_2$ . Then the order of interpolation accuracy can be computed as  $\log_2 \left( \frac{\|\hat{u}_2 - u\|}{\|\hat{u}_1 - u\|} \right)$  and similar for the derivatives. Results with the  $L^2$  norm are given in Table 4.2. The experimental accuracy perfectly matches the expected accuracy.

### 4.5.2 Smoothness

An important feature of the spline basis functions (4.25) and (4.27) is the continuous derivative on the whole time axis whereas shifted Lagrange basis functions (4.22) and (4.23) are only continuous. The discrete surface current

Table 4.2: Experimental order of interpolation accuracy.

| temporal basis function | $u$   | $u'$  | $u''$ |
|-------------------------|-------|-------|-------|
| quadratic Lagrange      | 3.000 | 1.994 | 0.995 |
| quadratic spline        | 3.000 | 2.005 | 1.000 |
| cubic Lagrange          | 3.999 | 2.990 | 1.992 |
| cubic spline            | 3.999 | 3.085 | 2.001 |

density calculated with the spline basis functions is therefore expected to be smooth. To verify this implication, the TDIE method will be used with a large time step size, for which the effect of smooth basis functions on the solution will appear. For the sphere and cube a time step size of 1.13 lm and 0.71 lm has been used, resp. As a reference solution, the MoT scheme has been applied with a small time step size of 0.014 lm and 0.029 lm for the sphere and cube, resp. The results depicted in Fig. 4.4 clearly show that the smoothness properties of the temporal basis functions lead to similar smoothness properties of the discrete electric surface current density.

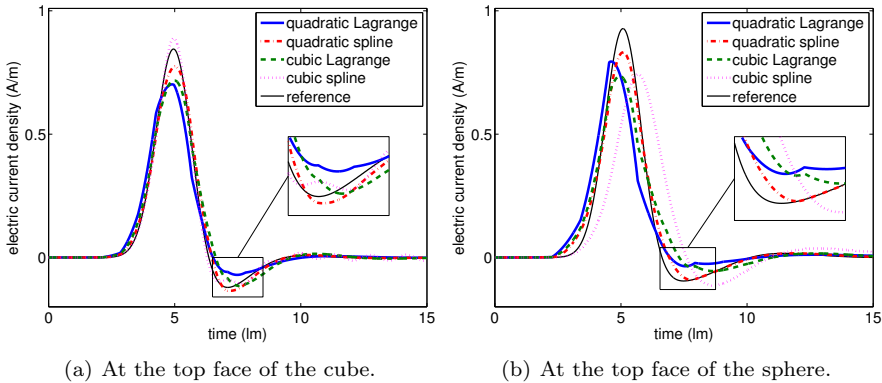


Figure 4.4: Electric surface current density.

### 4.5.3 Quadrature accuracy

Spatial integrals over the triangular surface mesh are present in the CFIE (2.17). Gaussian quadrature has been used to evaluate the integrals, which is effective for smooth integrands. The integrands in the CFIE depend on the temporal basis functions evaluated in retarded time levels. Smooth temporal basis functions therefore yield integrands that are smooth in space and the quadrature

accuracy is expected to improve. Remember that the quadrature procedure is applied to the outer integral only because the inner integral has been calculated with analytic expressions [84]. The sphere will be used as test problem, with the EFIE and a time step size of 0.14 nm.

The discretized EFIE (2.15) consists of the terms

$$V_{mn,j}^q = \iint_{\Gamma_q} \mathbf{f}_m(\mathbf{r}) \cdot \iint_{\Gamma} \frac{\mathbf{f}_n(\mathbf{r}') \ddot{T}_j(\tau)}{4\pi R} d\mathbf{r}' d\mathbf{r}, \quad (4.33a)$$

$$S_{mn,j}^q = \iint_{\Gamma_q} \nabla \cdot \mathbf{f}_m(\mathbf{r}) \iint_{\Gamma} \frac{\nabla' \cdot \mathbf{f}_n(\mathbf{r}') T_j(\tau)}{4\pi R} d\mathbf{r}' d\mathbf{r} \quad (4.33b)$$

where  $\Gamma_q$  denotes the surface mesh with  $q$  quadrature points on each triangular patch. These two terms can be related with the magnetic vector and scalar potential, respectively [69]. Notice that the value  $j$  determines the matrix  $Z_j$  in the MoT scheme (2.22) of which the discrete terms are an element. For each temporal basis function, both terms will be computed with different numbers of quadrature points. The convergence towards the reference experiment with 73 quadrature points will be considered. The relative error is therefore defined as

$$\frac{\|V_{mn,j}^q - V_{mn,j}^{73}\|}{\|V_{mn,j}^{73}\|}.$$

For a given  $j$ , the  $\ell^2$  norm

$$\|V_{mn,j}\|^2 = \sum_{m=1}^{N_s} \sum_{n=1}^{N_s} |V_{mn,j}|^2$$

over all edge pairs has been used. The convergence results for the vector potential term (4.33a) is depicted in Fig. 4.5(a) with  $j = 3$  and for the scalar potential term (4.33b) in Fig. 4.5(b) with  $j = 6$ .

For the cubic basis functions, the smoothness of the spline basis function indeed improves the convergence as depicted in Fig. 4.5(a). For the quadratic basis functions, however, exactly the same convergence is observed. This is expected because the vector potential term (4.33a) contains  $\ddot{T}$  only, which is the same for both quadratic Lagrange and spline basis function.

In the case of the scalar potential term, no time derivatives are present and the smoothness properties of the temporal basis functions are all different. Fig. 4.5(b) clearly shows that smoothness of the temporal basis function improves the convergence with respect to the number of quadrature points.

The positive influence of smooth basis functions on the quadrature accuracy of the discrete terms has been verified experimentally. However, a faster convergence for the elements of the interaction matrices does not necessarily imply more accurate solutions of the MoT scheme. It is therefore not evident



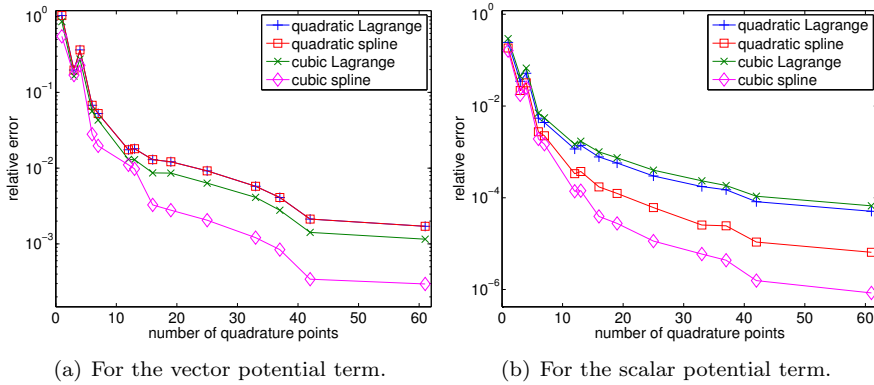


Figure 4.5: Relative quadrature error for the EFIE on a sphere.

that smoothness of temporal basis functions will also have a positive influence on the discrete surface current density of the TDIE method.

The solution of the EFIE has been computed with the MoT scheme for different numbers of quadrature points. The convergence towards the reference solution for 73 quadrature points will be considered. The relative error is given by

$$\frac{\|J_{n,j}^q - J_{n,j}^{73}\|}{\|J_{n,j}^{73}\|}$$

where  $J_{n,j}^q$  denotes the coefficients in Eq. (2.18) computed with  $q$  quadrature points. The norm is defined in both discrete space and time as

$$\|J_{n,j}\|^2 = \sum_{n=1}^{N_s} \sum_{j=1}^{100} |J_{n,j}|^2.$$

The convergence results depicted in Fig. 4.6 show a faster convergence for spline basis functions compared to shifted Lagrange basis functions of equal support. For this specific test case, the increase in convergence rate for the surface current density is not as prominent as for the matrix elements.

#### 4.5.4 Global accuracy

The global accuracy in time of TDIE methods depends on the interpolation accuracy but does not necessarily have to satisfy the same orders of accuracy. The global accuracy can be investigated experimentally with Richardson's extrapolation algorithm. To this end, let us consider three experiments with three different time step sizes, all on the same spatial mesh. The  $x$ -component of the discrete electric surface current density on top of the object is denoted

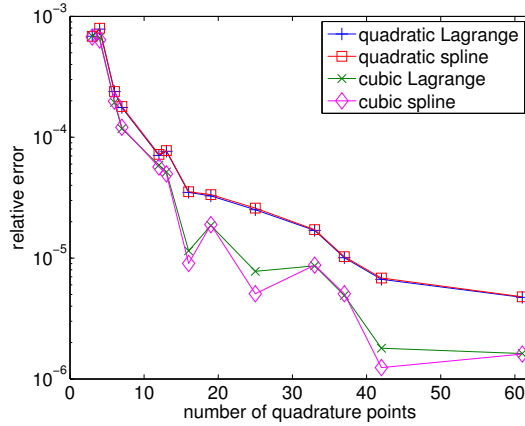


Figure 4.6: Relative error for the electric surface current density on a sphere.

by  $J_1(t)$ ,  $J_2(t)$ , and  $J_4(t)$ , for time step sizes  $\Delta t$ ,  $2\Delta t$ , and  $4\Delta t$ , respectively. The order of the global accuracy in time can be computed as  $\log_2 \left( \frac{\|J_4 - J_2\|}{\|J_2 - J_1\|} \right)$  where the  $L^2$  norm has been used for  $0 \leq t \leq 14$  nm. The results for the cube and sphere are listed in Table 4.3 and 4.4, resp.

Table 4.3: Experimental order of accuracy on a cube, with the smallest time step size listed.

| temporal basis function                               | 0.012 nm | 0.023 nm | 0.035 nm | 0.047 nm |
|-------------------------------------------------------|----------|----------|----------|----------|
| quadratic Lagrange                                    | 1.004    | 1.014    | 1.018    | 1.030    |
| quadratic spline                                      | 1.996    | 2.004    | 1.989    | 2.044    |
| cubic Lagrange                                        | 2.011    | 2.027    | 2.035    | 2.038    |
| cubic spline                                          | 4.133    | 3.611    | 4.047    | 4.551    |
| cubic $\mathcal{C}^1$ spline, $\alpha = -\frac{1}{2}$ | 2.989    | 2.916    | 2.8674   | 2.804    |
| cubic $\mathcal{C}^1$ spline, $\alpha = 0$            | 3.003    | 2.962    | 2.9568   | 2.935    |
| cubic $\mathcal{C}^1$ spline, $\alpha = \frac{1}{2}$  | 3.016    | 2.992    | 3.0196   | 3.038    |

The experimental order of accuracy converges to the expected  $\mathcal{O}(\Delta t)$  and  $\mathcal{O}(\Delta t^2)$  for the quadratic and cubic Lagrange basis functions, resp. However, a global error of  $\mathcal{O}(\Delta t^2)$  and  $\mathcal{O}(\Delta t^4)$  is observed for the quadratic and cubic spline basis function, respectively. Furthermore, the cubic  $\mathcal{C}^1$  spline basis function (4.31) results in a global accuracy of  $\mathcal{O}(\Delta t^3)$ . Apparently, the interpolation error does not restrict the global accuracy when the spline basis functions are used and higher orders of accuracy are obtained. Indeed, the



Table 4.4: Experimental order of accuracy on a sphere, with the smallest time step size listed.

| temporal basis function                               | 0.014 lm | 0.028 lm | 0.043 lm | 0.057 lm |
|-------------------------------------------------------|----------|----------|----------|----------|
| quadratic Lagrange                                    | 1.039    | 1.085    | 1.129    | 1.166    |
| quadratic spline                                      | 1.982    | 2.017    | 2.005    | 1.992    |
| cubic Lagrange                                        | 2.044    | 2.093    | 2.135    | 2.159    |
| cubic spline                                          | 4.079    | 4.229    | 4.028    | 4.016    |
| cubic $\mathcal{C}^1$ spline, $\alpha = -\frac{1}{2}$ | 2.955    | 2.9252   | 2.8291   | 2.7285   |
| cubic $\mathcal{C}^1$ spline, $\alpha = 0$            | 2.971    | 2.9748   | 2.9209   | 2.8586   |
| cubic $\mathcal{C}^1$ spline, $\alpha = \frac{1}{2}$  | 2.983    | 3.0064   | 2.9937   | 2.9799   |

smoothness is a clear difference between shifted Lagrange and spline basis functions, but the actual cause of this remarkably better accuracy for the spline basis functions is a topic for future research.

The present accuracy analysis has been derived for TDIE methods that use the MoT scheme. As explained in Chapter 3, discretely equivalent space-time Galerkin schemes can be derived. Evidently, equivalent schemes have the same accuracy properties. Recently, some computational experiments on the global accuracy of space-time Galerkin schemes have been published in [11]. Their computational results are in agreement with this thesis.

### 4.5.5 Condition number

In Sec. 4.4.3 a family of temporal basis function has been derived with the aim to influence the conditioning of the leading interaction matrix such that the linear solver in the TDIE method becomes more effective. The *spectral condition number* of the matrix can be used as a first estimate for the effectiveness of linear solvers [76] and is defined as the ratio of the largest and smallest eigenvalue. The influence of the shape of the temporal basis function on the conditioning of the leading interaction matrix will be analyzed experimentally. To this end, the spectral condition number will be computed for several values of  $\alpha$  in the cubic spline basis function (4.31).

First, let us consider several other numerical properties of the leading interaction matrix. The sparsity of the matrix depends on the time step size. More specifically, only the interaction of all spatial test and basis function with distance at most  $c\Delta t$  result in nonzero elements in the leading interaction matrix. Therefore, the larger the time step size compared to the surface mesh size, the more nonzero elements. The sparsity pattern for a typical choice of time step size is depicted in Fig. 4.7(a).

The exact formulation of the elements of the discrete interaction matri-

ces is symmetric. That is, the influence of the spatial test function  $m$  on basis function  $n$  equals the influence of  $n$  on  $m$ . However, because different quadrature rules are used for the source and observer patches, the symmetry is lost during the matrix evaluation. Still, the matrices are almost symmetric and the computed eigenvalues are most often real valued. Furthermore, the continuous formulation of the leading interaction matrix is positive definite when the time step size is small enough [91]. Computational experiments suggest that this still holds in the discrete case, as illustrated by the spectrum depicted in Fig. 4.7(b).

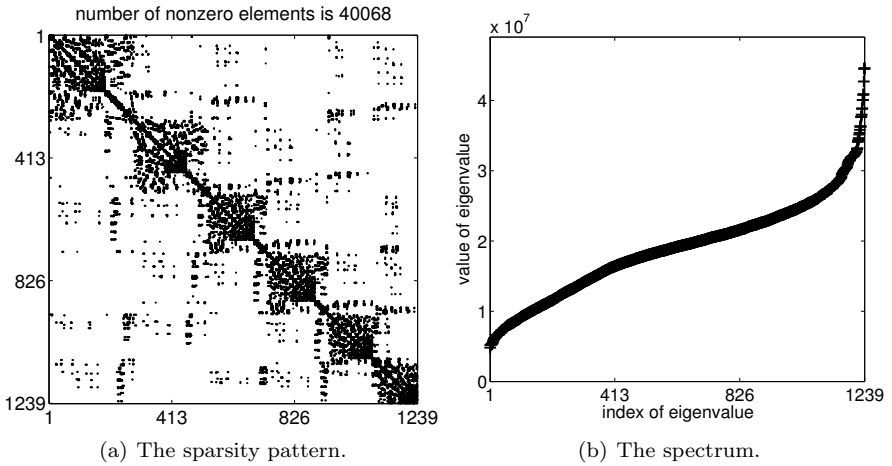


Figure 4.7: The leading interaction matrix on a unit sized cube with 1239 edges,  $\Delta t = 0.1$  lm, and the cubic spline basis function (4.31) with  $\alpha = 0$ . Quasi-exact integration has been used with 7 quadrature points.

Now, let us return to the influence of the temporal basis function on the conditioning of the leading interaction matrix. Several computational experiments will be performed for which the spectral condition number is computed. Different values of the shape parameter in the cubic spline basis function (4.31) are used, with the shifted Lagrange and quadratic spline basis function as references. The results for a cube and a generic aircraft are given in Table 4.5.

The number of nonzero elements confirms that the larger the time step size, the more populated the leading interaction matrix. This makes the system of linear equations harder to solve, as confirmed by the larger spectral condition number. For small time step sizes, the contribution of radiation fields in the leading interaction matrix is small and the differences between temporal basis functions on the spectral condition number are negligible. For large time step sizes, many discrete interactions contribute to each matrix and the influence of the temporal basis function on the conditioning becomes apparent.



Table 4.5: For a given time step size  $\Delta t$ , the leading interaction matrix has ‘nnz’ nonzero elements. The spectral condition number is given for the quadratic Lagrange (qL), quadratic spline (qs), cubic Lagrange (cL), and cubic spline (cs( $\alpha$ )) basis functions.

(a): A unit sized cube modeled with a surface mesh of 1239 edges.

| $\Delta t$ | nnz       | qL     | qs       | cL    |         |       |
|------------|-----------|--------|----------|-------|---------|-------|
| 0.01 lm    | 16 035    | 5.72   | 5.96     | 5.85  |         |       |
| 0.1 lm     | 40 068    | 20.8   | 12.9     | 11.6  |         |       |
| 1 lm       | 1 080 971 | 1825   | 914      | 912   |         |       |
| $\Delta t$ | nnz       | cs(-1) | cs(-0.5) | cs(0) | cs(0.5) | cs(1) |
| 0.01 lm    | 16 035    | 5.96   | 5.96     | 5.96  | 5.96    | 5.96  |
| 0.1 lm     | 40 068    | 10.4   | 10.0     | 9.26  | 8.11    | 6.03  |
| 1 lm       | 1 080 971 | 710    | 670      | 609   | 508     | 306   |

(b): A generic aircraft modeled with a surface mesh of 6756 edges and scaled to fit within a unit sized cube. This scaling allows for a fair comparison with the results for the cube.

| $\Delta t$ | nnz        | qL                | qs                | cL                |                   |                   |
|------------|------------|-------------------|-------------------|-------------------|-------------------|-------------------|
| 0.01 lm    | 288 897    | $3.52 \cdot 10^4$ | $2.73 \cdot 10^4$ | $2.23 \cdot 10^4$ |                   |                   |
| 0.1 lm     | 4891 833   | $2.75 \cdot 10^6$ | $1.38 \cdot 10^6$ | $1.38 \cdot 10^6$ |                   |                   |
| 1 lm       | 45 643 096 | $2.74 \cdot 10^8$ | $1.37 \cdot 10^8$ | $1.37 \cdot 10^8$ |                   |                   |
| $\Delta t$ | nnz        | cs(-1)            | cs(-0.5)          | cs(0)             | cs(0.5)           | cs(1)             |
| 0.01 lm    | 288 897    | $2.24 \cdot 10^4$ | $2.14 \cdot 10^4$ | $1.99 \cdot 10^4$ | $1.75 \cdot 10^4$ | $1.25 \cdot 10^4$ |
| 0.1 lm     | 4891 833   | $1.07 \cdot 10^6$ | $1.01 \cdot 10^6$ | $9.20 \cdot 10^5$ | $7.68 \cdot 10^5$ | $4.63 \cdot 10^5$ |
| 1 lm       | 45 643 096 | $1.07 \cdot 10^8$ | $1.01 \cdot 10^8$ | $9.15 \cdot 10^7$ | $7.62 \cdot 10^7$ | $4.57 \cdot 10^7$ |

The computational experiments show that a larger shape parameter  $\alpha$  in the cubic spline basis function (4.31) improves the spectral condition number of the leading interaction matrix. Remember that the definition of the leading interaction matrix depends on the support in  $(-\Delta t, 0]$  of the temporal basis function only. The distribution of the temporal basis functions between immediate interactions, characterized by the support  $(-\Delta t, 0]$ , and the retarded interactions on  $(0, \ell \Delta t]$  is therefore not of influence on the conditioning of the leading interaction matrix. In other words, the spectral condition number of  $Z_0$  is a purely local parameter and depends on the shape of the temporal

basis function in  $(-\Delta t, 0]$  only. Although it is clear from the computer simulations that the condition number is influenced by the shape of the temporal basis function, no clear relation with a certain shape characteristic has been found. For example, the quadratic Lagrange and spline basis functions have equal second derivative, but result in different spectral condition numbers. Further research is required to specify the relation between the shape of the temporal basis function and the conditioning of the interaction matrices.

The computational experiments clearly confirm that the shape of the temporal basis function has influence on the conditioning of the leading matrix and thus the effectiveness of the linear solver. However, the improvements in the spectral condition number are moderate, especially for small time step sizes. Notice that these smaller time step sizes are the typical choice for computer simulations. Furthermore, the linear solver consumes only very little computation time in the TDIE method for current test cases. This makes the improvement of the condition number less important than other design criteria for the temporal basis function. As a final remark, preliminary results with a diagonal preconditioner do not change the observations made in this section.





# Chapter 5

## Robustness

### 5.1 The influence of numerical errors on stability

Stability of the TDIE method is essential to its potential application in an industrial environment. A functional analysis has been performed in Chapter 3 that results in a stability theorem. For correctly chosen temporal basis functions in the MoT scheme, stability of a specific variational formulation of the EFIE is guaranteed. In this chapter, it will be shown that this is not yet sufficient to obtain stable computer simulations in a robust manner.

After choosing the temporal basis function, the MoT scheme is given by a marching procedure consisting of discrete interaction matrices. Each element of the interaction matrices is given by the discrete radiation field for a source and observer mesh element at a specific retarded time level. The evaluation of these elements requires the evaluation of two surface integrals. In general, this can not be performed exactly on a computer architecture. The use of approximation procedures such as numerical quadrature and floating point representation are necessary. Consequently, *numerical errors*, such as quadrature and rounding errors, are always present in computer simulations.

The stability proof does not take these numerical errors into account. It is therefore possible that numerical errors ruin the theoretical stability. Computational experiences suggest that the stability is very sensitive to numerical accuracy. More precisely, standard implementations of simple quadrature procedures most often fail to obtain the numerical accuracy required for stable simulations. Stability can only be achieved with high confidence when quadrature procedures are used that are specifically designed for the TDIE method. Moreover, in this chapter we will show that a straightfor-



ward formulation in finite precision arithmetic of accurate quadrature procedures is not yet sufficient. Well-behaved formulations will be derived and employed in the MoT scheme resulting in improved stability and robustness of the TDIE method.

In frequency-domain CEM, similar expressions for the elements of the discretization matrix have to be evaluated with high precision as well. In particular, highly accurate computation of singular and near-singular integrals have to be performed to obtain accurate simulations. Different techniques based on singularity extraction and singularity cancellation have been designed [104, 36]. However, these algorithms can not readily be used in TDIE methods, because the definitions of the integrals are different and no influence of the impulsive nature in time of the Green's function is present, which considerably simplifies the integration regions.

The chapter will start with an introduction to quasi-exact integration methods, which can obtain a very high accuracy in the evaluation of the discrete interaction matrices. Sec. 5.2 will also explain the importance of well-behaved expressions for computation in finite precision arithmetic. The analytical formulation of radiation fields that are used in the quasi-exact integration method will be summarized in Sec. 5.3. Their evaluation in finite precision arithmetic is ill behaved as explained in Sec. 5.4. To this end, a robust formulation with specific tolerance regions will be derived in Sec. 5.5 and 5.6. The computational experiment in Sec. 5.7 confirms that the newly designed robust formulation is necessary to obtain stability.

## 5.2 Quasi-exact integration methods

Numerical accuracy is dominated by the choice of quadrature procedure. The numerical quadrature is used to approximate the four-dimensional integrals over the scattering surface that are present in the discretized equations. To be precise, an arbitrary element of an interaction matrix in the MoT scheme (2.22) for the EFIE is given by

$$\begin{aligned} (Z_i)_{mn} = & \frac{1}{c} \iint_{\Gamma} \mathbf{f}_m(\mathbf{r}) \cdot \iint_{\Gamma} \frac{\mathbf{f}_n(\mathbf{r}') \dot{T}(i\Delta t - \frac{|\mathbf{r}-\mathbf{r}'|}{c})}{4\pi|\mathbf{r}-\mathbf{r}'|} d\mathbf{r}' d\mathbf{r} \\ & + c \iint_{\Gamma} \nabla \cdot \mathbf{f}_m(\mathbf{r}) \iint_{\Gamma} \frac{\nabla' \cdot \mathbf{f}_n(\mathbf{r}') T(i\Delta t - \frac{|\mathbf{r}-\mathbf{r}'|}{c})}{4\pi|\mathbf{r}-\mathbf{r}'|} d\mathbf{r}' d\mathbf{r}. \end{aligned} \quad (5.1)$$

In general, numerical quadrature is effective when the integrand is smooth. Remember that the temporal basis functions used in this thesis are differentiable only to a limited degree, see Sec. 4.4.2. The integrand is therefore nonsmooth and special quadrature procedures are necessary for high accuracy.

To reduce the quadrature errors in the TDIE method, there are mainly two avenues to proceed: increase the smoothness of the integrand or improve the

quadrature procedure. An increase in smoothness can be achieved by using different temporal basis functions than the piecewise polynomials (2.29), for instance BLIFs [102]. However, this is at the expense of other design criteria for temporal basis functions, most notably the efficiency and will therefore not be considered, see Sec. 4.2. Improving the accuracy of the quadrature procedure can not be achieved by increasing the number of quadrature points in standard quadrature procedures, because the integrand is nonsmooth. The idea is to design highly accurate quadrature procedures that locate the discontinuities and use separate quadrature procedures on the subregions in which the integrand is smooth.

Necessary for these so-called *composite quadrature* is the locating of subregions in which the integrand is smooth. In the case of TDIE methods with a Green's function for scattering in an unbounded homogeneous space, these subregions are given by the intersection of light cones and mesh elements, see Fig. 5.1. Computing these shadow regions is highly technical and is known only for lower-order schemes employing triangular patches.

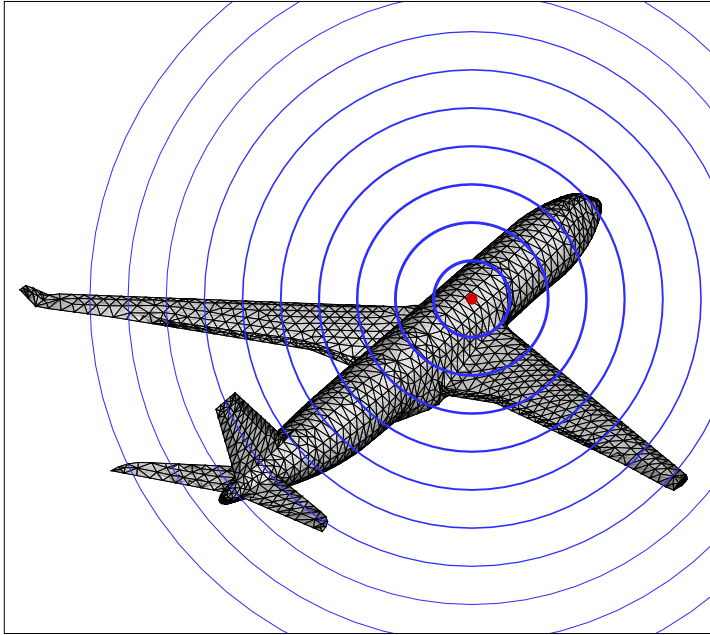


Figure 5.1: For each quadrature point, the integrand is smooth inside each shell of light cones.

The accuracy of the composite quadrature procedures can be improved further when combined with analytical expressions for the integrals. In this way, two quasi-exact methods have been established for TDIE methods in

electromagnetics on arbitrary three-dimensional objects [84, 87]. The first method uses analytical expressions of radiation fields to compute the inner two integrals exactly. The second method uses analytical expressions for the inner three integrals, leaving one integral to be evaluated by numerical quadrature.

The choice of integration method is based on a trade-off between accuracy, efficiency, and implementation effort. Here, exact evaluation of the radiation fields [84] will be used, because this method is in our experience necessary and sufficient to obtain stability. The analytical expressions of the radiation fields can be applied to specific basis functions only, namely the RWG spatial basis functions (2.23) and the family of piecewise polynomial temporal basis functions (2.29). Since these are the commonly practiced choices, it is no stringent requirement.

This work builds upon the elegant analytical expressions for the radiation fields as function of the geometrical properties of a source triangle and an observation point, as introduced in [84]. We will analyze the evaluation of these expressions in finite precision arithmetic, which is, in our experience, a crucial element of a robust numerical scheme.

In this chapter, it will be shown that the analytical expressions of [84] are ill behaved for certain important limit cases, for example when the observation point is projected close to a vertex of the source triangle. Because of this, a straightforward formulation in finite precision arithmetic can result in large errors in the radiation fields, and basically undermines the accuracy of the exact evaluation of the radiation fields. A computational experiment confirms this and shows it can even lead to late-time instability of the MoT scheme.

Therefore, a robust formulation will be derived that will be shown to be well behaved for all limit cases. This results in highly accurate evaluation of interaction matrices, also in finite precision arithmetic. In fact, the same computational experiment remains stable in late time. The novel formulation thus improves the robustness and stability of the TDIE method and is an important step towards industrial application.

### 5.3 Analytical formulation of radiation fields

This section describes the analytical formulation of the radiation fields and explains its incorporation in the MoT scheme. Most of the material discussed here has been introduced in [84]. This section aims to introduce the nomenclature that will be used in subsequent sections and provides additional details for the analysis of the evaluation in finite precision arithmetic.

For conciseness, only the application to the differentiated EFIE (2.15) will be considered in this chapter, but the same algorithm can also be used for other boundary integral equations, including the MFIE, PMCHWT, and Müller equations [84].

### 5.3.1 Derivation of standard intersection integrals

The goal of this section is to rewrite the elements of the discretization matrix (5.1) into a standardized form. First, the local support of the RWG function (2.23) is used to simplify the integration domain into pairs of observer and source triangular facets, denoted by  $\Gamma_p$  and  $\Gamma_q$ , resp. A numerical quadrature procedure will be used for the outer integral over the observer triangle. Then, the radiation fields are expressed by an integral operator with respect to an *observer point*, denoted by  $\mathbf{r}^*$ . The expressions can be simplified by considering the *projection point*, denoted by  $\tilde{\mathbf{r}}$  and defined as the orthogonal projection of  $\mathbf{r}^*$  onto the plane through source triangle  $\Gamma_q$ . This introduces the *projection height*, denoted by  $h = |\tilde{\mathbf{r}} - \mathbf{r}^*|$ .

The temporal basis functions (2.29) are defined as piecewise polynomials. To obtain a single expression for the radiation field, the integration over the source triangle  $\Gamma_q$  should be partitioned into regions where the temporal basis functions are uniquely defined. This is the case for all source points  $\mathbf{r}'$  satisfying  $j \leq |\mathbf{r}^* - \mathbf{r}'|/(c\Delta t) < j + 1$  for an integer  $j$ . This represents the discrete light cone of observer point  $\mathbf{r}^*$  with interval  $\Delta t$ . The integration should thus be reduced to

$$\Gamma_{q,j} = \left\{ \mathbf{r}' \in \Gamma_q \mid j\Delta t \leq \frac{|\mathbf{r}^* - \mathbf{r}'|}{c} < (j+1)\Delta t \right\} \quad (5.2)$$

which is the intersection of the source triangle and the discrete light cone.

Now, each element of the discretization matrix can be written as a unique combination of *standard intersection integrals*, given by

$$\mathbf{I}_k(\mathbf{r}^*) = \iint_{\Gamma_{q,j}} (\mathbf{r}' - \tilde{\mathbf{r}}) |\mathbf{r}^* - \mathbf{r}'|^k d\mathbf{r}', \quad (5.3a)$$

$$I_k(\mathbf{r}^*) = \iint_{\Gamma_{q,j}} |\mathbf{r}^* - \mathbf{r}'|^k d\mathbf{r}' \quad (5.3b)$$

for  $k = -3, -1, 0, 1, \dots, \ell - 1$ .

### 5.3.2 Derivation of standard contour integrals

Using Gauss' theorem, the standard intersection integrals (5.3) can be rewritten into the *standard contour integrals*

$$\mathbf{I}_k(\mathbf{r}^*) = \frac{1}{k+2} \oint_{\partial\Gamma_{q,j}} |\mathbf{r}^* - \mathbf{r}'|^{k+2} \hat{\mathbf{d}} d\mathbf{r}', \quad (5.4a)$$

$$I_k(\mathbf{r}^*) = \frac{1}{k+2} \oint_{\partial\Gamma_{q,j}} \frac{|\mathbf{r}^* - \mathbf{r}'|^{k+2}}{|\mathbf{r}' - \tilde{\mathbf{r}}|^2} (\mathbf{r}' - \tilde{\mathbf{r}}) \cdot \hat{\mathbf{d}} d\mathbf{r}' \quad (5.4b)$$

for  $k = -3, -1, 0, 1, \dots, \ell - 1$ , where  $\hat{\mathbf{d}}$  denotes the unit outward normal on  $\partial\Gamma_{q,j}$  situated inside the plane through the triangle. Special care should

be devoted to the definition of the contour  $\partial\Gamma_{q,j}$ . The integrand of the scalar contour integrals (5.4b) contains a singularity at  $\mathbf{r}' = \tilde{\mathbf{r}}$ , which occurs when the observer point is projected onto the source triangle. This is an integrable singularity, so the integral operators converge and the singular point is called a *pole*. Hence, the inside of contour  $\partial\Gamma_{q,j}$  should exclude the pole, which can be done with a keyhole or indented contour, see Fig. 5.2. Then, a limit process will be performed such that the contour converges to the boundary of  $\Gamma_{q,j}$ . However, nonzero limit values of the standard contour integrals can be obtained at the pole, which will be denoted by  $I_k^{\text{pole}}$  for  $k = -3, -1, 0, 1, \dots, \ell-1$ , called the *standard pole integrals*.

Remember that  $\Gamma_{q,j}$  is given by the intersection of a triangle and a discrete light cone. Therefore, the contour  $\partial\Gamma_{q,j}$  consists of line segments and arcs only, see Fig. 5.3. The standard contour integrals can thus be written as a unique combination of standard line, arc, and pole integrals:

$$\mathbf{I}_k(\mathbf{r}^*) = \sum_{i=1}^{\#\text{line segments}} \mathbf{I}_k^{\text{line},i}(\mathbf{r}^*) + \sum_{i=1}^{\#\text{arcs}} \mathbf{I}_k^{\text{arc},i}(\mathbf{r}^*), \quad (5.5a)$$

$$I_k(\mathbf{r}^*) = \sum_{i=1}^{\#\text{line segments}} I_k^{\text{line},i}(\mathbf{r}^*) + \sum_{i=1}^{\#\text{arcs}} I_k^{\text{arc},i}(\mathbf{r}^*) + I_k^{\text{pole}}(\mathbf{r}^*) \quad (5.5b)$$

where the number of line segments and arcs depend on the intersection shape. These numbers range from zero to three. An analytical expression for the standard contour integrals can be derived separately for each line segment and arc.

### 5.3.3 Analytical expression for standard line integrals

Let us consider an arbitrary line segment that is part of the contour and denote its start and end point by  $\mathbf{r}_1$  and  $\mathbf{r}_2$ , resp. In order to derive an analytical expression of the standard contour integrals (5.4) on a line segment, let us introduce the local coordinate system  $(\hat{\mathbf{u}}, \hat{\mathbf{v}}, \hat{\mathbf{w}})$  defined by

$$\hat{\mathbf{u}} = (\mathbf{r}_2 - \mathbf{r}_1)/|\mathbf{r}_2 - \mathbf{r}_1|, \quad (5.6a)$$

$$\hat{\mathbf{v}} = \hat{\mathbf{u}} \times \hat{\mathbf{w}}, \quad (5.6b)$$

$$\hat{\mathbf{w}} = \hat{\mathbf{n}} \quad (5.6c)$$

where  $\hat{\mathbf{n}}$  denotes the unit outward normal on the surface mesh. The unit sized vectors  $\hat{\mathbf{u}}$  and  $\hat{\mathbf{v}}$  are situated in the plane of the triangular mesh element and are oriented parallel and perpendicular to the line segment, resp. The location of the projection point  $\tilde{\mathbf{r}}$  w.r.t. this line segment can be characterized

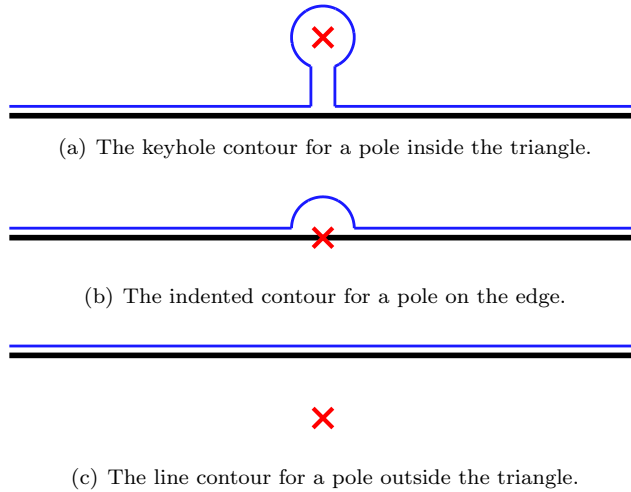


Figure 5.2: The three cases of the contour integration, with the edge (black), the projection point (red cross), and the contour (blue), where the inside of the triangle is located above the edge.

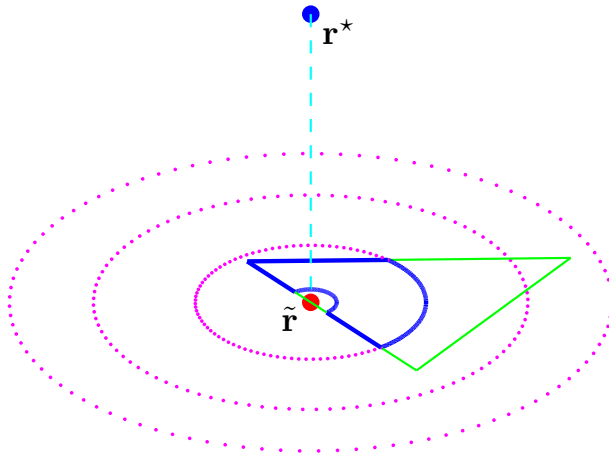


Figure 5.3: The contour of an intersection of a triangle and discrete light cone. Depicted are the triangle (green), observer point (blue point), projection (cyan dotted line), projection point (red point), discrete light cones on the projection plane (magenta dotted line) and contour (blue).



by the parameters

$$u_1 = (\mathbf{r}_1 - \tilde{\mathbf{r}}) \cdot \hat{\mathbf{u}}, \quad (5.7a)$$

$$u_2 = (\mathbf{r}_2 - \tilde{\mathbf{r}}) \cdot \hat{\mathbf{u}}, \quad (5.7b)$$

$$v_0 = (\mathbf{r}_1 - \tilde{\mathbf{r}}) \cdot \hat{\mathbf{v}}, \quad (5.7c)$$

$$w_0 = |(\mathbf{r}_1 - \tilde{\mathbf{r}}) \cdot \hat{\mathbf{w}}| = h. \quad (5.7d)$$

The analytical expression of the *vector line integrals* from Eq. (5.5) is given by

$$\mathbf{I}_k^{\text{line}}(\mathbf{r}^*) = \frac{L_k^{\text{vector}}}{k+2} \hat{\mathbf{v}} \quad (5.8)$$

for  $k = -3, -1, 0, 1, \dots, \ell - 1$ , with

$$L_{-3}^{\text{vector}} = \ln \left( \frac{u_2 + |\mathbf{r}_2 - \mathbf{r}^*|}{u_1 + |\mathbf{r}_1 - \mathbf{r}^*|} \right), \quad (5.9a)$$

$$L_0^{\text{vector}} = \frac{1}{2} |\mathbf{r}_2 - \mathbf{r}_1| \left( |\mathbf{r}_2 - \mathbf{r}^*|^2 + |\mathbf{r}_1 - \mathbf{r}^*|^2 - \frac{1}{3} |\mathbf{r}_2 - \mathbf{r}_1|^2 \right), \quad (5.9b)$$

$$L_k^{\text{vector}} = \frac{1}{k+3} \left( u_2 |\mathbf{r}_2 - \mathbf{r}^*|^{k+2} - u_1 |\mathbf{r}_1 - \mathbf{r}^*|^{k+2} \right) + \frac{k+2}{k+3} (v_{20} + h^2) L_{k-2}^{\text{vector}} \quad (5.9c)$$

for  $k = -1, 1, 2, 3, \dots, \ell - 1$ . The analytical expression of the *scalar line integrals* is given by

$$I_{-3}^{\text{line}}(\mathbf{r}^*) = \begin{cases} -\frac{1}{h} \left( \arctan \left( \frac{u_2}{v_0} \frac{h}{|\mathbf{r}_2 - \mathbf{r}^*|} \right) - \arctan \left( \frac{u_1}{v_0} \frac{h}{|\mathbf{r}_1 - \mathbf{r}^*|} \right) \right), & v_0 \neq 0 \text{ and } h \neq 0, \\ 0, & v_0 = 0 \text{ or } h = 0, \end{cases} \quad (5.10a)$$

$$I_0^{\text{line}}(\mathbf{r}^*) = \begin{cases} \frac{1}{2} h^2 \left( \arctan \left( \frac{u_2}{v_0} \right) - \arctan \left( \frac{u_1}{v_0} \right) \right) + \frac{1}{2} v_0 |\mathbf{r}_2 - \mathbf{r}_1|, & v_0 \neq 0, \\ 0, & v_0 = 0, \end{cases} \quad (5.10b)$$

$$I_k^{\text{line}}(\mathbf{r}^*) = \frac{v_0}{k+2} L_{k-2}^{\text{vector}} + \frac{k}{k+2} h^2 I_{k-2}^{\text{line}}(\mathbf{r}^*) \quad (5.10c)$$

for  $k = -1, 1, 2, 3, \dots, \ell - 1$ . Notice that the scalar line integrals are given by a recurrence relation (5.10c) which requires both an odd and even initial term, given by Eq. (5.10a) and (5.10b) for  $-3$  and  $0$ , resp.

### 5.3.4 Analytical expression for standard arc integrals

Let us consider an arbitrary arc that is part of the contour and denote its start and end point by  $\mathbf{r}_1$  and  $\mathbf{r}_2$ , resp. The analytical expression of the standard contour integrals (5.4) on an arc is given by

$$\mathbf{I}_k^{\text{arc}}(\mathbf{r}^*) = \frac{(\mathbf{r}_2 - \mathbf{r}_1) \times \hat{\mathbf{n}}}{k+2} |\mathbf{r}_1 - \mathbf{r}^*|^{k+2}, \quad (5.11a)$$

$$I_k^{\text{arc}}(\mathbf{r}^*) = \frac{\theta}{k+2} |\mathbf{r}_1 - \mathbf{r}^*|^{k+2} \quad (5.11b)$$

for  $k = -3, -1, 0, 1, \dots, \ell - 1$ , where  $\theta$  denotes the angle of the arc.

### 5.3.5 Analytical expression for standard pole integrals

The scalar standard contour integrals (5.5b) contain pole integrals, with the analytical expression given by

$$I_k^{\text{pole}}(\mathbf{r}^*) = -\varphi(\tilde{\mathbf{r}}) \frac{h^{k+2}}{k+2} \quad (5.12)$$

for  $k = -3, -1, 0, 1, \dots, \ell - 1$ , where  $\varphi$  denotes the circumscribed angle, given by

$$\varphi(\mathbf{r}) = \begin{cases} 2\pi, & \mathbf{r} \text{ inside triangle,} \\ \pi, & \mathbf{r} \text{ on edge,} \\ \alpha_i, & \mathbf{r} \text{ on vertex } i, \\ 0, & \mathbf{r} \text{ outside triangle} \end{cases} \quad (5.13)$$

where  $0 < \alpha_i < \pi$  denotes the inner angle of the two edges connecting to vertex  $i$ . Notice that the standard pole integrals (5.12) can be written as the recurrence relation

$$I_k^{\text{pole}}(\mathbf{r}^*) = \frac{k}{k+2} h^2 I_{k-2}^{\text{pole}}(\mathbf{r}^*) \quad (5.14)$$

for  $k = -1, 1, 2, 3, \dots, \ell - 1$ .

### 5.3.6 Zero projection height

When the projection height  $h$  is zero, the integrals  $I_{-3}^{\text{line}}$  and  $I_{-3}^{\text{pole}}$  are not correctly defined because of a division by  $h$ . Notice that these integrals are only present in the MFIE as the term  $(\tilde{\mathbf{r}} - \mathbf{r}^*) I_{-3}$  [84]. Because  $(\tilde{\mathbf{r}} - \mathbf{r}^*) = \pm h \hat{\mathbf{n}}$ , one can instead compute  $h I_{-3}$ , which is properly defined for zero projection height.

## 5.4 Finite precision arithmetic

In this section, a thorough analysis of the consequences of analytic evaluation of the contour integrals (5.4) in finite precision arithmetic will be derived. It will be shown that the analytical expressions of the radiation fields suffer from singular behavior when the projection of the observation point approaches the boundary of the source element. A straightforward evaluation in finite precision arithmetic will be given.

### 5.4.1 Straightforward formulation

The formulation of the analytical expressions of the radiation fields in finite precision arithmetic can best be explained for the standard pole integrals (5.12), that depend on the circumscribed angle (5.13). The piecewise definition of the circumscribed angle necessitates computing the location of the projection point w.r.t. the triangular facet. For instance, one has to check if the projection point  $\tilde{\mathbf{r}}$  coincides with a vertex  $\mathbf{v}_i$ . Due to rounding errors, the check  $|\tilde{\mathbf{r}} - \mathbf{v}_i| = 0$  is not meaningful in finite precision arithmetic. Instead, one has to use  $\|\mathbf{r} - \mathbf{v}_i\| < \epsilon$  for  $\epsilon > 0$  small compared to a characteristic length scale of the surface mesh elements. If the projection point is located in the *tolerance region*  $\{\mathbf{r} \in \mathbb{R}^3, \|\mathbf{r} - \mathbf{v}_i\| < \epsilon\}$  around the vertex, then they will be considered as if they coincide. Hence, the standard pole integrals read

$$\hat{I}_k^{\text{pole}}(\mathbf{r}^*) = -\hat{\varphi}(\tilde{\mathbf{r}}) \frac{h^{k+2}}{k+2}, \quad (5.15a)$$

$$\hat{\varphi}(\mathbf{r}) = \begin{cases} 2\pi, & \mathbf{r} \text{ inside triangle and outside tol. regions,} \\ \pi, & \mathbf{r} \text{ inside edge tolerance regions,} \\ \alpha_i, & \mathbf{r} \text{ inside tolerance region of vertex } i, \\ 0, & \mathbf{r} \text{ outside triangle and tolerance regions} \end{cases} \quad (5.15b)$$

for finite precision arithmetic. The full definition of the different tolerance regions will be given in Section 5.6.

Similarly, the scalar line integrals (5.10) are piecewise defined for  $v_0 = 0$  and  $v_0 \neq 0$ . Geometrically, this corresponds to projection on or outside an edge, resp. For finite precision arithmetic, a tolerance region around the edge will be necessary and the scalar line integrals are extended to

$$\hat{I}_k^{\text{line}}(\mathbf{r}^*) = \begin{cases} \frac{v_0}{k+2} L_{k-2}^{\text{vector}} + \frac{k}{k+2} h^2 \hat{I}_{k-2}^{\text{line}}(\mathbf{r}^*), & \tilde{\mathbf{r}} \text{ outside tol. region,} \\ 0, & \tilde{\mathbf{r}} \text{ inside tolerance region} \end{cases} \quad (5.16)$$

for  $k = -1, 1, 2, 3, \dots, \ell - 1$ , where the initial values  $\hat{I}_{-3}^{\text{line}}$  and  $\hat{I}_0^{\text{line}}$  are given by Eq. (5.10). The analytical expression of a standard contour integral and its extended expression for finite precision arithmetic are depicted in Fig. 5.4 and 5.5. For presentation, an extremely large tolerance region has been used.

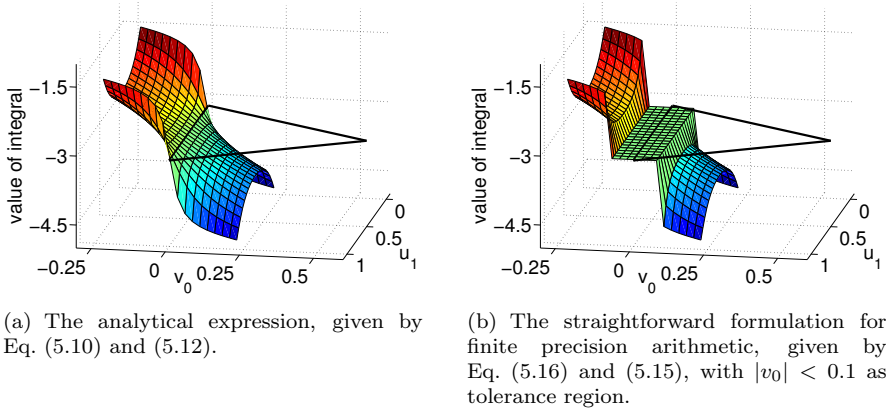


Figure 5.4: The value of  $I_0^{\text{line}} + I_0^{\text{pole}}$  w.r.t. projection points  $\tilde{\mathbf{r}}$  close to an edge. Horizontal axes denote the local coordinates  $(\hat{\mathbf{u}}, \hat{\mathbf{v}})$  from Eq. (5.6). The vertical axis and colors in the surface plot depict the value of the integral. The shape of the source triangle is depicted by the black lines.

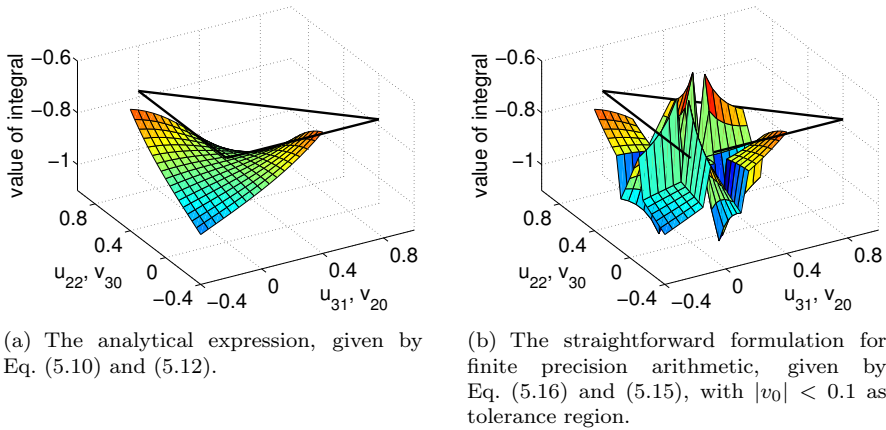


Figure 5.5: The value of  $I_0^{\text{line},2} + I_0^{\text{line},3} + I_0^{\text{pole}}$  w.r.t. projection points  $\tilde{\mathbf{r}}$  close to vertex 1. Horizontal axes denote the local coordinates  $(\hat{\mathbf{u}}, \hat{\mathbf{v}})$  from Eq. (5.6). The vertical axis and colors in the surface plot depict the value of the integral. The shape of the source triangle is depicted by the black lines.

Fig. 5.4 depicts the case where the projection point is located close to an edge. A constant approximation has been used inside the edge tolerance region, which results in a discontinuity at the boundary of the tolerance region.



When the observer point is projected close to a vertex, both a vertex tolerance region and an edge tolerance region for the adjacent edges are necessary. As depicted in Fig. 5.5, numerical errors are present in the straightforward formulation whereas the analytical expression of the contour integral is smooth. It will be shown in Section 5.5 that different terms in the analytical expression cancel out on the edges of the triangular facets. Because of the constant approximations inside the tolerance regions, this cancellation is not effective anymore, which causes inaccurate expressions for the standard contour integrals.

### 5.4.2 Requirements on robust formulations

In Section 5.4.1, an extended version of the analytical expressions of radiation fields has been introduced, which is necessary for finite precision arithmetic. This straightforward formulation results in discontinuous and inaccurate expressions for the standard contour integrals. Although these inaccuracies might be small for each radiation field, they could accumulate into inaccurate discretization matrix elements and ultimately in an unstable MoT scheme, as will be experimentally confirmed in Section 5.7.

Now, we aim to derive a robust formulation for the quasi-exact integration method which eliminates this specific cause of instability. To this end, all analytical expressions of radiation fields have to be *well behaved*, which we will define as *accurate* and *nonsingular*.

The accuracy is defined as the difference between the formulation for finite precision arithmetic and the analytical expression of the standard contour integrals. Outside the tolerance regions, the analytical expressions from Section 5.3 are used, which introduce no errors, apart from rounding errors. However, an approximation will be used inside the tolerance regions. In the straightforward formulation, a constant approximation has been used. In the next section, a robust formulation will be derived that is highly accurate. In fact, for most cases the novel formulation will be equivalent to the analytical expression.

The main reason for the necessity of tolerance regions is the singular dependence of the analytical expressions on the location of the observer point. In particular, the exact formulation contains a division by a parameter that becomes arbitrarily small when the observer point approaches the edge of a triangular patch. Although these singularities are properly defined for exact arithmetic, for finite precision arithmetic these singularities might cause excessive rounding errors. To this end, a division by a parameter in the robust formulation is only allowed when the absolute value of the parameter has a strictly positive lower bound.

## 5.5 Robust formulation of analytical expressions

In Section 5.4.1 a straightforward formulation has been introduced for the analytical expressions of the radiation fields when finite precision arithmetic is used. Because this straightforward formulation contains expressions that are not well behaved, a robust formulation will be derived in this section.

It can be shown that the scalar line (5.10) and pole integrals (5.12) are the only parts of the standard contour integrals (5.5) that are not well behaved, according to the requirements in Section 5.4.2. The deficiencies occur near the boundary of each triangular element and the novel expressions will therefore be used inside the tolerance regions only. Due to cancellation of some terms in their respective analytical expressions, one can only achieve well-behaved expressions when the sum of the contribution of the scalar line and pole integrals is considered, as opposed to considering these separately.

The expressions in the robust formulation are well behaved, even for finite precision arithmetic. That is, the radiation fields are represented very accurate and the singular behavior of the original formulation is completely eliminated.

### 5.5.1 Robust formulation near an edge

First, a robust formulation will be derived for projection points close to an edge of the source triangle, but sufficiently far away from the vertices. The scalar line integrals (5.10) contain terms in the form of  $\arctan(C/v_0)$  with a constant  $C > 0$ . The parameter  $v_0$ , given by Eq. (5.7c), represents the distance from the projection point to the edge and can therefore become arbitrary small. However, the limit

$$\lim_{v_0 \rightarrow 0} \arctan\left(\frac{C}{v_0}\right) = \begin{cases} \frac{\pi}{2}, & v_0 > 0, \\ -\frac{\pi}{2}, & v_0 < 0 \end{cases} \quad (5.17)$$

converges, where  $v_0 > 0$  and  $v_0 < 0$  correspond to a projection point inside or outside the source triangle, resp. This singularity can be rewritten with the calculus identity

$$\arctan\left(\frac{x}{y}\right) = \begin{cases} \frac{\pi}{2} - \arctan\left(\frac{y}{x}\right), & xy > 0, \\ -\frac{\pi}{2} - \arctan\left(\frac{y}{x}\right), & xy < 0 \end{cases} \quad (5.18)$$

for arbitrary nonzero  $x$  and  $y$ .

Because the scalar line and pole integrals satisfy the recurrence relations (5.10c) and (5.14), it suffices to rewrite the scalar line and pole integrals for  $k = -3$  and  $k = 0$  only. With the use of Eq. (5.18), the sum of the scalar



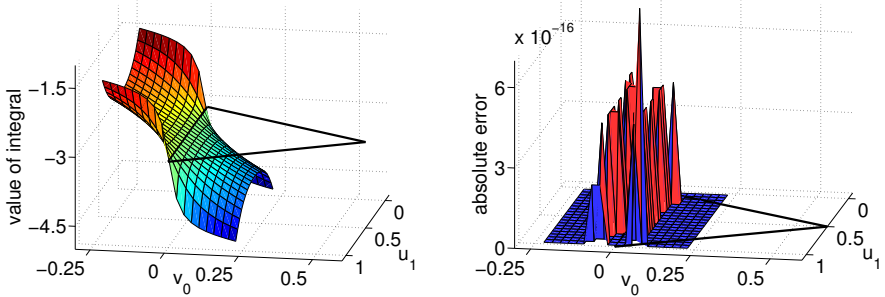
line and pole integrals can be rewritten as

$$\begin{aligned}
 & -h \left( I_{-3}^{\text{line}}(\mathbf{r}^*) + I_{-3}^{\text{pole}}(\mathbf{r}^*) \right) \\
 &= \begin{cases} \arctan\left(\frac{u_2}{v_0} \frac{h}{|\mathbf{r}_2 - \mathbf{r}^*|}\right) \\ - \arctan\left(\frac{u_1}{v_0} \frac{h}{|\mathbf{r}_1 - \mathbf{r}^*|}\right) - 2\pi, & v_0 > 0, \\ 0 - \pi, & v_0 = 0, \\ \arctan\left(\frac{u_2}{v_0} \frac{h}{|\mathbf{r}_2 - \mathbf{r}^*|}\right) \\ - \arctan\left(\frac{u_1}{v_0} \frac{h}{|\mathbf{r}_1 - \mathbf{r}^*|}\right) - 0, & v_0 < 0 \end{cases} \\
 &= \begin{cases} \frac{\pi}{2} - \arctan\left(\frac{v_0}{u_2} \frac{|\mathbf{r}_2 - \mathbf{r}^*|}{h}\right) \\ + \frac{\pi}{2} + \arctan\left(\frac{v_0}{u_1} \frac{|\mathbf{r}_1 - \mathbf{r}^*|}{h}\right) - 2\pi, & v_0 > 0, \\ -\pi, & v_0 = 0, \\ \frac{\pi}{2} - \arctan\left(\frac{v_0}{u_2} \frac{|\mathbf{r}_2 - \mathbf{r}^*|}{h}\right) \\ + \frac{\pi}{2} + \arctan\left(\frac{v_0}{u_1} \frac{|\mathbf{r}_1 - \mathbf{r}^*|}{h}\right), & v_0 < 0 \end{cases} \\
 &= \arctan\left(\frac{v_0}{u_1} \frac{|\mathbf{r}_1 - \mathbf{r}^*|}{h}\right) - \arctan\left(\frac{v_0}{u_2} \frac{|\mathbf{r}_2 - \mathbf{r}^*|}{h}\right) - \pi, \quad (5.19a)
 \end{aligned}$$

$$\begin{aligned}
 & \frac{2}{h^2} \left( I_0^{\text{line}}(\mathbf{r}^*) + I_0^{\text{pole}}(\mathbf{r}^*) \right) \\
 &= \begin{cases} v_0 \frac{|\mathbf{r}_2 - \mathbf{r}_1|}{h^2} + \arctan\left(\frac{u_2}{v_0}\right) \\ - \arctan\left(\frac{u_1}{v_0}\right) - 2\pi, & v_0 > 0, \\ 0 - \pi, & v_0 = 0, \\ v_0 \frac{|\mathbf{r}_2 - \mathbf{r}_1|}{h^2} + \arctan\left(\frac{u_2}{v_0}\right) \\ - \arctan\left(\frac{u_1}{v_0}\right) - 0, & v_0 < 0 \end{cases} \\
 &= \begin{cases} v_0 \frac{|\mathbf{r}_2 - \mathbf{r}_1|}{h^2} + \frac{\pi}{2} - \arctan\left(\frac{v_0}{u_2}\right) \\ + \frac{\pi}{2} + \arctan\left(\frac{v_0}{u_1}\right) - 2\pi, & v_0 > 0, \\ -\pi, & v_0 = 0, \\ v_0 \frac{|\mathbf{r}_2 - \mathbf{r}_1|}{h^2} + \frac{\pi}{2} - \arctan\left(\frac{v_0}{u_2}\right) \\ + \frac{\pi}{2} + \arctan\left(\frac{v_0}{u_1}\right), & v_0 < 0 \end{cases} \\
 &= v_0 \frac{|\mathbf{r}_2 - \mathbf{r}_1|}{h^2} + \arctan\left(\frac{v_0}{u_1}\right) - \arctan\left(\frac{v_0}{u_2}\right) - \pi. \quad (5.19b)
 \end{aligned}$$

This novel formulation is depicted in Fig. 5.6. Because an exact reformulation has been derived, no errors are introduced except of rounding errors. This is in contrast to the straightforward formulation, as can be clearly seen with a

comparison with Fig. 5.4(b), where the same tolerance region has been used.



(a) The robust formulation, given by Eq. (5.19), with edge tolerance region  $|v_0| < 0.1$ .

(b) The absolute difference between the robust formulation and analytical expression.

Figure 5.6: The value of  $I_0^{\text{line}} + I_0^{\text{pole}}$  w.r.t. projection points  $\tilde{\mathbf{r}}$  close to an edge. Horizontal axes denote the local coordinates  $(\hat{\mathbf{u}}, \hat{\mathbf{v}})$  from Eq. (5.6). The vertical axis and colors in the surface plot depict the value of the integral. The shape of the source triangle is depicted by the black lines.

Important to notice is that because of the use of identity (5.18) the singularities are shifted from small  $v_0$  to small  $u_1$  and  $u_2$ . Geometrically, the singularity has been replaced from the edge to the vertices. Therefore, vertices have to be excluded from the edge tolerance regions. This will be a requirement for the definition of the tolerance regions, see Section 5.6.

### 5.5.2 Robust formulation near the extension of an edge

The singularity for small  $v_0$  in the scalar line integrals (5.10) occurs not only for projection near an edge, also for projection near the extension of an edge. Therefore, a novel formulation has to be derived for projection points close to the rays that extend the edges. This *ray tolerance region* is depicted in yellow in Fig. 5.10. Because the ray tolerance region is always outside the source triangle, the standard pole integrals (5.12) are zero and only the scalar line integrals have to be rewritten. Similar to Eq. (5.19), the scalar line integrals can be expressed as

$$I_{-3}^{\text{line}}(\mathbf{r}^*) = \frac{1}{h} \arctan\left(\frac{v_0}{u_2} \frac{|\mathbf{r}_2 - \mathbf{r}^*|}{h}\right) - \frac{1}{h} \arctan\left(\frac{v_0}{u_1} \frac{|\mathbf{r}_1 - \mathbf{r}^*|}{h}\right), \quad (5.20a)$$

$$I_0^{\text{line}}(\mathbf{r}^*) = \frac{v_0}{2} |\mathbf{r}_2 - \mathbf{r}_1| + \frac{h^2}{2} \left( \arctan\left(\frac{v_0}{u_1}\right) - \arctan\left(\frac{v_0}{u_2}\right) \right) \quad (5.20b)$$

inside the ray tolerance regions.



### 5.5.3 Robust formulation near a vertex

For projection near a vertex, three parts of the standard contour integrals (5.5) have to be rewritten to enable a robust formulation. These are the scalar line integrals (5.10) on the two adjacent edges and the standard pole integrals (5.12). To this end, let us consider a projection point  $\tilde{\mathbf{r}}$  close to vertex 1, with edges 2 and 3 adjacent, as depicted in Fig. 5.7. The line integrals run from  $\mathbf{r}_2$  to  $\mathbf{v}_1$  and from  $\mathbf{v}_1$  to  $\mathbf{r}_3$  over edge 2 and 3, resp. Two sets of local coordinates (5.6) and parameters (5.7) have to be used, namely  $(\hat{\mathbf{u}}_2, \hat{\mathbf{v}}_2, \hat{\mathbf{w}}_2), (u_{21}, u_{22}, v_{20}, w_0)$  for edge 2 and  $(\hat{\mathbf{u}}_3, \hat{\mathbf{v}}_3, \hat{\mathbf{w}}_3), (u_{31}, u_{32}, v_{30}, w_0)$  for edge 3.

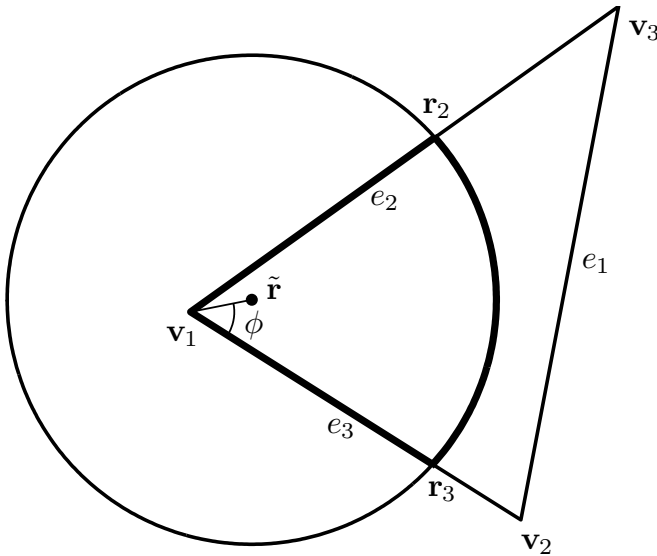


Figure 5.7: An arbitrary projection point  $\tilde{\mathbf{r}}$  and triangle with vertices  $(\mathbf{v}_1, \mathbf{v}_2, \mathbf{v}_3)$  and edges  $(e_1, e_2, e_3)$ . The contour is given by two line segments and one arc passing through points  $(\mathbf{r}_2, \mathbf{v}_1, \mathbf{r}_3)$ . The angle of the projection point w.r.t. vertex 1 is denoted by  $\phi$ .

If the projection point is located on vertex 1, all parameters  $u_{22}$ ,  $u_{31}$ ,  $v_{20}$ , and  $v_{30}$  are zero. The parameters  $u_{21} < 0$  and  $u_{32} > 0$  have a lower bound, which allows for the use of

$$\arctan\left(\frac{u_{21}}{v_{20}}\right) = -\frac{\pi}{2} - \arctan\left(\frac{v_{20}}{u_{21}}\right), \quad (5.21a)$$

$$\arctan\left(\frac{u_{32}}{v_{30}}\right) = \frac{\pi}{2} - \arctan\left(\frac{v_{30}}{u_{32}}\right), \quad (5.21b)$$

equivalent to calculus identity (5.18). By geometrical identities,

$$\arctan\left(\frac{u_{22}}{v_{20}}\right) = \begin{cases} \phi - \alpha_1 - \frac{\pi}{2}, & -\pi < \alpha_1 - \phi < 0, \\ \phi - \alpha_1 + \frac{\pi}{2}, & 0 < \alpha_1 - \phi < \pi, \end{cases} \quad (5.22a)$$

$$\arctan\left(\frac{u_{31}}{v_{30}}\right) = \begin{cases} \phi + \frac{\pi}{2}, & -\pi < \phi < 0, \\ \phi - \frac{\pi}{2}, & 0 < \phi < \pi \end{cases} \quad (5.22b)$$

where  $\alpha_1$  denotes the angle of vertex 1 and  $\phi$  the angle from edge 3 to the projection point, as depicted in Fig. 5.7. The identities (5.21) and (5.22) are sufficient to derive a well-behaved expression for the standard contour integral  $I_0$ . Notice that in the derivation, given by Eq. (5.24b), only three location cases of the projection point w.r.t. the vertex have been given, whereas the derivation for the other cases is similar.

The standard contour integral  $I_{-3}$  cannot be rewritten exactly into a well-behaved expression, because the geometrical identities (5.22) are not valid. Instead, one can combine it with the approximations

$$\arctan\left(\frac{u_{22}}{v_{20}} \frac{h}{|\mathbf{v}_1 - \mathbf{r}^*|}\right) = \arctan\left(\frac{u_{22}}{v_{20}}\right) + \mathcal{O}(|v_{20}|^2), \quad (5.23a)$$

$$\arctan\left(\frac{u_{31}}{v_{30}} \frac{h}{|\mathbf{v}_1 - \mathbf{r}^*|}\right) = \arctan\left(\frac{u_{31}}{v_{30}}\right) + \mathcal{O}(|v_{30}|^2) \quad (5.23b)$$

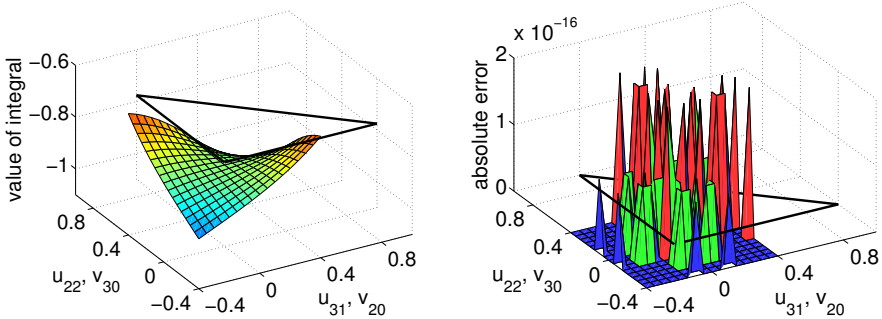
that have been derived with a Taylor series. Notice that when  $|v_0| < \epsilon$  holds inside the tolerance region, the truncation error is  $\mathcal{O}(\epsilon^2)$ . The derivation of  $I_{-3}$  is given in Eq. (5.24a). Remember that for larger  $k$  the recurrence relations (5.10c) and (5.14) can be used.

$$\begin{aligned} & -h \left( I_{-3}^{\text{line},2} + I_{-3}^{\text{line},3} + I_{-3}^{\text{pole}} \right) \\ &= \begin{cases} \arctan\left(\frac{u_{22}}{v_{20}} \frac{h}{|\mathbf{v}_1 - \mathbf{r}^*|}\right) - \arctan\left(\frac{u_{21}}{v_{20}} \frac{h}{|\mathbf{r}_2 - \mathbf{r}^*|}\right) \\ \quad + \arctan\left(\frac{u_{32}}{v_{30}} \frac{h}{|\mathbf{r}_3 - \mathbf{r}^*|}\right) - \arctan\left(\frac{u_{31}}{v_{30}} \frac{h}{|\mathbf{v}_1 - \mathbf{r}^*|}\right) - 2\pi, & \text{inside triangle,} \\ \arctan\left(\frac{u_{22}}{v_{20}} \frac{h}{|\mathbf{v}_1 - \mathbf{r}^*|}\right) - \arctan\left(\frac{u_{21}}{v_{20}} \frac{h}{|\mathbf{r}_2 - \mathbf{r}^*|}\right) - \pi, & \text{on edge 3,} \\ -\alpha_1, & \text{on vertex 1} \end{cases} \\ &\approx \begin{cases} \left( \phi - \alpha_1 + \frac{\pi}{2} \right) + \left( \frac{\pi}{2} + \arctan\left(\frac{v_{20}}{u_{21}} \frac{|\mathbf{r}_2 - \mathbf{r}^*|}{h}\right) \right) \\ \quad + \left( \frac{\pi}{2} - \arctan\left(\frac{v_{30}}{u_{32}} \frac{|\mathbf{r}_3 - \mathbf{r}^*|}{h}\right) \right) - \left( \phi - \frac{\pi}{2} \right) - 2\pi, & \text{inside triangle,} \\ \left( \phi - \alpha_1 + \frac{\pi}{2} \right) + \left( \frac{\pi}{2} + \arctan\left(\frac{v_{20}}{u_{21}} \frac{|\mathbf{r}_2 - \mathbf{r}^*|}{h}\right) \right) - \pi, & \text{on edge 3,} \\ -\alpha_1, & \text{on vertex 1} \end{cases} \\ &= \arctan\left(\frac{v_{20}}{u_{21}} \frac{|\mathbf{r}_2 - \mathbf{r}^*|}{h}\right) - \arctan\left(\frac{v_{30}}{u_{32}} \frac{|\mathbf{r}_3 - \mathbf{r}^*|}{h}\right) - \alpha_1, \quad (5.24a) \end{aligned}$$

~~~~~

$$\begin{aligned}
& \frac{2}{h^2} \left( I_0^{\text{line},2} + I_0^{\text{line},3} + I_0^{\text{pole}} \right) \\
&= \begin{cases} v_{20} \frac{|\mathbf{v}_1 - \mathbf{r}_2|}{h^2} + \arctan\left(\frac{u_{22}}{v_{20}}\right) - \arctan\left(\frac{u_{21}}{v_{20}}\right) \\ \quad + v_{30} \frac{|\mathbf{r}_3 - \mathbf{v}_1|}{h^2} + \arctan\left(\frac{u_{32}}{v_{30}}\right) - \arctan\left(\frac{u_{31}}{v_{30}}\right) - 2\pi, & \text{inside triangle,} \\ v_{20} \frac{|\mathbf{v}_1 - \mathbf{r}_2|}{h^2} + \arctan\left(\frac{u_{22}}{v_{20}}\right) - \arctan\left(\frac{u_{21}}{v_{20}}\right) - \pi, & \text{on edge 3,} \\ -\alpha_1, & \text{on vertex 1} \end{cases} \\
&= \begin{cases} v_{20} \frac{|\mathbf{v}_1 - \mathbf{r}_2|}{h^2} + \left(\phi - \alpha_1 + \frac{\pi}{2}\right) + \left(\frac{\pi}{2} + \arctan\left(\frac{v_{20}}{u_{21}}\right)\right) \\ \quad + v_{30} \frac{|\mathbf{r}_3 - \mathbf{v}_1|}{h^2} + \left(\frac{\pi}{2} - \arctan\left(\frac{v_{30}}{u_{32}}\right)\right) - \left(\phi - \frac{\pi}{2}\right) - 2\pi, & \text{in triangle,} \\ v_{20} \frac{|\mathbf{v}_1 - \mathbf{r}_2|}{h^2} + \left(0 - \alpha_1 + \frac{\pi}{2}\right) + \left(\frac{\pi}{2} + \arctan\left(\frac{v_{20}}{u_{21}}\right)\right) - \pi, & \text{on edge 3,} \\ -\alpha_1, & \text{on vertex 1} \end{cases} \\
&= v_{20} \frac{|\mathbf{v}_1 - \mathbf{r}_2|}{h^2} + v_{30} \frac{|\mathbf{r}_3 - \mathbf{v}_1|}{h^2} + \arctan\left(\frac{v_{20}}{u_{21}}\right) - \arctan\left(\frac{v_{30}}{u_{32}}\right) - \alpha_1.
\end{aligned} \tag{5.24b}$$

The standard contour integral  $I_0$  computed with the robust formulation is depicted in Fig. 5.8(a). A comparison with the straightforward formulation, depicted in Fig. 5.5(b) with the same tolerance regions, shows that the robust formulation improves the accuracy tremendously. The error is approximately  $10^{-16}$ , as depicted in Fig. 5.8(b), which confirms the quadrature accuracy has been diminished up to rounding errors.



(a) The robust formulation, given by Eq. (5.24) and (5.19), with  $|v_0| < 0.1$  as tolerance region.

(b) The absolute difference between the robust formulation and analytical expression.

Figure 5.8: The value of  $I_0^{\text{line},2} + I_0^{\text{line},3} + I_0^{\text{pole}}$  w.r.t. projection points  $\tilde{\mathbf{r}}$  close to vertex 1. Horizontal axes denote the local coordinates  $(\hat{\mathbf{u}}, \hat{\mathbf{v}})$  from Eq. (5.6). The vertical axis and colors in the surface plot depict the value of the integral. The shape of the source triangle is depicted by the black lines.

Fig. 5.9(a) and 5.9(b) depict the standard contour integral  $I_{-3}$  for the straightforward and robust formulation, resp., for the same tolerance region. It is apparent that the accuracy of the robust formulation is very high compared to the straightforward formulation. At first sight, it looks as if no quadrature errors are present in the robust formulation. However, an error in the order of  $10^{-2}$  is present, see Fig. 5.9(c), which is larger than the rounding error. This quadrature error is due to the approximation (5.23) that has been used in the derivation of the robust formulation. Remember that for illustration purposes, the tolerance regions in these figures have been chosen extremely large. When applied to the MoT scheme, the tolerance regions will be orders of magnitude smaller and the approximation error will drop below machine precision. This has been verified experimentally, as depicted in Fig. 5.9(d). For large tolerance values, the approximation error convergences quadratically, as derived in Eq. (5.23). For tolerance values smaller than  $10^{-8}$ , the error remains  $10^{-16}$  because the rounding error dominates the truncation error.

#### 5.5.4 Summary of robust formulation

The robust formulation that has been derived in sections 5.5.1–5.5.3 has to be incorporated into the evaluation of the radiation fields. For a given observer point  $\tilde{\mathbf{r}}$  and source triangle  $\Gamma_q$ , different expressions for the standard contour integrals (5.5) have to be used. That is,

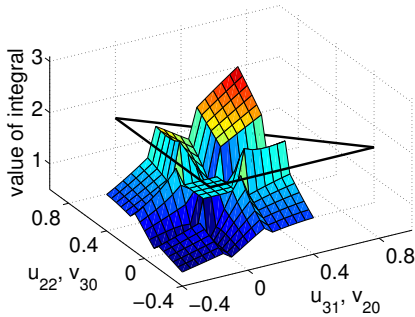
- Eq. (5.19) for  $\tilde{\mathbf{r}}$  inside edge tolerance regions,
- Eq. (5.20) for  $\tilde{\mathbf{r}}$  inside ray tolerance regions,
- Eq. (5.24) for  $\tilde{\mathbf{r}}$  inside vertex tolerance regions, and
- Eq. (5.10) and (5.12) for  $\tilde{\mathbf{r}}$  outside tolerance regions,

where the tolerance regions will be defined in Section 5.6. All expressions in this robust formulation are well behaved, because no singular behavior is present and the radiation fields are approximated with a very high accuracy. In fact, all expressions outside the vertex tolerance regions are exact, except of rounding errors. Inside the vertex tolerance regions, an approximation with quadratic convergence w.r.t. the size of the tolerance region has been used.

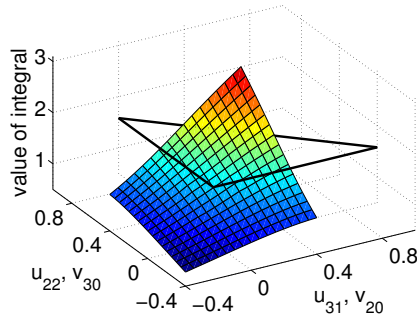
#### 5.5.5 Zero projection height

The robust formulation is used when the projection of the observer point is located close to the boundary of the source triangle. However, the derivation is not valid for zero projection height  $h$ . This combination of projection on the triangle boundary and a zero projection height can only happen when a

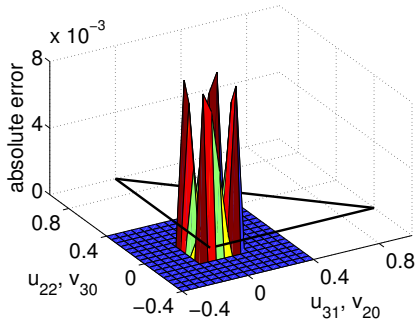




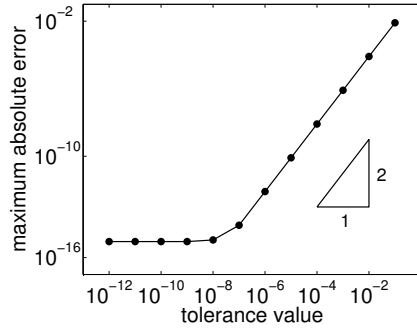
(a) The straightforward formulation, given by Eq. (5.16) and (5.15), with  $|v_0| < 0.1$  as tolerance region.



(b) The robust formulation, given by Eq. (5.24) and (5.19), with  $|v_0| < 0.1$  as tolerance region.



(c) The absolute difference between the robust formulation and analytical expression.



(d) The convergence of the error in the robust formulation w.r.t. the tolerance value.

Figure 5.9: The value of  $I_{-3}^{\text{line},2} + I_{-3}^{\text{line},3} + I_{-3}^{\text{pole}}$  w.r.t. projection points  $\tilde{\mathbf{r}}$  close to vertex 1. Horizontal axes denote the local coordinates  $(\hat{\mathbf{u}}, \hat{\mathbf{v}})$  from Eq. (5.6). The vertical axis and colors in the surface plot depict the value of the integral. The shape of the source triangle is depicted by the black lines.

quadrature point is located on the triangle boundary. This will never happen for the Gaussian quadrature rules [28]. In fact, the tolerance values are required to be smaller than the distance from each quadrature point to the triangle boundary, which is easily satisfied for most quadrature rules. Consequently, no additional formulations inside edge and vertex tolerance regions are necessary for zero projection height.

On the other hand, the projection height can be zero inside ray tolerance regions. Then, the robust formulation (5.20a) for odd indices is not valid anymore. Because a ‘zero divided by zero’ is present in the limit, the same trick can not be used. Instead, the limit value will be used in the ray tolerance

region, i.e.,  $I_k^{\text{line}} = 0$  for odd  $k$ . Additionally, for this limit case, the vector line integral (5.8) for odd  $k$  is not properly defined anymore, because a ‘logarithm of zero’ has to be computed. Again, the limit of the integral will be used in the ray tolerance region, i.e.,  $\mathbf{I}_{-3}^{\text{line}} = \text{sign}(u_1)(\log(u_1) - \log(u_2))$  and  $\mathbf{I}_k^{\text{line}} = \text{sign}(u_1)(u_2^{k+3} - u_1^{k+3})/((k+2)(k+3))$  for odd  $k > -3$ .

## 5.6 Tolerance regions

The tolerance regions are required for finite precision arithmetic, as explained in Section 5.4. In Section 5.5, accurate expressions for the standard contour integrals have been derived for use within the edge, ray and vertex tolerance regions. In this section, the full definition of the tolerance regions will be established for specific design criteria.

### 5.6.1 Requirements on tolerance regions

The tolerance regions will be defined according to the following requirements:

1. the shape is based on parameters  $u_1$ ,  $u_2$ , and  $v_0$  only;
2. regions are disjoint;
3. regions fully cover the triangle boundary; and
4. tolerance values are dimensionless.

The singularities present in the analytical expression of the radiation fields are related to the local parameters  $u_1$ ,  $u_2$ , or  $v_0$ , defined by Eq. (5.7). Only these parameter cause singularities at certain locations of the projection point, for which a robust formulation is necessary. Therefore, the tolerance regions will be based on the parameters  $u_1$ ,  $u_2$ , and  $v_0$  only. To this end, two different tolerance values will be used, one for tolerance regions based on  $u_1$  and  $u_2$  and the other for  $v_0$ , which will be denoted by  $\epsilon_{\text{vertex}}$  and  $\epsilon_{\text{edge}}$ , resp.

For the exact evaluation of radiation fields, the standard pole integrals have to be evaluated only once for each contour. In the robust formulation, the standard pole integrals are evaluated in each tolerance region. Therefore, the projection point has to be located in only one tolerance region and hence disjoint tolerance regions are required. Because singularities are present on the whole boundary of the source triangle, the tolerance regions should cover the full boundary.

Dimensionless tolerance values will be used because the robust formulation should be applicable to all surface meshes, independent of their length scale and local refinement. To this end, the tolerance values will depend on a characteristic length scale of the source triangle. Here, a factor  $\sqrt{A_q}$  will be used, where  $A_q$  denotes the area of source triangle  $\Gamma_q$ .



### 5.6.2 Definition of tolerance regions

The edge, ray, and vertex tolerance regions are denoted by  $\mathcal{E}_{\text{edge}}^i$ ,  $\mathcal{E}_{\text{ray}}^i$ , and  $\mathcal{E}_{\text{vertex}}^i$  for  $i = 1, 2, 3$ . They are defined by

$$\begin{aligned} \mathcal{E}_{\text{edge}}^1 = \{ \tilde{\mathbf{r}} \in \mathbb{R}^3 \mid & |v_{10}| < \tilde{\epsilon}_{\text{edge}} \\ & \wedge |v_{20}| \geq \tilde{\epsilon}_{\text{edge}} \wedge |v_{30}| \geq \tilde{\epsilon}_{\text{edge}} \\ & \wedge u_{11} \geq \tilde{\epsilon}_{\text{vertex}} \wedge -u_{12} \geq \tilde{\epsilon}_{\text{vertex}} \}, \end{aligned} \quad (5.25a)$$

$$\begin{aligned} \mathcal{E}_{\text{ray}}^1 = \{ \tilde{\mathbf{r}} \in \mathbb{R}^3 \mid & |v_{10}| < \tilde{\epsilon}_{\text{edge}} \wedge |v_{20}| \geq \tilde{\epsilon}_{\text{edge}} \wedge |v_{30}| \geq \tilde{\epsilon}_{\text{edge}} \\ & \wedge (-u_{11} \geq \tilde{\epsilon}_{\text{vertex}} \vee u_{12} \geq \tilde{\epsilon}_{\text{vertex}}) \}, \end{aligned} \quad (5.25b)$$

$$\begin{aligned} \mathcal{E}_{\text{vertex}}^1 = \{ \tilde{\mathbf{r}} \in \mathbb{R}^3 \mid & (|u_{22}| < \tilde{\epsilon}_{\text{vertex}} \wedge |v_{20}| < \tilde{\epsilon}_{\text{edge}}) \\ & \vee (|u_{31}| < \tilde{\epsilon}_{\text{vertex}} \wedge |v_{30}| < \tilde{\epsilon}_{\text{edge}}) \\ & \vee (|v_{20}| < \tilde{\epsilon}_{\text{edge}} \wedge |v_{30}| < \tilde{\epsilon}_{\text{edge}}) \} \end{aligned} \quad (5.25c)$$

and similar for  $i = 2, 3$ , where  $\tilde{\epsilon}_{\text{edge}} = \epsilon_{\text{edge}} \sqrt{A_q}$  and  $\tilde{\epsilon}_{\text{vertex}} = \epsilon_{\text{vertex}} \sqrt{A_q}$ . Clearly, the tolerance regions are based on the parameters  $u_1$ ,  $u_2$ , and  $v_0$  only and the tolerance values are dimensionless. As can be derived, the tolerance regions are disjoint and cover the full boundary of the triangle. This can be seen in Fig. 5.10 where the tolerance regions are depicted. Thus, all requirements on the tolerance regions are satisfied.

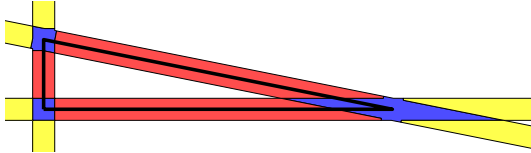


Figure 5.10: The tolerance regions with  $\epsilon_{\text{edge}} = 0.1$ ,  $\epsilon_{\text{vertex}} = 0.1$  for a triangle given by vertices  $([0, 0], [2, 0], [0, 0.4])$  and  $\sqrt{A} = 0.63$ . The vertex tolerance regions are depicted in blue, the edge tolerance regions in red, and the ray tolerance regions in yellow.

A striking feature of this definition is the vertex tolerance region, which is not a circle as one might expect. There are two reasons for the parallelogram shape. First, in order to establish disjoint tolerance regions, the intersection of two edge tolerance regions is considered as a vertex tolerance region. Second, the robust formulation in the edge tolerance regions dictates that the parameters  $u_1$  and  $u_2$  have a strictly positive lower bound. When circles, defined by  $\sqrt{(u_1)^2 + (v_0)^2} < \epsilon_{\text{circle}} \sqrt{A_q}$ , are used, the parameter  $u_1$  might become arbitrary small when  $v_0 \approx \epsilon_{\text{circle}} \sqrt{A_q}$  in edge tolerance regions.

## 5.7 Experimental confirmation

Two versions for the analytical computation of radiation fields in finite precision arithmetic have been derived in Section 5.4 and 5.5, namely a straightforward and a robust formulation, resp. The straightforward formulation can be considered as a standard and correct choice to enable finite precision arithmetic and serves its purpose in most cases. The robust formulation on the other hand is more sophisticated and uses well-behaved expressions for the radiation fields. It should be stressed that the two formulations only differ within the tolerance regions. Since tolerance values are very small, hardly any projection points are located inside the tolerance regions for small-scale objects. Therefore, the MoT solutions hardly differ for the two formulations. However, when the TDIE method will be applied for larger geometries, more mesh nodes are required and the likelihood that projection points are located inside the tolerance regions is increased.

Computational methods, like the TDIE method, have to be robust in order to be applied in industry. Using an example we will show that the accuracy of the evaluation of the radiation fields strongly influences the robustness of the algorithm. To this end, a configuration has been generated such that the impact of the tolerance regions is large, but without resorting to uncarefully chosen parameters. This configuration must include many observer points that are projected inside tolerance regions. Then, many radiation fields are computed different for the two exact formulations and differences in the MoT solutions are expected.

The object is given by a toroidal box of size  $1 \times 1 \times 0.1$  m, modeled with a surface mesh of 628 triangular facets, locally refined near the vertical edges of the box. As depicted in Fig. 5.11, all vertical edges of the box are artificially shifted  $10^{-10}$  m to create a challenging test case. Notice that this shift of mesh nodes is within the accuracy of almost all mesh generating programs. Because of the shift of the vertical edges of the box, all observer points on the adjacent face of the box are projected inside tolerance regions. The tolerance values are set as  $\epsilon_{\text{edge}} = 10^{-8}$  and  $\epsilon_{\text{vertex}} = 10^{-8}$ .

The EFIE (2.15) has been discretized with RWG test and basis functions in space and quadratic spline basis functions in time [108]. The outer integral over observer elements is evaluated with a 7-point Gaussian quadrature. The incident field is given by a Gaussian plane wave (2.35) with unit strength, pulse width 4 m, offset 6 lm, and polarization and propagation in the  $\hat{\mathbf{x}}$  and  $-\hat{\mathbf{z}}$  direction.

The magnitude of the electric surface current density is depicted in Fig. 5.12 for 1600 timesteps. Initially, no differences are visible between the two formulations. At late time, however, the straightforward formulation with constant approximation results in a surface current that grows beyond any bound. The novel robust formulation on the other hand remains stable. This difference in



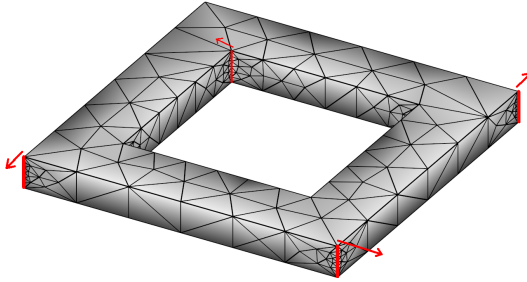


Figure 5.11: The surface mesh on the toroidal box of size  $1 \times 1 \times 0.1$  m, with the arrows depicting the  $10^{-10}$  m shift of the edges.

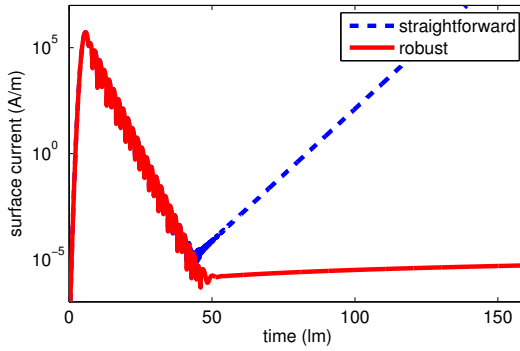


Figure 5.12: The magnitude of the electric surface current density at the point  $(0.967, 0.749, 0.1)$  on the toroidal box, with two different formulations for analytical expressions of the radiation fields.

stability has also been verified with a spectral analysis, depicted in Fig. 5.13. The MoT scheme is stable if the spectral radius  $\rho$  of the amplification matrix is smaller than one [3]. For this test case,  $\rho = 1.029$  and  $\rho = 1.0$  for the straightforward and robust formulation, resp.

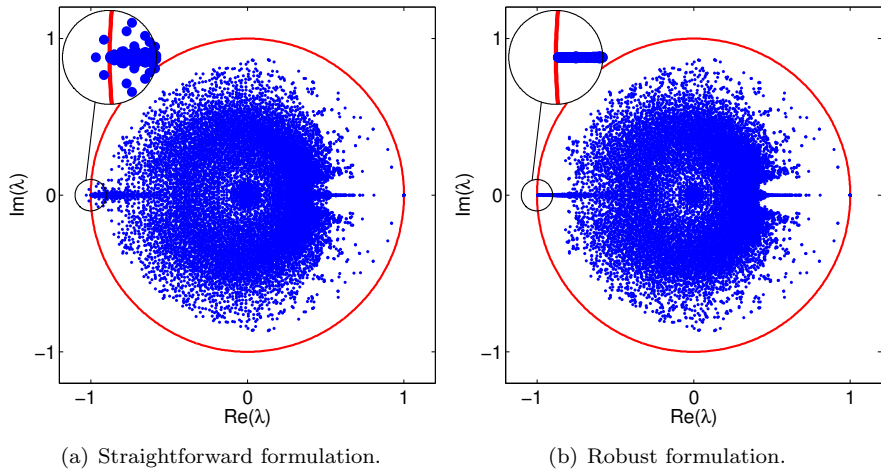


Figure 5.13: The eigenvalues (blue markers) of the MoT scheme on the toroidal box and the unit circle (red line) in the complex plane. The zoom box depicts the eigenvalues that determine stability.



# Chapter 6

## Application

### 6.1 Verification

In order to check our implementation of the TDIE method, a verification result will be presented in this section. In particular, the radar cross-section of a generic aircraft will be compared with a simulation from frequency-domain CEM.

The algorithm for the TDIE method that has been presented in this thesis has been implemented in the `Fortran90` programming language and compiled with the `Intel Fortran` compiler. Use has been made of `MKL` routines for the multiplication of interaction matrices and retarded solution vectors and the computation and solution of the LU-decomposition of the leading interaction matrix. Parallelization on shared-memory computer architecture has been performed with `OpenMP`. Simulations has been performed on a computer with two Intel Xeon E5-2650 8-core processors and 160 GB memory. Both `Matlab` and `TecPlot` have been used for postprocessing and visualization.

#### 6.1.1 The test case of a generic aircraft

Before presenting the computational results, let us first specify a scatterer that will be used throughout this chapter. A generic aircraft with a length of 60 m has been generated, as depicted in Fig. 6.1. The surface mesh consists of 6756 edges with a maximum edge length of 1.66 m and a minimum length of 3.74 cm. The ratio of 44 between smallest and largest edge originates from the mesh refinement for geometrical details. Local mesh refinement is commonly used in industry and the computational method should be able to handle this effectively. The TDIE method is effective for nonuniform meshes because no CFL condition is present. In order to capture the electromagnetic



wave field accurately, the minimum wavelength has to be larger than the diameter of the largest surface patch. For this surface mesh, the minimum wavelength is approximately 6 m. This yields an electrical size of  $10 \lambda$  of the generic aircraft and a maximum frequency of 50 MHz.

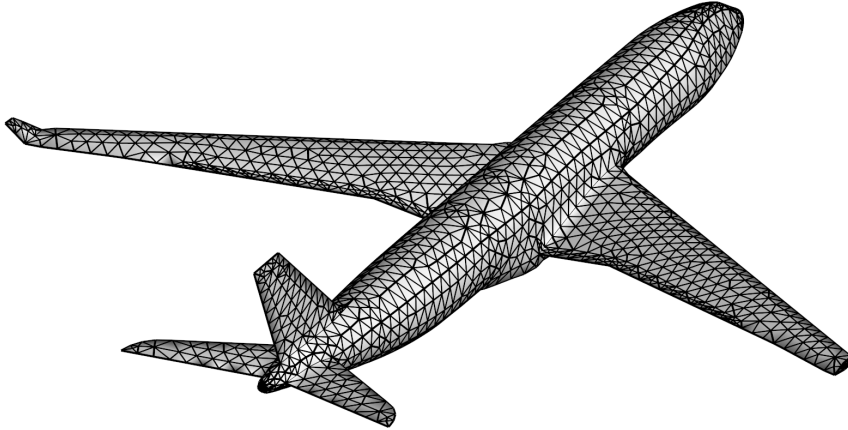


Figure 6.1: Surface mesh of a generic aircraft.

### 6.1.2 Comparison with the method of moments

The frequency-domain Method-of-Moments (MoM) is a broadly used computational method for the simulation of the radar visibility of aircraft [17]. The radar signature is often characterized by its radar cross-section (RCS), defined as

$$\sigma = \lim_{R \rightarrow \infty} 4\pi R^2 \frac{\|\mathbf{E}^s(R)\|^2}{\|\mathbf{E}^i\|^2} \quad (6.1)$$

where  $\mathbf{E}^s(R)$  denotes the scattered far field at distance  $R$  from the origin of the coordinate system. Usually, the RCS is measured for a specific angle of observation, given by an azimuth and altitude, and a specific angle of incidence, given by the propagation direction of the excitation. Often, the decibel scale  $10 \log_{10}(\sigma)$  is used.

In frequency-domain CEM, the scattered far field is commonly measured with the Euclidean norm, that is  $\|\mathbf{E}^s\| = |\mathbf{E}^s|$  the magnitude of the electric field. For time-domain methods, a space-time norm has to be used. However, because the goal is to compare the TDIE method with the MoM, the Euclidean norm of the Fourier transformed field will be used, i.e.,

$$\|\mathbf{E}^s\| = \left| \widehat{\mathbf{E}}^s(R, \lambda) \right|$$

where  $\widehat{\mathbf{E}}^s(R, \lambda) = \mathcal{F}(\mathbf{E}^s(R, t))$  denotes the Fourier transform of the scattered electric field intensity for a given wavelength  $\lambda$ .

In practice, the RCS (6.1) is computed for a finite distance  $R$  that is far away from the scatterer. The computation of the scattered field from the solution of a TDIE method will be explained in Sec. 6.2.1. No far-field approximations will be used.

The RCS simulated with our implementation of the MoT scheme will be compared with the RCS of the same structure computed with an implementation of a standard MoM that has been developed in-house at the National Aerospace Laboratory NLR and verified with commercial codes. Only preliminary verification results will be presented here, for only one test case.

### The RCS of a generic aircraft

Let us consider the generic aircraft introduced in Sec. 6.1.1. The MoM has been applied to the EFIE for an incident wave field with a wavelength of  $\lambda = 10$  m, and polarization and propagation in the  $+\hat{\mathbf{z}}$  and  $+\hat{\mathbf{x}}$  direction, resp. This means that the incident wave field approaches the aircraft at the nose, with a vertical polarization. The TDIE method discretizes the differentiated EFIE with a MoT scheme that employs quadratic spline basis functions (4.25). The time step size is 0.1 lm and 50 000 time levels have been simulated. Notice that the MoT scheme remains stable for the entire simulation time of  $500\lambda$  lm. The interaction matrices have been computed with the quasi-exact integration method using 7 quadrature points. As excitation, a causal sinusoidal plane wave field (2.38) has been used with the same wavelength as in the MoM simulation.

The RCS is obtained by first computing the scattered electric field intensity (6.2) on a circle with a radius of  $R = 400\lambda$  in the horizontal plane given by  $z = 0$ . For this, a 7-point quadrature rule has been used for 25 000 time intervals of size 0.1 lm, starting from time  $(R + 1000)/c$ , where the additional factor 1000 has been chosen such that the scattered field has become periodical and no transient effects from the zero initial conditions are visible anymore. The bistatic RCS is depicted in Fig. 6.2, that is, the radar source excites the aircraft with incidence on the nose and the scattered field is observed at a complete range of azimuth angles. Excellent correspondence between the MoT scheme and the MoM is obtained for this test case.



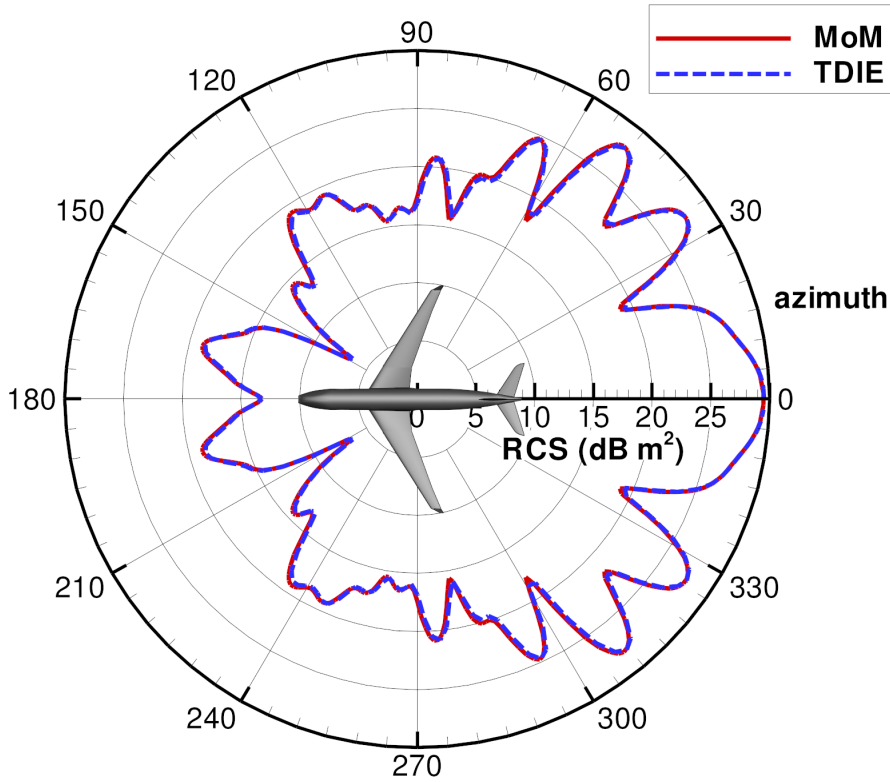


Figure 6.2: The bistatic RCS of a generic aircraft with incidence on the nose and vertical polarization.

## 6.2 Radar scattering analysis

The electromagnetic scattering of a PEC object is characterized by the electric surface current density. This variable has therefore been used in the experimental confirmation of the stability, accuracy, and robustness of the TDIE method. For application in stealth technology, the scattered electromagnetic field is more meaningful, because this represents the radar field that is detected. To this end, the electric fields will be computed from the electric surface current density.

### 6.2.1 Scattered electric field

The scattered electromagnetic field can be written as a function of the electric surface current density, as given in Eq. (2.13). In order to compute the scattered field from the discrete solution of the CFIE, the series expansion (2.18)

of the electric surface current density in terms of basis functions has to be substituted. The idea is to evaluate the electromagnetic field similar to the solution procedure of the CFIE. However, integration by parts can not be used thus necessitating the evaluation of the ‘gradient of the divergence’ term in the EFIE. More precisely,

$$\begin{aligned}
& \nabla \left( \frac{\int_{-\infty}^{\tau} \nabla' \cdot \mathbf{J}(\mathbf{r}', \bar{t}) \, d\bar{t}}{4\pi R} \right) \\
&= \int_{-\infty}^{\tau} \nabla' \cdot \mathbf{J}(\mathbf{r}', \bar{t}) \, d\bar{t} \, \nabla \left( \frac{1}{4\pi R} \right) + \frac{1}{4\pi R} \nabla \left( \int_{-\infty}^{\tau} \nabla' \cdot \mathbf{J}(\mathbf{r}', \bar{t}) \, d\bar{t} \right) \\
&= \int_{-\infty}^{\tau} \nabla' \cdot \mathbf{J}(\mathbf{r}', \bar{t}) \, d\bar{t} \left( \frac{-\mathbf{R}}{4\pi R^3} \right) + \frac{1}{4\pi R} (\nabla' \cdot \mathbf{J}(\mathbf{r}', \bar{t}))_{\bar{t}=\tau} \nabla(\tau) \\
&= -\frac{\mathbf{R}}{4\pi R^3} \int_{-\infty}^{\tau} \nabla' \cdot \mathbf{J}(\mathbf{r}', \bar{t}) \, d\bar{t} + \frac{(\nabla' \cdot \mathbf{J}(\mathbf{r}', \bar{t}))_{\bar{t}=\tau}}{4\pi R} \left( -\frac{1}{c} \nabla R \right) \\
&= -\frac{\mathbf{R}}{4\pi R^3} \int_{-\infty}^{\tau} \nabla' \cdot \mathbf{J}(\mathbf{r}', \bar{t}) \, d\bar{t} - \frac{(\nabla' \cdot \mathbf{J}(\mathbf{r}', \bar{t}))_{\bar{t}=\tau} \mathbf{R}}{4\pi c R} \\
&= -\frac{\mathbf{R}}{4\pi R^2} \left( \frac{\int_{-\infty}^{\tau} \nabla' \cdot \mathbf{J}(\mathbf{r}', \bar{t}) \, d\bar{t}}{R} + \frac{(\nabla' \cdot \mathbf{J}(\mathbf{r}', \bar{t}))_{\bar{t}=\tau}}{c} \right)
\end{aligned}$$

where it is assumed that  $R > 0$ , which is valid for the computation of the scattered field outside the surface. Substitution of the series expansion (2.18) into the scattered field results in the *discrete scattered electric field* given by

$$\begin{aligned}
\hat{\mathbf{E}}^s(\mathbf{r}, t) &= -\frac{1}{4\pi} \sum_{n=1}^{N_s} \sum_{j=1}^{N_t} J_{n,j} \iint_{\Gamma} \left( \mu \frac{\mathbf{f}_n(\mathbf{r}') \dot{T}_j(\tau)}{R} \right. \\
&\quad \left. + \frac{1}{\epsilon} \frac{\mathbf{R}}{R^2} \left( \frac{\int_{-\infty}^{\tau} (\nabla' \cdot \mathbf{f}_n(\mathbf{r}')) T_j(\bar{t}) \, d\bar{t}}{R} + \frac{(\nabla' \cdot \mathbf{f}_n(\mathbf{r}')) T_j(\tau)}{c} \right) \right) d\mathbf{r}' \\
&= -\frac{1}{4\pi} \sum_{n=1}^{N_s} \sum_{j=1}^{N_t} J_{n,j} \iint_{\Gamma} \left( \mu \frac{\mathbf{f}_n(\mathbf{r}') \dot{T}_j(\tau)}{R} \right. \\
&\quad \left. + \frac{1}{\epsilon} \frac{\mathbf{R}}{R^2} (\nabla' \cdot \mathbf{f}_n(\mathbf{r}')) \left( \frac{\int_{-\infty}^{\tau} T_j(\bar{t}) \, d\bar{t}}{R} + \frac{T_j(\tau)}{c} \right) \right) d\mathbf{r}'. \quad (6.2)
\end{aligned}$$

The RWG functions (2.23) and piecewise polynomials (2.29) can readily be substituted as basis functions in space and time, resp. Similarly, the *discrete*



scattered magnetic field reads

$$\begin{aligned}\hat{\mathbf{H}}^s(\mathbf{r}, t) &= \frac{1}{4\pi} \sum_{n=1}^{N_s} \sum_{j=1}^{N_t} J_{n,j} \iint_{\Gamma} \left( \left( \frac{\mathbf{f}_n(\mathbf{r}') \dot{T}_j(\tau)}{c} + \frac{\mathbf{f}_n(\mathbf{r}') T_j(\tau)}{R} \right) \times \frac{\mathbf{R}}{R^2} \right) d\mathbf{r}' \\ &= \frac{1}{4\pi} \sum_{j=1}^{N_s} \sum_{j=1}^{N_t} J_{n,j} \iint_{\Gamma} \left( \left( \frac{\dot{T}_j(\tau)}{c} + \frac{T_j(\tau)}{R} \right) \frac{\mathbf{f}_n(\mathbf{r}') \times \mathbf{R}}{R^2} \right) d\mathbf{r}'.\end{aligned}\quad (6.3)$$

Notice that the computation of the discrete scattered electromagnetic field intensity requires the evaluation of a surface integral. This can be performed efficiently with standard quadrature rules for the surface integral, because  $R > 0$ . In practice, one is interested in a range of locations and time levels on which the scattered field can be represented. In this thesis, a triangular surface mesh around the scatterer will be used on which the scattered field is computed in the cell centers. Capturing the highest frequency modes will require meshes for the scattered field that are as dense as the surface mesh on the scatterer. Moreover, the scattered field has to be computed on time intervals that are similar to the time step size of the TDIE method. Consequently, the visualization of the scattered field can be as computationally demanding as the TDIE method itself.

**Corner reflector** Let us consider a corner reflector consisting of two screens of unit size and zero thickness, with a right angle. The surface mesh consists of 15 075 edges with a maximum edge length of 3.83 cm and a minimum length of 1.53 cm. The TDIE method has been performed on the differentiated EFIE with quadratic spline basis functions (4.25) and a time step size of 0.01 lm. The interaction matrices have been computed with the quasi-exact integration method using 7 quadrature points. As excitation, a causal sinusoidal plane wave field (2.38) has been used with unit amplitude, a wave length of 20 cm, and polarization and propagation in the  $+\hat{\mathbf{z}}$  and  $-\hat{\mathbf{x}}$  direction, resp. This means that the incident wave field approaches the corner reflector at the front, with a polarization along the screens. The scattered electric field intensity (6.2) has been computed with a 1-point quadrature rule, for 600 time intervals of size 0.01 lm, and in the centroids of a triangular surface mesh on a horizontal plane given by  $z = 0.5$ , with 45 578 triangles and a mean edge length of 2.13 cm. The  $z$ -component of the total electric field  $\mathbf{E}^i + \hat{\mathbf{E}}^s$  is depicted for several time levels in Fig. 6.3, along with the magnitude of the electric surface current density on the corner reflector.

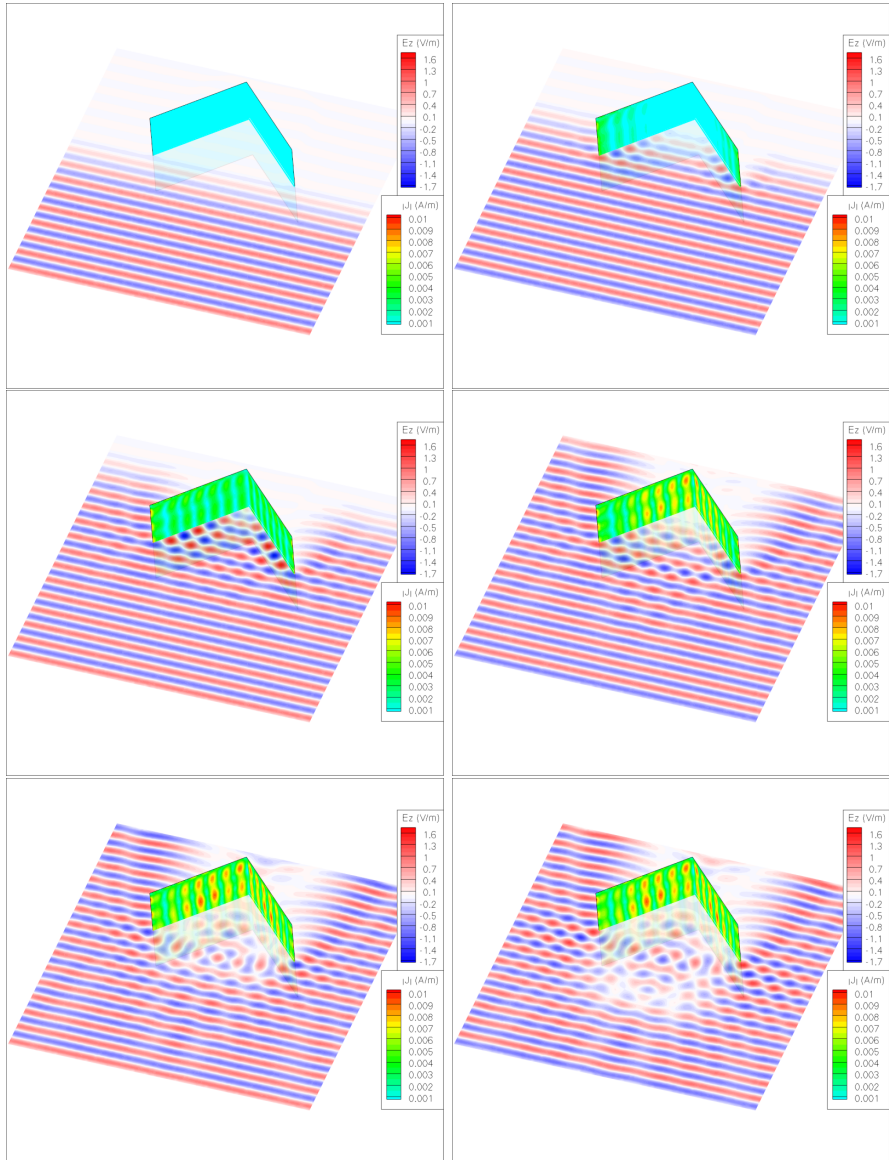


Figure 6.3: The magnitude of the electric surface current density on the surface of the corner reflector is depicted in a scale from light blue to red. The  $z$ -component of the electric field intensity on the horizontal plane  $z = 0.5$  is depicted in blue for negative and in red for positive values.



**Generic aircraft** Let us consider the generic aircraft introduced in Sec. 6.1.1. The TDIE method has been performed on the differentiated EFIE with quadratic spline basis functions (4.25) and a time step size of  $0.2\text{ lm}$ . The interaction matrices have been computed with the quasi-exact integration method using 7 quadrature points. As excitation, a causal sinusoidal plane wave field (2.38) has been used with unit amplitude, a wave length of  $6\text{ m}$ , and polarization and propagation in the  $+\hat{\mathbf{z}}$  and  $+\hat{\mathbf{x}}$  direction, resp. This means that the incident wave field approaches the aircraft at the nose, with a vertical polarization. The scattered electric field intensity (6.2) has been computed with a 1-point quadrature rule, for 1000 time intervals of size  $0.2\text{ lm}$ , and in the centroids of a triangular surface mesh on a horizontal plane given by  $z = 1.75$ , with 6800 triangles and a mean edge length of  $1.04\text{ m}$ . Fig. 6.4 depicts the electric surface current, the incident and the scattered electric field for several time levels.

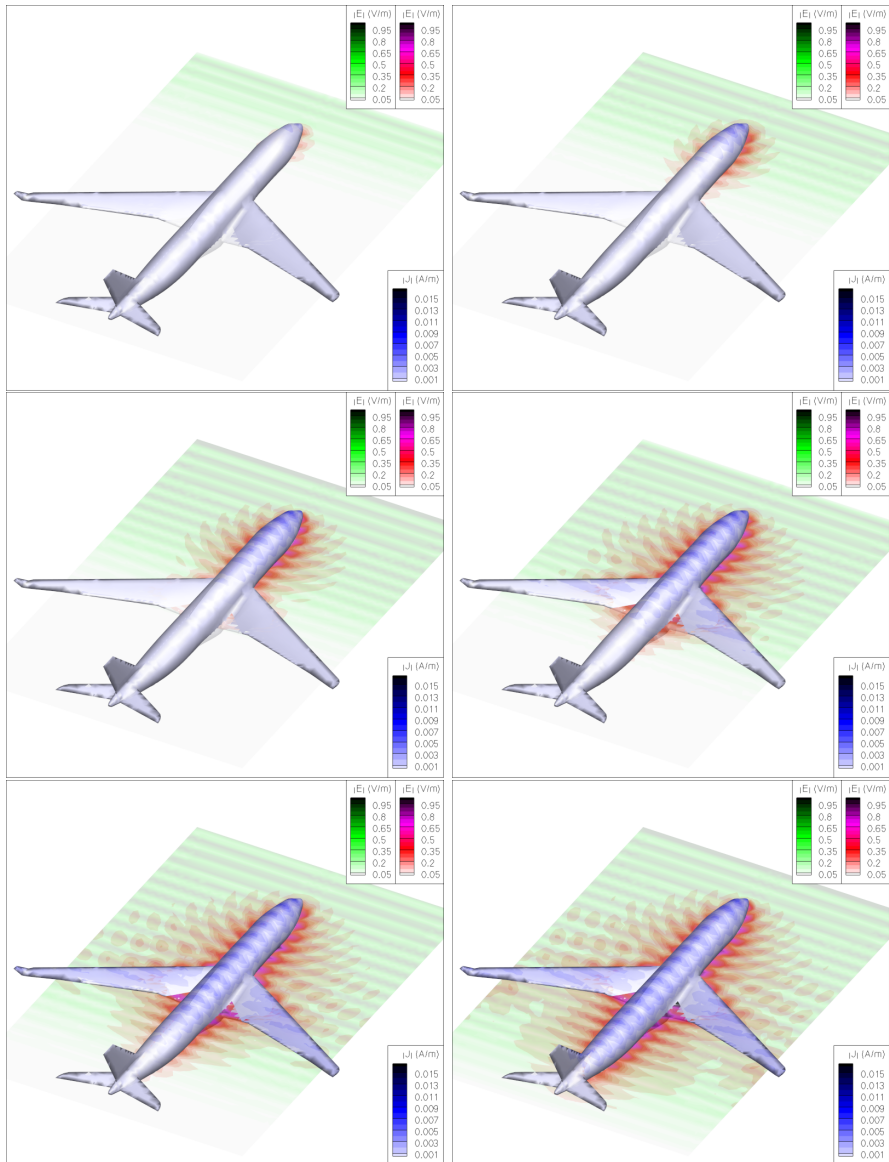


Figure 6.4: The magnitude of the electric surface current density on the surface of the generic aircraft is depicted in blue. The magnitude of the electric field intensity on the horizontal plane  $z = 1.75$  is depicted in green for the incident field and in red for the scattered field.

## 6.2.2 High resolution range profile

One of the techniques in automatic target recognition is the use of high resolution range profiles (HRRP) [42, 65]. A HRRP is a one-dimensional visualization of the radar signature of a target. The idea of using a HRRP is to locate *scatterer points* on the target, which are components of the target with a high radar reflection rate. In the case of an aircraft, typical scatterer points are the nose, wing, and tail, in particular the tips and fairings which have sharp edges. With the aid of a HRRP, characteristics of the target, such as its size and the location of the wings and tail can be determined. Since each aircraft has its own HRRP characteristics, comparison of the measured radar signal with a database can result in the recognition of a target.

Many different techniques exist to obtain a HRRP [100]. The most effective one is the use of a short radar pulse, which have high frequency modes and a small bandwidth in time. The high frequencies result in radar scattering of the target in the optical region, for which is easier to determine scatterer points because less resonances and creeping waves are present. The small support in time result in small excitation regions and highly concentrated scattered fields. Then, the location of scatterer points can be estimated with a high resolution. The drawback is that most radar equipment can generate short pulses only with a limited power, thus reducing the range of detection. This can be circumvented by using sophisticated waveforms with a range of frequencies.

Using a HRRP in automatic target recognition requires a database of the radar signature of common aircraft types. For military application, this also includes hostile platforms, for which physical measurement campaigns are not feasible. CEM methods can provide a HRRP for different platforms and angles of incidence. For frequency domain methods, the radar signature has to be simulated for a large range of frequencies. The HRRP is then obtained with an inverse discrete Fourier transform. Alternatively, time domain methods can simulate short pulses in a single run and the time signal can easily be transformed into a HRRP. This makes time domain methods more efficient and accurate in the computation of a HRRP than frequency domain methods.

Different definitions of a HRRP can be found in literature, with many specifically formulated for frequency-domain CEM [88, 113]. Basically any definition of a HRRP translates time into a relative position. The following definition is perhaps not standard, but can be used to identify objects and thus serves the purpose of the HRRP.

Let us assume that a given incident wave field with propagation in direction  $\hat{\mathbf{k}}$  has a sharp peak at offset  $t_0$ , for example a Gaussian plane wave (2.35) with a small pulse width. At an arbitrary point  $\mathbf{r}_{\text{sca}}$  on the scatterer, the incident wave field has a peak at time  $t_0 + (\mathbf{r}_{\text{sca}} \cdot \hat{\mathbf{k}})/c$ . The scattered field will reach an arbitrary observation point  $\mathbf{r}_{\text{obs}}$  at time  $t_0 + (\mathbf{r}_{\text{sca}} \cdot \hat{\mathbf{k}})/c + |\mathbf{r}_{\text{sca}} - \mathbf{r}_{\text{obs}}|/c$ .

Now, let us assume  $|\mathbf{r}_{\text{sca}} - \mathbf{r}_{\text{obs}}| = (\mathbf{r}_{\text{sca}} - \mathbf{r}_{\text{obs}}) \cdot \hat{\mathbf{k}}$ , which is valid for monostatic reflection. Then, the scattered field will reach the observation point at time  $t_0 + 2(\mathbf{r}_{\text{sca}} \cdot \hat{\mathbf{k}}) - \mathbf{r}_{\text{obs}} \cdot \hat{\mathbf{k}}$ . This leads to the definition of the HRRP given by

$$\begin{aligned} \mathbf{E}^{\text{HRRP}}(\mathbf{r}_{\text{HRRP}}) &= \mathbf{E}^s(\mathbf{r}_{\text{obs}}, t_0 + 2\mathbf{r}_{\text{HRRP}} - \mathbf{r}_{\text{obs}} \cdot \hat{\mathbf{k}}), \\ \mathbf{r}_{\text{HRRP}} &= \mathbf{r}_{\text{sca}} \cdot \hat{\mathbf{k}} \end{aligned} \quad (6.4)$$

where  $\mathbf{E}^s$  is the scattered electric field intensity (6.2). The dimension is in V/m, but it can be advantageous to consider the RCS (6.1) in decibel scale.

**Two cubes** Let us consider two cubes of unit size and separated 3m, as depicted in Fig. 6.5(a). The surface mesh consists of 534 edges. The TDIE method has been performed on the differentiated EFIE with quadratic spline basis functions (4.25) and a time step size of 0.01 lm. The interaction matrices have been computed with the quasi-exact integration method using 7 quadrature points. As excitation, a Gaussian plane wave field (2.35) has been used with unit amplitude, pulse width of 1 m, and polarization and propagation in the  $+\hat{\mathbf{y}}$  and  $+\hat{\mathbf{x}}$  direction, resp. The scattered electric field intensity (6.2) has been computed at location  $(-20, 0.5, 0.5)$  with 7 quadrature points on each mesh element for intervals of size 0.01 lm. The HRRP for the  $y$ -component of the electric field intensity is depicted in Fig. 6.5(b). The HRRP clearly show peaks in the RCS at the vertical faces of the cubes.

**Generic aircraft** Let us consider the generic aircraft introduced in Sec. 6.1.1. The TDIE method has been performed on the differentiated EFIE with quadratic spline basis functions (4.25) and a time step size of 0.12 lm. The interaction matrices have been computed with the quasi-exact integration method using 7 quadrature points. As excitation, a Gaussian plane wave field (2.35) has been used with unit amplitude, pulse width of 6 m, and propagation in the  $+\hat{\mathbf{x}}$  direction. Both  $+\hat{\mathbf{y}}$  and  $+\hat{\mathbf{z}}$  polarization has been simulated. The scattered electric field intensity (6.2) has been computed at location  $(-1200, 0, 3)$  with 7 quadrature points on each mesh element for intervals of size 0.12 lm.

The HRRP for the  $y$ - and  $z$ -component of the electric field intensity is depicted in Fig. 6.6(b) and 6.6(c), resp. A scattering peak can be seen at the nose of the aircraft. The wings result in a large contribution in the HRRP, especially for the horizontally polarized field, because the wings are aligned in the  $y$ -direction. For the same reason, the tail fin can be distinguished by the peak in the HRRP of the vertical polarized field. The high levels in RCS behind the aircraft are due to multiple scattering of the aircraft. The HRRP provides information on the size and layout of the aircraft and can thus be used for target recognition.

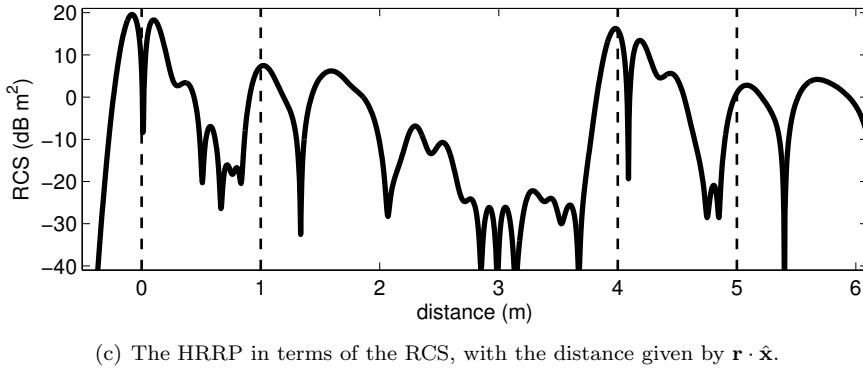
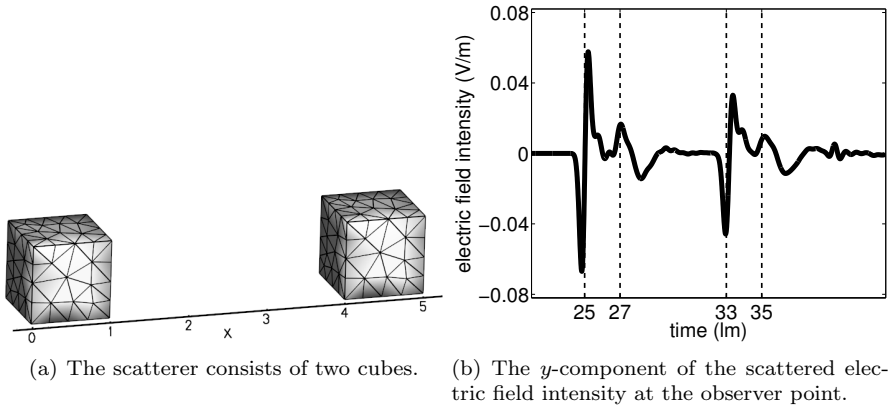
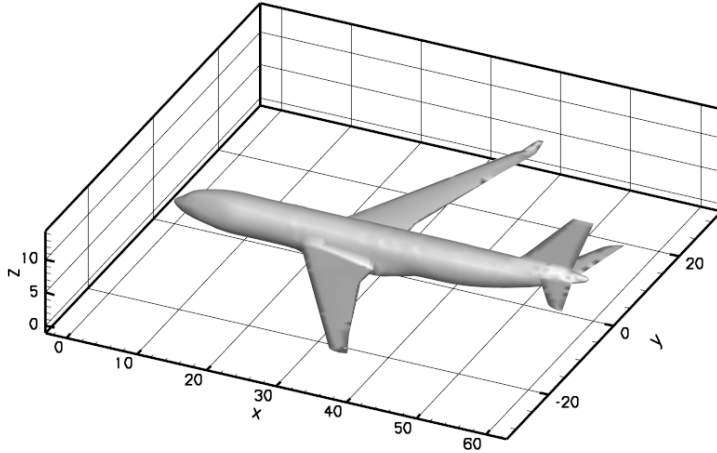


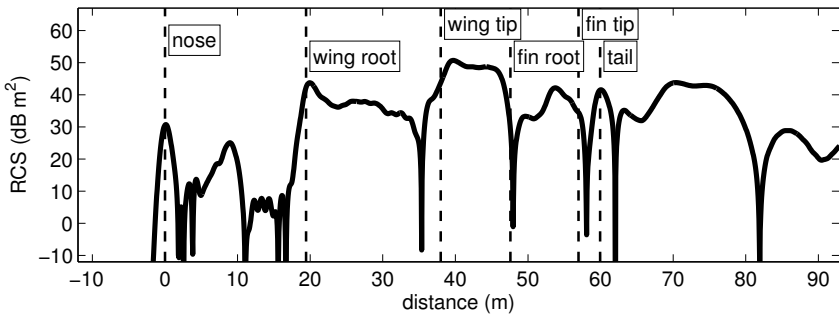
Figure 6.5: The scattered electric field and HRRP of two cubes.

## Discussion

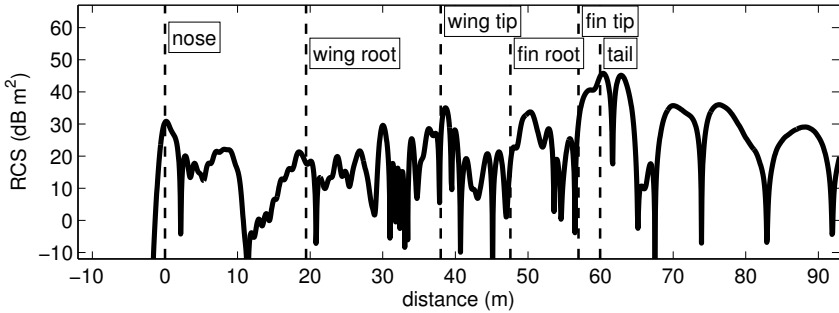
The computational results confirm that HRRP's can effectively be generated with the TDIE method. Still, this is only a proof of concept because coarse surface meshes have been used due to limits in efficiency of the current implementation. Consequently, the relatively large wave length of the excitation deteriorates the accuracy of the HRRP. That said, computing a HRRP is inherently more effective with time domain CEM than frequency domain CEM because short pulses with a wide frequency band can be simulated in a single run. Furthermore, surface integral methods are preferred because radiation conditions are automatically satisfied and the scattered field can be computed efficiently on arbitrary locations. Concluding, the simulation of a HRRP is a valuable merit of using the TDIE method.



(a) The dimensions of the generic aircraft.



(b) The  $y$ -component of the scattered electric field intensity for an excitation with  $+\hat{y}$  polarization.



(c) The  $z$ -component of the scattered electric field intensity for an excitation with  $+\hat{z}$  polarization.

Figure 6.6: The HRRP of a generic aircraft, with the distance given by  $\mathbf{r} \cdot \hat{\mathbf{x}}$ .





# Conclusions

The numerical analysis of the stability, accuracy, and robustness of the TDIE method that has been derived in this thesis results in the following conclusions:

## Stability

- The variational formulation of the differentiated EFIE admits a unique and bounded solution in  $\mathcal{H}^{\frac{1}{2}}$  if the testing space is  $\mathcal{H}^{-\frac{1}{2}}$  (Sec. 3.7).
- The space-time Galerkin scheme with step test functions and hat basis functions in time is discretely equivalent to the MoT scheme with quadratic spline basis functions in time (Sec. 3.8.2).
- The stability theorem of Terrasse holds for the differentiated EFIE when discretized with the MoT scheme using quadratic spline basis functions (Sec. 3.8).
- The stability theorem of Terrasse does not hold for the differentiated EFIE when discretized with the MoT scheme using quadratic Lagrange basis functions (Sec. 3.8).
- All computer simulations performed by the author have been stable so far, provided a MoT scheme is used with quadratic spline basis functions and the robust quasi-exact integration algorithm (Sec. 3.9.1).

### Accuracy

- Causal temporal basis functions applied to the differentiated CFIE achieve first order interpolation accuracy in time for a one-parameter family of piecewise quadratic polynomials (Sec. 4.3.2).
- Causal temporal basis functions applied to the differentiated CFIE achieve second order interpolation accuracy in time for a two-parameter family of piecewise cubic polynomials (Sec. 4.3.3).
- Temporal basis functions with maximum order of interpolation accuracy in time can achieve  $\mathcal{C}^1$  and  $\mathcal{C}^2$  continuity for piecewise quadratic and cubic polynomials, resp. (Sec. 4.4.2).
- Smoothness of the temporal basis function has a positive influence on the performance of the quadrature procedure in space (Sec. 4.5.3).
- Numerical experiments show an unexpected higher order of global accuracy in time for the spline basis functions than for the shifted Lagrange basis functions with equal support (Sec. 4.5.4).
- The shape of the temporal basis function influences the conditioning of the system of linear equations that has to be solved (Sec. 4.5.5).

### Robustness

- The accurate quasi-exact integration method for the evaluation of interaction matrices is necessary to obtain stability of the MoT scheme (Sec. 5.2).
- Straightforward implementation in finite precision arithmetic of available analytical expressions of the radiation fields are not well behaved for a number of limit cases (Sec. 5.4).
- A robust implementation with well-behaved expressions can be obtained only when tolerance regions are chosen carefully (Sec. 5.5).
- A computational experiment shows that for the same test case, the straightforward implementation results in an unstable simulation whereas the robust implementation remains stable (Sec. 5.7).

# Recommendations

## 8.1 Best practices

The goal of the numerical analysis of stability, accuracy, and robustness of the TDIE method is the design of a usable MoT scheme. This means that the numerical scheme should at least be stable and a robust implementation should be used. Then, a trade-off concerning efficiency can be made, that is, the computational method should be as accurate as possible and consume as little computation time and storage as possible. Based on information in literature and the numerical analysis in this thesis, the following choices are recommended:

- Use the *differentiated EFIE* as model equation, because it is more efficient than the original EFIE. Furthermore, a stability theorem for the variational formulation of the EFIE has been derived. The CFIE is only applicable to closed surfaces and requires different test functions than RWG functions in space to obtain accurate simulations.
- Use the *MoT scheme* as numerical discretization, because it is more efficient and easier to use than the space-time Galerkin and convolution quadrature scheme. Moreover, the solutions are accurate and are almost free of dispersion and dissipation. Remember that all these schemes can be written as a general space-time Petrov-Galerkin scheme and a discrete equivalence between specific schemes has been derived.
- Use the *quadratic spline basis functions* in time, because they fit within the stability theorem and result in an efficient marching procedure because of discrete causality and short support. Moreover, the highest order of smoothness and interpolation accuracy for piecewise quadratic

polynomials are obtained and the global accuracy in time has been experimentally determined to be of order two.

- Use the *quasi-exact integration method* to evaluate the interaction matrices, because this is necessary to obtain stability. Computational experiences suggest that 7 quadrature points for the outer integral are sufficient. The implementation is burdensome and robust formulations of the radiation fields in finite precision arithmetic are required.
- Use a *triangular surface mesh* with the *RWG functions* as test and basis functions in space, because flat triangular patches can model curved surfaces accurately and RWG functions are efficient, accurate, and stable. Moreover, quasi-exact integration methods have been derived for this choice. The size of the surface patches have to be small enough to capture all geometric features and the component of the excitation with smallest wavelength.
- Use a *time step size* given by an oversampling of the maximum frequency in the excitation, because this is the largest value that can model the incident wave field accurate enough, and thus the most efficient choice.

With these best practices, all computer simulations so far have been stable.

## 8.2 Future research

Performing high-confident computer simulations for the radar signature of modern stealth aircraft in an industrial environment was the goal of this thesis. This specific application required the use of the TDIE method, which should be best capable of simulating UWB radar and ferromagnetic RAM. Current implementations, even for classic radar and PEC structures, are not yet feasible in industry because of instabilities. In this thesis, a numerical analysis has been performed resulting in clear guidelines for the choice of the discretization scheme. Stable computer simulations have been obtained with high confidence for different PEC objects with sizes of several wavelengths. The two main aspects of future research are the stable implementation of accelerators and the incorporation of nonlinear constitutive equations.

**Accelerators** For application in airborne stealth technology, computational methods have to be able to simulate radar fields in the GHz-range. This means that the size of the object is hundreds of wavelengths. Accelerators are necessary to improve the efficiency. The PWTD method is the principal candidate because the computational work is superior to other methods for high resolution problems. Successful application to the MoT scheme has been reported in literature. Still, more research is required on the influence of PWTD acceleration on stability and robustness of the TDIE method.

**Nonlinear constitutive equations** Simple, linear constitutive equations can be used for PEC objects. Ferromagnetic materials that are frequently being used in RAM may require the use of nonlinear constitutive equations such as the LLG equation. The incorporation of nonlinear constitutive equation in TDIE methods is an open problem in literature. For ferromagnetic coatings, generalized impedance boundary conditions are attractive options. When ferromagnetic nanoparticles are used in load-bearing structures, volume methods inside this composite material have to be coupled with the TDIE method on the scatterer surface. Only preliminary results are available in literature, most for easier and linear models for the radar evolution in materials. Much research is therefore required for the simulation of scattering from ferromagnetic materials with the TDIE method. Furthermore, since obtaining a robust implementation of a stable TDIE method has always been the most challenging aspect in the design of MoT schemes, the implications of all different constitutive equations on stability has to be analyzed thoroughly.





# Curriculum vitae

Elwin van 't Wout was born on May 15, 1986, in Rotterdam, the Netherlands. He received secondary education, *atheneum*, at Farelcollege in Ridderkerk, 1998–2004. After enrolling at Delft University of Technology in 2004, he obtained his *B.Sc. Applied Mathematics* degree with distinction (*cum laude*) in 2007.

He obtained his *M.Sc. Applied Mathematics* degree with distinction (*cum laude*) in 2009. The title of his thesis is “Improving the linear solver used in the interactive wave model of a real-time ship simulator”. The research for his thesis was conducted at the Maritime Research Institute Netherlands (MARIN) in Wageningen during a 10-month internship.

He worked at the National Aerospace Laboratory NLR for four years, from 2009 to 2013, where he conducted research for his Ph.D. study at Delft University of Technology. There, he was member of the Numerical Analysis group within the Delft Institute of Applied Mathematics and was supervised by prof.dr.ir. C. Vuik.





# Publications

## Peer-reviewed journal papers

1. E. van 't Wout, D. R. van der Heul, H. van der Ven, and C. Vuik, "The influence of the exact evaluation of radiation fields in finite precision arithmetic on the stability of the time domain integral equation method," accepted for publication in *IEEE Transactions on Antennas and Propagation*, 2013.
2. E. van 't Wout, D. R. van der Heul, H. van der Ven, and C. Vuik, "Design of temporal basis functions for time domain integral equation methods with predefined accuracy and smoothness," *IEEE Transactions on Antennas and Propagation*, vol. 61, no. 1, pp. 271–280, January 2013.

## Peer-reviewed proceedings papers

1. E. van 't Wout, D. R. van der Heul, H. van der Ven, and C. Vuik, "Robust formulation of the exact evaluation of radiation fields in the time domain integral equation method," in *Proceedings of the 29<sup>th</sup> Annual Review of Progress in Applied Computational Electromagnetics*, Monterey, CA: ACES, March 2013, pp. 280–284.
2. E. van 't Wout, D. R. van der Heul, H. van der Ven, and C. Vuik, "A provably stable MoT scheme based on quadratic spline basis functions," in *Proceedings of the IEEE Antennas and Propagation Society International Symposium*, Chicago, IL, July 2012.
3. E. van 't Wout, D. R. van der Heul, H. van der Ven, and C. Vuik, "A framework to design temporal basis functions used in boundary element methods for transient electromagnetic scattering," in *Proceedings of Advanced Electromagnetics Symposium*, Paris, France, April 2012, pp. 675–679.
4. E. van 't Wout, D. R. van der Heul, H. van der Ven, and C. Vuik, "The accuracy of temporal basis functions used in the TDIE method," in *Pro-*

*ceedings of the IEEE Antennas and Propagation Society International Symposium*, Spokane, WA, July 2011, pp. 2708–2711.

5. E. van 't Wout, M. B. van Gijzen, A. Ditzel, A. van der Ploeg, and C. Vuik, “The deflated relaxed incomplete Cholesky CG method for use in a real-time ship simulator,” *Procedia Computer Science*, vol. 1, no. 1, pp. 249–257, May 2010.

### Talks at international conferences

1. “Using space-time Galerkin stability theory to define a robust collocation method for time-domain boundary integral equations in electromagnetics,” at *Mathematics of Finite Elements and Applications*, London, UK: Brunel University, June 2013.
2. “Robust formulation of the exact evaluation of radiation fields in the time domain integral equation method,” at *The 29<sup>th</sup> Annual Review of Progress in Applied Computational Electromagnetics*, Monterey, CA: ACES, March 2013.
3. “A provably stable MoT scheme based on quadratic spline basis functions,” at *IEEE Antennas and Propagation Society International Symposium*, Chicago, IL, July 2012.
4. “A framework to design temporal basis functions used in boundary element methods for transient electromagnetic scattering,” at *Advanced Electromagnetics Symposium*, Paris, France, April 2012.
5. “On the accuracy and smoothness of temporal basis functions used in the TDIE Method,” at *IEEE Antennas and Propagation Society International Symposium*, Spokane, WA, July 2011.
6. “On the accuracy and smoothness of temporal basis functions used in the TDIE method of electromagnetics,” at *Time Domain Boundary Integral Equations: Algorithms, Analysis, Applications*, Leipzig, Germany: Max Planck Institute for Mathematics in the Sciences, May 2011.
7. “The deflated relaxed incomplete Cholesky CG method for use in a real-time ship simulator,” *International Conference on Computational Sciences*, Amsterdam, the Netherlands, May 2010.

### Poster presentations

1. “Non-cooperative target recognition with the time domain integral equation method,” at the *38<sup>th</sup> Woudschoten Conference of the Dutch-Flemish Research Community Scientific Computing*, Zeist, the Netherlands, October 2013.

2. "A stability proof of time domain integral equation methods for electromagnetics," at the *37<sup>th</sup> Woudschoten Conference of the Dutch-Flemish Research Community Scientific Computing*, Zeist, the Netherlands, October 2012.
3. "Modelling radar response of ferromagnetic coatings - late-time instability of a delay differential equation," at the *35<sup>th</sup> Woudschoten Conference of the Dutch-Flemish Research Community Scientific Computing*, Zeist, the Netherlands, October 2010.
4. "Modelling radar response of ferromagnetic coatings," at *3TU Applied Mathematics Institute Opening Symposium*, Delft, the Netherlands, April 2010.





# Bibliography

- [1] T. Abboud, J.-C. Nédélec, and J. Volakis, “Stable solution of the retarded potential equations,” in *Proc. 17<sup>th</sup> ACES Conf.*, pp. 146–151. Monterey, CA: ACES, 2001.
- [2] F. P. Andriulli, H. Bağci, F. Vipiana, G. Vecchi, and E. Michielssen, “Analysis and regularization of the TD-EFIE low-frequency breakdown,” *IEEE Trans. Antennas Propag.*, vol. 57, no. 7, pp. 2034–2046, 2009.
- [3] F. P. Andriulli, K. Cools, F. Olyslager, and E. Michielssen, “Time domain Calderón identities and their application to the integral equation analysis of scattering by PEC objects Part II: Stability,” *IEEE Trans. Antennas Propag.*, vol. 57, no. 8, pp. 2365–2375, 2009.
- [4] K. Aygün, B. Shanker, and E. Michielssen, “Fast time-domain characterization of finite size microstrip structures,” *Int. J. Numer. Model.*, vol. 15, pp. 439–457, 2002.
- [5] H. Bağci, A. E. Yilmaz, J.-M. Jin, and E. Michielssen, “Time domain adaptive integral method for surface integral equations,” in *Modeling and Computations in Electromagnetics*, pp. 65–104, ser. Lecture Notes in Computational Science and Engineering. Berlin: Springer, 2008.
- [6] H. Bağci, A. E. Yilmaz, V. Lomakin, and E. Michielssen, “Fast solution of mixed-potential time-domain integral equations for half-space environments,” *IEEE Trans. Geosci. Remote Sens.*, vol. 43, no. 2, pp. 269–279, 2005.
- [7] C. A. Balanis, *Advanced engineering electromagnetics*. New York: John Wiley & Sons, 1989.



- [8] L. Banjai and S. Sauter, “Rapid solution of the wave equation in unbounded domains,” *SIAM J. Numer. Anal.*, vol. 47, pp. 227–249, 2008.
- [9] L. Banjai and M. Schanz, “Wave propagation problems treated with convolution quadrature and BEM,” in *Fast Boundary Element Methods in Engineering and Industrial Applications*, pp. 145–184, ser. Lecture Notes in Applied and Computational Mechanics. Berlin: Springer, 2012.
- [10] E. Bécache, “A variational boundary integral equation method for an elastodynamic antiplane crack,” *Int. J. Numer. Meth. Engng.*, vol. 36, pp. 969–984, 1993.
- [11] Y. Beghein, K. Cools, H. Bağci, and D. De Zutter, “A space-time mixed Galerkin marching-on-in-time scheme for the time-domain combined field integral equation,” *IEEE Trans. Antennas Propag.*, vol. 61, no. 3, pp. 1228–1238, 2013.
- [12] A. Bellen and M. Zennaro, *Numerical Methods for Delay Differential Equations*. Oxford, UK: Clarendon Press, 2003.
- [13] B. Borden, *Radar Imaging of Airborne Targets*. New York: Taylor & Francis, 1999.
- [14] A. Boryssenko, “Accurate and efficient quadratures for transient electromagnetic potentials,” in *Proc. AES*, pp. 680–684. Paris, France: Télécom ParisTech, Apr. 2012.
- [15] S. C. Brenner and L. R. Scott, *The Mathematical Theory of Finite Element Methods*, 3rd ed., ser. Texts in Applied Mathematics, vol. 15. New York: Springer, 2008.
- [16] Q. Chen, P. Monk, X. Wang, and D. Weile, “Analysis of convolution quadrature applied to the time-domain electric field integral equation,” *Commun. Comput. Phys.*, vol. 11, no. 2, pp. 383–399, 2012.
- [17] W. C. Chew, J.-M. Jin, E. Michielssen, and J. Song, *Fast and efficient algorithms in computational electromagnetics*. Boston, MA: Artech House, 2001.
- [18] K. Cools, F. P. Andriulli, and E. Michielssen, “A Calderón multiplicative preconditioner for the PMCHWT integral equation,” *IEEE Trans. Antennas Propag.*, vol. 59, no. 12, pp. 4579–4587, 2011.
- [19] K. Cools, F. P. Andriulli, F. Olyslager, and E. Michielssen, “Nullspaces of MFIE and Calderón preconditioned EFIE operators applied to toroidal surfaces,” *IEEE Trans. Antennas Propag.*, vol. 57, no. 10, pp. 3205–3215, 2009.

- [20] M. Costabel, “Time-dependent problems with the boundary integral equation method,” in *Encyclopedia of Computational Mechanics*, ch. 25. John Wiley & Sons, 2004.
- [21] G. G. Dahlquist, “A special stability problem for linear multistep methods,” *BIT*, vol. 3, pp. 27–43, 1968.
- [22] P. J. Davies and D. B. Duncan, “Averaging techniques for time-marching schemes for retarded potential integral equations,” *Appl. Numer. Math.*, vol. 23, pp. 291–310, 1997.
- [23] —, “On the behaviour of time discretisations of the electric field integral equation,” *Appl. Math. Comp.*, vol. 107, pp. 1–26, 2000.
- [24] —, “Stability and convergence of collocation schemes for retarded potential integral equations,” *SIAM J. Numer. Anal.*, vol. 42, no. 3, pp. 1167–1188, 2004.
- [25] —, “Convolution-in-time approximations of time domain boundary integral equations,” *SIAM J. Sci. Comput.*, vol. 35, no. 1, pp. 43–61, 2013.
- [26] —, “Convolution spline approximations for time domain boundary integral equations,” *arXiv:math*, vol. 1305.0646, 2013.
- [27] S. J. Dodson, S. P. Walker, and M. J. Bluck, “Implicitness and stability of time domain integral equation scattering analyses,” *ACES Journal*, vol. 13, pp. 291–301, 1998.
- [28] D. A. Dunavant, “High degree efficient symmetrical Gaussian quadrature rules for the triangle,” *Int. J. Numer. Meth. Engng.*, vol. 21, pp. 1129–1148, 1985.
- [29] A. A. Ergin, B. Shanker, and E. Michielssen, “Fast analysis of transient acoustic wave scattering from rigid bodies using the multilevel plane wave time domain algorithm,” *J. Acoust. Soc. Am.*, vol. 107, no. 3, pp. 1168–1178, 2000.
- [30] —, “Analysis of transient wave scattering from rigid bodies using a Burton-Miller approach,” *J. Acoust. Soc. Am.*, vol. 106, no. 5, pp. 2396–2404, 1999.
- [31] Z. H. Firouzeh, M. Ghaffari-Miab, R. Faraji-Dana, R. Moini, S. H. H. Sadeghi, and G. A. E. Vandenbosch, “Time-domain MoM for the scattering analysis of thin-wire structures within a ground using band-limited second-order Lagrange temporal basis functions,” in *Proc. 20<sup>th</sup> ICEE*, pp. 1102–1107. Tehran: IEEE, May 2012.

- [32] Z. H. Firouzeh, R. Moini, S. H. H. Sadeghi, R. Faraji-Dana, and G. A. E. Vandenbosch, "A new method for transient analysis of a dipole above a lossy ground using quadratic B-spline temporal basis functions," in *Proc. ICEAA*, pp. 982–985. Torino, Italy: IEEE, Sept. 2011.
- [33] A. Geranmayeh, W. Ackermann, and T. Weiland, "Temporal discretization choices for stable boundary element methods in electromagnetic scattering problems," *Appl. Numer. Math.*, vol. 59, pp. 2751–2773, 2009.
- [34] S. Gerschgorin, "Über die Abgrenzung der Eigenwerte einer Matrix," *Bulletin de l'Académie des Sciences de l'URSS*, pp. 749–754, 1931.
- [35] M. Ghaffari-Miab, Z. H. Firouzeh, R. Faraji-Dana, R. Moini, S. H. H. Sadeghi, and G. A. E. Vandenbosch, "Time-domain MoM for the analysis of thin-wire structures above half-space media using complex-time Green's functions and band-limited quadratic B-spline temporal basis functions," *Eng. Anal. Bound. Elem.*, vol. 36, pp. 1116–1124, 2012.
- [36] R. D. Graglia and G. Lombardi, "Machine precision evaluation of singular and nearly singular potential integrals by use of Gauss quadrature formulas for rational functions," *IEEE Trans. Antennas Propag.*, vol. 56, no. 4, pp. 981–998, 2008.
- [37] D. H. Griffel, *Applied functional analysis*. Chichester, UK: Ellis Horwood Ltd., 1985.
- [38] T. Ha-Duong, B. Ludwig, and I. Terrasse, "A Galerkin BEM for transient acoustic scattering by an absorbing obstacle," *Int. J. Numer. Meth. Engng.*, vol. 57, pp. 1845–1882, 2003.
- [39] T. Ha-Duong, "On retarded potential boundary integral equations and their discretisations," in *Topics in Computational Wave Propagation*, pp. 301–336, ser. Lecture Notes in Computational Science and Engineering, vol. 31. Berlin: Springer, 2003.
- [40] W. Hackbusch, W. Kress, and S. A. Sauter, "Sparse convolution quadrature for time domain boundary integral formulations of the wave equation by cutoff and panel-clustering," in *Boundary Element Analysis*, pp. 113–134, ser. Lecture Notes in Applied and Computational Mechanics. Berlin: Springer, 2007.
- [41] M. H. Haddad, M. Ghaffari-Miab, and R. Faraji-Dana, "Transient analysis of thin-wire structures above a multilayer medium using complex-time Green's functions," *IET Microw. Antennas Propag.*, vol. 4, no. 11, pp. 1937–1947, 2010.

- [42] R. van der Heiden, "Aircraft recognition with radar range profiles," Ph.D. dissertation, University of Amsterdam, 1998.
- [43] J.-L. Hu and C. H. Chan, "Novel approach to construct temporal basis functions for time-domain integral equation method," in *Proc. IEEE Antennas Propag. Soc. Int. Symp.*, vol. 4, pp. 172–175. Boston, MA: IEEE, July 2001.
- [44] J.-L. Hu, C. H. Chan, and Y. Xu, "A new temporal basis function for the time-domain integral equation method," *IEEE Microw. Wireless Compon. Lett.*, vol. 11, no. 11, pp. 465–466, 2001.
- [45] J.-L. Hu and C. H. Chan, "Improved temporal basis function for time domain electric field integral equation method," *Electron. Lett.*, vol. 35, no. 11, pp. 883–885, 1999.
- [46] G. X. Jiang, H. B. Zhu, G. Q. Ji, and W. Cao, "Improved stable scheme for the time domain integral equation method," *IEEE Microw. Wireless Compon. Lett.*, vol. 17, no. 1, pp. 1–3, 2007.
- [47] B. H. Jung, Z. Ji, T. K. Sarkar, M. Salazar-Palma, and M. Yuan, "A comparison of marching-on in time method with marching-on in degree method for the TDIE solver," *PIER*, vol. 70, pp. 281–296, 2007.
- [48] B. H. Jung, T. K. Sarkar, S. W. Ting, Y. Zhang, Z. Mei, Z. Li, M. Yuan, A. De, M. Salazar-Palma, and S. M. Rao, *Time and Frequency Domain Solutions of EM Problems*. Hoboken, NJ: John Wiley & Sons, 2010.
- [49] B. H. Jung, Y.-S. Chung, M. Yuan, and T. K. Sarkar, "Analysis of transient scattering from conductors using Laguerre polynomials as temporal basis functions," *ACES Journal*, vol. 19, no. 2, pp. 84–92, 2004.
- [50] G. Kaur and A. E. Yilmaz, "Accuracy-efficiency tradeoff of temporal basis functions for time-marching solvers," *Microw. Opt. Technol. Lett.*, vol. 53, no. 6, pp. 1343–1348, 2011.
- [51] L. Kielhorn and M. Schanz, "Convolution quadrature method-based symmetric Galerkin boundary element method for 3-D elastodynamics," *Int. J. Numer. Meth. Engng.*, vol. 76, no. 11, pp. 1724–1746, 2008.
- [52] E. F. Knott, J. F. Shaeffer, and M. T. Tuley, *Radar Cross Section*, 2nd ed. Raleigh, NC: SciTech Publishing, 2004.
- [53] P. Lacomme, J.-P. Hardange, J.-C. Marchais, and E. Normant, *Air and Spaceborn Radar Systems*. Norwich, NY: William Andrew Publ., 2001.

- [54] V. Lange, “Équations intégrales espace-temps pour les équations de Maxwell. Calcul du champ diffracté par un obstacle dissipatif,” Ph.D. dissertation, Université Bordeaux I, 1995.
- [55] S. Langer and M. Schanz, “Time domain boundary element method,” in *Computational Acoustics of Noise Propagation in Fluids - Finite and Boundary Element Methods*, pp. 495–516. Berlin: Springer, 2008.
- [56] C. Lubich, “Convolution quadrature and discretized operational calculus,” *Numer. Math.*, vol. 52, pp. 129–145, 413–425, 1988.
- [57] —, “On the multistep time discretization of linear initial-boundary value problems and their boundary integral equations,” *Numer. Math.*, vol. 67, pp. 365–389, 1994.
- [58] —, “Convolution quadrature revisited,” *BIT*, vol. 44, pp. 503–514, 2004.
- [59] D. Lynch Jr., *Introduction to RF Stealth*. Raleigh, NC: SciTech Publishing, 2004.
- [60] G. Manara, A. Monorchio, and R. Reggiannini, “A space-time discretization criterion for a stable time-marching solution of the electric field integral equation,” *IEEE Trans. Antennas Propag.*, vol. 45, no. 3, pp. 527–532, 1997.
- [61] Z. Mei, Y. Zhang, T. K. Sarkar, B. H. Jung, A. García-Lampérez, and M. Salazar-Palma, “An improved marching-on-in-degree method using a new temporal basis,” *IEEE Trans. Antennas Propag.*, vol. 59, no. 12, pp. 4643–4650, 2011.
- [62] E. Michielssen, “Progress in space, time, and spectrally adaptive time-domain integral equation solvers,” in *Proc. IEEE Antennas Propag. Soc. Int. Symp.* Chicago, IL: IEEE, July 2012.
- [63] A. F. Peterson, S. L. Ray, and R. Mittra, *Computational Methods for Electromagnetics*. New York: IEEE Press, 1998.
- [64] G. Pisharody and D. S. Weile, “Robust solution of time-domain integral equations using loop-tree decomposition and bandlimited extrapolation,” *IEEE Trans. Antennas Propag.*, vol. 53, no. 6, pp. 2089–2098, 2005.
- [65] J. Portegies Zwart, “Aircraft recognition from features extracted from measured and simulated radar range profiles,” Ph.D. dissertation, University of Amsterdam, 2003.

- [66] A. J. Pray, N. V. Nair, and B. Shanker, “A stable higher order TDIE solver using a separable approximation for convolution with the retarded potential,” in *Proc. IEEE Antennas Propag. Soc. Int. Symp.* Chicago, IL: IEEE, July 2012.
- [67] —, “A stable higher order time domain electric field integral equation solver,” in *Proc. 28<sup>th</sup> ACES Conf.*, pp. 1034–1039. Columbus, OH: ACES, Apr. 2012.
- [68] —, “Stability properties of the time domain electric field integral equation using a separable approximation for the convolution with the retarded potential,” *IEEE Trans. Antennas Propag.*, vol. 60, no. 8, pp. 3772–3781, 2012.
- [69] S. M. Rao and D. R. Wilton, “Transient scattering by conducting surfaces of arbitrary shape,” *IEEE Trans. Antennas Propag.*, vol. 39, pp. 56–61, 1991.
- [70] S. M. Rao, D. R. Wilton, and A. W. Glisson, “Electromagnetic scattering by surfaces of arbitrary shape,” *IEEE Trans. Antennas Propag.*, vol. 30, no. 3, pp. 409–418, 1982.
- [71] P. A. Raviart and J. M. Thomas, “A mixed finite element method for 2-nd order elliptic problems,” in *Math. Asp. Finite Elem. Meth.*, pp. 292–315. Berlin: Springer, 1977.
- [72] D. C. Rizos and D. L. Karabalis, “An advanced direct time domain BEM formulation for general 3-D elastodynamic problems,” *Comp. Mech.*, vol. 15, pp. 249–269, 1994.
- [73] D. C. Rizos and K. G. Loya, “Dynamic and seismic analysis of foundations based on free field B-spline characteristic response histories,” *J. Eng. Mech.*, vol. 128, pp. 438–448, 2002.
- [74] T. Rylander, P. Ingelström, and A. Bondeson, *Computational Electromagnetics*, 2nd ed., ser. Texts in Applied Mathematics, vol. 51. New York: Springer, 2013.
- [75] B. P. Rynne and P. D. Smith, “Stability of time marching algorithms for the electric field integral equation,” *JEMWA*, vol. 4, no. 12, pp. 1181–1205, 1990.
- [76] Y. Saad, *Iterative Methods for Sparse Linear Systems*, 2nd ed. Philadelphia, PA: SIAM, 2003.
- [77] S. Sauter and A. Veit, “A Galerkin method for retarded boundary integral equations with smooth and compactly supported temporal basis functions,” *Numer. Math.*, vol. 123, pp. 145–176, 2013.

- [78] T. Sayah, “Méthodes des potentiels retardés pour les milieux hétérogènes et l’approximation des couches minces par conditions d’impédance généralisées en électromagnétisme,” Ph.D. dissertation, Université de Paris 6, 1998.
- [79] M. Schanz and H. Antes, “A new visco- and elastodynamic time domain boundary element formulation,” *Comp. Mech.*, vol. 20, pp. 452–459, 1997.
- [80] M. Schanz, “A boundary element formulation in time domain for viscoelastic solids,” *Commun. Numer. Meth. Eng.*, vol. 15, pp. 799–809, 1999.
- [81] B. Shanker, A. A. Ergin, K. Aygün, and E. Michielssen, “Analysis of transient electromagnetic scattering from closed surfaces using a combined field integral equation,” *IEEE Trans. Antennas Propag.*, vol. 48, no. 7, pp. 1064–1074, 2000.
- [82] —, “Analysis of transient electromagnetic scattering phenomena using a two-level plane wave time-domain algorithm,” *IEEE Trans. Antennas Propag.*, vol. 48, no. 4, pp. 510–523, 2000.
- [83] B. Shanker, A. A. Ergin, M. Lu, and E. Michielssen, “Fast analysis of transient electromagnetic scattering phenomena using the multilevel plane wave time domain algorithm,” *IEEE Trans. Antennas Propag.*, vol. 51, no. 3, pp. 628–641, 2003.
- [84] B. Shanker, M. Lu, J. Yuan, and E. Michielssen, “Time domain integral equation analysis of scattering from composite bodies via exact evaluation of radiation fields,” *IEEE Trans. Antennas Propag.*, vol. 57, no. 5, pp. 1506–1520, 2009.
- [85] Y. Shi, H. Bağcı, and M. Lu, “On the internal resonant modes in marching-on-in-time solution of the time domain electric field integral equation,” *IEEE Trans. Antennas Propag.*, vol. 61, no. 8, pp. 4389–4392, 2013.
- [86] Y. Shi and S. Li, “A solution of time domain integral equation using Hermite polynomials,” in *Proc. IEEE Int. Symp. MAPE*, pp. 864–867. Hangzhou, China: IEEE, Aug. 2007.
- [87] Y. Shi, M.-Y. Xia, R.-S. Chen, E. Michielssen, and M. Lu, “Stable electric field TDIE solvers via quasi-exact evaluation of MOT matrix elements,” *IEEE Trans. Antennas Propag.*, vol. 59, no. 2, pp. 574–585, 2011.

- [88] C. R. Smith and P. M. Goggans, "Radar target identification," *IEEE Antennas Propag. Mag.*, vol. 35, no. 2, pp. 27–38, 1993.
- [89] P. D. Smith, "Instabilities in time marching methods for scattering: Cause and rectification," *Electromagn.*, vol. 10, no. 4, pp. 439–451, 1990.
- [90] J. A. Stratton, *Electromagnetic Theory*. New York: McGraw-Hill, 1941.
- [91] I. Terrasse, "Résolution mathématique et numérique des équations de Maxwell instationnaires par une méthode de potentiels retardés," Ph.D. dissertation, École Polytechnique, 1993.
- [92] L. N. Trefethen and M. Embree, *Spectra and pseudospectra - The Behavior of Nonnormal Matrices and Operators*. Princeton, NJ: Princeton University Press, 2005.
- [93] B. Troclet, S. Alestra, V. Srithammavanh, and I. Terrasse, "A time domain inverse method for identification of random acoustic sources at launch vehicle lift-off," *J. Vibr. Acoust.*, vol. 133, no. 2, pp. 1–11, 2011.
- [94] F. Valdés, M. Ghaffari-Miab, F. P. Andriulli, K. Cools, and E. Michielssen, "High-order Calderón preconditioned time domain integral equation solvers," *IEEE Trans. Antennas Propag.*, vol. 61, no. 5, pp. 2570–2588, 2013.
- [95] K. J. Vinoy and R. M. Jha, *Radar Absorbing Materials - From Theory to Design and Characterization*. Boston, MA: Kluwer, 1996.
- [96] S. P. Walker, M. J. Bluck, and I. Chatzis, "The stability of integral equation time-domain computations for three-dimensional scattering; similarities and differences between electrodynamics and elastodynamics," *Int. J. Numer. Model. Electron. Networks Dev. Fields*, vol. 15, pp. 459–474, 2002.
- [97] P. Wang, M. Y. Xia, J. M. Jin, and L. Z. Zhou, "Time-domain integral equation solvers using quadratic B-spline temporal basis functions," *Micro. Opt. Technol. Lett.*, vol. 49, no. 5, pp. 1154–1159, 2007.
- [98] X. Wang and D. S. Weile, "Implicit Runge-Kutta methods for the discretization of time domain integral equations," *IEEE Trans. Antennas Propag.*, vol. 59, no. 12, pp. 4651–4663, 2011.
- [99] X. Wang, R. A. Wildman, D. S. Weile, and P. Monk, "A finite difference delay modeling approach to the discretization of the time domain integral equations of electromagnetics," *IEEE Trans. Antennas Propag.*, vol. 56, no. 8, pp. 2442–2452, 2008.

- [100] D. R. Wehner, *High-Resolution Radar*, 2nd ed. Boston, MA: Artech House, 1995.
- [101] D. S. Weile, "A hybrid approach to the time marching solution of Maxwell's equations," in *Proc. MAFELAP Conf.*, p. 291. London, UK: BICOM, June 2013.
- [102] D. S. Weile, G. Pisharody, N.-W. Chen, B. Shanker, and E. Michielssen, "A novel scheme for the solution of the time-domain integral equations of electromagnetics," *IEEE Trans. Antennas Propag.*, vol. 52, no. 1, pp. 283–295, 2004.
- [103] R. A. Wildman, G. Pisharody, D. S. Weile, B. Shanker, and E. Michielssen, "An accurate scheme for the solution of the time-domain integral equations of electromagnetics using higher order vector bases and bandlimited extrapolation," *IEEE Trans. Antennas Propag.*, vol. 52, no. 11, pp. 2973–2984, 2004.
- [104] D. R. Wilton, S. M. Rao, A. W. Glisson, D. H. Schaubert, O. M. Al-Bundak, and C. M. Butler, "Potential integrals for uniform and linear source distributions on polygonal and polyhedral domains," *IEEE Trans. Antennas Propag.*, vol. 32, no. 3, pp. 276–281, 1984.
- [105] E. van 't Wout, D. R. van der Heul, H. van der Ven, and C. Vuik, "The accuracy of temporal basis functions used in the TDIE method," in *Proc. IEEE Antennas Propag. Soc. Int. Symp.*, pp. 2708–2711. Spokane, WA: IEEE, July 2011.
- [106] —, "A provably stable MoT scheme based on quadratic spline basis functions," in *Proc. IEEE Antennas Propag. Soc. Int. Symp.* Chicago, IL: IEEE, July 2012.
- [107] —, "A framework to design temporal basis functions used in boundary element methods for transient electromagnetic scattering," in *Proc. AES*, pp. 675–679. Paris, France: Télécom ParisTech, Apr. 2012.
- [108] —, "Design of temporal basis functions for time domain integral equation methods with predefined accuracy and smoothness," *IEEE Trans. Antennas Propag.*, vol. 61, no. 1, pp. 271–280, 2013.
- [109] —, "The influence of the exact evaluation of radiation fields in finite precision arithmetic on the stability of the time domain integral equation method," accepted for publication in *IEEE Trans. Antennas Propag.*
- [110] —, "Robust formulation of the exact evaluation of radiation fields in the time domain integral equation method," in *Proc. 29<sup>th</sup> ACES Conf.*, pp. 280–284. Monterey, CA: ACES, Mar. 2013.

- 
- [111] —, “Using space-time Galerkin stability theory to define a robust collocation method for time-domain boundary integral equations in electromagnetics,” in *Proc. MAFELAP Conf.*, p. 279. London, UK: BICOM, June 2013.
  - [112] C. G. Wu and G. X. Jiang, “Stabilization procedure for the time-domain integral equation,” *JEMWA*, vol. 21, no. 11, pp. 1507–1512, 2007.
  - [113] A. E. Yilmaz, J.-M. Jin, and E. Michielssen, “Time domain adaptive integral method for surface integral equations,” *IEEE Trans. Antennas Propag.*, vol. 52, no. 10, pp. 2692–2708, 2004.
  - [114] —, “A stable time-domain integral equation formulation for composite structures,” in *Proc. IEEE Antennas Propag. Soc. Int. Symp.*, pp. 2963–2966. Albuquerque, NM: IEEE, July 2006.
  - [115] A. E. Yilmaz, J.-M. Jin, E. Michielssen, and D. S. Weile, “A fast Fourier transform accelerated marching-on-in-time algorithm for electromagnetic analysis,” *Electromagn.*, vol. 21, pp. 181–197, 2001.
-